Universitat Politècnica de València
Departamento de Máquinas y Motores Térmicos

Doctoral Thesis

Analysis of a stratified pre-chamber spark ignition system under lean mixture conditions

Presented by:
Vincenzo Pagano

Supervised by:
Dr. Joaquín de la Morena Borja

in fulfilment of the requirements for the degree of
Doctor of Philosophy

Valencia, July 2020

Ph.D. Thesis

Analysis of a stratified pre-chamber spark ignition system under lean mixture conditions

Written by: Mr. Vincenzo Pagano
Supervised by: Dr. Joaquín de la Morena Borja

Examination committee:

Chairman: Dr. Jesús Vicente Benajes Calvo
Secretary: Dr. Octavio Armas Vergel
Member: Dr. Hua Zhao

Reviewing board:

Dr. Rosario Ballesteros Yañez
Dr. Michele Bardi
Dr. Hua Zhao

Valencia, July 2020

Abstract

In the current work, the characterization of the combustion process inside a stratified pre-chamber spark ignition (PCSI) system is performed. An extensive bibliographical review about the pre-chamber systems developed from the second half of the 20th century until modern times is presented. The review shows that the latest generation systems have the potential to accomplish the emissions limits while providing high performance and low fuel consumption. Nevertheless, many efforts of the scientific community are still needed to allow the large-scale application of the technology. Indeed, based on the outstanding challenges observed, the investigation plan is developed including both experimental and numerical parts.

All experiments were performed by means of the rapid compression-expansion machine (RCEM) in the CMT-Motores Térmicos laboratory. The original cylinder head layout was modified to allow the housing of the pre-chamber itself, fuel injectors, spark plug, pressure transducers in both chamber, and a thermocouple. The test methodology involved the acquisition of the pressure evolution in both main chamber and pre-chamber, the piston position (used to compute the instantaneous cylinder volume), the duration of the auxiliary injection, and the spark ignition point. These are used as input for the zero-dimensional thermodynamic model which simulates the fundamental parameters aims to characterize the PCSI system working cycle. Therefore, a deeper knowledge of the mass interchanged process, induced turbulence field, heat release rate, combustion speed, and flame regime is generated.

Subsequently, to calibrate the zero-dimensional model coefficients under motoring conditions, several 3D CFD simulations were carried out by means of Converge software. Hence, the results of the simulations in terms of interchanged mass and pre-chamber turbulent kinetic energy have been used to calibrate the nozzle discharge coefficient and the turbulence sub-model coefficients for all the pre-chamber geometries. Furthermore, the 3D CFD simulations outputs are analysed to fully understand the flow field structure and the local effect induced by the different nozzles at the spark activation time. The turbulent kinetic energy in terms of intensity and orientation is investigated over several relevant pre-chamber sections. The results reveal a clear relationship between the turbulence developed within the pre-chamber and the orifices structure. Straight orifices or perpendicular jets impact, promote more intense local turbulence due to direct collision while tilted orifices guarantee more homogeneity due to the swirling motion. Additionally, increase the orifice numbers shows benefits on the fluid dynamic homogeneity.

Thus, preceding the experimental campaign several fundamental aspects of

the system are evaluated. The cycle-to-cycle dispersion is explored by means of the statistical assessment showing low pressure peak deviation. The auxiliary injection pressure and timing are optimized for avoiding wall wetting phenomena while ensuring proper air/fuel mixing. Finally, the spark activation point is chosen as a function of the theoretically maximum turbulent flame speed.

Thereby, the experimental campaign is carried out according to tests matrix, in order to evaluate the effect of the equivalence ratio of both chambers, and how the orifices diameter, number, and distribution affect the combustion process. Moreover, chemiluminescence visualization tests, performed by means of the available optical access of the RCEM, are combined with zero-dimensional and 3D CFD results to shed light on the work cycle.

Conclusions suggest a slightly rich mixture inside the pre-chamber combined with the highest number of tilted orifices as the better configuration for improving combustion efficiency under lean and ultra-lean main chamber mixture conditions. Nevertheless, axial orifices should be considered for further investigations. Finally, the author proposes a series of developments considered interesting in both the experimental and numerical fields.

Resumen

En el presente trabajo se realiza la caracterización del proceso de combustión dentro de un sistema de encendido por pre-cámara bajo carga estratificada. Por lo tanto, se presenta una extensa revisión bibliográfica sobre los sistemas de pre-cámara desarrollados desde la segunda mitad del siglo XX hasta los tiempos modernos. El resumen muestra que los sistemas de última generación tienen el potencial de cumplir con los límites de las emisiones, al tiempo que proporcionan un alto rendimiento y un bajo consumo de combustible. No obstante, todavía se necesitan muchos esfuerzos de la comunidad científica para permitir la difusión a gran escala de la tecnología. De hecho, sobre la base de los desafíos abiertos observados, se desarrolla el plan de investigación incluyendo tanto una parte experimental como numérica.

Todos los experimentos se realizan mediante la máquina de compresión-expansión rápida (RCEM) de que dispone el laboratorio CMT-Motores Térmicos . La disposición original de la culata se modificó para permitir el alojamiento de la propia pre-cámara, los inyectores , la bujía, los sensores de presión y un termopar. La metodología de ensayo implica la adquisición de la evolución de la presión tanto en cámara principal como en pre-cámara, el volumen del cilindro, la duración de la inyección auxiliar y el punto de ignición de la bujía. Estos se utilizan como parámetros de entrada para el modelo termodinámico cero-dimensional que devuelve los parámetros fundamentales que caracterizan ciclo de trabajo del sistema PCSI. Por lo tanto, se genera un conocimiento más profundo del proceso de intercambio de masas, del campo de turbulencias inducidas, de la tasa de liberación de calor, de la velocidad de combustión y del régimen de la llama.

Posteriormente, para calibrar los coeficientes del modelo cero-dimensional bajo condiciones de arrastre, se llevaron a cabo varias simulaciones CFD en 3D mediante el software Converge. Por lo tanto, los resultados de las simulaciones en términos de masa intercambiada y energía cinética turbulenta de la pre-cámara se han utilizado para calibrar el coeficiente de descarga de la tobera y los coeficientes del sub-modelo de turbulencia para todas las geometrías de la pre-cámara. Además, se analizan los resultados de las simulaciones CFD para comprender plenamente la estructura del campo de flujo y el efecto local inducido por las diferentes geometriás en el tiempo de activación de la chispa. La energía cinética turbulenta en términos de intensidad y orientación se investiga en varias secciones relevantes de la pre-cámara. Los resultados revelan una clara relación entre la turbulencia desarrollada dentro de la pre-cámara y la estructura de los orificios. Los orificios rectos o los chorros perpendiculares, promueven una turbulencia local más intensa debido a la colisión directa

mientras que los orificios inclinados del campo fluido y del dosado.

Precedentemente al desarrollo de la campaña experimental se evalúan varios aspectos fundamentales del sistema. La dispersión ciclo a ciclo se explora por medio de la evaluación estadística que muestra una baja desviación de los picos de presión. La presión y el punto de inyección auxiliar se optimizan para evitar los fenómenos de mojado de las paredes, asegurando al mismo tiempo una mezcla adecuada de aire/combustible. Finalmente, el punto de activación de la chispa se elige en función de la velocidad máxima teórica de la llama turbulenta.

De este modo, la campaña experimental se lleva a cabo de acuerdo con la matriz de pruebas, con el fin de evaluar el efecto del dosado equivalente de ambas cámaras, y cómo el diámetro, el número y la distribución de los orificios afectan al proceso de combustión. Además, las pruebas de visualización de quimioluminiscencia, realizadas mediante el acceso óptico disponible de la RCEM, se combinan con resultados de CFD y resultados del modelo cero-dimensional para arrojar luz sobre el ciclo de trabajo.

Las conclusiones sugieren que una mezcla ligeramente rica dentro de la pre-cámara combinada con el mayor número de orificios desfasados es la mejor configuración para garantizar un elevada eficiencia de la combustión en condiciones de mezcla pobre y ultra-pobre de la cámara principal. No obstante, los orificios axiales deben ser considerados para investigaciones futuras. Por último, el autor propone una serie de desarrollos considerados interesantes tanto en el campo experimental como en el numérico.

Resum En el present treball es realitza la caracterització del procés de combustió dins d'un sistema d'encesa de pre-cambra soto càrrega estratificada. Per tant, es presenta una extensa revisió bibliogràfica sobre els sistemes de pre-cambra desenvolupats des de la segona meitat del segle XX fins als temps moderns. El resum mostra que els sistemes d'última generació tenen el potencial de complir amb els límits de les emissions, al mateix temps que proporcionen un alt rendiment i un baix consum de combustible. No obstant això, encara es necessiten molts esforços de la comunitat científica per a permetre la difusió a gran escala de la tecnologia. De fet, sobre la base dels desafiaments oberts observats, es desenvolupa el pla d'investigació incloent tant una part experimental com numèrica. Tots els experiments es realitzen mitjançant la màquina de compressió-expansió ràpida (RCEM) de què disposa el laboratori CMT-Motors Tèrmics. La disposició original de la culata es va modificar per a permetre l'allotjament de la pròpia pre-cambra, els injectors , la bugia, els sensors de pressió i un termoparell. La metodologia d'assaig implica l'adquisició de l'evolució de la pressió tant en cambra principal com en pre-cambra, el volum del cilindre, la duració de la injecció auxiliar i el punt d'ignició de l'espurna. Aquests s'utilitzen com a paràmetres d'entrada per al model termodinàic zero-dimensional que retorna els paràmetres fonamen-tals que caracteritzen cicle de treball del sistema PCSI. Per tant, es genera un coneixement més profund del procés d'intercanvi de masses, del camp de turbulències induïdes, de la taxa d'alliberament de calor, de la velocitat de combustió i del règim de la flama. Posteriorment, per a calibrar els coefi-cients del model zero-dimensional sota condicions d'arrossegament, es van dur a terme diverses simulacions CFD en 3D mitjançant el programari Converge. Per tant, els resultats de les simulacions en termes de massa intercanviada i energia cinètica turbulenta de la pre-cambra s'han utilitzat per a calibrar el coeficient de descàrrega de la tovera i els coeficients del sub-model de turbulència per a totes les geometries de la pre-cambra. A més, s'analitzen els resultats de les simulacions CFD per a comprendre plenament l'estructura del camp de flux i l'efecte local induït per les diferents geometries en el temps d'activació de l'espurna. L'energia cinètica turbulenta en termes d'intensitat i orientació s'investiga en diverses seccions rellevants de la pre-cambra. Els resultats revelen una clara relació entre la turbulència desenvolupada dins de la pre-cambra i l'estructura dels orificis. Els orificis rectes o els dolls perpendiculars, promouen una turbulència local més intensa a causa de la collisió directa mentre que els orificis inclinats garanteixen una major homogeneïtat a causa de la generació d'un macro-remolí. A més, l'augment del nombre d'orificis mostra beneficis en l'homogeneïtat fuid-dinàmica. Llavors, abans de la campanya experimental s'avaluen diversos aspectes fonamentals del sistema. La

dispersió cicle a cicle s'explora per mitjà de l'avaluació estadística que mostra una baixa desviació dels pics de pressió. La pressió i el punt d'injecció auxiliar s'optimitzen per a evitar els fenòmens de mullat de les parets, assegurant al mateix temps una mescla adequada d'aire/combustible. Finalment, el punt d'activació de l'espurna es tria en funció de la velocitat màxima teòrica de la flama turbulenta. D'aquesta manera, la campanya experimental es duu a terme d'acord amb la matriu de proves, amb la finalitat d'avaluar l'efecte del dosatge equivalent de totes dues cambres, i com el diàmetre, el número i la distribució dels orificis afecten el procés de combustió. A més, les proves de visualització de quimioluminescència, realitzades mitjançant l'accés òptic disponible de la RCEM, es combinen amb resultats de CFD i resultats del model zero-dimensional per a llançar llum sobre el cicle de treball. Les conclusions suggereixen que una mescla lleugerament rica dins de la pre-cambra combinada amb el major nombre d'orificis desfasats és la millor configuració per a garantir un elevada eficiència de la combustió en condicions de mescla pobra i ultra-pobre de la cambra principal. No obstant això, els orificis axials han de ser considerats per a investigacions futures. Finalment, l'autor proposa una sèrie de desenvolupaments considerats interessants tant en el camp experimental com en el numèric.

"Culture is the only good of humanity that divided between us all, instead of diminishing, will become greater."
Hans-Georg Gadamer

En primer lugar, quiero agradecer al director de mi tesis Joaquín de la Morena por su apoyo incondicional a cualquier hora del día. Además de director, es un buen amigo y compañero de trabajo sin el cual la realización de este proyecto no hubiera sido posible. Por esto y mucho mas le debo una cantidad indefinida de cafés, pizzas y cervezas.

También quiero agradecer al director del centro de investigación CMT - Motores Termicos, José M. Desantes, a J.Benajes y J.V.Pastor para facilitarme todos los medio necesarios para desarrollar la investigación presentada en mi tesis. Ademas quiero agradecer del trato recibido desde el per-sonal de secretaria e informática sin las cuales estaria perdidos en las tareas burocráticas.

A la vez quiero agradecer a todos los miembros de mi linea de investigación empezando por el jefe R.Payri que siempre han dejado las puertas abiertas para cualquier dudas profesionales y personales. También agradezco el trabajo de todos los técnicos de laboratorio: Omar que ha estado presente desde el primer ensayo llevado a cabo con éxito (y en muchos mas). José Enrique, cuya opinión técnica ha sido indispensable a la hora de tomar decisiones importantes. El Torner Jose que ha arreglado miles de desastres que he hecho en el laboratorio. Sergi para la ayuda con las herramientas eléctricas. En este elenco tampoco pueden faltar mis compañeros de despacho lo cual hicieron que fuera un placer ir a trabajar: Sebas y Mary los primeros años, y Maria y Kike los ultimos. De la misma manera, no voy a olvidar el señor Dario una de las personas más inteligentes que he conocido en mi vida, cuya ayuda fue indispensable en las primeras etapas del desarrollo de la tesis. Finalmente quiero agradecer todos los compañeros que colaboraron conmigo a lo largo de estos años: Jorge,Cristina,David,Alvaro,Santi,Lucas,etc.

A toda esta gente le digo gracias desde el corazón por ser en primer lugar grandes personas y también grandes profesionales.

De igual forma tengo que agradecer amigos personales que contribuyeron a que esta ciudad maravillosa se convertiera en mi segundo hogar. Los amigos del IIE: Fran, Alex y Rafa. Natasha y Charly siempre a mi lado desde que he llegado a Valencia. Los amigos del baile y del fútbol. Abian y Maria para las vacaciones increíbles que hemos pasado juntos. Todos los compañeros de piso: Miky, David, Julian, Ilaria, Francy, Santi, Giulia, Ago, Felix, Gabry, Mattia, Lucas, Alberto, Gianf, Tom, Cris.

Por ultimos (pero solo en orden temporal) Fran, Marina, Armando, Dieghini, Marco, Jesus, Santi, los Mario, Lucas, Cesar, Tomas, Rami, Victor, Alberto y todos lo que me estoy olvidando por el camino: muchissimas gracias.

Doveroso é anche il ringraziamento alle persone che hanno reso i 3 mesi di lavoro presso General Motor a Torino, un esperienza indimenticabile: a Francesco, Giacomo, Antonello, Andres, Francesca e Manuel va il mio abbraccio piú affettuoso. Un grazie infinite anche ai numerosi amici italiani conosciuti qui a Valencia: Miky, J, il Biondo, Jacopo, il Vecchio, Simo, Mauri e tutti gli altri.

E finalment vogl ricere grazie a tutt é perzone cchiú important ra vita mi: cumpá Zaffon, Toto, o Papir, zio Snodo, o Caput, o Pobosk, er Socio, e tutt e frat fidat ro rion. A fratm Luca e Alfredo, mammema Maria, la mia seconda madre zi Aida e in general a tutt a famiglia mi, vogl ricer che vi amo immensament.

Concludendo ringrazio una persona speciale, che mi sopporta ormai da molti anni: la mia anima gemella Rita. Grazie per esserci sempre stata e sopratutto per avermi appoggiato sempre e comunque. Che il futuro ci riservi l'ennesima tappa insieme, ti amo!

Contents

List of Figures

List of Tables

Chapter 1

Introduction

1.1 Background and Motivation

Global warming and pollution (especially in dense urban areas) are two of the most critical factors for the sustainability of the environment and air quality. The Intergovernmental Panel on Climate Change (IPCC) of the United States of America affirmed that man-made generation of CO_2 and CO is the principal cause of the global warming problem [1, 2]. Rahmstrof et al. [3] established that for the next 100 years the global temperature will increase between 2.5 and $6.0°C$, almost 5 times the temperature rise achieved over the past 100 years. In the last decades, public opinion has strongly criticized the exponential increase of pollution in the urban air, pushing the world government executives to implement new measures against such phenomena [4]. These reasons, combined with the continuous search for improving engine performance, motivated the scientific community to investigate alternative methods to conventional combustion systems able to fulfill the current and future requirements. Nowadays, some of the most promising alternatives can be grouped into: usage of alternative fuels (including biofuels), powertrain electrification and advanced combustion methods.

Biofuels have been investigated due to their potential to reduce the net CO_2 thanks to the positive contribution reached during the lifetime of the vegetable source generally used for their synthesis, as well as the reduction of dependence from fossil fuels. Selvam and Valdivel [5] studied the engine performance and tail pipe emissions of a direct injection diesel engine fuelled with methyl esters of beef tallow compared with conventional diesel fuel.

For biodiesel and its blends (B5-25-50-75) the Brake Specific Fuel Consumption (BSFC) is higher than for standard diesel fuel, while the brake torque slightly decreases at full load engine operation. The authors concluded that the proposed alternative fuel and its blends can be used as a diesel surrogates without any engine modifications, pointing out the HC, CO and smoke emissions reduction. Altaie et al. [6] found similar results for a conventional diesel engine fuelled with palm oil methyl ester and methyl oleate blends. They confirmed the higher brake specific fuel consumption and lower brake torque for the biodiesel, linking it to his lower calorific value. Furthermore CO, HC and exhaust gas temperature reductions were also observed, probably induced by higher cetane number and oxygen content in methyl esters, affecting the ignition delay and subsequent combustion phasing.

In addition, other researchers have focused their attention on the main parameters that control the combustion evolution with biofuels [7–9]. Ozturk [10] performed an experimental campaign with a single-cylinder direct injection engine fuelled with blends of diesel and a mixture of canola oil-hazelnut soapstock biodiesel. He concluded that the ignition delay, the maximum in-cylinder pressure and the maximum heat release rate decrease as biodiesel percentage increases. Ozturk results have been confirmed by Labeckas and Slavinskas [11] also for blends with rapeseed oil methyl ester. The engine performance was examined for light, medium and high loads at different engine speed (1400 and 2200 revolutions per minute) showing a decrease in terms of ignition delay and maximum heat release rate.

Taylor et al.[12] explored the performance of 4 gasoline/alcohol blends as fuel surrogates. Methanol, ethanol, iso-propanol, and n-propanol, have been tested in a multi-valve engine in order to evaluate the exhaust emissions and burning rate. As main conclusions, the gasoline and alcohol blends are able to deeply reduce the CO, HC and NO emissions (more than 50%), helping significantly to improve air quality. Moreover, gasoline/alcohol blends have a higher octane number compared with pure gasoline, thus allows the engine compression ratio to increase without the risk of knock [13]. Also, the vapour pressure of alcohols is far lower than the gasoline so cold-starts are facilitated [14, 15].

Looking to the future, electric and hybrid vehicles are likely to become a large-scale reality, or at least increase their market share compared to the current scenario. Lombardi et al. [16] studied the life cycle assessment of 4 types of vehicles (conventional gasoline, pure electric, hybrid gasoline-electric, and fuel cell-battery vehicle). The results underlined that electric and hybrid technologies allow a reduction of several environmental indicators, related to

cumulative energy demand, global warming, fossil resource depletion, and particulate matter formation. In this scenario, hybrid vehicle showed the best results, confirming that the pure electric performance is still fully dependent on the battery technology and electric production process. In this perspective, the increase in renewable sources for energy production would help the large-scale diffusion [17]. Huang et al. [18] carried out experimental tests, comparing performance and emissions between an hybrid car and a conventional gasoline one on real-driving conditions (RDC). Despite both technologies showed to be capable to meet current emission limits, there was no perceivable reduction of HC and CO emissions for the hybrid vehicle in RDE tests. The authors concluded that, while it is possible to achieve the targets in fuel consumption reduction, hybrid cars do not bring the expected benefits to urban air quality. Actually, the electrification of the powertrain reduces the heating delivered to the aftertreatment system (low exhaust gas temperature), whose efficiency drops dramatically [19, 20].

Over the past thirty years, researchers have identified low-temperature combustion [21] as an alternative method to increase thermal efficiency while decreasing pollutants formation [22]. Onish et al. [23] investigated the HCCI concept for a two-stroke gasoline engine, observing a significant improvement in fuel consumption and reduction in engine-out emissions. Foster and Najt [24] further explored the work to four-stroke engine, concluding that HCCI has a difficult control on the ignition process and a limited operating range compared with conventional technologies. Shim et al [25] compared different concepts of low combustion temperature as HCCI and PCCI combustion by means of a single-cylinder diesel engine. Although good results were achieved in terms of NOx and PM emissions, the THC and CO emissions increase significantly due to problems in combustion control and quenching effects. Dual fuel PCCI may partially solve the problem thanks to an easier control on the combustion start. Despite the CO_2 reduction, the THC emission level was still too high. Benajes et al. evaluated the potential of dual-mode RCCI and conventional diesel engine strategies through homologation cycle simulations [26]. The results show that duel fuel strategy under real drive emissions cycle (RDE) allows reducing NO_x, Soot, HC and CO levels around 50% when comparing with conventional diesel combustion [27]. Desantes et al. [28, 29] conducted more basic analysis on the autoignition propagation under HCCI conditions by means of a rapid compression-expansion machine. They characterized the ignition delay for pure fuels as well as different blends, evaluating the autoignition repeatability, the pressure waves development, the combustion velocity and characteristic combustion duration.

The previous works highlight the need for a proper control of the ignition when operating in the low-temperature combustion regime. Several technological concepts have been investigated as potential replacements for conventional ignition methods, including the laser-induced ignition [30], the plasma igniter [31] and the pre-chamber ignition systems [32]. The primary benefits of the laser ignition are the possibility to choose the location and timing of the ignition to better control the burning process in real time [30]. In addition, the plasma ignition shows to be faster and allows to extend the standard ignition limits. Even if the HC emissions may decrease due to better combustion stability, the outstanding challenge is the high flame temperature leading to high NOx production [33].

The advanced pre-chamber spark-ignition (PCSI) concept aims to overcome the latter limitations. Toulson et al.[34] analysed several configurations of pre-chamber ignition system, evaluating the ways in which this type of combustion system can operate. The authors claimed that the concept of a small pre-chamber volume fed with an auxiliary injection in the pre-chamber is the most likely future application of this technology. Attard et al.[35] showed the performance, efficiency and emissions of a pre-chamber spark ignition engine. The authors demonstrated the improvement in thermal efficiency with near zero engine out NOx emission under ultra-lean mixture conditions [36]. Indeed, with growing global concerns regarding the environment and energy supply, the benefits offered by pre-chamber jet ignition combustion could be the way forward, hence it is envisioned that this system will be further developed to meet future world requirements. Nevertheless, several outstanding challenges about the system control strategy over the complete engine map, hardware complexity, reduction of knock appearance, combustion stability, etc. have to be resolved before the large-scale spread of these systems on the market.

1.2 Research questions and Objectives

Despite the wide amount of work carried out by the scientific community, there are still research fields to be explored to fully understand the dynamics of the PCSI system. This thesis aims to answer the following research open points by means of experimental and numerical studies:

1. How do the main chamber and pre-chamber interact? Are the pre-chamber nozzles working in subsonic or choked conditions? Do the flames propagate through these nozzles?

2. How does the turbulence cascade develop in the pre-chamber? What are the main production and dissipation turbulence sources?

3. In which combustion regime does the flame propagate in the pre-chamber? How do the pre-chamber auxiliary injection and the mixture conditions affect the heat release rate and flame propagation characteristics?

4. How can the existing correlations for heat losses, turbulence and flame propagation prediction be adapted for the pre-chamber?

5. How does the pre-chamber orifices configuration affect the jet structure incoming into the main chamber?

6. How many combustion regimes do the jets induce as they travel towards the main chamber walls? Will the flame be self-sustainable at lean conditions once the discharge from pre-chamber is finished?

The main goal of the present work is to deeply characterize the combustion development in the pre-chamber spark ignition system under stratified mixture conditions. To accomplish the objectives, the author made use of the facilities and tools made available by CMT Motores Térmicos. First of all, the combustion chamber layout of a rapid compression-expansion machine (RCEM) has been adapted to include the pre-chamber geometries, and the fuel injection and ignition systems. Then, the experimental campaigns have been carried out, recording the instantaneous piston position and pressure traces for a set of operating conditions. Thus, the acquired data have been processed and analysed by means of a MatLab zero-dimensional home-made codes. Finally the 0D model results, have been coupled with visualization test (performed by means of the available RCEM optical windows) and 3D CFD simulations carried out with CONVERGE software.

1.3 Thesis outline

The thesis is organized in seven chapters, starting with this brief introduction (**chapter 1**), that presented the background, motivation and primary objectives of the work completed.

Chapter 2 describes the fundamental concepts of the lean and turbulent combustion as much in the conventional spark ignition engine as in the pre-chamber systems. The description mainly focuses on the modern pre-chamber concept with a small volume.

Chapter 3 outlines the facilities, equipment and methodologies used for the experimental campaign. The rapid compression-expansion machine, the fuel injection and ignition systems are described, together with the corresponding working principles and test procedure. The optical techniques are detailed as well, along with the general data and image processing approach.

Chapter 4 explains the main and pre-chamber thermodynamic models, including the 0D model equations that control the mass interchange, turbulence, heat release rate, laminar and turbulent flame propagation. Then, the 3D CFD numerical models and methodologies for the turbulence prediction under motored condition are introduced. Finally, 3D-CFD results are used as baseline to adjust a K-k-ϵ zero-dimensional model for the pre-chamber. In addition, the turbulence analysis is extended to other pre-chamber geometries with the aim of correlating the turbulent field with the combustion results.

Chapter 5 is focused on the experimental analysis of the pre-chamber combustion concept. First of all, the results are described in terms of pressure ratio between pre-chamber and main chamber, the exchanged mass, the turbulence field, the heat release rate and the combustion velocities for the baseline case. Subsequently, the influence of both chambers equivalence ratio on the combustion process is evaluated.

In **chapter 6**, the influence of the pre-chamber nozzle geometry on the combustion development is depicted. The main aspects considered are the number of orifices and their distribution. The analysis is presented according to the structure of chapter 5.

Lastly, **chapter 7** presents a summary of the work performed, as well as the main conclusions drawn from it. In addition, some ideas for future research are proposed from the knowledge and experience acquired during the development of this Thesis.

References

[1] Truth, An Inconvenient. "directed by Davis Guggenheim". In: *Performed by Al Gore* (2006).

[2] James, Revis, Richels, Richard, Blanford, Geoff, and Gehl, Steve. "The power to reduce CO {sub 2} emissions: the full portfolio. Discussion paper". In: (2007).

[3] Rahmstorf, Stefan, Foster, Grant, and Cahill, Niamh. "Global temperature evolution: recent trends and some pitfalls". In: *Environmental Research Letters* 12.5 (2017), p. 054001.

[4] Bose, Bimal K and Wang, Fei. "ENERGY, ENVIRONMENT, POWER ELECTRONICS, RENEWABLE ENERGY SYSTEMS, AND SMART GRID". In: *Power Electronics in Renewable Energy Systems and Smart Grid: Technology and Applications* (2019), pp. 1–83.

[5] Selvam, D John Panneer and Vadivel, K. "Performance and emission analysis of DI diesel engine fuelled with methyl esters of beef tallow and diesel blends". In: *Procedia Engineering* 38 (2012), pp. 342–358.

[6] Altaie, Mohamad A Hasan et al. "Performance and exhaust emission characteristics of direct-injection diesel engine fueled with enriched biodiesel". In: *Energy conversion and management* 106 (2015), pp. 365–372.

[7] Ballesteros, R, Guillén-Flores, J, and Barba, J. "Environmental and health impact assessment from a heavy-duty diesel engine under different injection strategies fueled with a bioethanol–diesel blend". In: *Fuel* 157 (2015), pp. 191–201.

[8] Muralidharan, K, Vasudevan, D, and Sheeba, KN. "Performance, emission and combustion characteristics of biodiesel fuelled variable compression ratio engine". In: *Energy* 36.8 (2011), pp. 5385–5393.

[9] Agarwal, Avinash Kumar et al. "Effect of fuel injection pressure and injection timing of Karanja biodiesel blends on fuel spray, engine performance, emissions and combustion characteristics". In: *Energy Conversion and Management* 91 (2015), pp. 302–314.

[10] Öztürk, Erkan. "Performance, emissions, combustion and injection characteristics of a diesel engine fuelled with canola oil–hazelnut soapstock biodiesel mixture". In: *Fuel Processing Technology* 129 (2015), pp. 183–191.

[11] Labeckas, Gvidonas and Slavinskas, Stasys. "Combustion phenomenon, performance and emissions of a diesel engine with aviation turbine JP-8 fuel and rapeseed biodiesel blends". In: *Energy Conversion and Management* 105 (2015), pp. 216–229.

[12] Taylor, Andrew B et al. *Gasoline/alcohol blends: exhaust emissions, performance and burn-rate in a multi-valve production engine*. Tech. rep. SAE Technical Paper, 1996.

[13] García, Antonio, Monsalve-Serrano, Javier, Martínez-Boggio, Santiago, Roso, Vinícius Rückert, and Santos, Nathália Duarte Souza Alvarenga. "Potential of bio-ethanol in different advanced combustion modes for hybrid passenger vehicles". In: *Renewable Energy* 150 (2020), pp. 58–77.

[14] Lapuerta, Magín, Ballesteros, Rosario, and Barba, Javier. "Strategies to introduce n-butanol in gasoline blends". In: *Sustainability* 9.4 (2017), p. 589.

[15] Thring, RH. "Alternative fuels for spark-ignition engines". In: *SAE transactions* (1983), pp. 715–725.

[16] Lombardi, Lidia, Tribioli, Laura, Cozzolino, Raffaello, and Bella, Gino. "Comparative environmental assessment of conventional, electric, hybrid, and fuel cell powertrains based on LCA". In: *The International Journal of Life Cycle Assessment* 22.12 (2017), pp. 1989–2006.

[17] Benajes, Jesús, García, Antonio, Monsalve-Serrano, Javier, and Martínez-Boggio, Santiago. "Emissions reduction from passenger cars with RCCI plug-in hybrid electric vehicle technology". In: *Applied Thermal Engineering* 164 (2020), p. 114430.

[18] Huang, Yuhan et al. "Fuel consumption and emissions performance under real driving: Comparison between hybrid and conventional vehicles". In: *Science of The Total Environment* 659 (2019), pp. 275–282.

[19] Knorr, Thomas, Ellmer, Dietmar, Baensch, Simon, and Schatz, Dr Axel. "Optimization of the 48 Volt Hybrid Technology to Minimize Local Emissions in the RDE". In: *Aachener Colloquium*. 2018, pp. 08–10.

[20] Pham, Allen and Jeftic, Marko. *Characterization of Gaseous Emissions from Blended Plug-In Hybrid Electric Vehicles during High-Power Cold-Starts*. Tech. rep. SAE Technical Paper, 2018.

[21] John, B. "Heywood, Internal combustion engine fundamentals". In: *Pub: McGraw Hill International Editions* (1988).

[22] Bunce, Michael, Blaxill, Hugh, Kulatilaka, Waruna, and Jiang, Naibo. *The effects of turbulent jet characteristics on engine performance using a pre-chamber combustor*. Tech. rep. SAE Technical Paper, 2014.

[23] Onishi, Shigeru, Jo, Souk Hong, Shoda, Katsuji, Jo, Pan Do, and Kato, Satoshi. "Active thermo-atmosphere combustion (ATAC)âa new combustion process for internal combustion engines". In: *SAE Transactions* (1979), pp. 1851–1860.

[24] Najt, Paul M and Foster, David E. "Compression-ignited homogeneous charge combustion". In: *SAE Transactions* (1983), pp. 964–979.

[25] Shim, Euijoon, Park, Hyunwook, and Bae, Choongsik. "Comparisons of advanced combustion technologies (HCCI, PCCI, and dual-fuel PCCI) on engine performance and emission characteristics in a heavy-duty diesel engine". In: *Fuel* 262 (2020), p. 116436.

[26] Benajes, Jesús, García, Antonio, Monsalve-Serrano, Javier, and Sari, Rafael Lago. "Fuel consumption and engine-out emissions estimations of a light-duty engine running in dual-mode RCCI/CDC with different fuels and driving cycles". In: *Energy* 157 (2018), pp. 19–30.

[27] Benajes, Jesús, Pastor, José V, García, Antonio, and Monsalve-Serrano, Javier. "The potential of RCCI concept to meet EURO VI NOx limitation and ultra-low soot emissions in a heavy-duty engine over the whole engine map". In: *Fuel* 159 (2015), pp. 952–961.

[28] Desantes, José M, López, J Javier, García-Oliver, José M, and López-Pintor, Darío. "A phenomenological explanation of the autoignition propagation under HCCI conditions". In: *Fuel* 206 (2017), pp. 43–57.

[29] Desantes, José M, López, J Javier, Molina, Santiago, and López-Pintor, Darío. "Theoretical development of a new procedure to predict ignition delays under transient thermodynamic conditions and validation using a Rapid Compression–Expansion Machine". In: *Energy Conversion and Management* 108 (2016), pp. 132–143.

[30] Ronney, Paul D. "Laser versus conventional ignition of flames". In: *Optical Engineering* 33.2 (1994), pp. 510–522.

[31] Smy, PR, Clements, RM, Simeoni, D, and Topham, DR. "Plasma expulsion from the plasma jet igniter". In: *Journal of Physics D: Applied Physics* 15.11 (1982), p. 2227.

[32] Castilla Alvarez, Carlos Eduardo, Couto, Giselle Elias, Roso, Vinícius Rückert, Thiriet, Arthur Braga, and Valle, Ramon Molina. "A review of prechamber ignition systems as lean combustion technology for SI engines". In: *Applied Thermal Engineering* 128 (2018), pp. 107–120.

[33] Thelen, Bryce C, Chun, Daekeun, Toulson, Elisa, and Lee, Tonghun. "A study of an energetically enhanced plasma ignition system for internal combustion engines". In: *IEEE Transactions on Plasma Science* 41.12 (2013), pp. 3223–3232.

[34] Toulson, Elisa, Schock, Harold J, and Attard, William P. "A review of pre-chamber initiated jet ignition combustion systems". In: (2010).

[35] Attard, William P and Parsons, Patrick. "A normally aspirated spark initiated combustion system capable of high load, high efficiency and near zero NOx emissions in a modern vehicle powertrain". In: *SAE International Journal of Engines* 3.2 (2010), pp. 269–287.

[36] Attard, William P and Blaxill, Hugh. "A single fuel pre-chamber jet ignition powertrain achieving high load, high efficiency and near zero NOx emissions". In: *SAE International Journal of Engines* 5.3 (2012), pp. 734–746.

Chapter 2

Premixed combustion in spark ignition engine: fundamentals and developments

2.1 Introduction

As already introduced, the current thesis analyses the potential of a pre-chamber spark ignition system to achieve lean combustion operation. Therefore, this chapter starts highlighting the fundamentals of the lean (or dilute) premixed combustion process, detailing the main advantages and concerns related to its application to spark ignition engines [1, 2]. Then, a historical review of the pre-chamber system is depicted. Finally, the main findings in the literature regarding modern pre-chamber systems are summarized.

2.2 Lean and diluted combustion in spark ignition engines

Spark ignition combustion under stoichiometric conditions has been worldwide spread in production engines mainly for the following reasons:

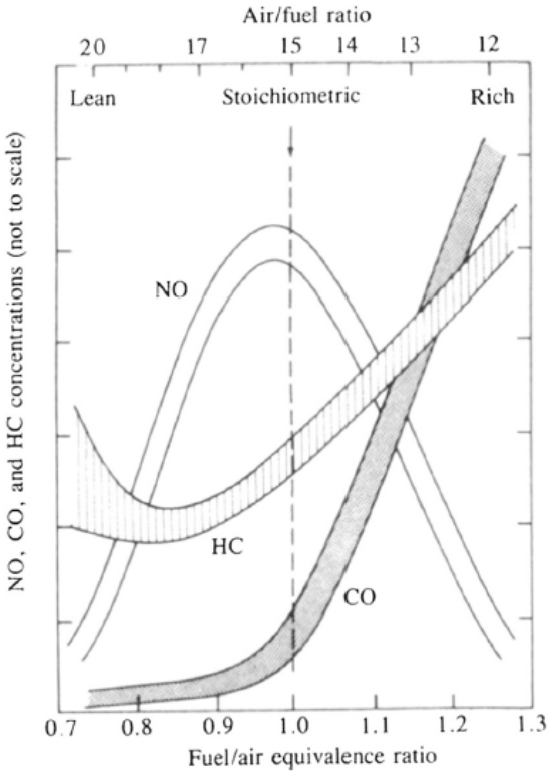

Figure 2.1: Spark ignition engine emissions as a function of fuel-air equivalence ratio [1]

- The maximum engine power can obtained by maximizing the flame burning speed. Stoichiometric or slightly rich mixtures ($1.0 < \phi < 1.1$) ensure high laminar flame speed.
- Stoichiometric mixture ensures an acceptable cycle-to-cycle variation and avoids misfire or partial burning problems.
- Stoichiometric operation allows a good balance in the three way catalyst operation, allowing a simultaneous abatement of nitrogen oxides, carbon monoxide and unburned hydrocarbons.
- Cold start of vehicle emission test cycle is the most critical phase due to the low engine and catalyst temperature. With aim of minimize the cold start time, the aftertreatment system must reach a minimum operation

temperature as fast as possible [3]. Therefore, stoichiometric combustion ensures a quick temperature rise, due to the high average combustion temperature.

Due to the continuing demand for fuel savings and emission reductions, the scientific community has been driven to find viable alternatives to traditional combustion methods. Since the beginning of the twentieth century lean combustion spark ignition engines show several advantages in terms of efficiency [4], fuel consumption [5] and reduction of carbon monoxide and oxides of nitrogen emissions [6, 7] (Fig.2.1). Additionally, in modern supercharged SI engines a slightly rich mixture is used to keep the exhaust temperature below the turbine damage threshold. This enrichment induces a degradation in the fuel consumption and an increase of the CO and HC emissions. Hence, alternative strategies such as EGR dilution or lean combustion are seen as more efficient alternatives to reduce the exhaust gas temperature [8]. However, lean and diluted combustion has open challenges in terms of combustion speed and stability.

In this section the fundamental positive and negative impacts of lean combustion in terms efficiency, emissions and performance will be summarized and compared with conventional stoichiometric combustion.

2.2.1 Thermal efficiency

The ideal thermal efficiency of an internal combustion engine primarily depends on two parameters:

1. The compression ratio.
2. The specific heat ratio of the working fluid.

Increasing the compression ratio in a conventional spark-ignition engine, means to raise the risk of knock occurrence [9] due to the resulting high flame temperature [10] and the end-gas compression ignition [11]. Moreover, high compression ratio promotes pre-ignition, before the spark discharging, caused by hot spots, and local residual gas [12]. Lean or dilute combustion induces lower temperature during the combustion process thanks to the heat absorbed by the extra air or inert gases. This allows the engine to be designed for higher compression ratio without knocking appearance [13]. In addition, for the particular case of the lean operation, the combined effect of decreasing the average combustion temperature and increasing the amount of air maximizes

the specific heat ratio [14], resulting in an improvement in the theoretical thermal efficiency.

Caton [15] analysed the combustion process for several operation modes and their combinations. The research engine selected was a 5.7l , V-8 setup with an initial compression ratio equal to 8.0 operated at 2000 rpm. The main goal was to determine the single impacts of high CR, fast burn, EGR strategy and lean mixture on the engine thermal efficiency.

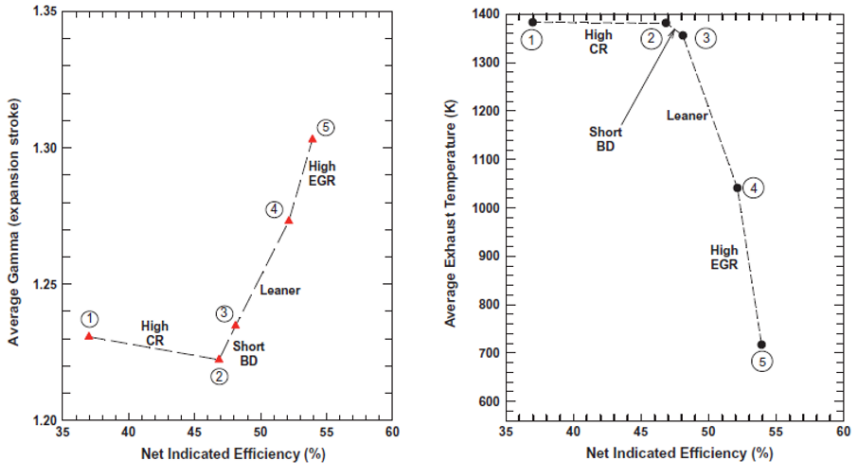

Figure 2.2: Right: Average ratio of specific heats (right) and average exhaust gas temperature (left) as functions of the net indicated efficiency.

Figure 2.2 summarizes the main conclusions of this research. On the left, the higher compression ratio (from 8 to 16) significantly increased the efficiency despite the slight decrease of the γ. The charge dilution, achieved as leaner mixture and/or high EGR rate, provided significant efficiency improvement due to the γ increase and combustion average temperature decrease. Finally, results showed reduced NOx emissions while running the engine combining the four upgrades. Nonetheless, it is important to point out that the low exhaust temperature (low enthalpy) can affect the turbocharger efficiency, thus further investigations are necessary to confirm or refute these results over the whole engine map.

2.2.2 Lean flammability limits and ignition limits

The start of combustion in the spark-ignition engine is induced by the energy released through the spark plug activation. The energy supplied to the air/fuel mixture must be sufficient to force the chemical chain reactions, responsible for the initial flame kernel formation and its propagation inside the combustion chamber. As first step, the spark discharge heats up the mixture around the electrodes, initiating its combustion. Subsequently, the energy released by the combustion of this initial mixture will serve as the ignition energy for the surrounding region, inducing the flame propagation. This process is directly linked to the characteristics of the fuel-air mixture (temperature, pressure and composition), and also related to other aspects which affect heat transfer and dissipation (flow field, turbulence, vicinity to walls, etc).

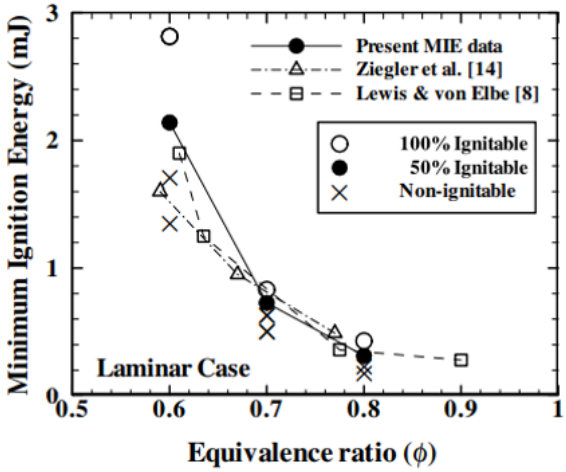

Figure 2.3: Minimum ignition energy under quiescent condition as function of ϕ for lean fuel-air mixture [16]

Figure 2.3 shows the minimum ignition energy under quiescent conditions for lean methane-air mixtures as a function of the equivalence ratio ϕ. As the mixture becomes leaner, more energy is needed to force the start of combustion [16] due to the higher heat absorbed by the extra air (reducing the temperature reached during the discharge) and the lower fuel quantity and energy available between the spark electrodes.

Indeed, two lean limits should be considered for the SI lean burn engine: the lean flammability limit (LFL) and the lean ignition limit (LIL). The first

one is a direct function of the pressure and temperature conditions inside the combustion chamber, and is the leanest mixture that allows a successful ignition independently on the engine and ignition hardware used. Zabetakis [17] states that LFL can be extended by increasing the combustion chamber temperature, according to the modified Burgess-Wheeler correlation:

$$LFL = L - (0.75/H_C) * (T - 25) \tag{2.1}$$

where L is the volume percentage of fuel, and $/H_C$ is the fuel lower heating value.

The lean ignition limit instead is defined by the minimum energy (supplied by the ignition system) that should be provided to a differential mixture volume in order to raise its temperature over the ignition threshold [18] for a specific engine hardware, taking into account aspects such as the combustion chamber design, the air flow field or the spark plug location. Hence, the spark plug type, discharge duration [19], electrode gap and material [20] are relevant parameters to define this lean ignition limit for lean combustion compared to stoichiometric one.

When running the engine under lean or dilute mixtures, it is possible that the lean ignition limit is reached, leading to misfire, partial combustion, or flame extinguishing.

2.2.3 Laminar flame speed

The laminar flame speed has been object of intensive research due to its crucial role in the spark-ignition engine development.

Metghalchi-Keck [21] performed laminar flame speed measurements of air mixed with methanol, isoctane and indolene over a wide range of temperatures and pressure by means of a constant volume bomb method run at engine like conditions. This method included measurements and corrections to take into account several phenomena as temperature gradient in the burned gas, heat losses through the walls, energy introduced by the spark plug system or heat losses between the electrodes. The measurements of the burning velocity have been fitted to the following correlation:

$$S_L(\phi, T_u, P_u) = S_{L0} \left(\frac{T_u}{T_0}\right)^{\alpha} \left(\frac{p_u}{p_0}\right)^{\beta} \tag{2.2}$$

$$\alpha(\phi) = 2.18 - 0.8(\phi - 1) \tag{2.3}$$

$$\beta(\phi) = 0.16 - 0.22(\phi - 1) \tag{2.4}$$

where T_u, p_u are the temperature and pressure of the unburned mixture, S_{L0} is the velocity measured at $T_u = T_0$ and $p_u = p_0$ for a given equivalence ratio, and α and β are the tuning constants depending on the mixture composition.

DiStaso et al. [22] used the Metghalchi-Keck correlations, extending the higher and lower limits of the validation range for commercial pure fuels and their blends. The α and β coefficient were modelled as follows:

$$\alpha(\phi) = \alpha_2\phi^2 - \alpha_1\phi + \alpha_0 \tag{2.5}$$

$$\beta(\phi) = -\beta_2\phi^2 + \beta_1\phi - \beta_0 \tag{2.6}$$

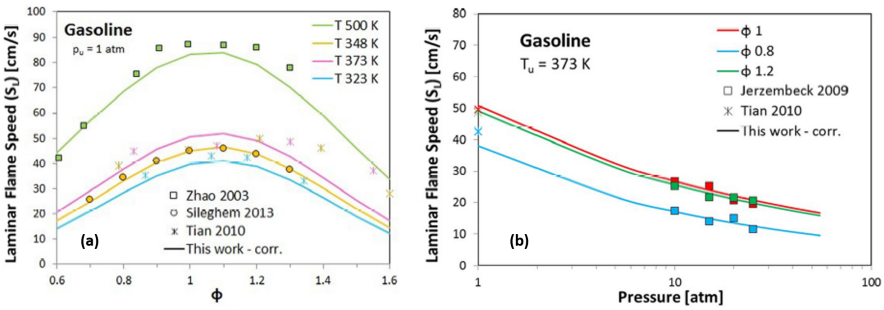

Figure 2.4: Initial temperature influence on gasoline laminar flame speed at room pressure (a). Initial pressure influence at three different equivalence ratios and at an initial temperature of 373K (b)[22].

Fig.2.4 shows the behaviour of the laminar flame speed under different unburned mixture temperature (a) and pressure (b) as function of the equivalence ratio (ϕ). According with the empirical correlation, the laminar combustion speed is maximum for a slightly rich mixture while it decreases for excessively rich or poor mixtures leading to misfire and flame quenching. Furthermore, it can be observed the opposite effects of temperature versus pressure according to the correlation exponents α and β.As the unburned mixture temperature rises, the laminar flame speed increase, while on contrary the pressure rise causes a velocity decrease.

2.2.4 Flame quenching

The study of flame-wall interactions is crucial for the understanding of the combustion evolution close to the combustion chamber surfaces. As is known, a turbulent premixed flame stops propagating towards the wall due to deceleration of the chemical reactions, as a result of high heat losses through the surfaces.

The extinction phenomena depends on several factors regarding not only the surface state (geometry, temperature) but also the air/fuel mixture parameters (temperature, composition). Many theoretical and experimental studies have led to the characterization of the flame quenching distance/diameter and extinguishing parameters for flames propagates in pipes between two plates. Therefore, the combustion chamber geometry optimization is strictly related to the flame quenching, responsible for the production of undesirable unburned hydrocarbons.[23, 24].

Ferguson and Keck [25] developed a correlation of quenching diameter based on a Péclet number, laminar flame speed and lean limit flame temperature. The Péclet number is defined as follows:

$$Pe = \frac{u_C * \delta_q}{\alpha} \tag{2.7}$$

where u_C is the combustion speed, δ_q is the quenching distance and α is the thermal diffusivity as a function of the thermal conductivity (k), mixture density (ρ), and specific heat at constant pressure (C_p). Close to the wall the combustion speed is equal to the laminar flame speed (S_L), and the flame thickness is function of the laminar flame speed and thermal diffusivity. Taking into account this consideration, when the Pe number is equal to the unit, the quenching lower limit is reached after which the heat released by the flame is lower than the heat dissipated through the wall.

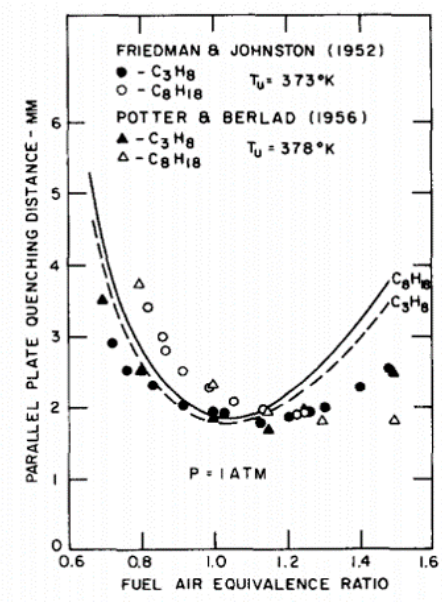

Figure 2.5: Flame quenching distance as function of the equivalence ratio for propane and isoctane fuels[25].

Then, isoctane and propane laminar flame speed correlations have been used for the estimation of the quenching distance in a SI engine as function of the fuel/air equivalence ratio (fig.2.5). The lower values of the quenching distance are achieved using a stoichiometric or slightly rich mixture associated with the higher laminar flame speed and combustion temperature. Under lean or rich mixture conditions the laminar flame speed decreases, thus increasing the quenching distance as depicted in figure 2.5.

Enomoto[26] analysed the head-on and side quenching phenomena, by means of shadowgraphy visualization technique for flame thickness measurements in a closed vessel. Additionally, the experimental data were matched with the numerical ones obtained on the basis of Mayer's thermal theory [27]. The main simplification concerned the temperature distribution between the flame and wall, assumed as linear function of the distance.

Bellenoue et al.[28] characterized the quenching distance during side-wall quenching and head-on quenching of premixed methane/air flame. Direct photography method was used to record the flame position near to the combustion chamber walls. Fig.2.6 shows the side-wall and head-wall quenching distances

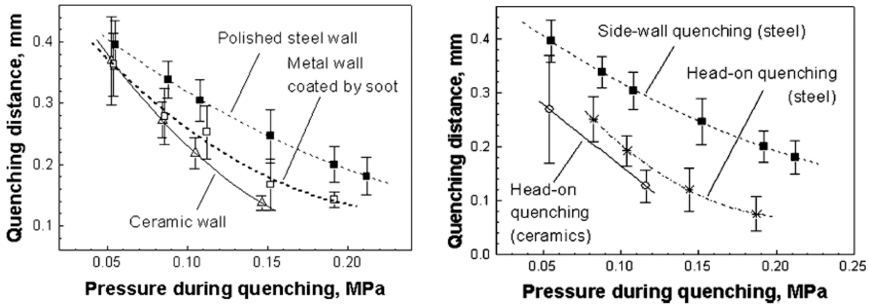

Figure 2.6: Flame quenching distance as function of the pressure and plate materials[28]

as function of the initial chamber pressure for different wall materials. In general for all wall materials used, the flame extinguishing distance decreased with increasing initial chamber pressure. Then, the experimental value of the quenching distance have been used for heat flux peak estimation.

Despite the great effort of the scientific community in trying to fully characterize a very complex phenomenon, further studies both experimental and numerical, are necessary in order to build and validate theoretical models [29, 30].

2.2.5 Emissions

Most of the SI engines on the market, theoretically run with stoichiometric mixture in order to ensure a proper operation of the three-way catalyst (TWC). As stated, during the cold start the catalyst is not able to reduce the exhaust emissions until its temperature is raised above the minimum operating threshold [31, 32]. In addition, TWC efficiency is most balanced operation when the engine runs under stoichiometric mixture. After combustion, the exhaust gases entering inside the catalytic converter include a mixture of Carbon Monoxide (CO), Unburned Hydrocarbons (UHC) and Oxides of Nitrogen (NO_x), which are harmful to the environment. As the gases enter inside the after-treatment system, the nitrogen oxides molecules are the first to react with Platinum and Rhodium. The TWC allows the reduction of nitrogen oxides combined with carbon monoxide into nitrogen, oxygen and carbon dioxide (CO_2). Then, the gases arrive into a ceramic block where it reacts with Platinum and Palladium. Here the remaining carbon monoxide

reacts with oxygen molecules to form carbon dioxide, while the unburned hydrocarbons also react with oxygen to form water and CO_2. Considering this, an oxygen-rich environment as the one achieve through lean combustion operation would promote the second block reaction (oxidation of CO and UHC) but inhibit the first one, since the available CO in the exhaust gases would not be sufficient. The opposite behaviour would appear if the environment is oxygen-poor.

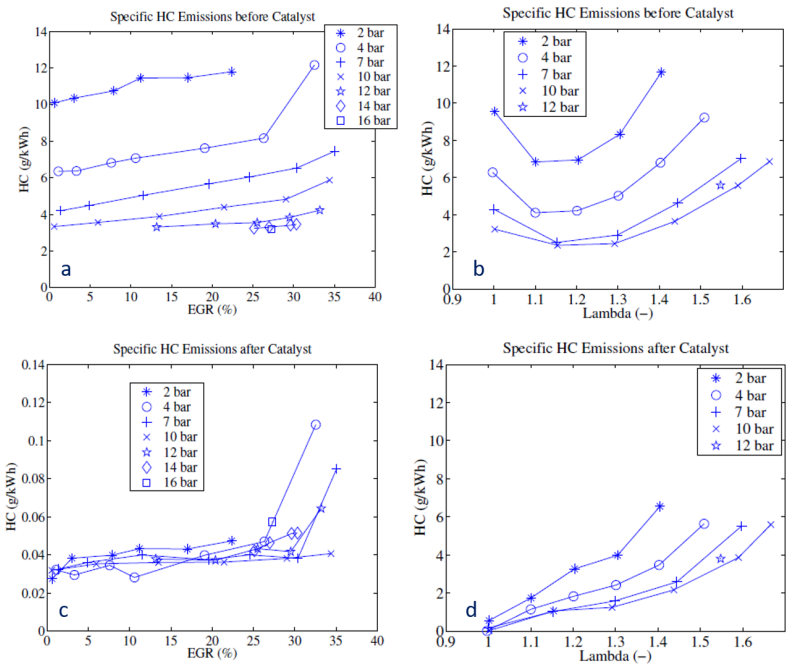

Figure 2.7: Top: HC emissions as function of EGR and Lambda before catalyst system. Bottom: HC emissions as function of EGR and Lambda after catalyst system.

Theoretically, lean burning systems could significantly reduce engine-out emissions due to the air excess and low combustion temperature, thus not needing complex after-treatment architecture. In real-world operation, working with extra surplus of air can lead to incomplete combustion cycles, resulting in high production of carbon monoxide and especially hydrocarbons. Additionally, as stated before lean operation increases the quenching distance, increasing the unburned hydrocarbons associated to this phenomenon.

Einewall et al. [33] analysed the engine performance and emissions of lean-burn strategy compared with stoichiometric operation with high EGR dilution and 3-way catalyst. The TG130/G10A engine was a V6, 1.6 litres, port fuel injection, with compression ratio equal to 12, and was modified by Volvo for natural gas operation. Three ways of ignition and dilution strategies were explored:

- Stoichiometric with EGR, max pressure at 12°aTDC.
- Lean air/fuel mixture, max pressure at 12°aTDC.
- Lean burn operation with ignition time set for low NOx strategy.

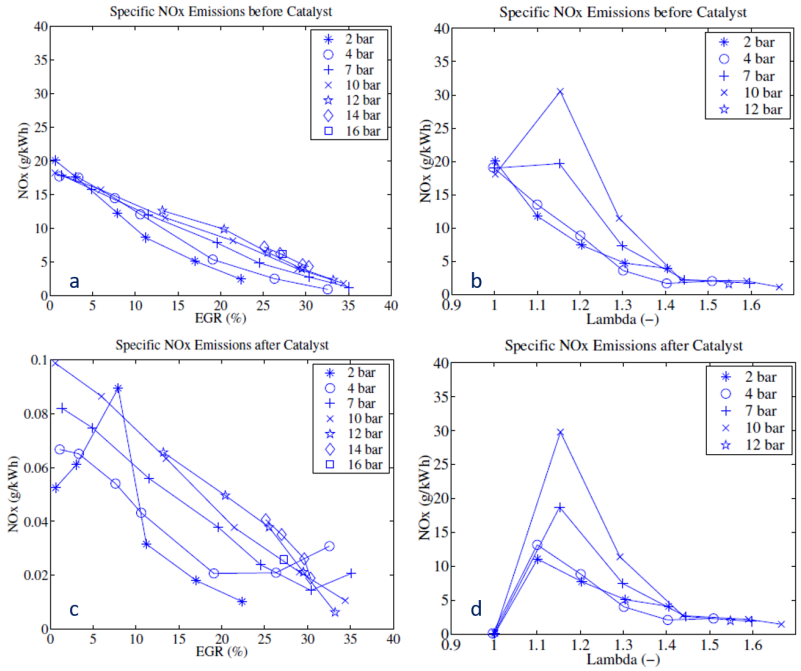

Figure 2.8: Top: NO_x emissions as function of EGR and Lambda before catalyst system. Bottom: NO_x emissions as function of EGR and Lambda after catalyst system.

HC emissions increased with higher EGR rate and decreasing the engine load. High recirculation of exhaust gas increased the combustion duration

while decreased the mean mixture temperature, worsening the laminar flame speed.

Comparing stoichiometric and lean low NOx strategies in fig.2.7 (top), HC measured before the aftertreatment system, increases due to less oxygen (left side) for conventional combustion, and due to slower and colder combustion for the lean mode (right side). Once the mixture exceed the flammability and ignition limits, HC emissions increase significantly due to partial burn or misfire.

By analysing emissions after the catalyst (fig.2.7bottom), a complete reduction of HC emissions can be observed under all EGR conditions. On the contrary, when the engine works with air excess, the catalyst efficiency drops down, making almost worthless its function.

The figure 2.8 reports the same analysis for NOx emissions before and after the after-treatment system. The general trend shows a decrease in NOx as the EGR rate or the air dilution of the mixture increases. After the catalyst, almost 98% of reduction is achieved for $\lambda = 1$ condition, while the lower NOx level is reached only from $\lambda > 1.5$ to leaner mixtures.

The authors concluded suggesting stoichiometric operation with EGR and three-way catalyst as the preferred strategy, until the lean technology limits, outweigh the advantages offered in terms of thermal efficiency, fuel saving and thus CO reduction.

2.2.6 Cycle-to-cycle dispersion

Cycle-to-cycle variation in the in-cylinder pressure for SI engines is a key parameter for controlling and monitoring of the engine performance and combustion evolution. It is well known that even under stationary boundary conditions, each working cycle can be affected by different turbulent flow field, local equivalence ratio dispersion, and mixing effects between EGR and fresh charge [34].

Fig.2.9 shows the cycle-to-cycle variation magnitude on the evolution of the in-cylinder curve in case of $\phi = 1.0$ from motored to fired conditions. The graphs on the right emphasize both the decrease of the absolute value and the increase of the peak pressure dispersion when the mixture becomes leaner. Considering that in the real engines several cylinders coexist, the phenomenon is even amplified, leading to different work produced in each cycle. A high level of fluctuation in engine speed and torque [36] includes turbocharger and aftertreatment systems issues, leading to a really annoying driveability loss and emissions increase.

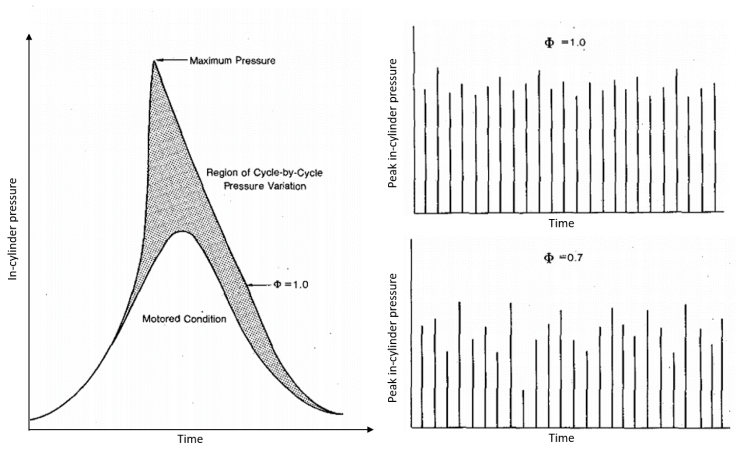

Figure 2.9: Cycle-to-cycle variation of In-cylinder pressure for stoichiometric condition (left). Peak cylinder pressure over high number of cycle for ϕ = 1.0 and ϕ = 0.7 (right) [35]

Stone et al. [37] affirmed that early stage of combustion could have a high impact on the late stage, thus on the engine cycle variation. At the start of combustion, the flame is small compared to the turbulence eddies length scale, thus can be convected away from the spark plug. Hence, the turbulence flow must enhance the combustion starting from the instant in which the flame propagation is steady [38] (to avoid the initial flame kernel displacement).

2.2.7 Summary and development trends

In general, to improve the lean burning system control (increase the engine thermal efficiency while reducing the cycle-to-cycle variation) several strategies have been explored. As stated, lean mixtures are difficult to ignite [39] and the air/fuel burning rate is much slower compared to the conventional stoichiometric SI engine [40]. Indeed, any technologies able to help the initial flame kernel development or the combustion enhancement should be useful.

Evans [41] developed a partial stratification concept in order to extend the lean limit ignition. The main injection (around 95% of the total fuel) is performed in a conventional GDI mode, while the residual fuel is injected during the compression stroke (close to TDC), aims to form a stratified mixture with local rich spot between the spark plug electrodes. Hence, the relatively rich

mixture near the spark leads to a strong initial flame kernel able to ensure flame self-sustainability and low work cycles variation.

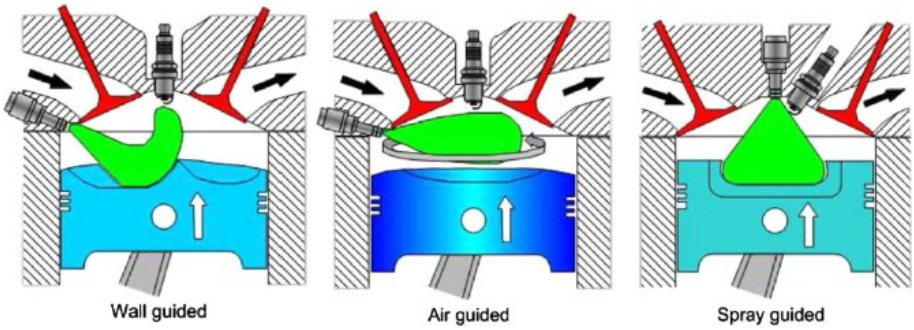

Figure 2.10: Direct injection spark ignition strategies: wall guided, air guided, spray guided

Harada et al. [42] characterized the first generation of wall and air guided stratified DI engines (Fig.2.10), pointing out several warnings about the emissions increase due to the wall impingement on the cylinder walls and piston. Subsequently, Takahiro [43] focused on spray-guided strategies and spray pattern, avoiding the wall impingement issues. Reducing the fuel impact against the combustion chamber walls means a reduction in terms of smoke, hydrocarbon emissions and fuel consumption.

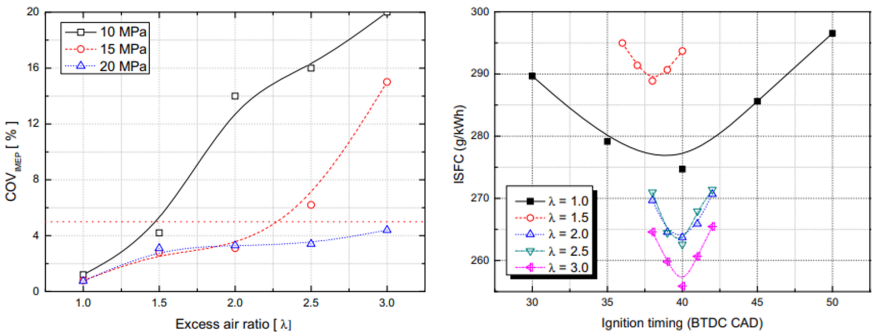

Figure 2.11: COV of the IMEP as function of the λ at different injection pressure (left). ISFC as function of the ignition timing with a 20 MPa injection pressure at each excess air ratio (right).

Afterward, Park et al. [44] further investigate the applicability of the stratified ultra-lean strategy. The authors performed an experimental study with a single-cylinder, direct injection, 4-stroke gasoline engine using a piezo-actuated injector, aims to evaluate the engine performance and emissions. Results show that under high injection pressure it is possible to create a rich mixture field close to the spark plug even at ultra-lean conditions ($\lambda = 2.0$), achieving low NOx and THC emissions while limiting the in-cylinder pressure coefficient of variation (COV) and fuel consumption (fig.2.11). Despite, fuel impingement still caused higher smoke emissions compared to the conventional SI strategy.

Another way to extending the lean ignition limit is the combustion enhancement (high burning rate) by means of high turbulent flow field during the spark plug discharge and combustion evolution [14]. In conventional SI engine turbulence is generated through the combustion chamber, piston or intake manifold geometry [45]. A rotating flow induced by swirl and tumble motions, combined with squish movement can play a fundamental role to increase the flame propagation speed under partial of fully stratified combustion [46].

In summary, lean combustion offers considerable advantages in terms of global cycle efficiency and fuel savings compared with conventional stoichiometric combustion. Furthermore, NOx production is suppressed by the low combustion temperature, while the CO emissions are reduced by the oxygen surplus. Despite all the advantages, it is not trivial to achieve successful control of lean combustion under all the engine map conditions. Air excess or high EGR dilution degrade the laminar flame speed increases the risk of misfire, quenching or partial combustion leading to high cycle-to-cycle variability (in-cylinder pressure) and huge unburned hydrocarbon production. Nowadays, the development of pre-chamber spark ignition engines seems to be the best alternative to the conventional one. The characteristics of pre-chamber systems will be discussed in the following section highlighting the main works carried out by the scientific community to fulfill the LTC requirements.

2.3 History of the pre-chamber ignition systems

Since the first years of the 20th century, many researchers have been involved in the pre-chamber (PC) system developments. The original idea of that concept was to accelerate the flame by means of a convergent-divergent nozzle[47], in order to compensate the decrease of the laminar flame speed under lean combustion strategy.

Over the years, car manufacturers have developed different concepts that can be classified as: homogeneous [48–51] and stratified systems[52–54].

The homogeneously system does not require substantial modifications in the combustion engine architecture and control. The pre-chamber is typically located at the top of the cylinder head. The cylinder filling process is realized according to the traditional methods, i.e. using the carburetor (in the old system), port fuel or gasoline direct injection into the main chamber. During the compression stroke the air/fuel mixture is forced to pass into the pre-chamber trough the nozzle. Therefore, combustion may be induced by the spark plug activation [55, 56] or by the autoignition of the premixed compressed charge [57, 58], thus propagates from the pre-chamber to the main chamber.

The stratified PC system requires a more complex hardware compared to the homogeneous one. The filling process is once again carried out in the conventional way. Meanwhile, during the compression stroke the pre-chamber mixture is enriched by means of a mechanical valve (like in the older PC systems) or through an auxiliary injector. The aim is to extend the flammability limits by creating more favourable local conditions for flame propagation in the pre-chamber, taking into account a more complex system to deal with.

The main difference between older and modern systems is related to the pre-chamber geometry. First pre-chamber generation was characterized by a large volume and a single orifice with a large diameter. Over time, the volume has been reduced to deal with the high heat losses due to the surface to volume ratio, and the number of orifices increased. The original concept of flame acceleration was replaced by the turbulent jet ignition [59–61]. The modern systems enhance the ejection of highly reactive jets that burn the main chamber mixture even under ultra lean condition [62, 63].

This chapter is primarily dedicated to the PC systems description, from the birth to modern times. Afterwards both experimental and numerical works performed in the last generation PC systems will be discussed, in order to highlight the advantages and disadvantages of this promising technology.

2.3.1 First pre-chamber system generation: Flame ignition

First pre-chamber systems were characterized by a large pre-chamber volume and a single nozzle orifice. The general idea of these first concepts aimed to promote the flame acceleration, increasing the low burning rate typical of the lean combustion.

The 2-stroke Ricardo Dolphin engine is one of the oldest models in this category (fig.2.12). The pre-chamber is placed in the upper part of the cylinder

head. The system allows an auxiliary injection by means of a mechanical valve, to enrich the mixture in correspondence of the pre-chamber. Thus, the combustion starts as the spark ignites the local rich mixture and propagates through the nozzle until the main chamber. This engine takes advantage from the converged-divergent nozzle shape to accelerate the flame propagation, ensuring high burning rate of the overall lean mixture.

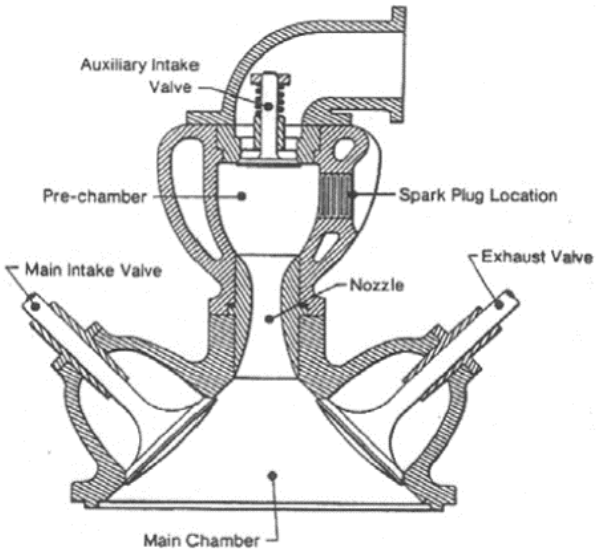

Figure 2.12: Ricardo 2-stroke divided chamber stratified charge engine

Similar 3-valve stratified concepts were patented by researchers such as Mallory [52] and Barnes [53] inspired by the 2-stroke Ricardo engine.

Subsequently, car manufacturers such as Ford [48], Toyota [49], Volkswagen [50], developed the homogeneous pre-chamber concepts, removing the mechanical valve.

Adams investigated the design and use of a aspirated torch chamber combustion system to promote a turbulence flow interacting with the initial flame kernel to reduce the burn time of lean mixtures [48] (fig.2.13). The aims of the investigation was to determinate the effect of the nozzle geometry on the fuel economy, power and engine-out emissions. The author concluded that the highest burn rate achieved the lowest fuel consumption and meanwhile maximized the HC and NO_x emissions. A modified nozzle orientation lead to a better compromise between fuel saving and emissions.

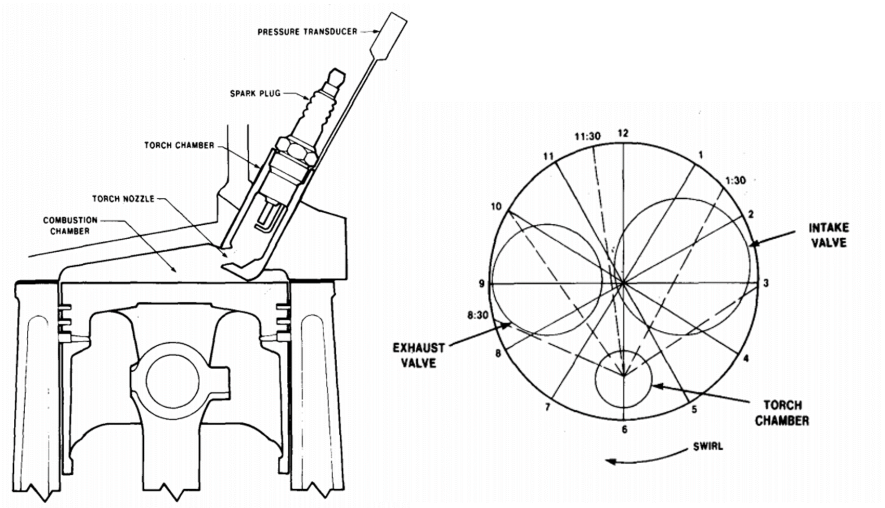

Figure 2.13: Ford torch ignition chamber layout [48]

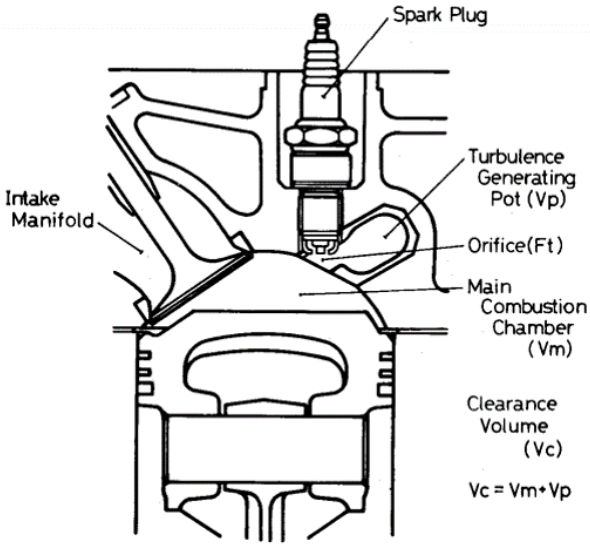

Figure 2.14: Combustion chamber layout of Toyota lean burn engine [49]

Noguchi et al.[49] developed a system called Turbulence Generating Pot (TGP) which aimed to increase the turbulence close the spark plug promoting high flame propagation while extending the misfire lean limits. Their work is focused on how the spark plug location affect the flammability limits and engine performance. The authors concluded by highlighting the spark plug position as a key parameter for this technology, suggesting to place it inside the orifice as the best option. In addition, the results allow a vehicle equipped with this system to fulfil the 1976 Japanese passenger car emission standards.

Figure 2.15: Combustion chamber layout of Honda CCVC engine [54]

One of the greatest successes of this first generation of pre-chamber systems is surely the engine conceived by the Honda engineers, called CVCC engine[54]. The theoretical approach of stratified pre-chamber system with auxiliary valve elaborated in the late 1960s became a real engine (able to respect the emissions limits of the time without the after-treatment system) in the early 1970s.

Consequently, similar systems have been explored by General Motors[51], Porsche SKS[64], Broderson Conta[65, 66]

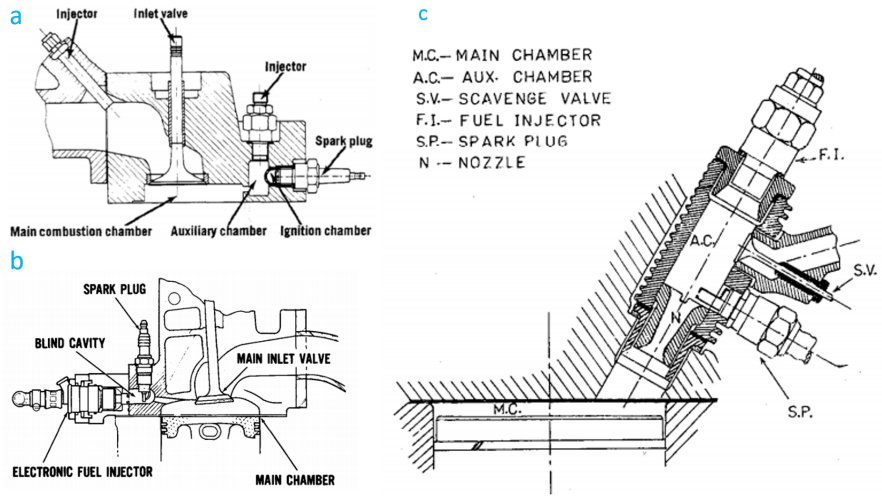

Figure 2.16: Porsche SKS Engine (a). GM Pre-chamber Torch Ignition Engine (b). Broderson Conta Engine (c).

2.3.2 Second pre-chamber system generation: Torch jet ignition

The first relevant change in pre-chamber ignition systems was explored by the work of Gussak [67] through a considerable reduction of the pre-chamber volume in a stratified charge system. The revolutionary idea (under the name of Lavinia Aktivatisia Gorenia LAG or Avalanche Activated Combustion) was to exploit the high reaction energy offered by the active radicals produced as consequence of a rich partial combustion in the pre-chamber. The nozzle outlet diameter was minimized to cause the flame extinction once it approaches the wall. The partial products of combustion were ejected at high speed into the main chamber, thus acting as an ignition source for ultra-lean fresh charge.

The figure 2.17 summarises the combustion process compared with the first PC generation concept: on the right side an accelerated flame front in a duct (typical of the first generation of pre-chambers), and on the left side the avalanche activated combustion [68].

Gussak et al. analysed the effect of the pre-chamber volume and the relative cross section on the ejection process. The authors affirmed that pre-chamber optimal volume should not exceed of 2-3% of the main chamber one, while the relative output cross-section should be around 0.03-0.04 cm^2 per cen-

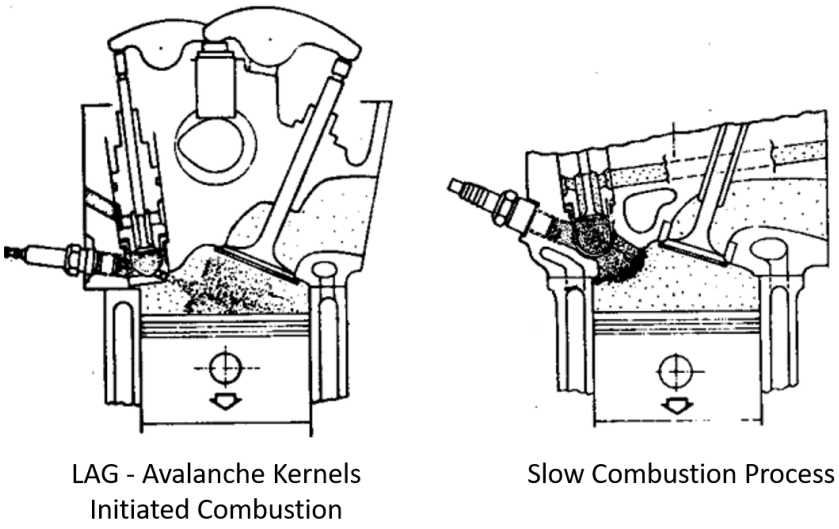

Figure 2.17: The LAG process with active radicals from a quenched flame vs slow combustion process [67].

timetre of the pre-chamber volume. The experimental campaign (performed with research single-cylinder engine) showed the best trade-off in terms of lowest fuel consumption, highest specific engine power and highest stability when the engine run under pre-chamber rich stratified mixture ($0.4 < \phi < 0.7$) and ultra-lean main chamber homogeneous mixture ($1.5 < \phi < 2.0$).

In the subsequent years, Yamaguchi [69] combustion group further investigated the ignition and burning mechanisms of the main chamber mixture under the LAG process, by means of Schlieren and OH chemiluminescence techniques. They classified the torch ignition process according to the chemical and physical characteristics developed in the main chamber:

1. If the nozzle diameter is low enough to induce the flame quenching, thus the torch jet ignites the main chamber mixture by means of active radicals ejection. After a relative long induction period, the main charge ignites and rapidly burns due to a chemical chain reaction.

2. Increasing the nozzle diameter, the torch jet ignition includes a small amount of flame kernels which promote the ignition of the main chamber

mixture. The induction period is shorter and ignition occurs as a result of both chemical and thermal effects.

3. Larger nozzle diameter and lower ejection velocity, characterized the so-called "flame kernel torch ignition" in which there is no flame quenching into the pre-chamber. The ignition is induced by the flame kernels.

4. "The flame torch ignition" regime is defined by an even larger nozzle diameter and a further decrease in the jet ejection speed. The flame surface is weakly wrinkled due to the low turbulence flow and ignite the main charge due to the propagation.

The authors have proven that active pre-chamber radicals are able to ignite the main chamber mixture, recommending the pattern two as the most successful in terms of flammability limits extension.

Watson et al. [70, 71] developed the hydrogen assisted jet ignition (HAJI) system, considered as the father of the modern pre-chamber spark ignition systems. The HAJI system is composed by a small pre-chamber and an auxiliary injector (aims to correct the ultra-lean charge). Toulson et al.[62, 63, 72] analyzed the performance of the HAJI system under different combinations of liquid and gaseous fuel. Figure 2.18 shows an effective extension of the flammability limits by comparing with the conventional system (in red), achieving the best results when combining the LPG as main fuel with hydrogen auxiliary injection.

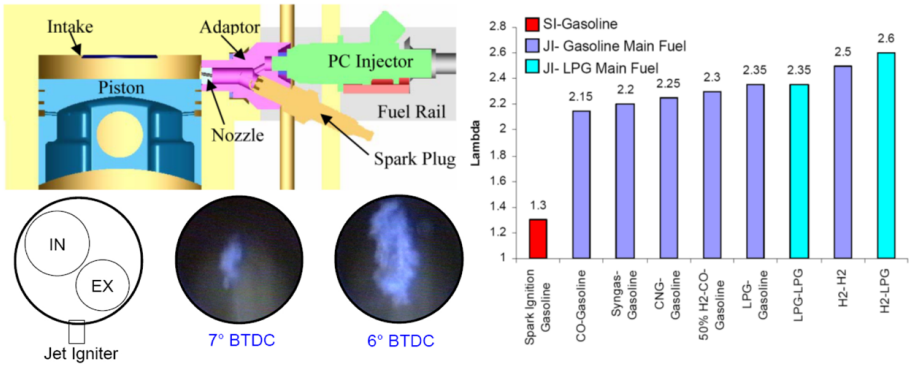

Figure 2.18: Hydrogen assisted jet ignition system

Hence, similar systems have been explored focusing on the ignition mode[56, 73], on the pre-chamber and main chamber geometries [74–76], point-

ing to the achieve the best trade-off between combustion control and emission reduction without any performance losses.

2.3.3 Modern pre-chamber spark ignition system: Turbulent jet ignition

The modern Pre-Chamber Spark Ignition (PCSI) systems aim to overcome the lean combustion drawbacks discussed in the previous chapters. The conventional spark plug is replaced by a small volume pre-chamber with purpose to increase the ignition energy delivered to the lean main chamber mixture (Fig. 2.19).

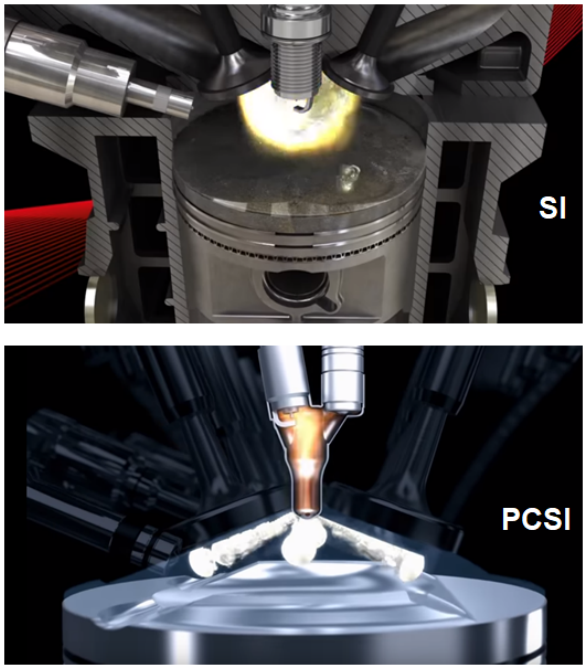

Figure 2.19: Conventional pentroof spark ignition system (top) and Pre-chamber spark ignition system (bottom)

In a standard work cycle, during the compression stroke the main chamber mixture is forced to pass into the pre-chamber by means of several nozzle orifices. Then, depending on the combustion strategy (homogeneous or stratified) the pre-chamber mixture can be enriched by an auxiliary injection to facilitate the start of combustion. The mixture is ignited by the spark plug,

thus the pressure rises as the flame front propagates and forces the active radicals and hot products to discharge through the nozzle into the main chamber at high velocity [77]. The turbulent jets entering into the main chamber act as high energy ignition sources, promoting fast burn rate of the charge thanks to the combination of high local turbulence intensity and multiple ignition points.

In the next section, the last generation of PCSI systems will be deeply explored.

2.4 The latest generation of pre-chamber spark ignition system

This section is centered on the description of the most significant works performed by the scientific community regarding the PCSI engines. In detail, the description will focus on how the high turbulent ignition energy affects the thermal efficiency, cyclic variability, flammability limits, flame propagation velocity, and pollutant emissions.

2.4.1 Lean flammability limits and combustion stability

Attard's combustion group was one of the first that deeply explored the potentialities of a modern PCSI system under homogeneous and stratified turbulent jet ignition mode with different liquid and gaseous fuels. Figure 2.20 shows on the left a general scheme of the engine: in the pentroof combustion chamber the spark plug is replaced by the pre-chamber, inside which the ignition system and the auxiliary injector are located. At the bottom right side, a detail of the orifice distribution on the nozzle circular crown is depicted. Single-cylinder experimental results at 1500 rev/min have shown that the Turbulent Jet Ignition (TJI) combustion system is able of overtaking the conventional spark ignition combustion performance.

Attard et al. assert that the combination of liquid gasoline (as main chamber fuel) and gas propane (as pre-chamber fuel) shows the best results in term ignition and flammability limits extension (maximum lambda at 2.1) while ensuring combustion stability (COV of the Indicated Mean Effective Pressure $< 5\%$) [78]. The engine working range extension is due to the enhanced combustion speed in the main chamber, promoted by the distributed ignition spots induced through the pre-chamber outgoing jets (fig.2.21). The thermal efficiency benefits are due to a combination of several combustion optimization, reduced heat losses (reduced pre-chamber volume), the almost elimination of

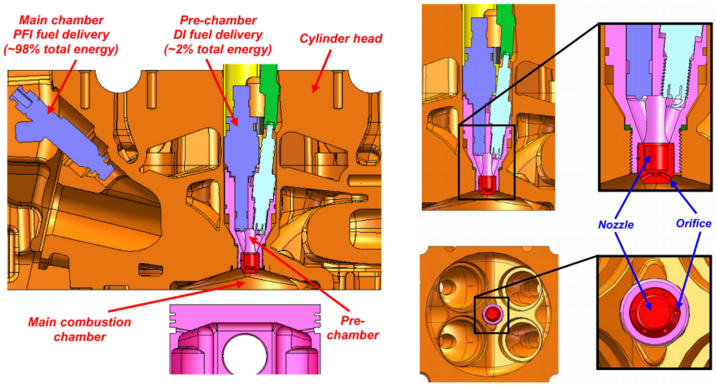

Figure 2.20: Turbulent jet ignition engine layout (left). Nozzle, orifices and pre-chamber details (right).

chemical dissociation thanks to low combustion temperatures and the reduction of engine throttling at part load.

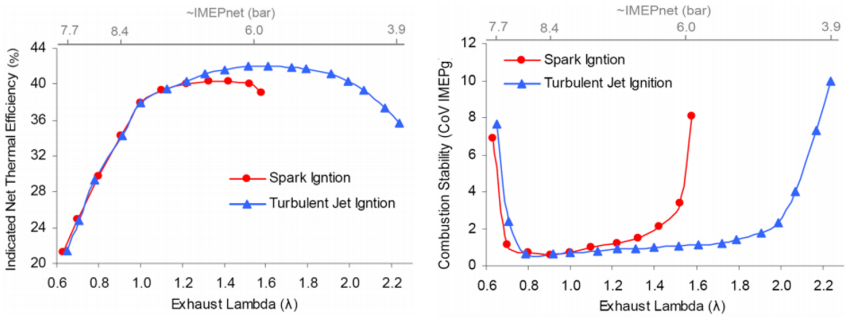

Figure 2.21: Indicate Net Thermal Efficiency as function of exhaust lambda (left). Combustion Stability as function of lambda (right).

To overcome the complex hardware needed for dual fuel operations, Attard et al. show that the combustion system can also operate with a single fuel keeping high performance, and making the system more practical for production applications[79]. Figure2.22 shows an acceptable combustion stability (COV less than $< 5\%$) also for single-fuelled engine until $\lambda = 1.9$. Indeed, the net thermal efficiency keep rising while the dilution of the charge is increased.

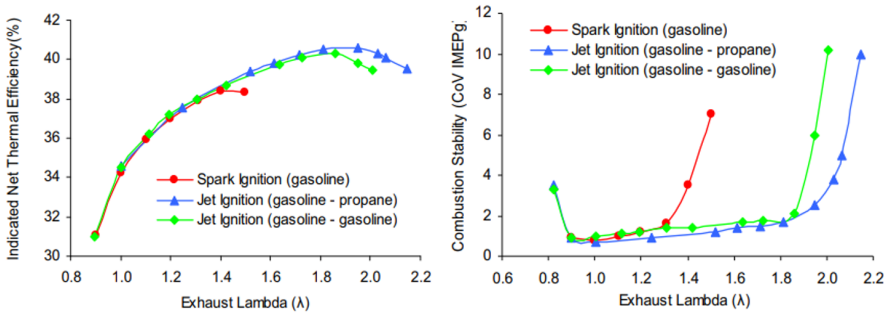

Figure 2.22: Combustion COV (left) and Indicated Net Thermal Efficiency (right).

Furthermore, experiments incorporate the variation of parameters found to affect the dilution limits in conventional spark ignition engine such as spark plug type, location, orientation, and electrode gap. Results highlighted (Fig. 2.23) that only the spark plug depth (a secondary factor in a conventional engine) slightly affects the extension of the lean limits [80].

Finally, Bureshaid et al. [81] evaluated the effect of the auxiliary injection mass and timing on combustion stability using the turbulent jet ignition unit on a single-cylinder engine, concluding that ethanol promotes less cycle-to-cycle dispersion when compared with the gasoline.

2.4.2 Combustion speed

When analysing the combustion speed for the PCSI systems, it is necessary to refer on two types of velocities related with different phenomena. The first is the pre-chamber flame speed, function of the laminar flame speed, thermochemical properties of the mixture, ignition system and turbulence flow field. The second one is the main chamber combustion speed, function of the thermochemical main chamber conditions and related with the pre-chamber jets ejection.

In agreement with the equation proposed by DiStaso, the laminar flame speed for a specified thermodynamic conditions (pressure and temperature of the unburned mixture) is basically function of the equivalent ratio, and more precisely is maximum for slightly rich mixtures.

According to this, a PCSI system working in stratified mode (auxiliary injection in pre-chamber for enrich the mixture) should not suffer any ignition

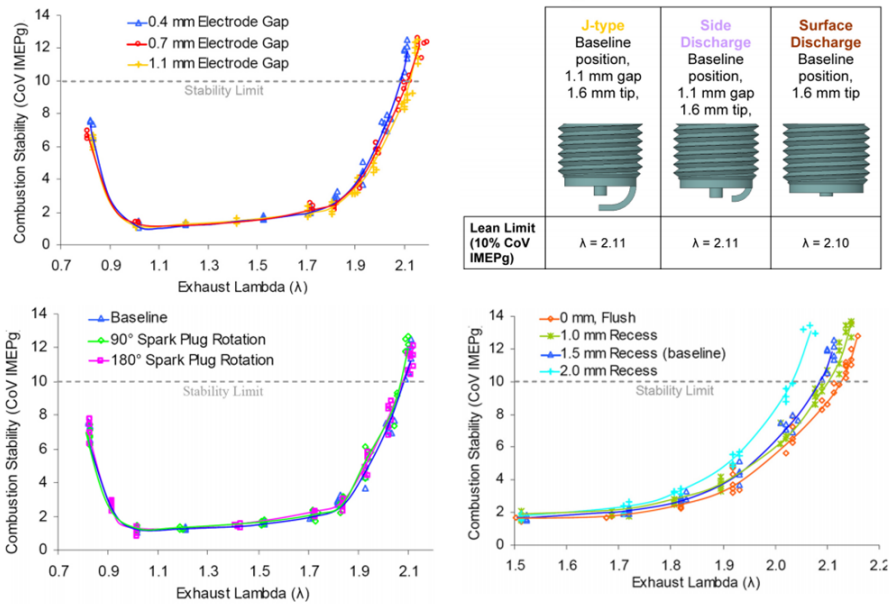

Figure 2.23: Combustion Stability as function of lambda for several spark plug electrodes air gap (top). Combustion Stability as function of lambda for several spark plug orientations (bottom - left) and positions (bottom - right).

or propagation problems inside the pre-chamber. On the contrary, the equivalence ratio of the main and pre-chamber cannot be controlled independently under homogeneous strategy. Indeed, working with lean mixtures inside the pre-chamber degrades the flame propagation speed, increasing the elapsing time between the spark plug activation and the beginning of the ejections.

Once the flame front approaches the nozzle orifices, the turbulent jets are ejected into the main chamber, thus burning the lean charge in two phases. Hiraoka et al.[82] described in detail the combustion process of the main chamber mixture. The initial burning rate, so-called torch jet ignition is assumed to depend on the fresh charge entrainment by the burned ejected jets. Hence, the torch jet velocity drives the combustion speed. Therefore, after the ejection, the flame propagates between the burned area according to the turbulent flame propagation theory.

Gentz et al.[83] studied the flame propagation speed of an air/propane mixture in a rapid compression machine (RCM) under the homogeneous strategy by means of pressure trace analysis and combustion visualization. The facility performances with three different nozzle diameters (1.5, 2.0, 3.0 mm)

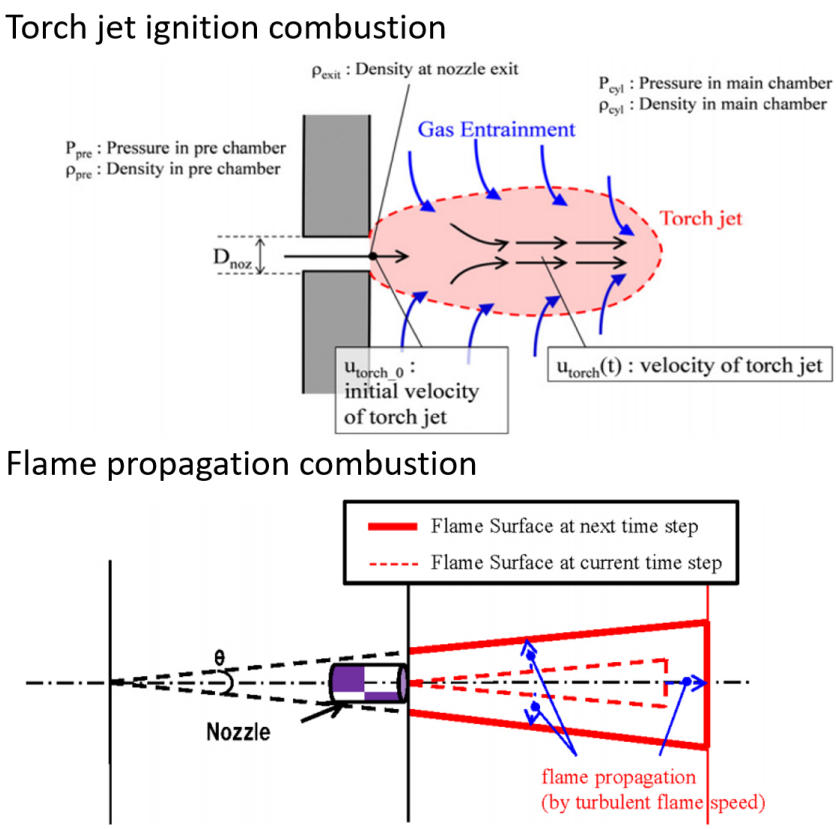

Figure 2.24: Torch jet ignition combustion (top). Flame propagation combustion (bottom)[82].

have been assessed, under stoichiometric and lean mixture, aim to combine the diameter and equivalence ratio impact on the combustion duration. As expected the combustion duration increase as the mixture becomes leaner. Moreover, the orifice diameter has a significant impact on the jet shape and structure, thus on the 10-90% burn duration, showing maximum propagation speed with minimum diameter (Fig.2.25).

Gentz concluded by identifying the orifice diameter as a critical parameter for the shape and structure of the ejected flame. Further studies were conducted by the same authors [84], to assess the impact of diameter and number of orifices on flame propagation in a stratified PCSI system.

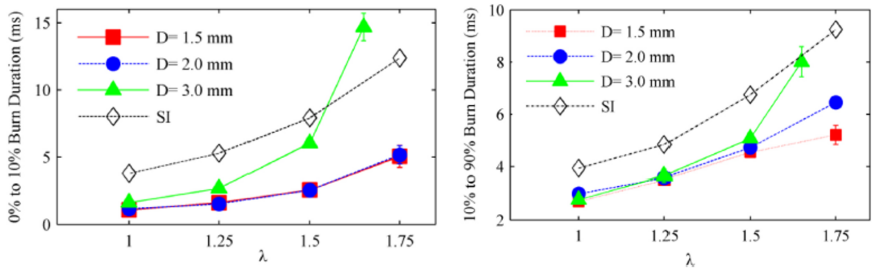

Figure 2.25: CA0-10 and CA10-90 as function of lambda for different pre-chamber nozzles under homogeneous strategy [83].

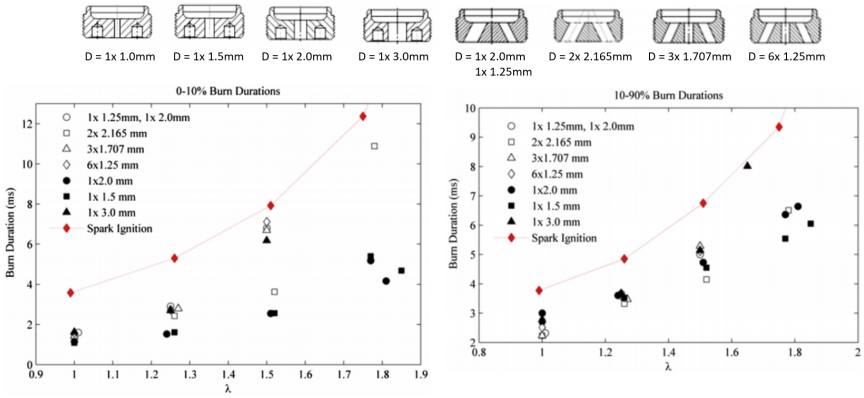

Figure 2.26: CA0-10 and CA10-90 as function of lambda for different pre-chamber nozzles under stratified strategy.

The 8 different nozzle geometries are shown in the upper part of the figure 2.26. The burn duration of the early (CA 0-10%) and late (CA 10-90%) combustion phases is clearly faster then the baseline spark ignition case for any nozzle geometry. In addition, Gentz highlighted that only under stratified mode a significant ignition limits extension is obtained.

2.4.3 Emissions

The biggest challenge for the PCSI system is to reduce NOx, CO and HC emissions simultaneously [85, 86]. Ultra lean combustion ensures a low combustion

temperature that inhibits NO_x formation. Fuel saving decreases the CO production, easily reduced in an oxygen-rich environment. Fast combustion with high thermal efficiency guarantees the reduction of unburned hydrocarbons.

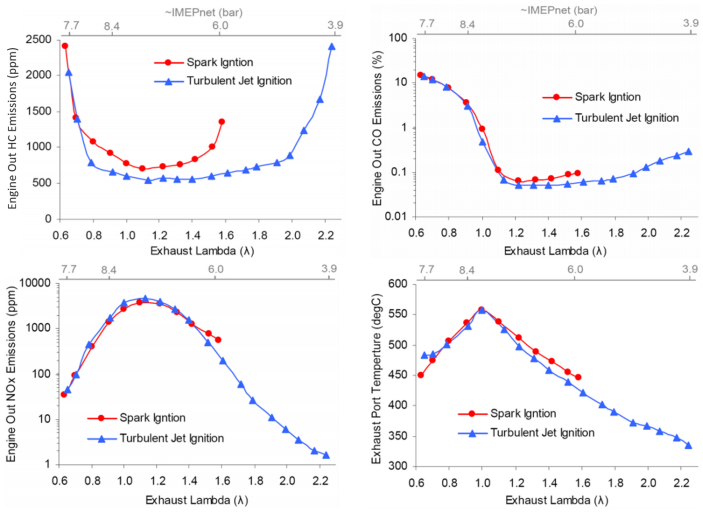

Figure 2.27: HC, CO, NO_x, Temperature measurments as function of lambda [78].

Regarding Attard's already-discussed work [78], a significant reduction in terms of emissions has been achieved under stratified strategy. As the mixture become leaner, the average combustion temperature decreases, leading to a near zero NOx production for $\lambda > 1.8$. The main source of NO_x production is theoretically the pre-chamber, in which combustion reaches a high temperature. Nevertheless, the small amount of fuel injected in the pre-chamber is not relevant compared to the overall lean homogeneous field of the main chamber.

Concerning the HC and CO, a substantial drop over the range $0.9<\lambda<1.4$ was issued. Differently, when the engine operates near the rich and lean dilution limits, a high emissions production due to misfires and partial combustion that increase the cycle-to-cycle variability was founded.

Similar results were found by Jamirokez et al.[85], during the experimental campaign carried out with a PCSI engine single-cylinder system under stratified mode. The performances of the PCSI engine powered by single fuel LPG gas or dual fuel LPG+gasoline have been compared with a conventional spark ignition strategy. The figure 2.28 illustrates the benefits in terms of lean operation limit (until $\lambda = 2.0$), and the substantial emissions reduction.

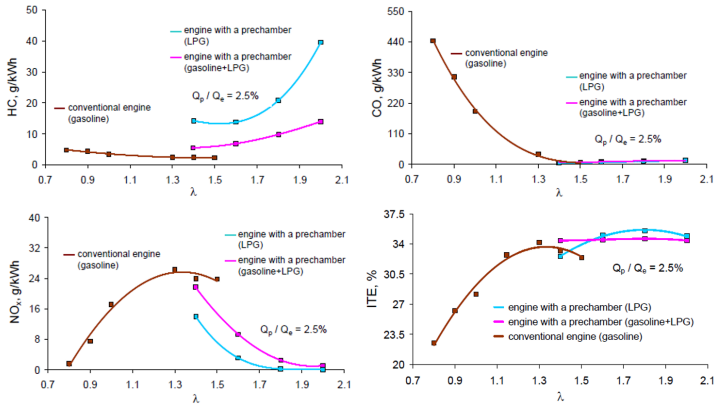

Figure 2.28: HC, CO, NO_x, Indicate Thermal Efficiency as function of lambda [85].

2.4.4 Modelling

In order to deeply understand the combustion process in the PCSI systems, several researchers have focused their efforts on adjusting existing models. Accurate thermodynamic models for post-processing experimental data are powerful tool for the combustion diagnostic. In addition, combining experimental results with 3D CFD simulations is the path to make PCSI systems reliable and high-performing.

In [82], Hiraoka analysed the interaction between the main and prechamber, developing a phenomenological 0D model. First, he describes the mass interchange between the chambers by modelling the nozzle velocity through a basic equation in compressed fluid-dynamics theory. In addition, the nozzle speed was coupled with the Ikegami k-ϵ turbulence model [87] to estimate the generation and dissipation of the turbulent kinetic energy. Moreover, the combustion rate and the flame speed were predicted by appyling Tabaczynski's model witch assumes the semi-spheric propagation front of the flame, after the spark ignition time [88].

Finally, the authors highlighted two different stages in the main mixture combustion process. The gas jet theory has been used to model the heat released accounted on the turbulent jet ejection into the main chamber (torch jet ignition stage). Then, the flame propagation is assumed self-sustained due to the turbulence enhancement in the main chamber, as well in the conventional engine.

Bardis et al. [89] developed a quasi-dimensional model of pre-chamber gas spark ignition engine aims to predict temperature, pressure and turbulence flow evolutions. First, a review of the main turbulence models widely used in the literature for the spark ignition engine was carried out. Then, the authors modified the energy cascade (K-k-ϵ) equations of the Fogla turbulence model [90]taking into account the turbulent kinetic energy dissipation through the pre-chamber walls introduced by the Borgnakke[91] and Achuth[92] investigations. Furthermore, Bardis adapted Bargende's correlation [93] to improve the heat losses prediction by associating the characteristic velocity to the gas orifice velocity. To support the new quasi-dimensional model results, the pressure, temperature, turbulent kinetic energy and length scale traces have been validated against 3D CFD simulations for different pre-chamber geometries. Nevertheless, the analysis was limited only to the compression stroke with no combustion model coupled.

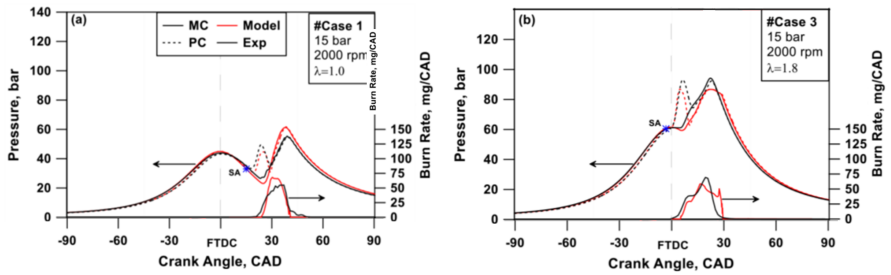

Figure 2.29: In-cylinder and Burn Rate experimental and numerical trends for several lambda [94].

Bozza et al. [94] proposed a quasi-dimensional model for stratified pre-chamber engine, combining a geometrical model for the flame surface estimation [95] with a previously developed combustion fractal model [96, 97]. The model has been validated against single-cylinder research engine, over 13 representative operating points, including several engine speeds and loads as well as relative equivalence ratio. The validation results in figure 2.29 show good agreement in terms of the pressure evolution of both chambers and the related burn rate trends.

Jamrozik et al. [98] combined experimental tests on 2 stage PCSI engine powered with LPG gas with numerical simulations, providing data on spatial and temporal distributions of turbulent kinetic energy, pressure and temperature for different nozzle diameters. The modelling results have been

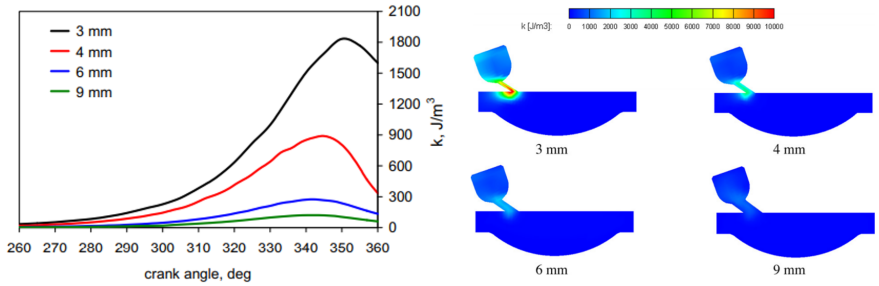

Figure 2.30: Average turbulent kinetic energy for different pre-chamber geomerty

first matched with the experimental one, and then analysed with aim of pre-chamber layout optimization. Fig.2.30 shows the average and the spatial distribution of the pre-chamber turbulent kinetic energy for 4 different nozzle diameters. As it is known, the velocity through the orifices is the main source of turbulence generation. Hence, decreasing the nozzle diameter means to increase the mass flow speed and therefore the amount of kinetic energy incoming in the pre-chamber.

2.4.5 Outstanding challenges

Despite the great efforts of the scientific community over the last ten years, the new generation of pre-chamber spark ignition systems have to deal with several outstanding challenges. The objective of this Thesis is to improve the basic knowledge of some specific aspects under motored and fired condition to shed light on how pre-chamber spark ignition systems work.

According to the previous literature review, stratified (or active) PCSI systems are required to extract the highest benefits of the system when combined with very lean main chamber mixture. Most of the investigations performed on stratified systems using gaseous fuels, especially in the pre-chamber. This helps to overcome potential difficulties related to the atomization and evaporation of liquid fuels inside the pre-chamber, which may induce wall wetting and subsequent stability or emissions issues. However, for transportation engines which currently operate mostly with liquid fuels, such strategy would require a dual fuel injection system, increasing cost and complexity. For this reason, the current work focuses at exploring the stratified system with liquid fuel injection in both chambers.

Although there is already a wide experimental database on these systems, there are still uncertainties related to how the combustion develops inside the pre-chamber and propagates to the rest of the cylinder. On the one hand, engine experiments are subjected to uncertainties related to the composition and thermodynamic conditions inside the pre-chamber at the spark activation time. For instance, variabilities in the pre-chamber scavenging process and subsequent residual mass fraction at the cycle start can significantly affect the combustion evolution. On the other hand, the limited space available in the cylinder head hardens the possibility to have a proper instrumentation of the instantaneous pressure in the pre-chamber, which is necessary for a proper evaluation not only of the combustion evolution (through a first law of thermodynamics analysis) but also of the mass exchange process itself (in combination with the pressure in the main chamber), necessary for a proper control of the equivalence ratio in the pre-chamber as well as to evaluate the conditions of the discharge that initiates the main chamber combustion. In this sense, the rapid compression-expansion machine used in the current Thesis offers many advantages for the investigation of basic aspects of the work cycle without any external interference (valves opening and closing phases, turbulence induced by main chamber filling processes, cycle residual gas, etc.) and with a more simple instrumentation of both pressures. Additionally, the geometry of the cylinder head and the combustion piston can be easily modified, allowing parametric studies in reduced time and cost. Finally, it also allows the characterization of the ejected flame structure (jet penetration, flame surface, dispersion angle) and its interaction with the main chamber thanks to its optical access. The knowledge of these parameters is critical for the geometrical optimization of the whole combustion chambers, to avoid the occurrence of knocking, misfire or flame quenching.

From the literature studies, the geometry of the pre-chamber is indicated as the most critical parameter for the proper combustion development. In this sense, the ratio of the pre-chamber volume to orifices transversal area is identified as the key parameter for the filling process, while the orifice diameter, number and distribution drive the ignition and combustion evolution in the main cylinder. However, there are still uncertainties related to how these geometrical aspects may affect the flow field, turbulence generation and combustion development in the pre-chamber, and therefore the ejection and initial combustion development in the rest of the cylinder. For this purpose the current work combines 3D CFD simulations of the filling process in the pre-chamber, the validation of a zero-dimensional thermodynamic and combustion model based on the instantaneous pressure traces in both chambers, and visualization tests focused on the combustion development in the cylinder.

References

[1] John, B. "Heywood, Internal combustion engine fundamentals". In: *Pub: McGraw Hill International Editions* (1988).

[2] Peters, Norbert. *Turbulent combustion*. Cambridge Univer, 1941.

[3] Culbertson, David, Khair, Magdi, Zhang, Sanhong, Tan, Julian, and Spooler, Jacob. "The study of exhaust heating to improve SCR cold start performance". In: *SAE International Journal of Engines* 8.3 (2015), pp. 1187–1195.

[4] Cordier, Matthieu, Laget, Olivier, Duffour, Florence, Gautrot, Xavier, and De Francqueville, Loic. *Increasing modern spark ignition engine efficiency: a comprehension study of high CR and Atkinson cycle*. Tech. rep. SAE Technical Paper, 2016.

[5] Tanuma, Takeshi, Sasaki, Kenichi, Kaneko, Touru, and Kawasaki, Hajime. "Ignition, combustion, and exhaust emissions of lean mixtures in automotive spark ignition engines". In: *SAE Transactions* (1971), pp. 663–673.

[6] Lee, RC and Wimmer, Donn Braden. "Exhaust emission abatement by fuel variations to produce lean combustion". In: *SAE Transactions* (1968), pp. 3025–3044.

[7] John, James EA. *Lean burn engine concepts-emissions and economy*. Tech. rep. SAE Technical Paper, 1975.

[8] Duchaussoy, Yorick, Lefebvre, Alain, and Bonetto, Robert. *Dilution interest on turbocharged SI engine combustion*. Tech. rep. SAE Technical Paper, 2003.

[9] Zhen, Xudong et al. "The engine knock analysis–An overview". In: *Applied Energy* 92 (2012), pp. 628–636.

[10] Pischinger, Stefan and Heywood, John B. "A model for flame kernel development in a spark-ignition engine". In: *Symposium (international) on Combustion*. Vol. 23. 1. Elsevier. 1991, pp. 1033–1040.

[11] Konig, G and Sheppard, CGW. "End gas autoignition and knock in a spark ignition engine". In: *SAE transactions* (1990), pp. 820–839.

[12] Feng, Dengquan, Buresheid, Khalifa, Zhao, Hua, Wei, Haiqiao, and Chen, Ceyuan. "Investigation of lubricant induced pre-ignition and knocking combustion in an optical spark ignition engine". In: *Proceedings of the Combustion Institute* 37.4 (2019), pp. 4901–4910.

[13] Duan, Xiongbo et al. “Performance, combustion and knock assessment of a high compression ratio and lean-burn heavy-duty spark-ignition engine fuelled with n-butane and liquefied methane gas blend”. In: *Energy* 158 (2018), pp. 256–268.

[14] Rapp, V, Killingsworth, N, Therkelsen, P, and Evans, R. “Lean-burn internal combustion engines”. In: *Lean Combustion*. Elsevier, 2016, pp. 111–146.

[15] Caton, Jerald A. “The thermodynamic characteristics of high efficiency, internal-combustion engines”. In: *Energy Conversion and Management* 58 (2012), pp. 84–93.

[16] Huang, CC, Shy, SS, Liu, CC, and Yan, YY. “A transition on minimum ignition energy for lean turbulent methane combustion in flamelet and distributed regimes”. In: *Proceedings of the Combustion Institute* 31.1 (2007), pp. 1401–1409.

[17] Zabetakis, Michael George. *Flammability characteristics of combustible gases and vapors*. Tech. rep. Bureau of Mines Washington DC, 1965.

[18] Chigier, Norman A. *Energy, combustion, and environment*. McGraw-Hill New York, 1981.

[19] Maly, R, Saggau, B, Wagner, E, and Ziegler, G. “Prospects of ignition enhancement”. In: *SAE transactions* (1983), pp. 405–422.

[20] Nakamura, Norihiko, Kobayashi, Tatsuo, Hanaoka, Masanori, and Takagi, Noboru. *A new platinum tipped spark plug extends the lean misfire limit and useful life*. Tech. rep. SAE Technical Paper, 1983.

[21] Metghalchi, Mohamad and Keck, James C. “Burning velocities of mixtures of air with methanol, isooctane, and indolene at high pressure and temperature”. In: *Combustion and flame* 48 (1982), pp. 191–210.

[22] Amirante, Riccardo, Distaso, Elia, Tamburrano, Paolo, and Reitz, Rolf D. “Laminar flame speed correlations for methane, ethane, propane and their mixtures, and natural gas and gasoline for spark-ignition engine simulations”. In: *International Journal of Engine Research* 18.9 (2017), pp. 951–970.

[23] Daniel, WA. “Flame quenching at the walls of an internal combustion engine”. In: *Symposium (International) on Combustion*. Vol. 6. 1. Elsevier. 1957, pp. 886–894.

[24] Alkidas, AC. “Combustion-chamber crevices: the major source of engine-out hydrocarbon emissions under fully warmed conditions”. In: *Progress in energy and combustion science* 25.3 (1999), pp. 253–273.

[25] Ferguson, Colin R and Keck, James C. "On laminar flame quenching and its application to spark ignition engines". In: *Combustion and Flame* 28 (1977), pp. 197–205.

[26] Enomoto, Masaru. "Head-on quenching of a premixed flame on the single wall surface". In: *JSME International Journal Series B Fluids and Thermal Engineering* 44.4 (2001), pp. 624–633.

[27] Mayer, El. "A theory of flame propagation limits due to heat loss". In: *Combustion and Flame* 1.4 (1957), pp. 438–452.

[28] Bellenoue, M, Kageyama, T, Labuda, SA, and Sotton, J. "Direct measurement of laminar flame quenching distance in a closed vessel". In: *Experimental thermal and fluid science* 27.3 (2003), pp. 323–331.

[29] Popp, P and Baum, M. "Analysis of wall heat fluxes, reaction mechanisms, and unburnt hydrocarbons during the head-on quenching of a laminar methane flame". In: *Combustion and Flame* 108.3 (1997), pp. 327–348.

[30] Poinsot, TJ, Haworth, Daniel Connell, and Bruneaux, Gilles. "Direct simulation and modeling of flame-wall interaction for premixed turbulent combustion". In: *Combustion and Flame* 95.1-2 (1993), pp. 118–132.

[31] Collins, Neil R and Twigg, Martyn V. "Three-way catalyst emissions control technologies for spark-ignition enginesârecent trends and future developments". In: *Topics in Catalysis* 42.1-4 (2007), pp. 323–332.

[32] De Petris, C, Diana, S, Giglio, V, and Police, G. "High efficiency stoichiometric spark ignition engines". In: *SAE transactions* (1994), pp. 1059–1067.

[33] Einewall, Patrik, Tunestål, Per, and Johansson, Bengt. *Lean burn natural gas operation vs. stoichiometric operation with EGR and a three way catalyst*. Tech. rep. SAE Technical Paper, 2005.

[34] Young, Michael B. "Cyclic dispersion in the homogeneous-charge spark-ignition engineâa literature survey". In: *SAE Transactions* (1981), pp. 49–73.

[35] Germane, Geoff J, Wood, Carl G, and Hess, Clay C. "Lean combustion in spark-ignited internal combustion engines-a review". In: *SAE Technical Paper* (1983).

[36] Macián, V, Luján, JM, Bermúdez, V, and Guardiola, C. "Exhaust pressure pulsation observation from turbocharger instantaneous speed measurement". In: *Measurement Science and Technology* 15.6 (2004), p. 1185.

[37] Stone, CR, Brown, AG, and Beckwith, P. *Cycle-by-cycle variations in spark ignition engine combustion-part ii: Modelling of flame kernel displacements as a cause of cycle-by-cycle variations*. Tech. rep. SAE Technical Paper, 1996.

[38] De Soete, GC. "Propagation behaviour of spark ignited flames in the early stages". In: *International Conference on Combustion in Engineering*. Vol. 1. 1983, p. 93.

[39] Quader, Ather A. "Lean combustion and the misfire limit in spark ignition engines". In: *SAE transactions* (1974), pp. 3274–3296.

[40] Cho, HM and He, B-Q. "Combustion and emission characteristics of a lean burn natural gas engine". In: *International Journal of Automotive Technology* 9.4 (2008), pp. 415–422.

[41] Evans, Robert Lancelot. *Control method for spark-ignition engines*. US Patent 6,032,640. 2000.

[42] Harada, Jun, Tomita, Tsutomu, Mizuno, Hiroyuki, Mashiki, Zenichiro, and Ito, Yasushi. "Development of direct injection gasoline engine". In: *SAE transactions* (1997), pp. 767–776.

[43] Noyori, Takahiro. *Experimental study of smoke emission on small-displacement spark-ignition direct-injection engine*. Tech. rep. SAE Technical Paper, 2006.

[44] Park, Cheolwoong, Kim, Sungdae, Kim, Hongsuk, and Moriyoshi, Yasuo. "Stratified lean combustion characteristics of a spray-guided combustion system in a gasoline direct injection engine". In: *Energy* 41.1 (2012), pp. 401–407.

[45] Poulos, Stephen G and Heywood, John B. "The effect of chamber geometry on spark-ignition engine combustion". In: *SAE transactions* (1983), pp. 1106–1129.

[46] Martinez, Santiago, Irimescu, Adrian, Merola, Simona Silvia, Lacava, Pedro, and Curto-Riso, Pedro. "Flame front propagation in an optical GDI engine under stoichiometric and lean burn conditions". In: *Energies* 10.9 (2017), p. 1337.

[47] Ricardo, Harry R. *Internal combustion engine of the liquid fuel injection type*. US Patent 2,066,228. 1936.

[48] Adams, Tim G. *Torch ignition for combustion control of lean mixtures.* Tech. rep. SAE Technical Paper, 1979.

[49] Noguchi, M, Sanda, S, and Nakamura, N. "Development of Toyota lean burn engine". In: *SAE Transactions* (1976), pp. 2358–2373.

[50] Brandstetter, Walter. "The volkswagen lean burn pc-engine concept". In: *SAE Transactions* (1980), pp. 1804–1821.

[51] Wyczalek, Floyd A, Harned, John L, Maksymiuk, S, and Blevins, Jerry R. *EFI prechamber torch ignition of lean mixtures.* Tech. rep. SAE Technical Paper, 1975.

[52] Marion, Mallory. *Internal combustion engine.* US Patent 2,121,920. 1938.

[53] Barnes, WB. "Improvements in or Relating to Internal Combustion Engines". In: *British Patent* 683 (1952), p. 162.

[54] Date, Tasuku, Yagi, Shizuo, Ishizuya, Akira, and Fujii, Isao. *Research and development of the Honda CVCC engine.* Tech. rep. SAE Technical Paper, 1974.

[55] Getzlaff, J, Pape, J, Gruenig, C, Kuhnert, D, and Latsch, R. "Investigations on pre-chamber spark plug with pilot injection". In: *SAE Transactions* (2007), pp. 421–433.

[56] Lezanski, T, Kesler, M, Rychter, T, Teodorczyk, A, and Wolanski, P. *Performance of pulsed jet combustion (PJC) system in a research engine.* Tech. rep. SAE Technical Paper, 1993.

[57] Kojic, Aleksandar, Hathout, Jean-Pierre, Cook, David, and Ahmed, Jasim. *Control of auto-ignition timing for combustion in piston engines by prechamber compression ignition.* US Patent 6,953,020. 2005.

[58] Kojic, Aleksandar, Hathout, Jean-Pierre, Cook, David, and Ahmed, Jasim. *Control of auto-ignition timing for homogeneous combustion jet ignition engines.* US Patent 7,107,964. 2006.

[59] Attard, William. *Turbulent jet ignition pre-chamber combustion system for spark ignition engines.* US Patent 8,857,405. 2014.

[60] Durling, Harold E and Ralph, Joseph G. *Directed jet spark plug.* US Patent 6,213,085. 2001.

[61] Durling, Harold E, Johnston, Robert P, and Polikarpus, Kaius K. *Torch jet spark plug.* US Patent 5,421,300. 1995.

[62] Toulson, Elisa, Watson, Harry C, and Attard, William P. *Modeling alternative prechamber fuels in jet assisted ignition of gasoline and LPG*. Tech. rep. SAE Technical Paper, 2009.

[63] Toulson, Elisa, Watson, Harry C, and Attard, William P. *The lean limit and emissions at near-idle for a gasoline HAJI system with alternative pre-chamber fuels*. Tech. rep. SAE Technical Paper, 2007.

[64] Garrett, T Ken. "Porsche stratified charge engine". In: *Environmental Science & Technology* 9.9 (1975), pp. 826–830.

[65] Varde, Keshav S and Lubin, MJ. *The Roll of Connecting Nozzle and the Flame Initiation Point in the Performance of a Dual Chamber Stratified Charge Engine*. Tech. rep. SAE Technical Paper, 1974.

[66] Broderson, Neil O. *Method of operating internal-combustion engines*. US Patent 2,615,437. 1952.

[67] Gussak, LA, Karpov, VP, and Tikhonov, Yu V. "The application of lag-process in prechamber engines". In: *SAE Transactions* (1979), pp. 2355–2380.

[68] Gussak, LA. "x0201C; Method of Precham ber&# x002d; Torch Ignition in Internal Combus tion Engines. &# x0201D; US Pat". In: *Off* 3.230 (1963), p. 939.

[69] Yamaguchi, Shigeki, Ohiwa, Norio, and Hasegawa, Tatsuya. "Ignition and burning process in a divided chamber bomb". In: *Combustion and flame* 59.2 (1985), pp. 177–187.

[70] Watson, Harry C. *Internal combustion engine ignition device*. US Patent 5,611,307. 1997.

[71] Hamori, Ferenc and Watson, Harry C. "Hydrogen assisted jet ignition for the hydrogen fuelled SI engine". In: *world hydrogen energy conference*. 15. 2006.

[72] Toulson, Elisa. "Applying alternative fuels in place of hydrogen to the jet ignition process". PhD thesis. 2008.

[73] Robinet, Cyril, Higelin, Pascal, Moreau, B, Pajot, O, and Andrzejewski, J. "A New Firing Concept for Internal Combustion Engines:" I'APIR"". In: *SAE transactions* (1999), pp. 973–988.

[74] Durling, Harold E. *Igniter for internal combustion engines operating over a wide range of air fuel ratios*. US Patent 7,021,275. 2006.

[75] Latsch, Reinhard. "The swirl-chamber spark plug: a means of faster, more uniform energy conversion in the spark-ignition engine". In: *SAE transactions* (1984), pp. 365–377.

[76] Weng, Volker et al. *Investigation of the Bowl-Prechamber-Ignition (BPI) Concept in a Direct Injection Gasoline Engine at Part Load.* Tech. rep. SAE Technical Paper, 1999.

[77] Toulson, Elisa, Schock, Harold J, and Attard, William P. "A review of pre-chamber initiated jet ignition combustion systems". In: (2010).

[78] Attard, William P and Parsons, Patrick. "A normally aspirated spark initiated combustion system capable of high load, high efficiency and near zero NOx emissions in a modern vehicle powertrain". In: *SAE International Journal of Engines* 3.2 (2010), pp. 269–287.

[79] Attard, William P and Blaxill, Hugh. "A single fuel pre-chamber jet ignition powertrain achieving high load, high efficiency and near zero NOx emissions". In: *SAE International Journal of Engines* 5.3 (2012), pp. 734–746.

[80] Attard, William P and Parsons, Patrick. "Flame kernel development for a spark initiated pre-chamber combustion system capable of high load, high efficiency and near zero NOx emissions". In: *SAE International Journal of Engines* 3.2 (2010), pp. 408–427.

[81] Bureshaid, Khalifa, Shimura, Ray, Feng, Dengquan, Zhao, Hua, and Bunce, Mike. "Experimental Studies of the Effect of Ethanol Auxiliary Fueled Turbulent Jet Ignition in an Optical Engine." In: *SAE International Journal of Engines* 12.4 (2019), pp. 387–400.

[82] Hiraoka, Kenji, Nomura, Kazutoshi, Yuuki, Akihiro, Oda, Yuji, and Kameyama, Toshiyuki. "Phenomenological 0-Dimensional Combustion Model for Spark-Ignition Natural Gas Engine Equipped with Pre-Chamber". In: *SAE Technical Paper* (2016).

[83] Gentz, Gerald, Thelen, Bryce, Litke, Paul, Hoke, John, and Toulson, Elisa. "Combustion visualization, performance, and CFD modeling of a pre-chamber turbulent jet ignition system in a rapid compression machine". In: *SAE International Journal of Engines* 8.2 (2015), pp. 538–546.

[84] Gentz, Gerald et al. "A study of the influence of orifice diameter on a turbulent jet ignition system through combustion visualization and performance characterization in a rapid compression machine". In: *Applied Thermal Engineering* 81 (2015), pp. 399–411.

[85] Jamrozik, Arkadiusz. "Lean combustion by a pre-chamber charge stratification in a stationary spark ignited engine". In: *Journal of Mechanical Science and Technology* 29.5 (2015), pp. 2269–2278.

[86] Bureshaid, Khalifa, Feng, Dengquan, Zhao, Hua, and Bunce, Mike. "Combustion and emissions of gasoline, anhydrous ethanol, and wet ethanol in an optical engine with a turbulent jet ignition system". In: *Proceedings of the Institution of Mechanical Engineers, Part D: Journal of Automobile Engineering* 233.13 (2019), pp. 3528–3537.

[87] Ikegami, Makoto, Shioji, M, and Koike, M. "A stochastic approach to model the combustion process in direct-injection diesel engines". In: *Symposium (International) on Combustion*. Vol. 20. 1. Elsevier. 1985, pp. 217–224.

[88] Tabaczynski, Rodney J, Trinker, Frederick H, and Shannon, Ben AS. "Further refinement and validation of a turbulent flame propagation model for spark-ignition engines". In: *Combustion and Flame* 39.2 (1980), pp. 111–121.

[89] Bardis, Konstantinos, Xu, Guoqing, Kyrtatos, Panagiotis, Wright, Yuri M, and Boulouchos, Konstantinos. "A zero dimensional turbulence and heat transfer phenomenological model for pre-chamber gas engines". In: *SAE Technical Paper* (2018).

[90] Fogla, Navin, Bybee, Michael, Mirzaeian, Mohsen, Millo, Federico, and Wahiduzzaman, Syed. "Development of a K-k-e Phenomenological Model to Predict In-Cylinder Turbulence". In: *SAE International Journal of Engines* 10.2 (2017), pp. 562–575.

[91] Borgnakke, C, Davis, GC, and Tabaczynski, RJ. "Predictions of in-cylinder swirl velocity and turbulence intensity for an open chamber cup in piston engine". In: *SAE Transactions* (1981), pp. 964–978.

[92] Achuth, Munnannur and Mehta, Pramod S. "Predictions of tumble and turbulence in four-valve pentroof spark ignition engines". In: *International Journal of Engine Research* 2.3 (2001), pp. 209–227.

[93] Bargende, Michael. *Ein Gleichungsansatz zur Berechnung der instationären Wandwärmeverluste im Hochdruckteil von Ottomotoren*. na, 1990.

[94] Bozza, Fabio et al. "A Quasi-Dimensional Model of Pre-Chamber Spark-Ignition Engines". In: *SAE Technical Paper* (2019).

[95] De Bellis, Vincenzo, Bozza, Fabio, and Tufano, Daniela. *A Comparison Between Two Phenomenological Combustion Models Applied to Different SI Engines*. Tech. rep. SAE Technical Paper, 2017.

[96] Baratta, M, Catania, AE, Spessa, E, and Vassallo, A. "Development of an improved fractal model for the simulation of turbulent flame propagation in SI engines". In: *SAE Technical Paper* (2005).

[97] Xu, Guoqing, Kotzagianni, Maria, Kyrtatos, Panagiotis, Wright, Yuri M, and Boulouchos, Konstantinos. "Experimental and numerical investigations of the unscavenged prechamber combustion in a rapid compression and expansion machine under engine-like conditions". In: *Combustion and Flame* 204 (2019), pp. 68–84.

[98] Jamrozik, Arkadiusz, Tutak, Wojciech, Kociszewski, Arkadiusz, and Sosnowski, Marcin. "Numerical simulation of two-stage combustion in SI engine with prechamber". In: *Applied Mathematical Modelling* 37.5 (2013), pp. 2961–2982.

Chapter 3

Experimental setup and methodology

3.1 Introduction

In this chapter, all the resources needed in order to carried out the experimental campaign are described. First, the facility used for the experimental characterization of the pre-chamber spark ignition system is detailed, including the Rapid Compression-Expansion Machine and the geometry of the pre-chamber nozzles used. In addition, the characteristics of the ignition system and the fuel injectors will be depicted. Then, the optical setup will be discussed in terms of the hardware used and the fundamentals of the technique itself. In the last two sections, the experimental methodology and the test matrix will be described. All measurements were carried out in the facilities of CMT-Motores Térmicos .

3.2 Combustion system

The arrangement used to perform the experimental work is composed by the following main components:

- Rapid compression-expansion machine (RCEM)
- Pre-chamber

- Fuel injection and ignition systems

3.2.1 Rapid Compression-Expansion Machine (RCEM)

The RCEM (Figure 3.1) is an experimental facility able to replicate the engine working process during the compression and initial expansion strokes, but allowing a better control of the initial boundary conditions [1]. The machine is composed by a set of pistons which are pneumatically driven, while an additional hydraulic circuit is used to couple these pistons and adjust some of the boundary conditions for the experiments (such as the distance from the cylinder head to the piston at bottom dead centre). The RCEM is the upgrade of the already well known rapid compression machine (RCM) and is used worldwide for studies related to chemical kinetics and auto-ignition analysis [2–4].

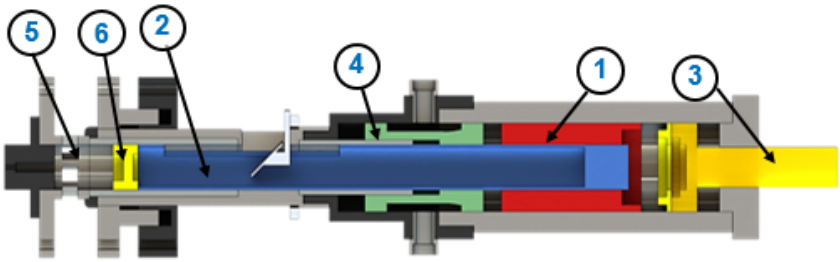

1	Pushing piston	4	Air piston
2	Driver piston	5	Combustion chamber
3	Displacement piston	6	Combustion piston

Figure 3.1: Rapid compression-expansion machine

Critical combustion parameters such as the compression ratio, the piston velocity (which can be expressed in terms of an equivalent engine speed), and the displacement stroke can be adjusted by varying the oil and air volumes. In this way, the system is able to replicate a wide range of engine layouts and different operating conditions. The displacement piston controls the stroke, while the pistons number 1 and 4 change their initial position according to the machine input parameters and allow the perfect inertial balance of the system during the tests. The driver piston operates due to the pressure differential between the combustion and the driving gas volumes. Moreover it is

hydraulically coupled to the piston 3 and mechanically coupled to the combustion piston. The latest has a diameter of $84mm$, and its shape can be varied by changing the aluminum central part to induce different engine-like turbulence motions. Furthermore, it is possible to replace this aluminium part with a quartz window, allowing to perform optical tests.

Under the original operation mode, five main phases can be identified: the preparation (equivalent to the engine intake stroke), compression, combustion, expansion and cleaning (or scavenging). It is important to underline that only the compression, combustion and the early expansion instants are directly comparable to an engine cycle, thus are relevant in terms of scientific research.

The filling process of the driving gas volume (to achieve the desired pushing pressure) and combustion chamber (to achieve the initial pressure) takes about 90 seconds and is completed 1 minute before the beginning of the test, ensuring an homogeneous temperature and mixture field. Compression is divided in two phases: a slow one (duration around 0.85s), driven by the hydraulic decoupling of pushing and driver pistons, and a rapid one (duration around 0.03s). During the first phase, according to the desired compression ratio or engine equivalent speed, the combustion chamber pressure and the air pushing pressure are selected. In this way the oil behind the piston 1 will be pressurized and ready to push the driver piston (piston 2).

The test initiates by means of an hydraulic valve activation which recirculates the pressurized oil towards the base of the driven piston obtaining the slow compression stroke. Once the driver piston reaches the $29mm$ of the total compression stroke, the volume of recirculated oil increases exponentially generating a grater pushing force (rapid compression phase). The combustion chamber pressure increases and balances the pushing force until TDC. Then, the piston performs the expansion stroke by means of higher pressure in the chamber compared to the pushing pressure. This principle replaces the connecting rod-crank mechanism typical of conventional engines and allows, in accordance with the two initial pressures, to vary parameters that are geometrically fixed in an engine. During the last phase, the combustion chamber is cleaned by means of a vacuum pump which ensures the exhaust gas evacuation. More details on the RCEM working process can be found in [5–7]. The technical characteristics of the RCEM can be seen in Table 3.1.

In this study, the maximum compression stroke allowed (the distance between the combustion piston head and the cylinder head) is set to $120mm$ and the compression ratio varies from 10:1 to 13:1 depending on the test. It is important to underline that boosting the air driving pressure increases the piston stroke, thus raising the compression ratio. In terms of instrumen-

Table 3.1: Geometrical characteristics and operational ranges of the RCEM.

Bore	84 mm
Stroke	120-249 mm
Compression ratio	5:25
Maximum in-cylinder pressure	20 MPa
Initial pressure	0.1-0.5 MPa
Initial temperature	25-180°C
Equivalent engine speed	600-3000 rpm

tation, a Yokogawa DL850V high-frequency acquisition system (at 10MHz) records the temporal evolution of the pressure inside the cylinder as well as in the pre-chamber, obtained by means of two piezoelectric pressure transducers (Kistler 6045A for both chambers). The pressure sensors are calibrated in the RCEM in both static and motored conditions after the modification of the original cylinder head for the pre-chamber housing. The calibration constants are adjusted to obtain the same pressure evolution with the two transducers for different thermodynamic conditions (initial pressure and temperature) and configuration (compression ratio) under conventional spark ignition layout (i.e. with the pre-chamber dismounted from the cylinder head) at motored conditions.

Once the sensors are calibrated, the pre-chamber is mounted and the pressure difference between the two chambers is checked. The instantaneous evolution of the piston position is recorded by means of an electromagnetic ruler and two AMO LMK102 incremental position sensors, with a resolution of $0.01mm$. The average temperature in the combustion chamber at the beginning of the experiment is acquired by a commercial K-type thermocouple. The next sections concern the pre-chamber geometries used for the thesis work, the positions and technical characteristics of the ignition and injection systems.

3.2.2 Pre-chamber geometries

To carry out the experimental campaign, several different pre-chambers are designed and manufactured to analyse the impact of the geometry (orifices numbers, diameter and displacement) on combustion.

The pre-chamber is easily interchangeable by removing the screws that fix it against the cylinder head (left side of figure 3.2). Additionally, all the combustion chambers components are shown in the figure 3.2 (right side):

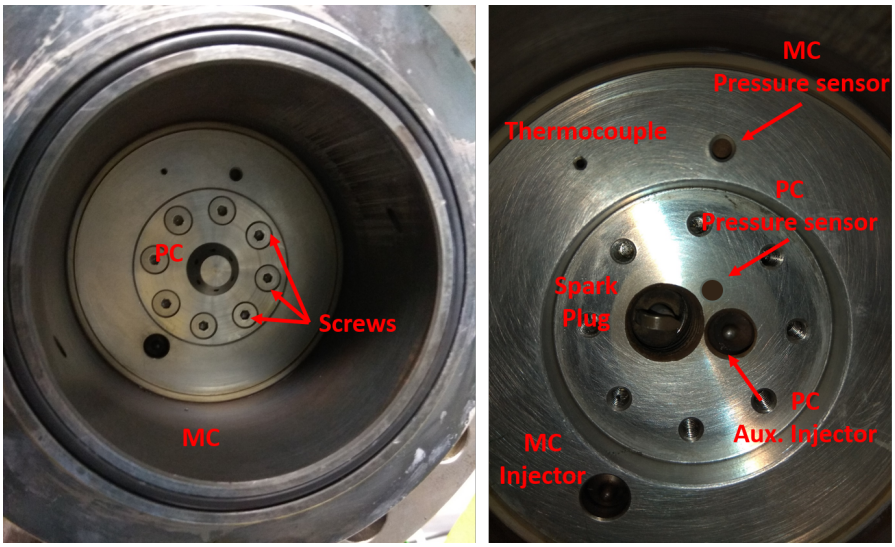

Figure 3.2: Combustion chamber layout

- Main chamber and pre-chamber piezoelectric pressure sensors (Kistler 6045A).
- Commercial thermocouple for air temperature measurements.
- Main chamber single-orifice injector (nozzle diameter equal to $156\mu m$).
- Commercial NGK spark plug (LZKRS106 model)
- Pre-chamber single-orifice injector (nozzle diameter equal to $90\mu m$).

Regarding the spark plug housing, it is important to point out that it is decentred with respect to the pre-chamber axis due to geometry constrains (unlike the traditional pentroof layout of a standard SI engine), thus the distance between the spark plug electrodes and each pre-chamber orifices is variable.

All the pre-chamber geometries and their main geometric parameters are depicted in the figure 3.4:

- PC01 - The baseline pre-chamber with 6 straight orifices with $1.5mm$ diameter.
- PC02 - The pre-chamber with 6 tilted orifices and $1.5mm$ diameter.

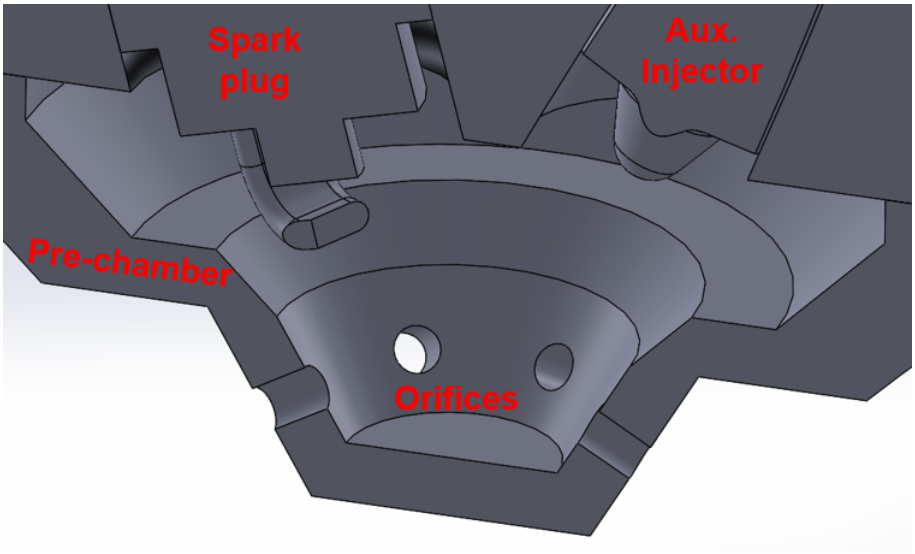

Figure 3.3: Pre-chamber section

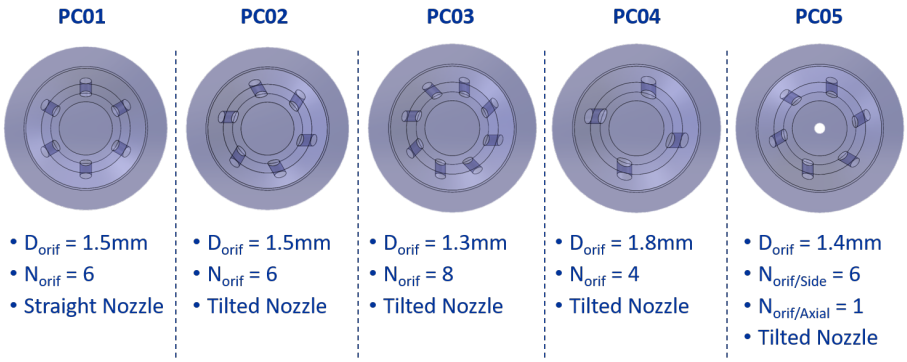

Figure 3.4: Pre-chamber geometries

- PC03 - The pre-chamber with 8 tilted orifices and 1.3mm diameter.
- PC04 - The pre-chamber with 4 tilted orifices and 1.8mm diameter.
- PC05 - The pre-chamber with 6 tilted side orifices and 1 axial orifice of 1.4mm diameter.

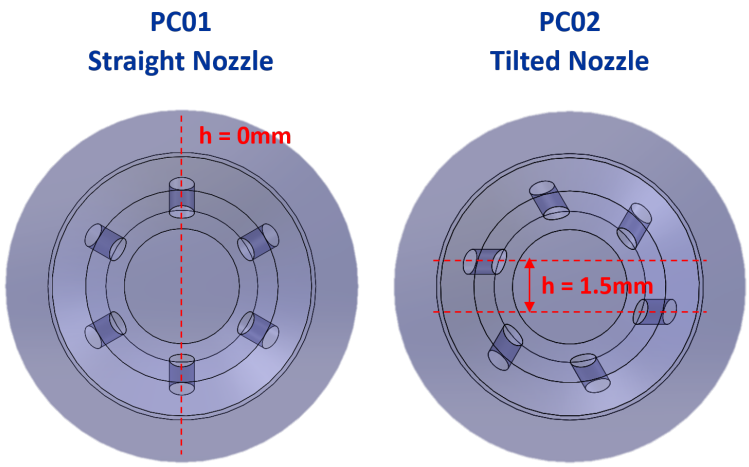

Figure 3.5: Straight nozzle (PC01) vs Tilted nozzles (PC02-03-04-05)

Geometries PC01 and PC02 are employed to assess the impact of the tilted nozzle respect to straight nozzle, while geometries PC02, PC03, and PC04 are utilized to determine the influence of the orifices number on the combustion. Finally the axial orifice effects are evaluated with the pre-chamber PC05 nozzle. All the other critical parameters as the orifice cross-section $A_{cross} = 10.6mm^2$, the pre-chamber volume $V_{prec} = 3.3cm^3$, and the orifices length $L_{orif} = 2mm$, do not vary between the different geometries in order to understand the influence of single parameters on the phenomenon. In addition, the main chamber inlet angle (defined as the angle between the orifice axis and the pre-chamber axis) is around 60° for all the orifices and all the geometries. The figure 3.5 shows in further detail the differences between PC01 and PC02 nozzles. In the first case, the axis of the symmetrical orifices coincides, while in the second one is displaced of $1.5mm$.

3.2.3 Fuel injection and ignition systems

In order to control the main and pre-chamber equivalence ratio, both injectors are hydraulically characterized by means of ROI meter based on the Bosch method [8, 9].

Two single-orifice solenoid injectors are chosen for the current work, in order to limit the possible wall wetting due to the system geometry. Both injectors are fed from a single high-pressure common-rail system driven by

a Genotec trigger/pulse generator. To control low fuel injection quantity a small nozzle diameter around $90\mu m$ is housed in the pre-chamber. Meanwhile, a bigger nozzle diameter around $156\mu m$ is installed for the main chamber injection. As expected, the injected mass is a direct function of the injection pressure and the solenoid energizing time (Figures 3.6,4.9). As is known, the spray's evaporation, atomization and mixing processes, the turbulence field, and the wall wetting are all phenomena affected by the injection pressure [10]. Hence, the injected mass is characterized for three rail pressures. In addition, to avoid hardware complexity, the two injectors are actuated by the same injection system. In other words, it is not possible to independently change the injection pressure of each injector.

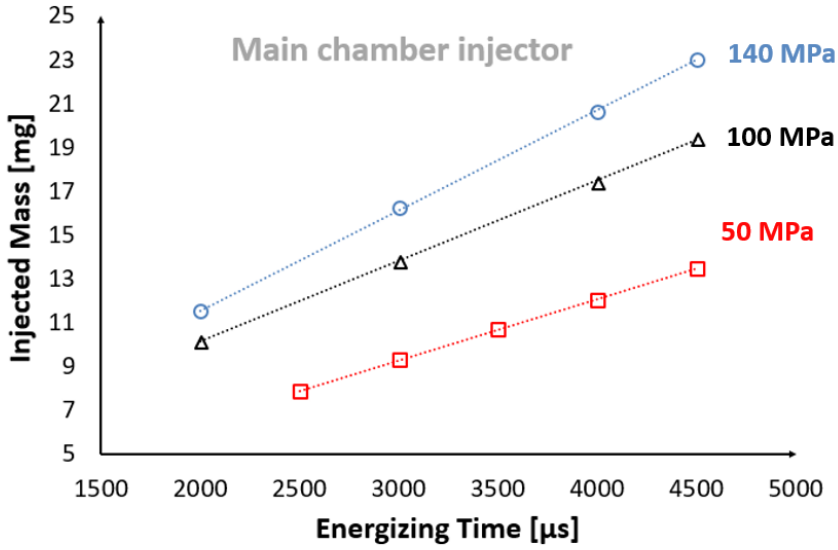

Figure 3.6: Injected mass as function of the energizing time under different injection pressure for the main chamber injector

The main chamber injection is performed at the beginning of the working cycle, thus in a low density environment (low pressure). Despite the spray's fast penetration linked to this low density condition, the piston is still far enough (BDC) from the injector tip, ensuring the complete fuel evaporation and mixing before the piston wall is approached. On the contrary, the reduced distance between the injector tip and the pre-chamber walls (about $12mm$) can

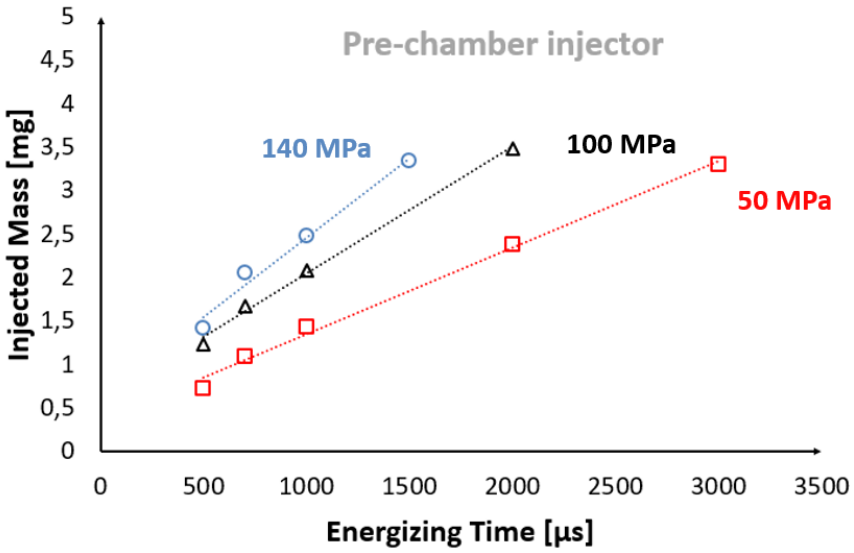

Figure 3.7: Injected mass as function of the energizing time under different injection pressure for the pre-chamber injector

be a critical factor when the auxiliary injection is performed [11]. Although the injection pressure is a secondary factor in the liquid length prediction [12, 13], it affects the injection velocity thus can have a big impact on the wall wetting in the reduced pre-chamber volume. Indeed, to limit the impact of the liquid fuel, a low injection pressure is the best solution. However, low injection pressure reduced the induced turbulence (lower injection velocity and spray momentum) and increase the air/fuel mixing time (higher energizing time needed) before the spark plug activation[14].

The effects of the wall wetting are evaluated (previously the start of the experimental campaign) performing the same test, changing the injection pressure. Results are consistent, in terms of pressure peak and shape, when comparing 50 MPa and 100 MPa. On the contrary, a deterioration of pre-chamber combustion is observed when using an injection pressure of 140 MPa. More details will be depicted in in the later sections.

Finally, the intermediate rail pressure of 100 MPa is used during the combustion tests, being a fair compromise in terms of induced turbulence and mixing time. Nevertheless, further studies are needed to deeply investigate the wall wetting in systems using liquid fuel.

The injected fuel during the experimental tests is pure iso-octane used as gasoline fuel surrogate (C_8H_{18}), which main chemical and physical characteristics are resumed in table below 3.2.

Table 3.2: Iso-octane main chemical and physical characteristics

Density (at 25°C, 0.1MPa)	692 Kg/m^3
Dynamic Viscosity (at 25°C, 0.1MPa)	0.473 mPa
Vapor pressure (at 21°C)	5.5 kPa
Heat capacity (at 25°C)	190 J/mol
Lower Heating Value	44310 kJ/kg

The ignition system is composed by a commercial NGK spark plug (LZKRS106 model) triggered by a multicharge Delphi system. The system can operate in two different modes. In the multicharge mode (MC operation) the coil provides in a fast sequence high voltage to the spark plug electrode and ionizes the gap to generate a long quasi-continuous spark with sufficient energy to help igniting the combustion mixture under all conditions. The MC coil can also be operated in a standard single charge mode (SC operation) if MC operation is not required, like in the thesis work. Each coil contains a smart electronics with an integrated driver, which forms the interface between the Engine Management System and the ignition coil.

The ignition coil is able to deliver up to 80 mJ and 33 kV on maximum performance during single spark ignition mode.

3.3 Optical setup and technique for flame visualization

Optical techniques are commonly used for macroscopic and microscopic characterization of the injected spray and combustion flames. Optical diagnosis coupled with CFD models is a powerful tool for engine critical process optimization such as injection, atomization, evaporation, air-fuel mixing, wall wetting, early combustion stage, an turbulent flame propagation [15].

Indeed, these techniques can often be hard to implement and very expensive due to advanced equipment required (especially the ones with the laser). One of the most easily and used optical technique for flame structure characterization is the direct visualization method for chemiluminescence measurements.

Toulson et al. [16] performed a visualization analysis of a natural gas spark ignition and propane turbulent jet ignition combustion by means of an optical single cylinder engine. The study focused on the flame propagation rates measurements as function of the different fuel and the equivalence ratio. Optical images demonstrating stable combustion even under ultra-lean condition ($\lambda > 1.8$) resulting in a clean and efficiency combustion.

Gholamisheeri et al. [17] investigated the flame structure as function of air dilution by means of high speed chemiluminescence visualization, through the optical access of the rapid compression machine. The optical results are compared with 3D CFD simulations in order to validate combustion models. In addition, accurate jet ignition models are used for the evaluation of parameters that are difficult to quantify experimentally, such as cold pre-chamber jet, unburned mixture backflow from the main chamber, and later combustion stage.

For this thesis, the visualization tests are performed through the side optical access available in the RCEM. The central part of the combustion piston are replaced by a quartz window allowing visualization from the bottom to the central 46mm diameter out of the total 84mm bore.

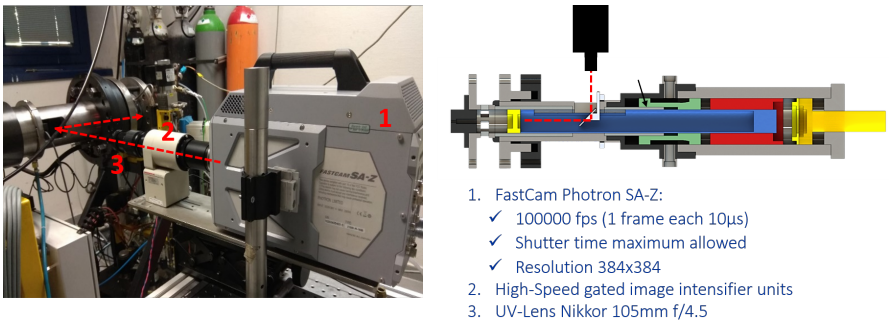

Figure 3.8: RCEM optical setup for chemiluminescence measurements

The figure 3.8 shows the main components of the RCEM optical arrangement:

1. FastCam Photron SA-Z.
2. High Speed Intensifier, model C10880-03C.
3. UV Lens Nikkor 105mm f/4.5

A Photron's SA-Z high-speed camera records the images with a resolution of 0.1 MHz ($10\mu s$). Furthermore, a high speed gated image intensifier (C1088003F model),amplifies the natural light emitted by the lean combustion. A UV-Nikkor 105mm f/4.5 lens is coupled with the intensifier allowing to capture a broadband light emission (between 220nm and 900nm).

3.3.1 Image post-processing

The post-processing method basically depends on the parameters to be analysed. In order to study the flame penetration, speed, spread angle and other fundamental combustion parameters, the segmentation of the jet and background is required. The main stages of the video's post-analysis routine can be summarized as follows:

1. Picture masking. Once loaded from the code, the image is visualized as a matrix of values representing the normalized intensity of each pixel on a gray scale from 0 to 1 (black to white). It is identified as a mask, a matrix (same size of the picture) in which the value 1 represents the area of interest and the value 0 the one to exclude. Multiplying the two matrices we obtain the cropped image.

2. Background elimination. The next step, is to separate the background from the cropped image. According to the Beer-Lambert law[18], the average background intensity before the combustion event are subtracted from all the pictures.

3. Contour tracing and analysis. Once the jet are segmented from the background, its contour was obtained binarizing the image with a threshold intensity level[19, 20]. Taking into account, that the contour can be very dependent on the binarization level, a sensitivity analysis of this parameter is conducted by analysing the jet penetration with several threshold.

3.4 Matrix test

In this section the experimental tests matrix is discussed. First, it is important to underline all the parameters which are fixed and the variables parameters under investigation, of the overall experimental campaign.

Fixed parameters:

- Compression stroke = 120mm

- Compression ratio = 11:1, unless specified otherwise
- Equivalent engine speed = 1500 rpm
- Piston shape = Flat piston
- Driving gas air pressure = 2.2 MPa
- Spark ignition time = t (s = 105mm)
- Initial combustion chamber pressure = 0.15 MPa
- Initial combustion chamber temperature = 360K
- Fuel = Iso-octane

The listed parameters are intended to represent the characteristics of a modern turbocharged spark ignition engine. Unfortunately, the RCEM only allows one degree of freedom in choosing between the compression ratio and the equivalent engine speed. All the listed parameters are considered fixed and kept constant for the overall experimental campaign.

Variables parameters under investigation:

- Pre-chamber equivalence ratio = $0.9 < \phi < 1.1$
- Main chamber equivalence ratio = $0.3 < \phi < 0.5$
- Start of injection (SOI) and injection pressure (P_{inj})
- Pre-chamber nozzle geometry = PC01 - 05

The performance of the PCSI system with the baseline set-up (pre-chamber - PC01) are assessed according to the following test matrix:

1. The pre-chamber auxiliary injection (performed during the compression stroke) impact on combustion is explored. As stated, the injection event modifies the turbulence flow field and air-fuel mixing distribution. Indeed, early injection allows large evaporation and mixing time before the spark plug activation. On the contrary, late injection reduces the air-fuel mixing time but promotes a high turbulent flow at start of combustion. In addition, late injections help to reduce the wall wetting impact. As the piston compresses the chamber mixture, the average temperature and pressure increase, promoting a low penetration and high evaporation of

the liquid spray. For the purpose of the injection settings investigation, the injection pressure varies between 140 MPa and 100 MPa, while the injection event is triggered a two timings: around half of the compression stroke (65mm) and close to the spark time (87mm). Additionally, two compression ratios around 12 and 13 are considered. Finally, equivalence ratios in both chambers at set at $\phi_{PC} = 1.1$ and $\phi_{MC} = 0.5$.

2. The pre-chamber equivalence ratio at spark instant, are varied from lean to rich conditions. According to the empirical correlation of DiStaso, the laminar flame speed is a function of the equivalence ratio, affecting all the combustion performances. By means of the auxiliary injected mass, 2 different pre-chamber equivalence ratios are investigated: 0.9 and 1.1. This investigation is performed at a constant equivalence ratio in the main chamber ($\phi_{MC} = 0.5$) and auxiliary fuel injection timing (SOI = 87mm).

3. The main chamber equivalence ratio at spark plug activation is swept from lean $\phi_{MC} = 0.5$ to ultra-lean $\phi_{MC} = 0.3$ conditions. The analysis focused on how the pre-chamber jets interact with different mixture conditions, and how the combustion develops in the main chamber. The equivalence ratio in the pre-chamber and the auxiliary injection timing are set at $\phi_{PC} = 1.1$ and SOI = 87mm.

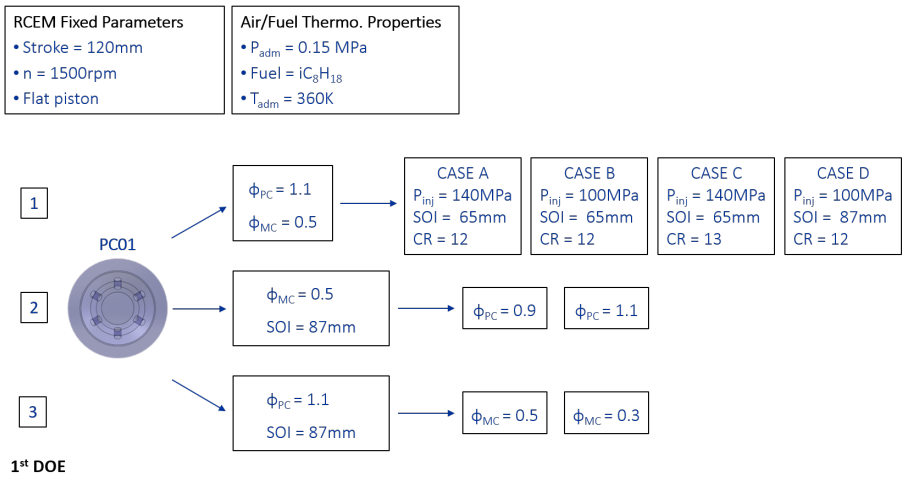

Figure 3.9: Test matrix - part 1: impact of operating conditions

The second set of experiments included in the campaign aims at evaluating how the pre-chamber geometry affects the combustion. More specifically, the orifices number (from 4 to 8), diameter (1.3-1.8 mm) and distribution effects on combustion are analysed. All the geometries are design with the same pre-chamber internal geometry (and therefore volume) and also the same total transversal area in the orifices connecting both chambers. For this investigation, all the pre-chamber geometries (PC01-05) are tested under lean ($\phi_{MC} = 0.5$) and ultra-lean ($\phi_{MC} = 0.3$) main chamber mixture conditions, with $\phi_{PC} = 1.1$ and the auxiliary injection timing at 87mm.

The following figures illustrate a summary of the full test matrix, highlighting the first (fig.3.9) and second (fig.3.10) parts of the experimental campaign.

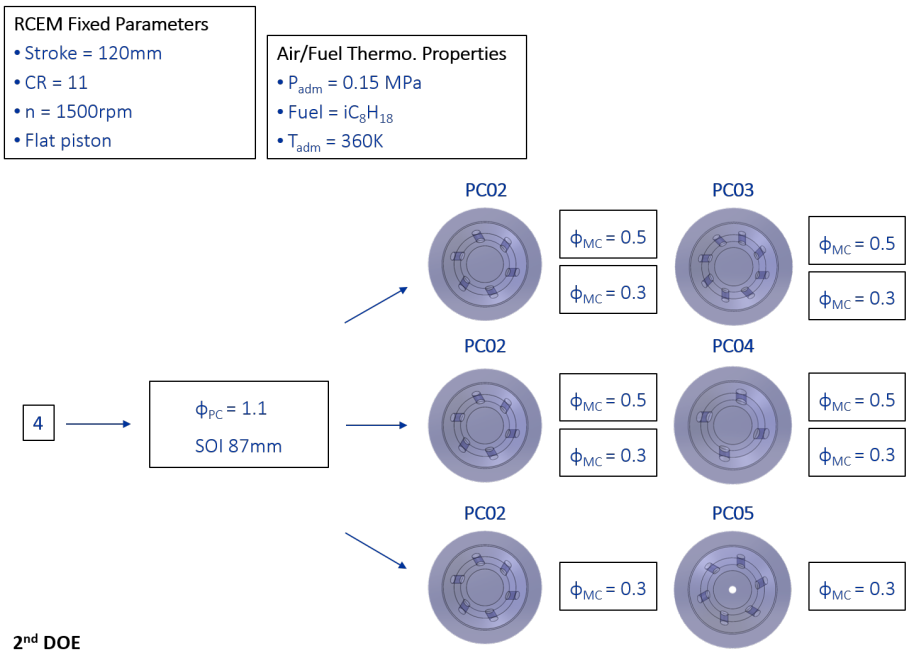

Figure 3.10: Test matrix - part 1: impact of orifice number and orientation

3.5 Test methodology

In this section the experimental test methodology will be explained.

After the modification of the combustion chamber layout according to the PCSI system scheme, the RCEM calibration is performed to fix the follow parameters:

- The allowed piston compression stroke is adjusted to 120 mm
- The combustion chamber pressure is set to 0.15 MPa
- The driving gas pressure is adjusted to achieve the required compression ratio (11:1).

Once, the warm up phase is completed, the RCEM is ready to run. The figure 3.11 shows an example of test results under fired conditions that will be useful for understanding the methodology steps. The orange line describes the piston position evolution, the blue lines show to the in-cylinder pressure (continuous for the MC, and dotted for the PC). The dashed curves in black and red colours refer respectively to the injection and the ignition system triggers. In addition, the top dead centre is highlighted in green.

1. The fuel is injected into the main chamber about one minute before the start of the test. Indeed, this relatively long time ensures the complete evaporation of the fuel, and the mixture homogeneity.
2. The system fills the driving gas volume and the combustion chamber until the desired pressure is achieved.
3. The piston starts to compress the mixture as showed by the orange and blue lines (fig.3.11). Only the fast compression is considered and analysed for research purposes (from 29mm until TDC).
4. In accordance with the test matrix, when the piston crosses a scheduled value (s = 65mm in the example), the RCEM sends a trigger (dotted vertical black line) to the injection system, performing the pre-chamber auxiliary injection.
5. The same routine is used for the ignition system activation (dotted vertical red line in the example).
6. Combustion propagates from the pre-chamber to the main chamber and the expansion phase is carried out.

7. When the test is completed a vacuum pump ensures the exhaust gas evacuation, preparing the facility for the next test.

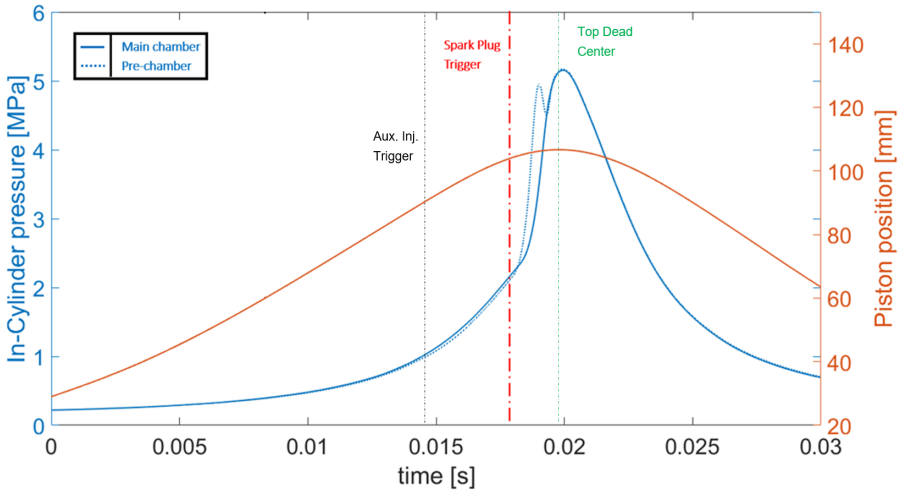

Figure 3.11: Test example under fired condition to understand the used methodology.

At the end of each test, the results in terms of main and pre-chamber pressure, piston position, injection and ignition instants are acquired and post-processed using the models described in the next chapter.

References

[1] Villela, Antonio Carlos Scardini, Egúsquiza, Julio César Cuisano, Machado, Guilherme Bastos, and Braga, Sérgio Leal. *Rapid Compression Machine Tests for Brazilian Otto Cycle Fuels*. Tech. rep. SAE Technical Paper, 2011.

[2] Desantes, José M, García-Oliver, José María, Vera-Tudela, Walter, and López-Pintor, Darío. "Study of ignition delay time and generalization of auto-ignition for PRFs in a RCEM by means of natural chemiluminescence". In: *Energy Conversion and Management* 111 (2016), pp. 217–228.

[3] Tripathi, Abhinav, Zhang, Chen, and Sun, Zongxuan. "Experimental investigation and analysis of auto-ignition combustion dynamics". In: *ASME 2018 Dynamic Systems and Control Conference*. American Society of Mechanical Engineers Digital Collection. 2018.

[4] Blomberg, Christopher Kim et al. "Extension of the phenomenological 3-Arrhenius auto-ignition model for six surrogate automotive fuels". In: *SAE International Journal of Engines* 9.3 (2016), pp. 1544–1558.

[5] Desantes, José M, López, J Javier, Molina, Santiago, and López-Pintor, Darío. "Theoretical development of a new procedure to predict ignition delays under transient thermodynamic conditions and validation using a Rapid Compression–Expansion Machine". In: *Energy Conversion and Management* 108 (2016), pp. 132–143.

[6] Schlatter, Stephanie, Schneider, Bruno, Wright, Yuri, and Boulouchos, Konstantinos. *Experimental study of ignition and combustion characteristics of a diesel pilot spray in a lean premixed methane/air charge using a rapid compression expansion machine*. Tech. rep. SAE Technical Paper, 2012.

[7] Pöschl, M and Sattelmayer, T. "Influence of temperature inhomogeneities on knocking combustion". In: *Combustion and Flame* 153.4 (2008), pp. 562–573.

[8] Payri, Raul, Salvador, FJ, Gimeno, J, and Bracho, G. "A new methodology for correcting the signal cumulative phenomenon on injection rate measurements". In: *Experimental techniques* 32.1 (2008), pp. 46–49.

[9] Bosch, W. "The fuel rate indicator: a new measuring instrument for display of the characteristics of individual injection. SAE paper 660749; 1966". In: *Google Scholar* ().

[10] Parrish, Scott E. "Evaluation of liquid and vapor penetration of sprays from a multi-hole gasoline fuel injector operating under engine-like conditions". In: *SAE International Journal of Engines* 7.2 (2014), pp. 1017–1033.

[11] Pei, Yiqiang et al. "Experimental investigation on free and impingement spray fueled with methanol, ethanol, isooctane, TRF and gasoline". In: *Fuel* 208 (2017), pp. 174–183.

[12] Payri, R, Salvador, FJ, Gimeno, J, and Zapata, LD. "Diesel nozzle geometry influence on spray liquid-phase fuel penetration in evaporative conditions". In: *Fuel* 87.7 (2008), pp. 1165–1176.

[13] Payri, Raul, Gimeno, Jaime, Bardi, Michele, and Plazas, Alejandro H. "Study liquid length penetration results obtained with a direct acting piezo electric injector". In: *Applied energy* 106 (2013), pp. 152–162.

[14] Gimeno, Jaime, Bracho, Gabriela, Martí-Aldaraví, Pedro, and Peraza, Jesús E. "Experimental study of the injection conditions influence over n-dodecane and diesel sprays with two ECN single-hole nozzles. Part I: Inert atmosphere". In: *Energy Conversion and Management* 126 (2016), pp. 1146–1156.

[15] Aleiferis, PG, Hardalupas, Y, Taylor, AMKP, Ishii, K, and Urata, Y. "Flame chemiluminescence studies of cyclic combustion variations and air-to-fuel ratio of the reacting mixture in a lean-burn stratified-charge spark-ignition engine". In: *Combustion and Flame* 136.1-2 (2004), pp. 72–90.

[16] Toulson, Elisa et al. "Visualization of propane and natural gas spark ignition and turbulent jet ignition combustion". In: *SAE International Journal of Engines* 5.4 (2012), pp. 1821–1835.

[17] Gholamisheeri, Masumeh, Thelen, Bryce, Gentz, Gerald, and Toulson, Elisa. "CFD modeling of an auxiliary fueled turbulent jet ignition system in a Rapid Compression Machine". In: *SAE Technical Paper* (2016).

[18] Swinehart, DF. "The beer-lambert law". In: *Journal of chemical education* 39.7 (1962), p. 333.

[19] Manin, Julien, Bardi, Michele, and Pickett, Lyle M. "Evaluation of the liquid length via diffused back-illumination imaging in vaporizing diesel sprays". In: *The Proceedings of the International symposium on diagnostics and modeling of combustion in internal combustion engines*. Vol. 8. Fukuoka, 2012, pp. 665–673. DOI: 10.1299/jmsesdm.2012.8.665.

[20] Payri, Raul, Gimeno, Jaime, Bracho, Gabriela, and Vaquerizo, Daniel. "Study of liquid and vapor phase behavior on Diesel sprays for heavy duty engine nozzles". In: *Applied Thermal Engineering* 107 (2016), pp. 365–378. DOI: 10.1016/j.applthermaleng.2016.06.159.

Chapter 4

Zero-dimensional turbulence model

4.1 Introduction

The current section describes the numerical models and methodologies used to evaluate the turbulence evolution inside the pre-chamber in motoring conditions. First, the three-dimensional CFD model used for the characterization of the turbulence inside the pre-chamber is described. In particular, the author summarizes the geometry, boundary conditions and numerical methods selected for this purpose. The results of this 3D simulation are the target to adjust a zero-dimensional K-k-ϵ turbulence model for the pre-chamber's geometries, which is described next. The model includes a compressible nozzle equation to calculate the mass transfer and velocity through the orifices communicating the pre-chamber and the main chamber, based on the instantaneous pressure evolution. The kinetic energy associated to this mass transfer is the most relevant source for the turbulent kinetic energy generation inside the pre-chamber. Then, a sensitivity analysis of the main parameters of the 0D turbulence model, and the final validation against the full 3D-CFD results are performed to complete the baseline PC01 and PC02 coefficients adjusting.

During the second phase the analysis is extended to PC03 and PC04 cases, exploring the model performance by means of the baseline coefficients. To fully understand the results, a deeper investigation of the 3D simulation outputs is carried out. The analysis takes into consideration the turbulent kinetic energy

and velocity local distributions for several pre-chamber cross-sections. Finally the model coefficients, readjusted on the basis of the assumptions made, are shown in the summary table including all the geometries utilized.

4.2 3D-CFD in motoring conditions

The mass flow exchange and turbulence generation inside the pre-chamber during the compression stroke are first determined by means of a 3D-CFD simulation in Converge [1]. In order to do so, a detailed model of the geometry used for the experiments (further described in 3.2), starting from the piston position at the start of the experiment (at $120mm$ distance from the cylinder head) is generated. The details of this model can be seen in Fig.4.1.

Once the simulation starts, the temporal evolution of the piston position acquired from a motoring test at a 11:1 compression ratio, an initial pressure at $0.15MPa$ and an initial temperature of $360K$ are imposed. The main chamber is initialized with an equivalence ratio $\phi = 0.5$ mixture of air and fuel (iso-octane), representative of an early injection before the rapid compression starts. Instead, the pre-chamber is assumed to be filled initially with air.

The turbulence is modelled by means of a Unsteady Reynolds-Averaged Navier-Stokes (U-RANS) strategy, in particular using the so called Rapid Distortion Re-Normalization Group (RNG) $k - \epsilon$ model[2], with a first-order upwind numerical scheme. Since the experiments start with the piston stopped at its minimum position, where there is no flow through the orifices of the pre-chamber, the turbulent kinetic energy (k) and turbulent dissipation (ϵ) are initialized at small values of $1m^2/s^2$ and $100m^2/s^3$, respectively, to take into account the residual flow from the filling process of the cylinder before the experiment starts. Other physical parameters (pressure, temperature, velocity, etc.) are solved with a MUSCL [3, 4] second order scheme and using the Pressure Implicit with Splitting of Operators (PISO) method for convergence[5].

One of the most important aspects in the modelling of the pre-chamber flow is related to the mesh characteristics. In particular, the mesh structure and size in the orifices connecting both volumes (main chamber and pre-chamber) are critical, since the velocity in these orifices is going to be the main driver for the turbulence generation inside the pre-chamber. Additionally, it is necessary to properly capture the turbulence dissipation both inside the core flow and around the pre-chamber walls.

In the current simulations, three different conditions for the mesh are imposed (after performing a mesh sensitivity analysis):

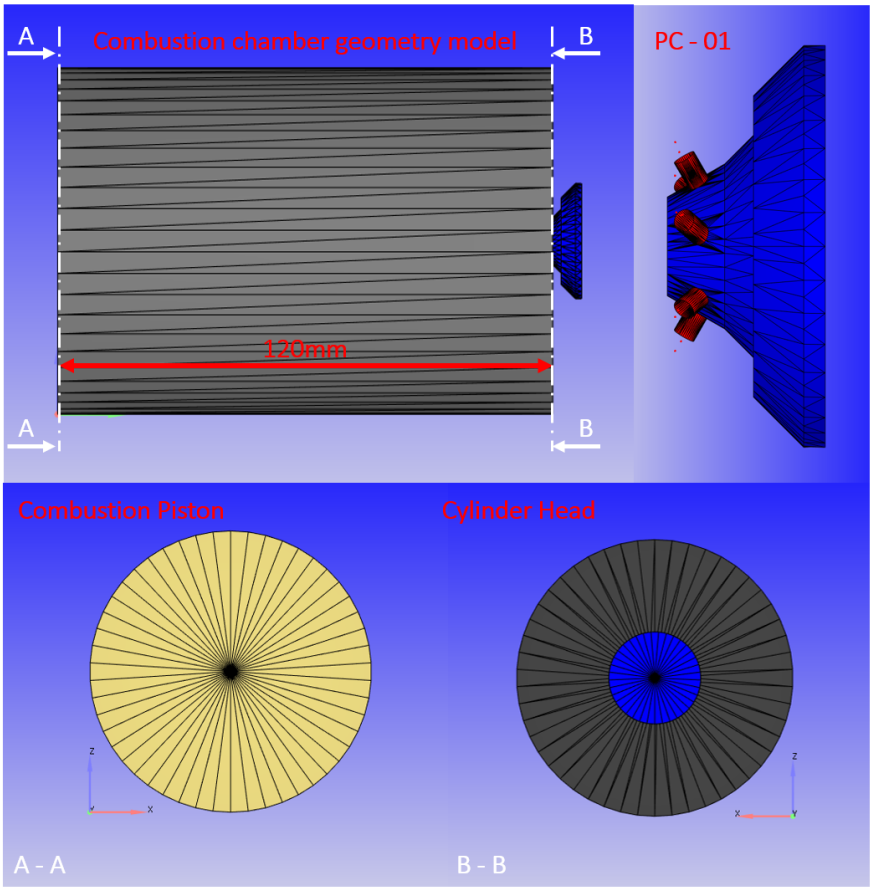

Figure 4.1: Top: CFD geometry of RCEM and pre-chamber details. Bottom: Side views of Cylinder head (B-B) and combustion piston (A-A)

- The parameter "base grid" represents the initial size of the mesh inside the main chamber. Based on previous experiences in the literature [6, 7], a value of $4mm$ is selected.
- From the base size, a mesh refinement is performed in the walls and volumes corresponding the orifices and the pre-chamber using the embedding tool, in order to ensure that the mesh in these critical parts of the geometry is fine enough to capture the main flow features. In particular, a five level refinement is applied to the orifices (Fig.4.2 C-D) and the pre-chamber volume (Fig.4.2 B-E), reaching a minimum value

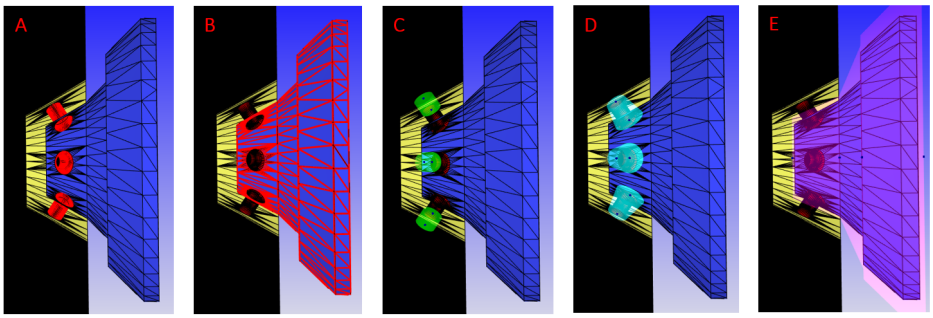

Figure 4.2: Embedding set-up: A) Orifices walls embedding (6 levels). B) Pre-chamber walls embedding (5 levels).C) Orifices inlet embedding (5 levels). D)Orifices volume embedding (5 levels). E) Pre-chamber volume embedding (5 levels).

of $0.125mm$. In the walls of the orifices, the refinement was done with one step more, leading to a mesh size of $0.0625mm$ (Fig.4.2 A).

- Finally, an Adaptive Mesh Refinement (AMR) methodology is imposed, where the mesh is refined as soon as a gradient equal or higher than 0.1 m/s between adjacent cells is reached. During this refinement, the minimum cell size is again $0.0625mm$.

In order to find these values, a mesh sensitivity analysis was preliminary performed. This information is presented in terms of the evolution of the mass (Fig.4.3) and the average turbulent kinetic energy (Fig.4.4) inside the pre-chamber, at spark time activation, as a function of the total cell count.

These two parameters are mainly a consequence of the velocity through the orifices, which is affected by the quality of the mesh inside them and their vicinity. For this reason, the number of cells is changed by inducing variations in the embedding and AMR parameters, while the base cell size inside the main chamber is kept constant. As it can be seen, the pre-chamber mass is almost insensitive to the number of cells except for the coarser configuration. Instead, the turbulent kinetic energy always increases as finer mesh is used. However, it has to be considered that the variation between the final two meshes is small, while further refinement of the mesh would imply a significant increase in computational cost. For this reason, the decision was to proceed with the last of the configurations presented, leading to a total cell count of approximately

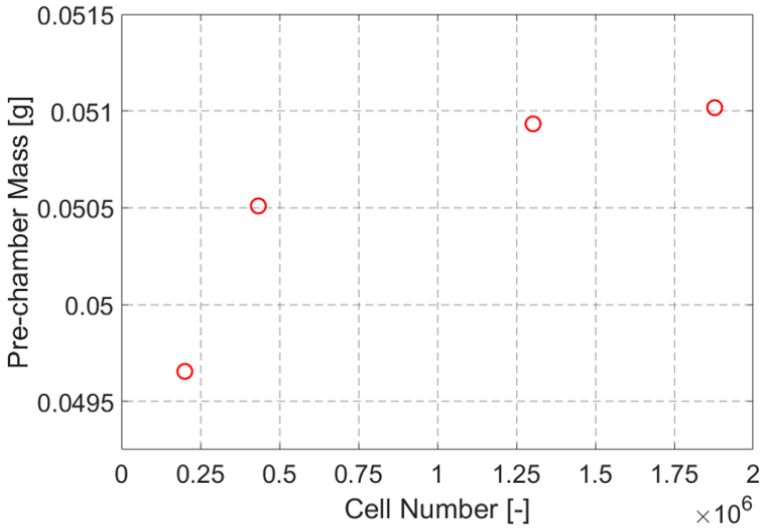

Figure 4.3: Results of mesh sensitivity analysis in terms of pre-chamber mass evolution at spark time.

1.85 million cells at the spark timing. The structure of the resultant mesh around the orifices based on this strategy can be seen in Figure 4.5

Finally, the results of the simulations are validated against the experimental operation of the RCEM for the baseline case PC01 (Figure 4.6). In this chart, the evolution of the pressure in the main chamber is depicted in blue colour, while the pressure in the pre-chamber is shown in orange. Additionally, the experimental trace is presented in continuous lines, while dash lines are used for the modelled results.

As it can be seen, there is almost a perfect match of the evolution both at the start of the rapid compression as well as in the vicinity of Top Dead Center (which is the most relevant region, since it is when the combustion in the pre-chamber takes place).

However, between instants t1 = 0.012s and t2 = 0.016s there is a slight underestimation of the pressure evolution. It has to be noted that this region corresponds to the maximum piston velocity operation. Therefore, on the one side the uncertainty in the piston position acquisition by means of the magnetic ruler is higher, and on the other hand the piston is more subjected to mechanical deformations induced by inertial terms [8, 9], which can affect slightly the real volume of the main chamber and, consequently, the pressure

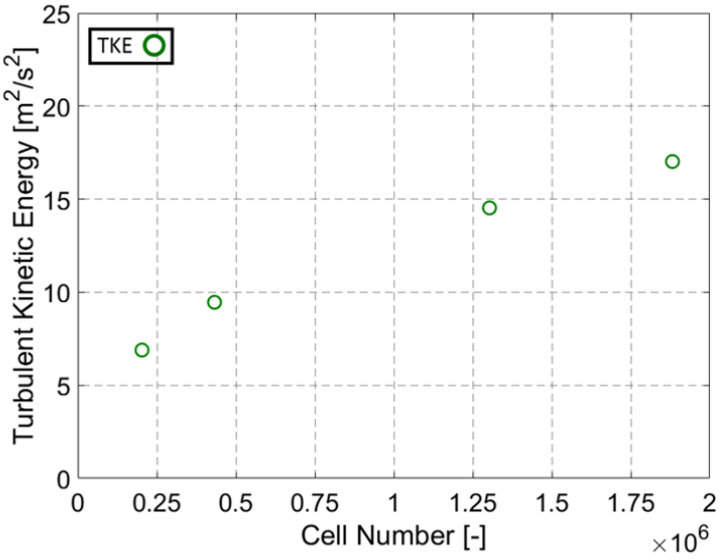

Figure 4.4: Results of mesh sensitivity analysis in terms of pre-chamber turbulent kinetic energy evolution during the compression stroke

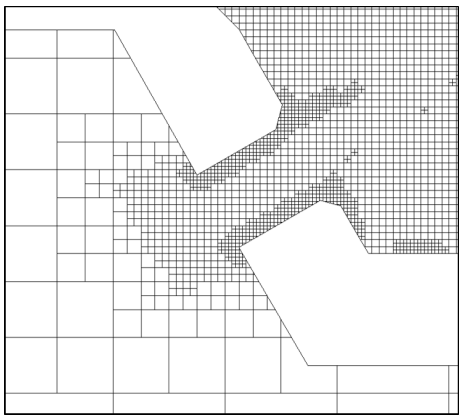

Figure 4.5: Structure of the final mesh around the orifice section close to top dead center

evolution. These deformations are reduced as the piston decelerates, which may be the reason why the pressure is better captured when approaching TDC. However, the pressure ratio between the main chamber and the pre-chamber,

which is the physical parameter driving the velocity through the orifices, is almost equal to the experimental value along the complete simulation.

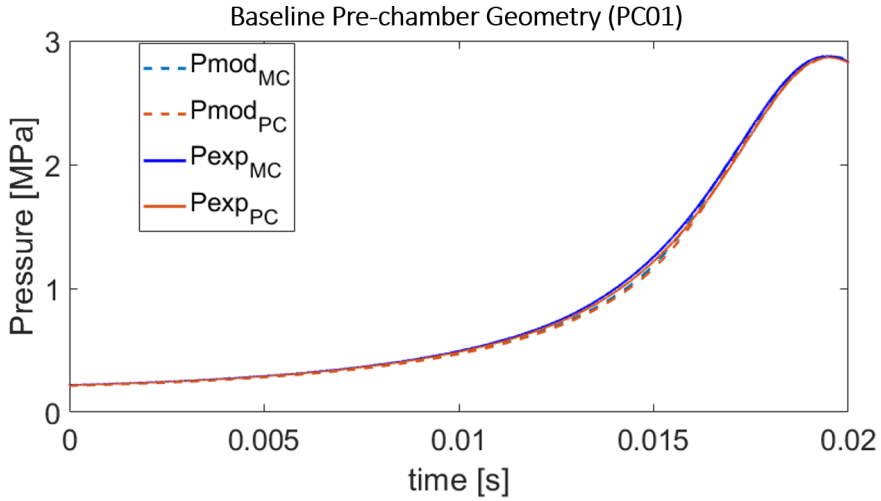

Figure 4.6: Validation of the CFD simulations in terms of pressure evolution in main-chamber (blue) and pre-chamber (orange) for PC01 case.

Once the baseline 3D model is validated against the experimental data, the same methodology is applied to the remaining 3 cases. In order to obtain a unique compression ratio, regardless the geometry used, the RCEM driving pressure is adjusted to obtain the same pressure evolution for all the cases. It is therefore trivial to extend the validation of the model to all the geometries used.

4.3 0D turbulence model

In order to perform a detailed analysis of the combustion development in the pre-chamber, it is necessary to evaluate separately the effects from the pre-chamber composition and thermodynamic conditions (mostly temperature and pressure), included in the laminar flame speed, as well as the interaction of the flame development with the turbulent flow. For this purpose, a 0-D turbulence model is proposed and evaluated.

The following hypothesis are considered for the formulation of this model:

- The entire combustion chamber is composed by two open systems (PC/MC) that interchange mass between them.
- Mixture homogeneity in both chambers. This means that at each time step there is a unique composition for each chamber.
- Ideal gas behaviour is supposed.
- The gas properties in each chamber are a function of respective temperature and gas composition, which is computed assuming a simple one-step single-reaction methodology. The heat capacity at constant pressure and the specific heat ratio tables are described in [10, 11].

The turbulence model validated in the current thesis is adapted from the $K-k-\epsilon$ one proposed by Fogla et al. [12] for the calculation of the turbulence induced by tumble motion in spark-ignition engines, and modified by Bardis et al. [13] for pre-chamber systems.

In this model, the following equations are considered:

$$\frac{\partial(m_{pc}K)}{\partial t} = P_{uK} - P_{kl} \tag{4.1}$$

$$\frac{\partial(m_{pc}k)}{\partial t} = P_{uk} + P_{kl} + P_{sw} - m_{pc}\epsilon - F_{wk} \tag{4.2}$$

$$\frac{\partial(m_{pc}\epsilon)}{\partial t} = P_{u\epsilon} + P_{\epsilon} + P_{sw}\frac{\sqrt{k}}{L_{pc}} - \frac{1.921 \cdot m_{pc}\epsilon^2}{k} - F_{w\epsilon} \tag{4.3}$$

Where K is the kinetic energy inside the pre-chamber, k the turbulent kinetic energy, ϵ the turbulence dissipation, m_{pc} is the mass in the pre-chamber, t is the time, the term P_{uX} is the production source term on each equation related to the flow entering through the orifices (being X the turbulent kinetic energy or dissipation, depending on the equation considered), P_{kl} corresponds to the conversion of mean kinetic energy into turbulent kinetic energy, P_{sw} is a production term on each equation induced by a swirl flow inside the pre-chamber, F_{wX} a dissipation term by viscous friction close to the walls, L_{pc} the Taylor's macroscale and P_ϵ represents the source of dissipation from the main pre-chamber flow.

However, compared to the work by Bardis et al. [13] the following simplifications have been made:

- Regarding the baseline nozzle geometry (PC01), since the orifices point to the centre of the pre-chamber, it is assumed that the structure of the flow does not induce any swirl-like vortices, so the term P_{sw} is neglected. This can be confirmed looking at the velocity vectors in the PC horizontal plane (C-C), obtained from the 3D-CFD simulations in Figure 4.7.

  The velocity field for baseline case (PC01) shows strong intensity in the central part, promoting chaotic and non-homogeneous flow structures from the centre to the edge. On the contrary, for the other PC geometries, the offset between the orifices generates an homogeneous macro-vortex in the horizontal plane of the pre-chamber (Fig. 4.7, right side). The turbulent energy produced and dissipated by the horizontal vortex is modelled by activating the P_{sw} term.

- Based on a previous sensitivity analysis, and considering the low rugosity of the internal walls of the pre-chamber available, the turbulence dissipation term in the walls F_{wX} is considered small compared to the standard dissipation. Therefore, only one dissipation term (corresponding to ϵ) is included.

- Taking into account the flow structure previously described, characterized by a vertical vortex for the PC01 (Fig. 4.8), the Taylor's macroscale L_{pc} is considered to be proportional to the pre-chamber height, while for the remaining geometries should be considered proportional to the PC average diameter. Considering that the height and the average diameter of the pre-chamber (for all the geometries) are almost identical (around $1mm$ of difference), the macroscale is modelled in a single way: h_{pc} ($L_{pc} = C_{len} \cdot h_{pc}$)

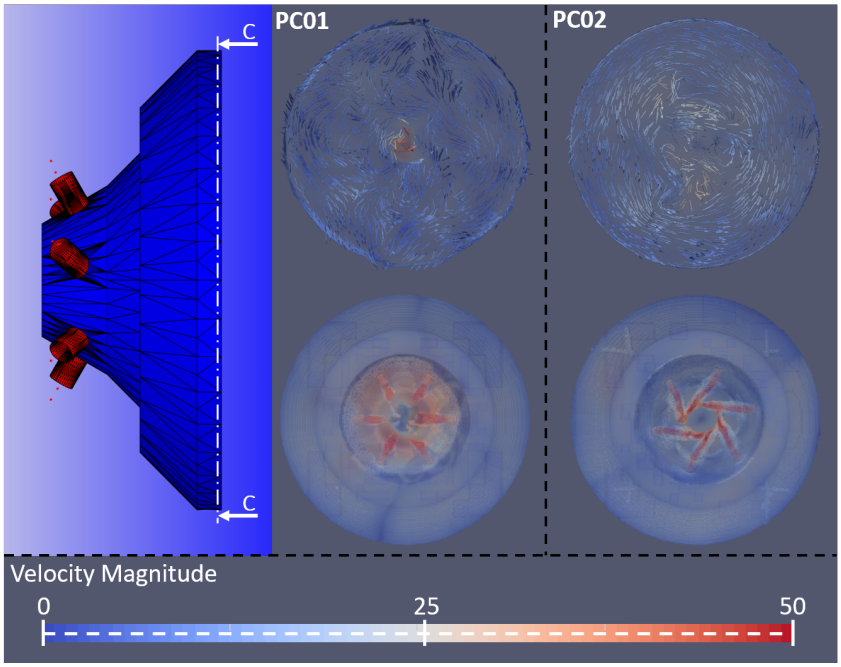

Figure 4.7: Velocity vectors field over the pre-chamber horizontal section. Left Side: Pre-chamber section. Central part: PC01. Right side: PC02.

The terms corresponding to the contribution of the flow through the orifices on each equation (P_{uK}, P_{uk} and $P_{u\epsilon}$) are described below:

$$P_{uK} = (1 - a_{in})(1 - C_T) \cdot \frac{1}{2} \sum_{n_{ori}} \dot{m}_{ori} u_{ori}^2 \tag{4.4}$$

$$P_{uk} = a_{in}(1 - C_T) \cdot \frac{1}{2} \sum_{n_{ori}} \dot{m}_{ori} u_{ori}^2 \tag{4.5}$$

$$P_{u\epsilon} = a_{in}(1 - C_T) C_\epsilon \cdot \frac{1}{2} \sum_{n_{ori}} \frac{u_{ori}}{D_{ori}} \dot{m}_{ori} u_{ori}^2 \tag{4.6}$$

In these equations, the term a_{in}, C_ϵ represent the fraction of the kinetic energy of the incoming flow that contributes directly to turbulence generation

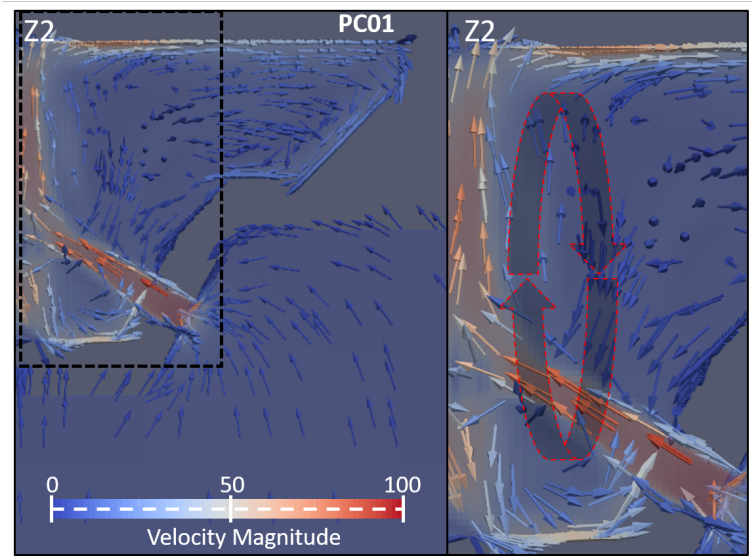

Figure 4.8: Velocity vectors over the pre-chamber vertical section at spark time instant for PC01 case.

and dissipation, respectively, C_T is a geometric coefficient related to the inclination of the orifices with respect to the pre-chamber axis, n_{ori} represents the number of orifices, D_{ori} the diameter of these orifices, while $\dot{m}_{ori}$ and u_{ori} are the mass flow and velocity in the orifices, calculated from the pressure ratio across the orifices through a compressible nozzle equation under subcritical conditions:

$$\dot{m}_{ori} = C_d A_{ori} \left(\frac{p_{out}}{p_{in}}\right)^{\left(\frac{1}{\gamma}\right)} \sqrt{\rho_{in} p_{in} \frac{2\gamma}{\gamma - 1} \left[1 - \left(\frac{p_{out}}{p_{in}}\right)^{\frac{\gamma-1}{\gamma}}\right]} \tag{4.7}$$

Where the subindices *in* and *out* represent the conditions in the chambers from which the flow comes and where the flow arrives, respectively, γ is the adiabatic coefficient, A_{ori} the transversal section of each orifices (independent on the flow direction since the orifice is cylindrical) and C_d is the orifice discharge coefficient. This parameter has been calibrated by adjusting the experimental pre-chamber mass evolution (calculated through the 0D model) against the 3D-CFD results during the compression and expansion stroke.

When the pre-chamber is filling (i.e. the pressure is higher in the cylinder) the discharge coefficient is defined as:

$$C_{d,fil} = 0.655 - \frac{0.095}{\sqrt{Re}} \tag{4.8}$$

while when the discharge from the pre-chamber to the cylinder takes place, the discharge coefficient is calculated as:

$$C_{d,dis} = 0.7 - \frac{0.127}{\sqrt{Re}} \tag{4.9}$$

Figure 4.9 shows a perfect alignment between the two curves, confirming the high accuracy of the calculated tuning constants.

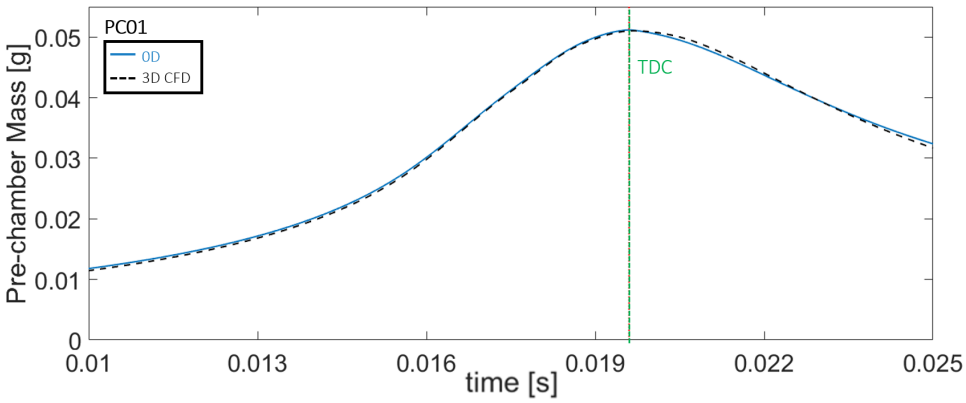

Figure 4.9: Validation of 0D model against 3D-CFD results in terms of pre-chamber mass evolution for Baseline PC01 case.

It has to be considered that, although the mass transfer through Equation 4.3 is calculated for the complete experiment, the corresponding production terms P_{uK}, P_{uk},and $P_{u\epsilon}$ are only active when the flow is incoming into the pre-chamber. Instead, when the discharge is initiated, the pre-chamber will lose kinetic energy and turbulence as a consequence of the mass drop.

Finally, the equations for the calculation of the terms P_{kl}, P_ϵ, and P_{sw} are described below:

$$P_{kl} = C_\beta \nu_T \frac{2 m_{pc} K}{L_{pc}^2} - \frac{2}{3} m_{pc} k \left(\frac{\dot{\rho}_{pc}}{\rho_{pc}} \right) - \frac{2}{3} m_{pc} \nu_T \left(\frac{\dot{\rho}_{pc}}{\rho_{pc}} \right)^2 \tag{4.10}$$

$$P_\epsilon = \frac{\epsilon}{k} \left[5.76 C_\beta \nu_T \frac{m_{pc} K}{L_{pc}^2} - 2 m_{pc} k \left(\frac{\dot{\rho}_{pc}}{\rho_{pc}} \right) - \frac{2.64}{3} m_{pc} \nu_T \left(\frac{\dot{\rho}_{pc}}{\rho_{pc}} \right)^2 \right] \tag{4.11}$$

where C_β is a constant representing the fraction of kinetic energy inside the pre-chamber that is transformed into turbulence, ν_T is the turbulent viscosity, estimated as $0.09 \frac{k^2}{\epsilon}$ consistently to the methodology used in the 3D-CFD simulations, ρ_{pc} is the average density in the pre-chamber and $\dot{\rho}_{pc}$ is the temporal derivative of this average density.

$$P_{sw} = C_{sw} \cdot L_{sw} \cdot \frac{\omega}{2} \cdot \left[\frac{\sqrt{k}}{r_{PC}} \right] \tag{4.12}$$

in which r_{PC} is the PC average radius, ω is the angular velocity of the vortex, and L_{sw} represents the angular momentum conservation corresponding to follow equation [14]:

$$\frac{dL_{sw}}{dt} = L - D \tag{4.13}$$

$$L = C_T \cdot \sum_{n_{ori}} \dot{m}_{ori} u_{ori} \cdot r_{PC} \tag{4.14}$$

$$D = L \cdot \left[\frac{\sqrt{k}}{r_{PC}} \right] \tag{4.15}$$

where the first term corresponds to the angular momentum production (L) and the second one is the vortex destruction (D) due to the turbulence effects.

Finally, it has to be acknowledged that the model described up to the current point includes only the turbulence generation by the flow velocity coming from the pre-chamber orifices. However, there is another potential source of turbulence generation when the pre-chamber operates in a so called active or stratified operation, which is the direct fuel injection inside the pre-chamber. In order to take into account this effect, a new term could be included into the K-k-ϵ equations with a similar structure as the one already seen for the flow from the main chamber:

$$P_{injK} = (1 - C_{inj}) \cdot \frac{1}{2} \dot{m}_{inj} u_{inj}^2 \tag{4.16}$$

$$P_{injk} = C_{inj} \cdot \frac{1}{2} \dot{m}_{inj} u_{inj}^2 \tag{4.17}$$

$$P_{inj\epsilon} = C_{inj} C_{\epsilon,inj} \cdot \frac{1}{2} \frac{u_{inj}}{D_{inj}} \dot{m}_{inj} u_{inj}^2 \tag{4.18}$$

where C_{inj} is the proportion of the fuel injection kinetic energy that contributes to turbulence generation, $\dot{m}_{inj}$ is the instantaneous injection rate (previously characterized in an injection rate meter, according to the methodology described in [15]), u_{inj} is the fuel injection velocity estimated from the aforementioned injection rate and the geometric outlet section of the injector nozzle, which is characterized by the diameter D_{inj} . Such description implies the need to calibrate an additional constant. In order to understand the sensitivity of the results to this parameters, a sweep between values of 0 (no contribution of the fuel injection to the turbulence field) and 1 (maximum contribution) has been performed. The results show an increase of the turbulence intensity during the fuel injection. However, the time between this injection and the spark activation is long enough to dissipate this turbulence, so the turbulence characteristics during the expected window of evolution of the pre-chamber combustion is almost identical. Nevertheless, further analysis by means of 3D-CFD simulations are needed to confirm aforementioned results. Therefore, in the proposed the fuel injection has been accounted for the calculation of the pre-chamber mass and equivalence ratio, but neglected into the turbulence evolution.

Figure 4.10 summarizes schematically the proposed model. As can be observed, the turbulence generation terms are represented by the incoming flow,

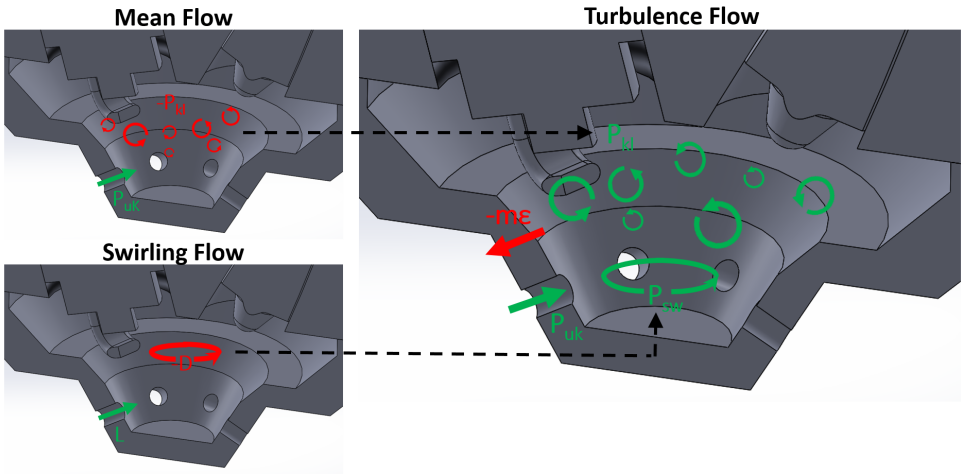

Figure 4.10: Turbulence model scheme

and by the mean and swirling flow dissipation. The terms representing the generation appear in green, while the contribution to the dissipation appears in red.

4.4 Model constants adjustment and sensitivity analysis

Considering the final equations seen in the previous section, the turbulence model includes four or five constants to be adjusted depending on the particular pre-chamber layout used:

- a_{in}, representing the amount of the mean kinetic energy of the inlet flow that is contributing to turbulence in the pre-chamber.
- C_β, which accounts for the conversion of mean kinetic energy inside the pre-chamber to turbulence.
- C_ϵ, accounting for the turbulence dissipation as a consequence of the incoming flow into the pre-chamber.
- C_{len}, used to estimate Taylor's macroscale from the pre-chamber height.

- C_{sw}, which accounts for the turbulence production rate by the swirling flow

To calibrate the aforementioned coefficients for all the pre-chamber geometries, 3D mass average evolution of the turbulent kinetic energy is used as target for 0D model results. The methodology used is described in the following sections

4.4.1 Baseline case: pre-chamber PC01

In order to adjust these constants, a surface response model and optimization process has been performed in the statistical software Statgraphics Centurion XVII [16]. For this purpose, and taking into account the relatively low computational effort required to run the 0D model, a full factorial design with five levels per variable has been selected (resulting in a total of 625 combinations) for the baseline pre-chamber geometry (so excluding the swirling flow coefficient). The levels have been selected based on the experience from the literature [13] and a preliminary study. The merit function from the optimization used to evaluate the capability of the model was the sum of the squared errors, calculated from the deviation between the 0D and 3D models in terms of the temporal evolution of the average turbulent kinetic energy in the pre-chamber.

As a first step, an Analysis of Variance (ANOVA) technique was used to identify the sensitivity of the model to the different constants. Then, the surface response model was created using quadratic functions and used to look for the coefficients that could minimize the error.

Constant	**Range**	**p-value**	**Optimized**
a_{in}	[0.1 0.7]	0.0002	0.3
C_{β}	[0.1 0.7]	0.047	0.2
C_{ϵ}	[0.01 0.1]	0.0000	0.03
C_{len}	[0.2 0.7]	0.049	0.57
$R^2 adjusted$		87.51%	

Table 4.1: Analysis of Variance and optimization.

All this information is summarized in Table 4.1. In this table, the third column (p-value) is related the significance of each model constant into the merit function, with a value of 0.05 indicating that this constants impacts

the result with a 95% confidence. As it can be seen, the most significant parameters are a_{in} and C_ϵ, since the p-value obtained is close to zero. Instead, the impact of C_β and C_{len} is much lower, although still significant considering the threshold of 95% confidence selected.

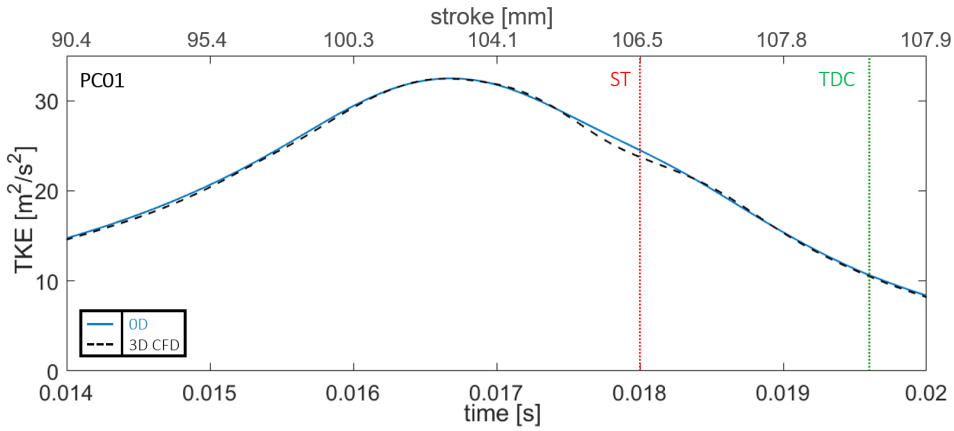

Figure 4.11: Validation of 0D model against 3D-CFD results in terms of turbulent kinetic energy inside the pre-chamber during compression for Baseline PC01 case.

It has to be noted that the value of C_{len} is close to 0.5, which means that Taylor's macroscale is close to half the pre-chamber height, which is consistent with the flow structure previously seen. Additionally, the adjusted R-squared value of 87.51% indicates that the response surface model used for the optimization is capable to reproduce the error trends with a reasonable accuracy.

The result of the 0D model with the optimized constants are evaluated against the 3D-CFD results in Figure 4.11 up to TDC (vertical dotted green line). In this chart, the continuous line represents the 0D model and the dashed line the 3D-CFD reference. The double X axis indicates the evolution of the TKE as function of the test time and piston position. An almost perfect match can be observed during the complete compression stroke for the PC01 case, which was the baseline used to determine the coefficients for the model (except C_{sw}).

Figure 4.12 shows the sensitivity to all the model constants around this optimal solution. For this purpose, a variation of ±25% over the final value

of each coefficient is performed. As it is expected from the previous ANOVA analysis, the results are very sensitive to the variations in a_{in} and C_ϵ, while secondary effect is observed when changing the other two.

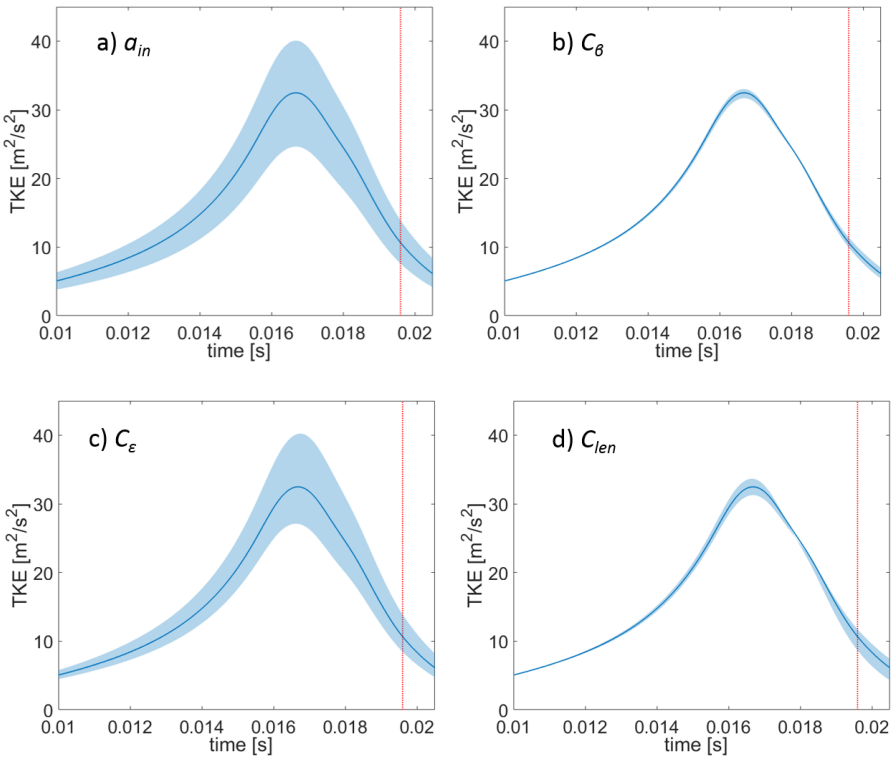

Figure 4.12: Sensitivity analysis of each model constant around the optimal solution.

4.4.2 PC02 case: swirling flow constant adjustment

Once the model was calibrated for the baseline case, the swirling flow coefficient is tuned to achieve the best match between 0D and CFD results for the PC02 case. The fifth coefficient, added to the baseline model (table4.1), that minimizes the root mean square error is equal to $C_{sw} = 0.0017$.

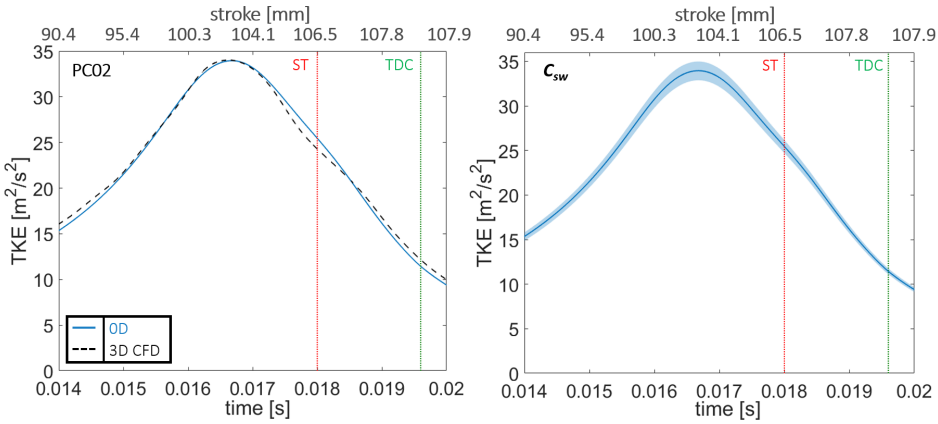

Figure 4.13: Left: Validation of 0D model against 3D-CFD results in terms of turbulent kinetic energy inside the pre-chamber during compression for PC02 case. Right: Sensitivity analysis of C_{sw} around the optimal solution.

Figure 4.13 (left side) presents the result of the turbulence model optimization for the PC02 case, and the sensitivity analysis around ±25% the swirling-flow coefficient optimal value (right side). Despite a slight deviation in some areas, the model is able to replicate the 3D global trend with high precision, which confirms the suitability of the methodology used.

Comparing the curves from both pre-chambers (with and without the swirl effect) it can be noted that the average TKE inside the pre-chamber does not suffer radical modifications. However, by analysing the velocity field vectors, significant differences at local level in terms of intensity and direction have been observed (Fig. 4.7). These differences can have a relevant effect on combustion development, although very similar TKE trends. These local effects will be considered afterwards when analysing the experimental results under firing conditions.

4.4.3 PC03 and PC04 cases: orifices shape and number effects

As next step, the five calibrated coefficients are utilized to explore the model flexibility on PC03 and PC04 cases. Following the previously described procedure, the 3D-CFD guideline and 0D results comparison is depicted in figure 4.21.

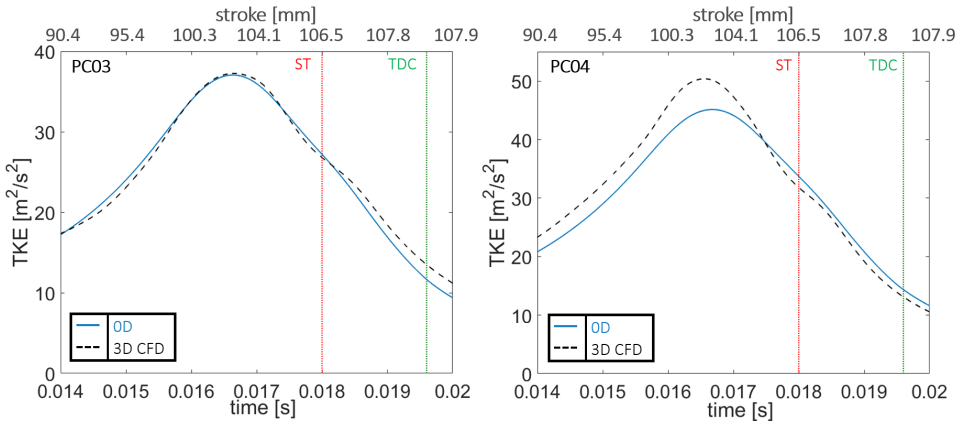

Figure 4.14: Validation of 0D model against 3D-CFD results in terms of turbulent kinetic energy inside the pre-chamber during compression for PC03 case (left) and PC04 case (right).

The model is able to capture the CFD trend with high precision for case PC03, especially until the spark time. Then, the two curves slightly diverge during the final phase of compression. On the contrary, the 0D model fails to reproduce the phenomenon in the case of the fourth pre-chamber (PC04), underestimating around 10% the TKE peak.

To shed light on these results, a deeper investigation on how the nozzle geometry affects the fluid-dynamic field inside the pre-chamber was required. Hence, 3D simulation outputs at TKE peak instant have been processed, aim to understand the local velocity and turbulence profiles.

For the purpose, several relevant cross-sections were selected (Figure 4.15): a horizontal plane corresponding to half pre-chamber height, a horizontal plane through the spark plug electrodes, and finally a vertical section in the centre of the geometry.

Independently from the setup (Figure 4.16, 4.17), observing the colour distribution, a central area with high speed and high turbulent kinetic energy

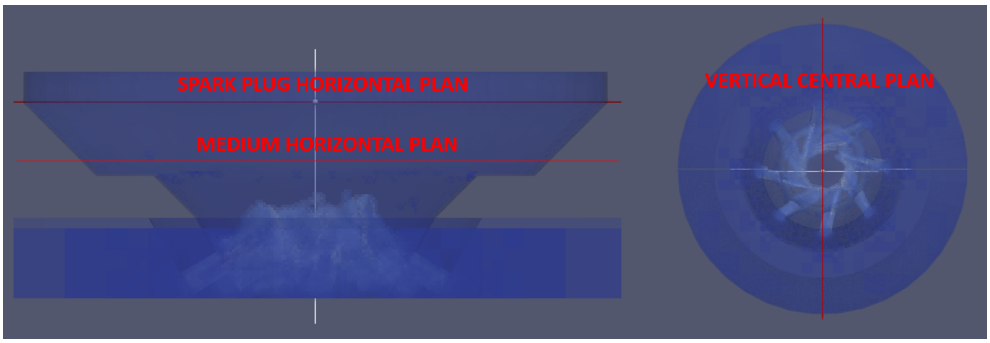

Figure 4.15: 3D scheme of the pre-chamber geometry: spark plug and medium pre-chamber horizontal plans onthe left. Vertical central plan on the right.

production can be identified. As expected, from the centre towards the edge the TKE is decreasing due to dissipation effects and the increasing distance from the main source of production (the flow through the orifices) .

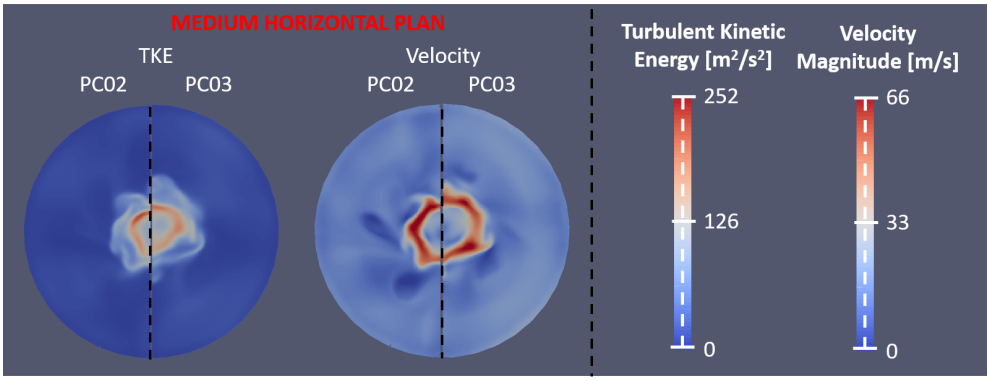

Figure 4.16: TKE and Velocity profiles on the medium horizontal plan for PC02 and PC03 cases.

Focusing on the central area, a similar flow field is shown between PC02 and PC03 cases, while a more powerful and extended red central zone is developed in PC04 case.

Indeed, the differences are more clear by plotting the 1D turbulent kinetic energy profile along pre-chamber radius (yellow dotted line). Figure 4.18 presents the TKE local trends from the centre of the section ($0mm$) until the

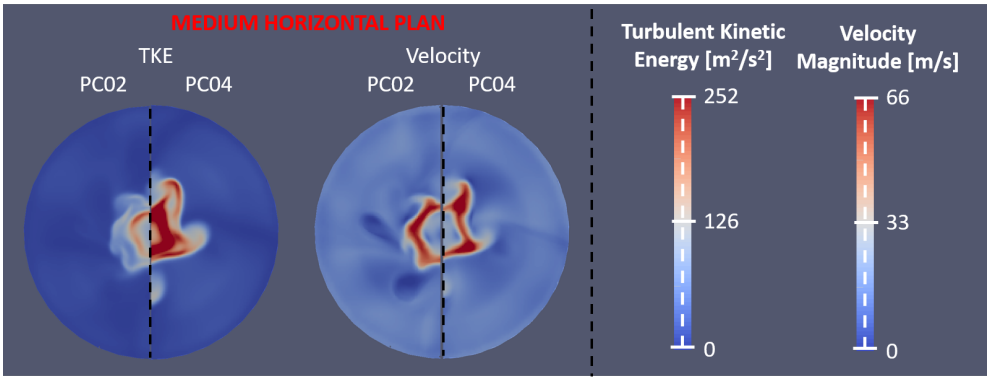

Figure 4.17: TKE and Velocity profiles on the medium horizontal plan for PC02 and PC04 cases at spark activation instant.

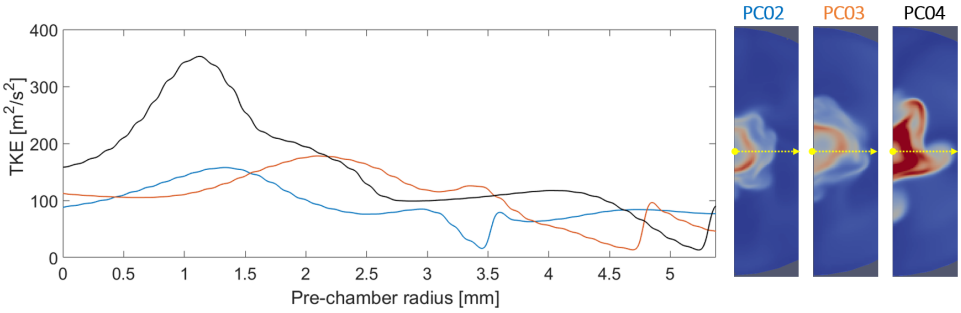

Figure 4.18: 1D evolution of TKE for PC02-03-04 cases along the pre-chamber radius (yellow line).

border of the high turbulent zone ($5.5mm$) for the three cases. Considering that the orifices cross-section is fixed between the different layouts, in other words the total mean kinetic energy at the PC inlet does not change, the 1D profiles confirm the higher conversion into turbulent energy for the PC04 case. In order to extend these considerations to the whole geometry, also the horizontal spark plug and the central vertical plans are checked.

Definitively, the figure confirms the general similarities and differences discussed for the medium horizontal plane. Nevertheless, the yellow dotted squares, highlight turbulence inhomogeneity towards the edge of the geometry. Therefore, despite a higher turbulent intensity should enhance the combustion

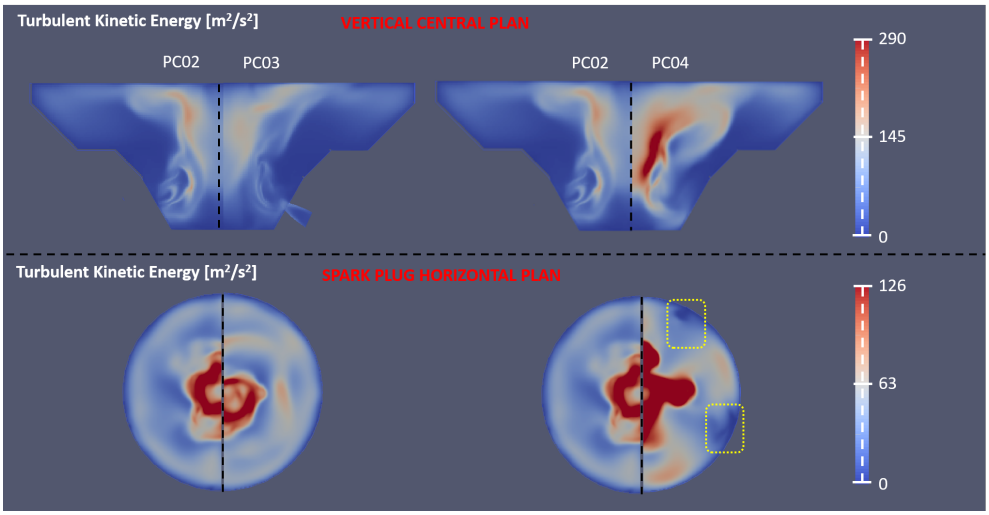

Figure 4.19: TKE distribution on spark plug horizontal plan and vertical central plan for PC02-03-04 geometries at spak ignition instant.

propagation during firing tests, this hypothesis has to face the stratification promoted by the orifices number reduction.

Finally, to better understand the orifice-to-orifice flow interaction, a 3D pre-chamber geometries overview is generated by means of the opacity Paraview filter (Figure 4.20). By decreasing the number of orifices from 8 to 4 the angle of impact between the jets, defined as the angle formed between the symmetry axis of two adjacent orifices (θ_{jet}), is modified from 45° to 90°. Increasing this parameter promotes the direct interaction between two adjacent jets, thus maximising the exchange of momentum flux and turbulence generation [17, 18]. In addition, larger orifice diameter and the higher velocity profile contribute to increase the turbulent energy due to bigger contact area and higher momentum of the jets.

In summary, a recalibration of the coefficients that control the mass average turbulent kinetic energy was necessary for the PC04 case.

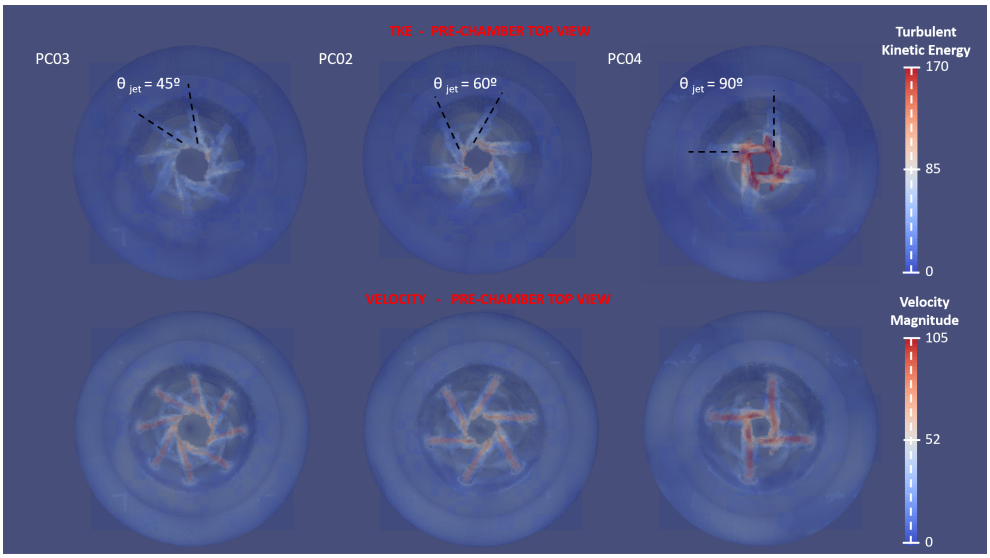

Figure 4.20: 3D pre-chamber geometries overview, with opacity filter, of TKE (top) and Velocity (bottom)

4.4.4 PC04 case: coefficients readjustment

The results obtained using the baseline (blue line) and new optimized coefficients (light blue line) for PC04 geometry are depicted against the CFD curve in figure 4 .21. A lthough t he m odel s lightly o verestimates t he 3 D t rend, the phenomenon is reproduced with acceptable accuracy along the entire compression stroke.

Furthermore, the table 4.2 summarizes the final c oefficients for all the geometries considered. It is important to emphasize that in order to correctly model the evolution of the turbulent kinetic energy for the PC04 case, as much the production (a_{in},C_{sw}) and conversion (C_β) coefficients as th e dissipation (C_ϵ) one have been increased. The coefficients variation is consistent with the hypotheses stated during the previous 3D local profile analysis.

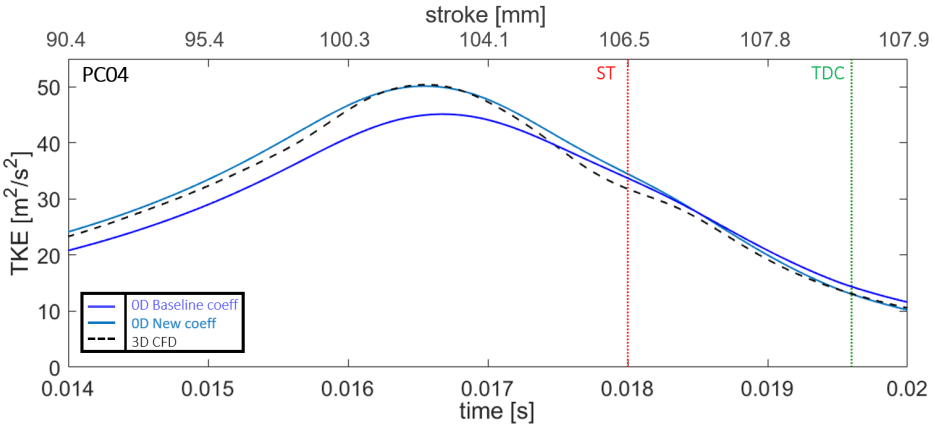

Figure 4.21: Comparison of 0D and 3D-CFD models in terms of turbulent kinetic energy during the compression for PC04 case after the coefficients adjusting (light blue).

	Baseline - PC01	PC02	PC03	PC04
a_{in}	0.3	0.3	0.3	0.4
C_β	0.2	0.2	0.2	0.3
C_ϵ	0.03	0.03	0.03	0.065
C_{len}	0.57	0.57	0.57	0.57
C_{sw}	-	0.0017	0.0017	0.01

Table 4.2: Final model coefficients for all the pre-chambers

References

[1] CONVERGE is a trade mark of Convergent Science. *https://convergecfd.com*.

[2] HanZ, ReitzRD. "Turbulencemodelingofinternalcomî bustionenginesusingRNGkî models". In: *CombustSciî enceandTechnology* 106 (1995), 267r295.

[3] Van Leer, Bram. "Towards the ultimate conservative difference scheme. V. A second-order sequel to Godunov's method". In: *Journal of computational Physics* 32.1 (1979), pp. 101–136.

[4] Fluent, ANSYS et al. *Theory guide*. 2015.

[5] Richards, K, Senecal, P, and Pomraning, E. "CONVERGE Manual-CONVERGE CFD 2.3". In: *Madison, WI* (2016).

[6] Gholamisheeri, Masumeh, Wichman, Indrek S., and Toulson, Elisa. "A study of the turbulent jet flow field in a methane fueled turbulent jet ignition (TJI) system". In: *Combustion and Flame* 183 (2017), pp. 194–206. DOI: 10.1016/j.combustflame.2017.05.008.

[7] Novella, R., Gomez-Soriano, J., Martinez-Hernandiz, P. J., and Libert, C. "Evaluation of the passive pre-chamber ignition concept for future high compression ratio turbocharged spark-ignition engines". In: *Applied energy* 248 (2019), pp. 576–588.

[8] López-Pintor, Darío. "Theoretical and experimental study on the autoignition phenomena of homogeneous reactive mixtures". PhD thesis. 2017.

[9] Martín, Jaime. "Contribución al diagnóstico de la combustión en motores Diesel de inyección directa". PhD thesis. Universitat Politècnica de València, 2007.

[10] Scott, Donald William. *Chemical Thermodynamic Properties of Hydrocarbons and Related Substances: Properties of the Alkane Hydrocarbons, C1 through C10, in the Ideal Gas State From 0 to 1500 K*. Vol. 666. US Department of the Interior, Bureau of Mines, 1974.

[11] Dadgostar, Nafiseh and Shaw, John M. "A predictive correlation for the constant-pressure specific heat capacity of pure and ill-defined liquid hydrocarbons". In: *Fluid Phase Equilibria* 313 (2012), pp. 211–226.

[12] Fogla, Navin, Bybee, Michael, Mirzaeian, Mohsen, Millo, Federico, and Wahiduzzaman, Syed. "Development of a K-k-e Phenomenological Model to Predict In-Cylinder Turbulence". In: *SAE International Journal of Engines* 10.2 (2017), pp. 562–575.

[13] Bardis, Konstantinos, Xu, Guoqing, Kyrtatos, Panagiotis, Wright, Yuri M, and Boulouchos, Konstantinos. "A zero dimensional turbulence and heat transfer phenomenological model for pre-chamber gas engines". In: *SAE Technical Paper* (2018).

[14] Grasreiner, Sebastian, Neumann, Jens, Luttermann, Christoph, Wensing, Michael, and Hasse, Christian. "A quasi-dimensional model of turbulence and global charge motion for spark ignition engines with fully variable valvetrains". In: *International Journal of Engine Research* 15.7 (2014), pp. 805–816.

[15] Payri, Raul, Salvador, FJ, Gimeno, J, and Bracho, G. "A new method-ology for correcting the signal cumulative phenomenon on injection rate measurements". In: *Experimental techniques* 32.1 (2008), pp. 46–49.

[16] Statgraphics Centurion XVII is a trademark of Statgraphics Technologies, Inc. *http://www.statgraphics.com/*.

[17] Johansson, Peter S and Andersson, Helge I. "Direct numerical simulation of two opposing wall jets". In: *Physics of Fluids* 17.5 (2005), p. 055109.

[18] Gilbert, B. "Turbulence measurements in a flow generated by the collision of radially flowing wall jets". In: *Experiments in fluids* 7.2 (1989), pp. 103–110.

Chapter 5

Combustion analysis on baseline design

5.1 Introduction

In this section, the performance of the PCSI system with baseline PC01 geometry are analysed. First of all, the thermodynamic zero-dimensional model used for post-processing the experiments will be explained, including the chemical, combustion and flames sub-models. Afterwards, the combustion development for an individual case (1.1 equivalence ratio in the pre-chamber and 0.5 in the main one) will be fully characterized by exploring several parameters: cycle-to-cycle dispersion, air/fuel mixing process, ignition point, chambers pressure, interchanged mass, turbulence regime, heat released, flame speed. Finally the influence of the equivalence ratio in both chambers will be assessed with the same methodology applied to the baseline case.

5.2 Thermodynamic model under combustion mode

This chapter explains all the theoretical principles and equations (used in the post-processing of the experimental data) that govern the PCSI system. As known, the chemical energy conversion during a combustion cycle is an accurate indicator of the combustion efficiency. Hence, one of the most used parameters to describe it is the heat release rate (HRR) predicted from applying the

energy balance to the combustion chamber, using as a basis the instantaneous pressure evolution [1, 2]. In internal combustion engines, the HRR depends on several factors such as the chamber geometry, engine speed, air/fuel ratio, ignition time or the residual mass, and can be used to build a closed-loop combustion control system [3]. For this purpose, a zero-dimensional model under firing conditions is developed in the next sections for the system under evaluation.

In order to perform the energy balance in the combustion chamber, several simplifications shall be made. In addition to the assumptions already discussed in chapter 4, the following hypothesis are taken into account:

- The entire open system is composed of two subsystems: the main chamber and the pre-chamber, which interchange mass as depicted by the compressible flow equation through the nozzle (chapter 4.3.)
- Mechanical deformations (which affect the instantaneous volume) are considered only for the main chamber.
- Blow-by leakages are neglected. Leakages have been previously evaluated by inducing different pressure values in the combustion chamber with the piston locked at its minimum position, producing less than 0.2 bar/min at the maximum combustion chamber pressure.
- The internal energy is calculated considering the mean gas temperature, evaluated by solving the equation of state. For the purpose, the main chamber is modelled as a single-zone [4]. This is the most severe hypothesis, since the burnt products are much warmer than the average temperature at the beginning of combustion, even if they become closer afterwards. Moreover, with the aim of obtaining an accurate prediction of the flame speed propagation, a hybrid model is adapted for the pre-chamber. The combustion products and fresh charge are modelled with two different zones in terms of mass and temperature estimation. For the rest of the parameters (such as turbulence, heat transfer, etc.) only one zone is considered.
- The composition of the burned products in both chambers is estimated assuming a single-step reaction mechanism as a function of the equivalence ratio. In addition, the dissociation of chemical species is considered from a specific temperature threshold.
- The current cut-off in the primary circuit of the ignition system is considered as the start of combustion in the pre-chamber (SOC_{PC}).

- The start of combustion in the main chamber (SOC_{MC}) is assumed as the instant in which the heat release rate exceeds 3% of its maximum value. It is important to underline that this parameter is linked to the ejection of jets from the pre-chamber.
- Combustion is considered completed when the cumulative burned mass fraction, computed from the instantaneous heat release rate, reaches the unit.
- Heat losses through the walls are accounted for both open systems. Considering a common SI engine, the ratio of heat loss to the fuel heating energy can be more than 30% under some operation conditions [5].

5.2.1 Chemical model

The mathematical model that controls the chemical composition during the combustion process, needed to predict the thermodynamic properties of the air/fuel mixture and their products, is composed by eleven chemical species: H_2O, H_2, OH, H, N_2, NO, N, CO_2, CO, O_2, O [6]. For the current analysis it is assumed that the air is composed of O_2 and N_2, as a simplifying hypothesis, and the fuel is iso-octane (iC_8H_{18}) already in gaseous phase (since evaporation takes place early after the fuel injection). Based on the chemical balance equations, the concentrations of combustion products can be quantified, which allows to determine its thermodynamic properties: mainly temperature (through ideal gas equation of state), heat capacity, internal energy and enthalpy. Therefore, the following reaction can be established for the main combustion products:

$$\mathrm{n}_f C_x H_y O_z + n_a(0.21O_2 + 0.79N_2) \rightarrow$$

$$\rightarrow n_{CO_2}CO_2 + n_{H_2O}H_2O + n_{N_2}N_2 + n_{O_2}O_2 \quad (5.1)$$

To solve the oxidation reaction without dissociation, a linear system of 4 unknowns is considered. In this case the equations are solved assuming a stoichiometric or lean equivalence ratio. In case of rich equivalence ratio, the reaction is carried out in stoichiometric mode, and the remaining fuel is left unconsumed as part of the products.

At high combustion temperatures the dissociation phenomena become more relevant, thus can significantly influence both the heat release and the thermodynamic properties of the mixture. Although it is known that dissociation is mostly related to local temperatures close to the flame front in the range of 2000 K, it must be taken into account that the current model is zero-dimensional, so only the average temperature is computed. For this reason, the model includes the activation of the equations that control the dissociation phenomenon from a temperature threshold of 1400K). In this case, eleven species are considered for the chemical equilibrium according to the following reaction mechanism:

$$\begin{aligned} \mathrm{n}_f C_x H_y O_z + n_a(0.21O_2 + 0.79N_2) \rightarrow \\ \rightarrow n_{CO_2}CO_2 + n_{H_2O}H_2O + n_{N_2}N_2 + n_{O_2}O_2 + \\ + \mathrm{n}_{H_2}H_2 + n_{CO}CO + n_{OH}OH + n_{NO}NO + n_O O + n_N N n_H H \end{aligned} \quad (5.2)$$

Taking into account the equations corresponding to the mass balance of carbon, hydrogen, oxygen and nitrogen species (4 equations), continuity (1 equation) and dissociation equilibrium (7 equations), a non-linear system of twelve unknowns is solved following the methodology explained by Jarquin [7] and Benson [8, 9].

5.2.2 Combustion model

According to the general hypotheses, the combustion model for the main and pre- chambers is depicted. One of the most critical issues is the estimation of the burn rate (related to the heat release rate) in both chambers [10]:

$$\dot{m}_{fb} = \frac{HRR}{LHV} \quad (5.3)$$

where $\dot{m}_{fb}$ is the fuel burning rate, HRR the heat release rate, and LHV the fuel low heating value. The heat release rate in the main chamber can

be calculated based on the first law of thermodynamics for an open system. From the mathematical development of the general energy balance equation:

$$HRR_{MC} = \frac{C_{P,MC}}{R} P_{MC} \frac{dV_{MC}}{dt} + \frac{C_{P,MC} - R}{R} V_{MC} \frac{dP_{MC}}{dt} + \dot{Q}_{MC,loss} + \dot{m}_{ori} h_{ori} \tag{5.4}$$

where $C_{P,MC}$ is the constant pressure specific heat of the main chamber mixture, R is the perfect gas constant, V_{MC} is the main chamber volume (function of the piston position and the mechanical deformations), dP_{MC} is the pressure rate, $\dot{Q}_{MC,loss}$ is the heat transfer through the main chamber walls, h_{ori} is the specific enthalpy of the mixture that goes through the nozzle, and $\dot{m}_{ori}$ is the mass flow rate through the nozzle. The sign of the latest is considered positive when the mass moves out of the system and negative when it enters into the system.

A proper prediction of the heat losses is extremely important for high accuracy combustion analysis. The starting point for the majority of 0D heat losses model is the Reynolds-Nusselt correlation for turbulent flow in pipes [5]. In the literature, the Woschni correlation [11], selected for the current study, is the most extensively used for the heat transfer coefficients prediction.

The model proposed by Woschni is summarized in the equations below:

$$h_{W,MC} = \alpha_W \cdot D_B^{-0.2} \cdot P_{MC}^{0.8} \cdot T_{MC}^{-0.53} \cdot u_{W,MC}^{0.8} \tag{5.5}$$

where $h_{W,MC}$ is the heat transfer coefficient, α_W the scaling factor dependent on the engine, D_B the engine bore and $u_{W,MC}$ the characteristic velocity, which can be calculated as:

$$u_{W,MC} = C_{W1} u_{mp} + C_{W2} \frac{V_S T_1}{V_1 P_1} (P_{MC} - P_{MC,mot}) \tag{5.6}$$

where u_{mp} stands for the mean piston velocity, V_S is the maximum cylinder volume (at bottom dead centre), T_1 and P_1 represent the thermodynamic conditions of the working gas related to the initial cylinder volume V_1 once the filling process is completed, P_{MC} and $P_{MC,mot}$ are the main chamber pressure under fired and motored conditions, and C_{W1} and C_{W2} are the model constants calibrated under motoring and firing conditions.

It is important to highlight that in the case of the PCSI system, the energy analysis during the motoring tests is not only affected by the heat transfer losses (as in a standard engine if blow-by losses are neglected), but also by the mass exchange between both chambers. Therefore, the adjustment of the Woschni constants is performed following the methodology explained in [12], once the discharge coefficient of the orifices was calibrated (section section 4.3). The final values associated with C_{W1} and C_{W2} are respectively equal to 3.65 and 3.24*10e-3.

Once the heat transfer coefficient is estimated, the total heat transfer rate through the walls is given by:

$$\dot{Q}_{MC,loss} = h_{W,MC} \cdot A_{MC} \cdot (T_{MC} - T_{MC,wall}) \tag{5.7}$$

where A_{MC} is the total surface of the main chamber walls (including the piston, liner and cylinder head), T_{MC} is the mean gas temperature and $T_{MC,wall}$ is the walls' temperature, which is assumed equal to the initial cycle temperature imposed through the RCEM heating system.

In the case of the pre-chamber, the energy balance can presented as:

$$HRR_{PC} = \frac{C_{P,PC}-R}{R} V_{PC} \frac{dP_{PC}}{dt} + \dot{Q}_{PC,loss} + \dot{Q}_{evap} + \dot{m}_{ori} h_{ori} \tag{5.8}$$

where $C_{P,PC}$ is the constant pressure specific heat of the pre-chamber mixture, V_{PC} is the pre-chamber volume, dP_{PC} is the pressure derivative, $\dot{Q}_{PC,loss}$ is the heat transfer through the pre-chamber walls, $\dot{Q}_{evap}$ is the heat absorbed by the auxiliary liquid fuel during the vaporization process, and $\dot{m}_{ori}$ and h_{ori} are the mass flow rate and the specific enthalpy of the mixture that goes through the orifices.

In this case, the Woschni model has not been considered suitable for an accurate prediction of heat losses inside the pre-chamber since the characteristic velocity should not be directly linked to the mean piston speed, but to the velocity of the flow through the orifices. The pre-chamber flow field is controlled by the gas velocity through the nozzle (an order of magnitude bigger than the piston speed) which generates a high turbulence intensity that influences the convective heat exchange. Indeed, the Bargende correlation [13,

14] was slightly modified by Bardis et al. [15] for pre-chamber applications, and is chosen for the heat losses estimation in the current work:

$$h_{B,PC} = \alpha_B \cdot V_{PC}^{-0.073} \cdot P_{PC}^{0.8} \cdot T_{PC}^{-0.53} \cdot u_{B,PC}^{0.78} \tag{5.9}$$

where the characteristic velocity is given by:

$$u_{B,PC} = \frac{1}{2}\sqrt{C_{B,k} \cdot \frac{8}{3}k + C_{B,u} \cdot u_{ori}^2} \tag{5.10}$$

$C_{B,k}$ and $C_{B,u}$ being two tuning constants for taking into account the velocity gradient inside the PC. For the same considerations previously stated for the Woschni model, Bargende's constants are also calibrated after the mass transfer model validation, reaching values of 1 and 0.6 respectively.

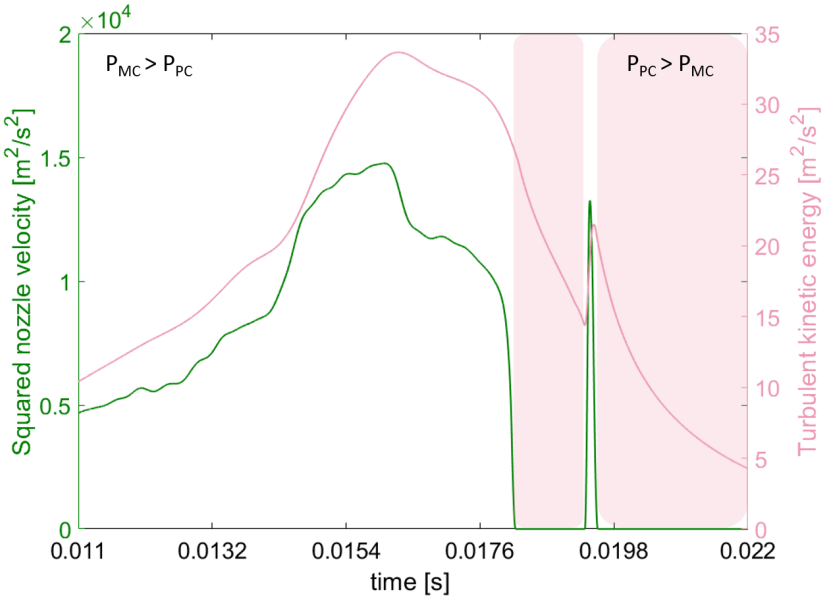

Figure 5.1: Contribution of the first and second term of the Bargende correlation for the characteristic speed estimation.

Figure 5.1 shows the individual contribution of the squared nozzle velocity (green line) and the turbulent kinetic energy (pink line) as function of time.

The following considerations are valid for all the tests and geometries analysed, so the boundary conditions of this specific test will be omitted, as they are not relevant for the scope. Starting from the pressure traces of the picture 3.11, showed for the test methodology description, the nozzle velocity and the turbulent kinetic energy are estimated by means of equations 4.3 and 4.3 respectively. It is important to emphasize that during the filling process ($P_{MC} > P_{PC}$), the squared nozzle velocity overcomes by two orders of magnitude the value of the turbulent kinetic energy which is irrelevant for the estimation of heat losses. Then, after combustion begins, the flow through the orifices reverses performing the first ejection. Indeed, when the gases are ejected from the pre-chamber ($P_{PC} > P_{MC}$), the contribution of the first term will be zero. Consequently, in the part highlighted with pink shades, heat losses are totally controlled by turbulent kinetic energy.

Therefore, the heat transfer rate through the walls is given by:

$$\dot{Q}_{PC,loss} = h_{W,PC} \cdot A_{PC} \cdot (T_{PC} - T_{PC,wall}) \tag{5.11}$$

where A_{PC} is the pre-chamber walls surface, T_{PC} is the mean gas temperature and $T_{PC,wall}$ is the walls' temperature.

Regarding the heat absorbed during the auxiliary fuel evaporation process, it is modeled including two contributions.

$$\dot{Q}_{evap} = \dot{m}_{inj} Cp_{fuel}(T_{evap} - T_{fuel}) + \dot{m}_{inj}\delta h_{evap} \tag{5.12}$$

The first is the heat necessary to raise the fuel temperature from the conditions inside the injector until the vaporization temperature at the pre-chamber thermodynamic conditions. To calculate this term, $\dot{m}_{inj}$ is the fuel injection rate (previously characterized by an injection rate analyser), Cp_{fuel} is the iso-octane specific heat at constant pressure at liquid state, T_{evap} is the vaporization temperature, and T_{fuel} is the fuel temperature. The second one refers to the heat absorbed for the complete evaporation of the fuel mass in which δh_{evap} is the enthalpy of vaporization. Again, starting from the pressure traces showed in chapter 3, the figure shows the evolution of the heat release rate in the pre-chamber during the auxiliary injection, with and without the contribution of the fuel evaporation.

Due to the fuel vaporization, the pre-chamber average temperature drops causing a pressure gradient that results in underestimation of the heat released

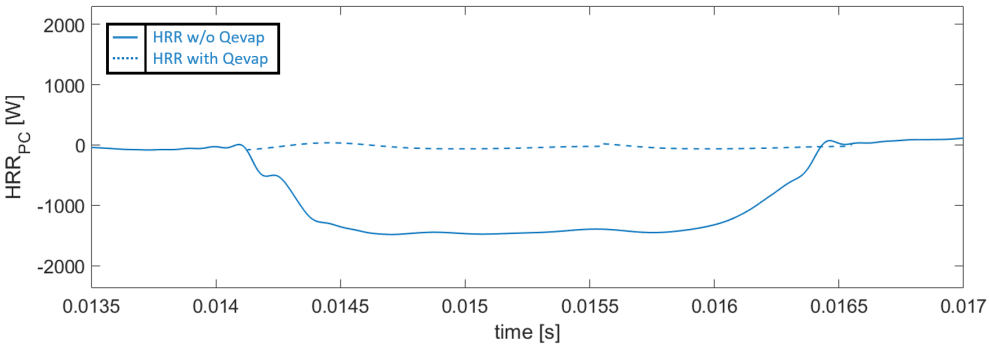

Figure 5.2: Heat release rate with and without the heat absorbed by the auxiliary fuel evaporation.

in that area. Hence, to accurately estimate the heat release evolution during compression it is necessary to take into account the contribution due to the evaporation process. All the parameters needed to solve the issue can be found in NIST's database [16].

Combustion model validation under motoring and fired conditions

Once completed, the zero-dimensional model is validated by monitoring the evolution of the heat release rate under fired and motoring conditions.

Fig. 5.3 shows the HRR under fired (continuous lines) and motored (dotted lines) operation mode, for an experiment fuelled with iso-octane at the following conditions: $T_0 = 360K$, $P_0 = 0.15MPa$, $CR = 11$, and $\phi = 0.5$. The values of the constants that characterize Woschni's and Bargende's heat losses models can be also seen in the figure. Finally, the heat release rate is plotted in blue colour for the main chamber, and in orange for the pre-chamber. In general, the heat released during the combustion of the main chamber mixture is one order of magnitude bigger with respect to the pre-chamber one. Moreover, it can be highlighted that the HRR under motored conditions, is almost zero or negligible for both chambers, which is a clear indicator of the good accuracy of the heat losses and mass transfer models. It is important to remember that the calibration of the above coefficients is done once the mass interchange model was adjusted against 3D CFD simulations, as shown in chapter 4.3.

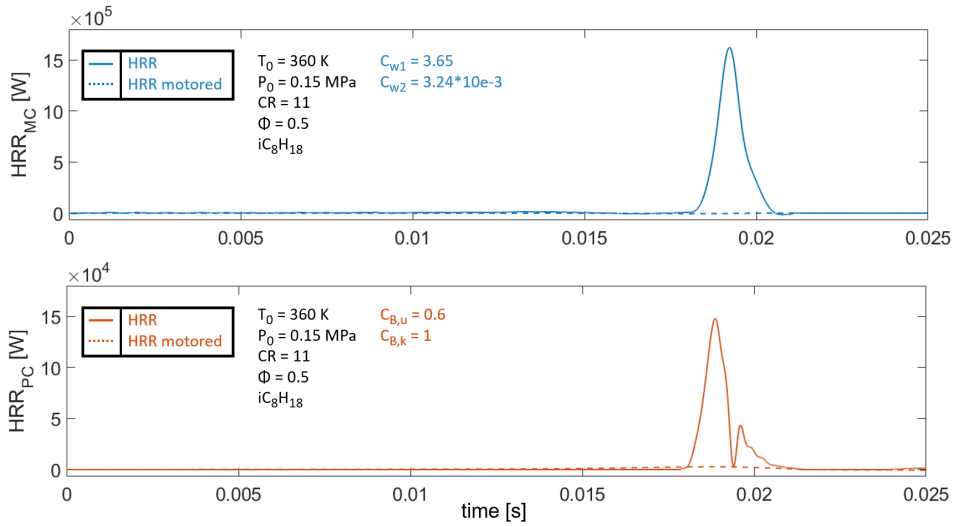

Figure 5.3: Heat release rate under fired (continuous line) and motored (dotted line) conditions for main (top) and pre-chamber (bottom).

5.2.3 Pre-chamber flame propagation model

Premixed turbulent flame speed is a critical parameter for the combustion analysis of PCSI engines simulations. By modelling the flame propagation as a function of the laminar flame speed, the turbulence intensity and the system geometry, it should be possible to create a model which yields predictive results even when individual parameters are changed [17]. This section describes the fundamental equations that control the proposed flame propagation model used for the combustion analysis. Distaso et al. [18] provided an empirical correlation for the laminar flame speed prediction under a wide range of equivalence ratio and unburned mixture pressure and temperature:

$$S_L(\phi, T_u, P_u) = S_{L0} \left(\frac{T_u}{T_0}\right)^{\alpha} \left(\frac{p_u}{p_0}\right)^{\beta} \tag{5.13}$$

where α and β are a function of the equivalence ratio ϕ, and S_{L0} is the laminar flame speed at standard conditions ($p_0 = 1\text{atm}$, $T_0 = 298\text{K}$)

As the previous equation states, the laminar flame speed is a direct function of only a few physical and chemical parameters. On the other hand,

turbulent flame speed is a function of the complex interaction between the initial laminar kernel with the turbulence field, which has been the focus of many different works in the literature, providing several correlations [19]. In this work, the correlation proposed by Kolla [20] is used for the turbulent flame speed estimation:

$$\frac{S_T}{S_L} = \left\{ \left[b - a \left(1 + \left(\frac{u'}{S_L} \right)^{1.5} \left(\frac{\delta}{L_{pc}} \right)^{0.5} \right)^{-0.4} \right] \right\}^{0.5} \tag{5.14}$$

$$\left\{ \cdot \frac{T_{PC} - T_u}{T_u} \cdot \frac{L_{pc}}{\delta} \cdot \frac{u'}{S_L} + S_d \right\}^{0.5} \tag{5.15}$$

$$S_d = \frac{d}{\left(\frac{u'}{S_L}\right)^{0.75} + \left(\frac{\delta}{L_{pc}}\right)^{-0.25}} \cdot \left(\frac{u'}{S_L} \right)^{2.75} \tag{5.16}$$

where a,b,d are the model constants, tuned for the used fuel and system layout. Furthermore, S_T depends on mean (T_{PC})/unburned(T_u) pre-chamber temperatures and turbulence key parameters as turbulent kinetic velocity (u'). Finally, the flame thickness (δ) is given by the Zeldovich-Blint correlation [21].

Finally, the mean expansion speed (U_B) can be estimated combining the turbulent flame speed with the mean gas speed (U_G), produced by the expansion of the hot combustion products, which can be evaluated once the heat release rate in the pre-chamber is known [5]. More specifically, the following relationships are used:

$$U_B = S_T + U_G \tag{5.17}$$

$$U_G = \frac{V_u}{\gamma_{PC} P_{PC} A_F} \cdot \frac{dP_{PC}}{dt} \tag{5.18}$$

$$A_F = \frac{\dot{m}_b}{\rho_u S_L} \tag{5.19}$$

where V_u and ρ_u are the unburned mixture volume and density, A_F is the real flame surface and $\dot{m}_b$ is the total (air more fuel) burned mass flow rate, calculated from the instantaneous heat release rate and the lower heating value of the fuel, assuming a one-step combustion mechanism.

5.3 PC01 - Baseline case analysis

This section is focused on the experimental analysis of the PCSI system combustion. First of all, the cycle-to-cycle dispersion will be evaluated in terms of pressure evolution for different compression ratio. Then, the assessment of the injection parameters as pressure and time will be presented. Furthermore, the selection of the ignition point will be discussed. Once completed this previous phase, the results obtained from the experimental campaign will be described starting from the pressure analysis in both chambers and the mass flow exchanged. Later on, the turbulence model described in section 4.3 is used to evaluate turbulent kinetic energy evolution in the pre-chamber during a combustion case. Based on this information, the heat release rate and the flame speed are evaluated. This flame speed is compared to the time elapsed from the spark for validation of the models used. Subsequently, the analysis is extended to other operating conditions in terms of the equivalence ratio in both chambers, showing consistent results.

5.3.1 Cycle-to-cycle dispersion

The cycle-to-cycle dispersion of the system is evaluated on two levels of compression ratio, by means of the statistical assessment of fifteen baseline case test repetitions. Figure 5.4 shows the pressure evolution in the main combustion chamber for two different compression ratio (CR = 11.5 blue lines, and CR = 10.5 orange lines) as function of the time elapsed from the beginning of the rapid compression. In details, the baseline PC01 case corresponds to a fuel-to-air equivalence ratio of 0.5 in the main chamber and 1.1 in the pre-chamber (at the spark activation time). The chamber and wall initial temperature is $360K$, the chamber pressure equal to $0.15MPa$, and the vertical dotted red line (in the graph) shows the time at which the spark is discharged in the pre-chamber.

Hence, a detailed statistical analysis in terms of the maximum in-cylinder pressure is performed, and depicted in table 5.1, in which $\bar{x}$ is the average, σ the standard deviation, COV the coefficient of variation.

The coefficient of variation is below the threshold of 2% for the two levels considered, thus ensuring a low cycle-to-cycle deviation of the pre-chamber spark ignition system.

In addition, the slight deviation between the pressure curves before the spark activation time, is due to slight changes in the compression ratio , resulting from the oscillation of the initial chamber pressure. It is important to take in mind that there is no rod-crank mechanism driving the RCEM, thus

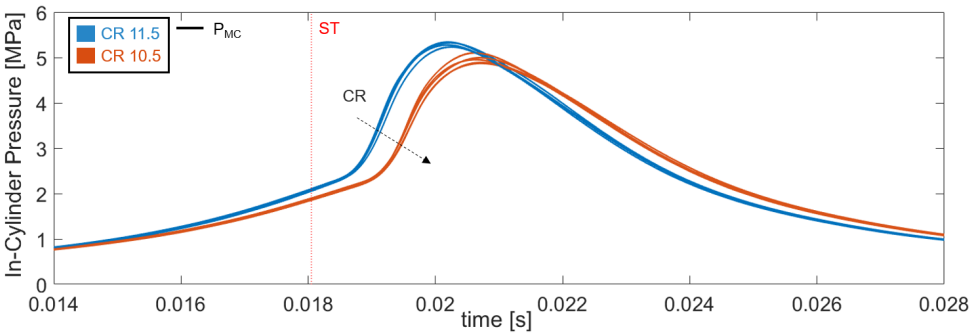

Figure 5.4: In-Cylinder pressure evolution for cycle-to-cycle dispersion evaluation. 2 compression ratio levels and 15 test repetitions each level.

	P_{max} (CR 11.5) [MPa]	P_{max} (CR 10.5) [MPa]
$\bar{x}$	5.285	4.954
σ	0.478	0.885
COV [%]	0.90	1.78

Table 5.1: Statistical analysis results of significant parameters for 15 repetitions of baseline test under several compression ratio.

small oscillations lead to a different pressure balance between the driving and chamber pressures. Therefore it is of crucial importance to monitor that this parameter does not widely fluctuate at the start of the test.

5.3.2 Auxiliary injection point

In this paragraph, the selection of the pre-chamber auxiliary injection pressure and point are discussed. It is necessary to underline that the injection events may influence two key aspects of the PCSI systems: the air/fuel mixing process and the turbulent fluid-dynamic field. Theoretically, an early injection promotes high mixing time in detriment of the turbulence, that is largely dissipated at the instant of spark plug activation [22]. In contrast, when performing late injection the mixing time is reduced, with aims to have more turbulence near the spark event.

Additionally, this matter may become critical because of the wall wetting phenomenon, occurring when injecting liquid fuel in a small volume [23, 24]. On the one hand, the incidence and accumulation of fuel in the pre-chamber

walls can lead to the appearance of a fuel film which deteriorates combustion, enhances the emission of carbon monoxide, unburned hydrocarbons and particulates, and leads to energy losses due to increased heat transfer [25]. On the other hand, the impact of the jet with a surface tends to increase the mixing of the fuel in the air both for the impact and for the subsequent expansion of the front part of the jet. Although the complexity of jet-wall impact phenomena has been extensively studied under "free jet" conditions [26], it is still an area of active research under engine-like conditions.

For the geometry under examination, the distance between the injector tip and the pre-chamber wall is about 12mm. As no significant data are available for the auxiliary injector in terms of liquid phase penetration, an investigation by varying the injection timing (along the compression stroke) and the injection pressure is performed.

According to the first point of the experimental matrix, the two injection pressure levels are 140 MPa and 100 MPa. Hence the analysis will be expanded, including two different injection points: the injection is triggered at two instants, one around half of the compression stroke ($65mm$) and another close to the spark time ($87mm$). Finally, the compression ratio effect is also taken into account. The pre-chamber start of combustion is around t = 0.01795 ms, while the target equivalence ratios are $\phi_{PC} = 1.1$ $\phi_{MC} = 0.3$ for all the cases. Furthermore, the table summarizes the main differences between the tests carried out. In details, the injection pressure P_{inj}, the compression ratio CR, the start of injection (SOI), the end of injection (EOI), the mixing time available (t_{mix}), and the pre-chamber density (ρ_{PC}) at the SOI are presented in the first column.

	CASE A	CASE B	CASE C	CASE D
P_{Inj} [MPa]	140	100	140	100
CR [-]	12	12	13	12
SOI [mm]/[s]	65 / 0.0095	65 / 0.0095	65 / 0.0094	87 / 0.0141
EOI [mm]/[s]	74 / 0.0112	78 / 0.0122	74 / 0.0111	100 / 0.0168
t_{mix} [s]	0.0057	0.0057	0.0058	0.0011
ρ_{PC} [Kg/m^3]	3.43	3.43	3.55	5.18

Table 5.2: Summary table of auxiliary injection tests boundary conditions.

Figure 5.5 compares the main and pre-chamber's pressure evolution for the four cases. In addition, the auxiliary injection time windows are highlighted in the graph. On the top of the figure, the injection pressure effect is analysed comparing case A (dotted lines) with case B (continuous lines). Case A shows

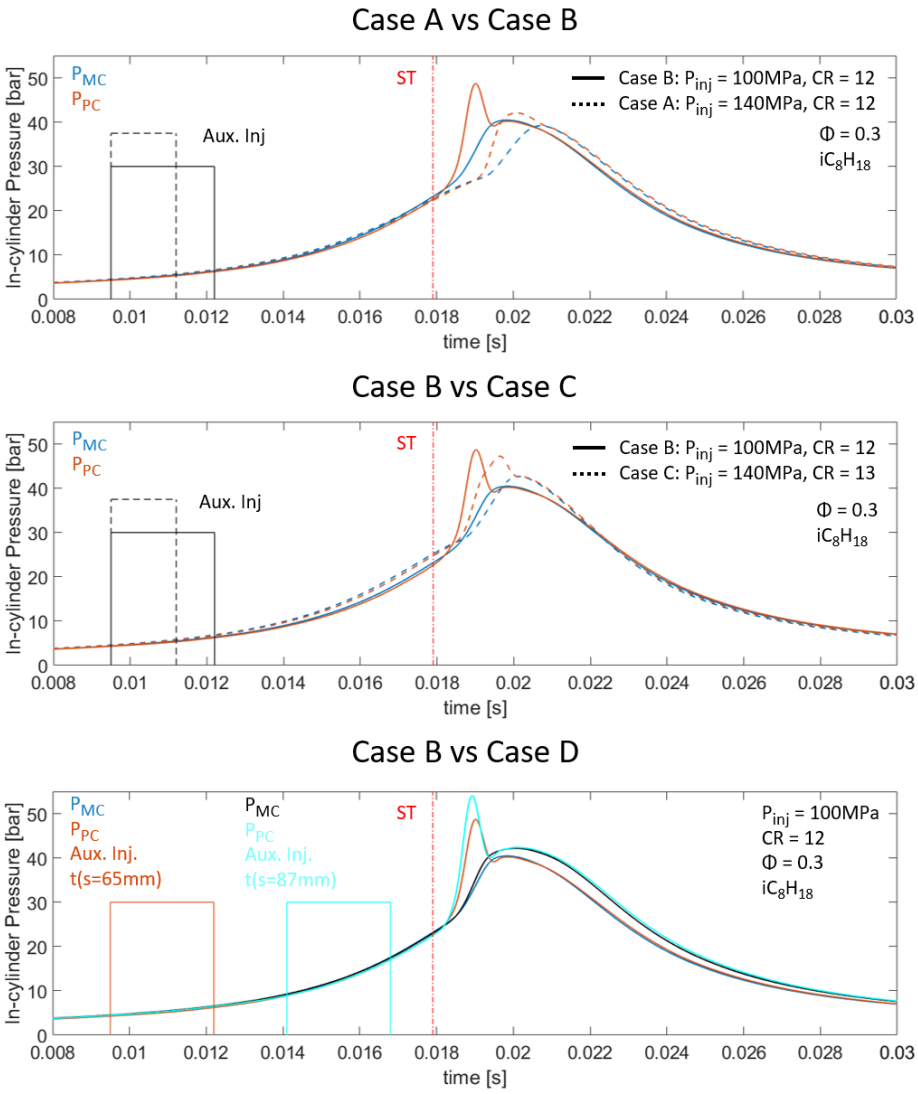

Figure 5.5: Pressure evolution analysis for injection system calibration. Top: Case A vs B, injection pressure effects with same CR. Middle: Case B vs C, injection pressure effects with different CR. Bottom: Case B vs D, injection instant effect with same CR and injection pressure.

a delay in the start of pre-chamber combustion, and significantly lower pressure peak and gradients in both chambers (orange lines for PC and blue lines for MC). As emphasized in chapter 3.2, the injection pressure is a secondary influence factor for the liquid length. However, the increase in the injection velocity as a function of rail pressure shall be taken into account. Considering that the incoming mixture flow during the filling process is opposite to the injection direction, decreasing the injection velocity helps to contain the progression of the fuel liquid phase towards the wall. Thus, it is evident that despite a longer mixing time, as the injection pressure increases, more liquid fuel fraction will impact against the wall resulting in combustion efficiency losses.

Identical conclusions are achieved by increasing the compression ratio (case B vs. case C in the middle of fig. 5.5) in order to obtain better conditions in terms of mixture temperature (positive effect on laminar flame velocity). Finally, the injection point effects are depicted on the bottom of figure, comparing case B vs D. Despite a considerably reduced air/fuel mixing time (end of injection is close to ST), the graph displays a similar start of combustion, and a significant improvement in both pre-chamber (light-blue) and main chamber (black line) combustion for case D. Delaying the injection point has two positive effects on combustion: first, as pre-chamber temperature and pressure increase during the compression, chamber conditions promote fuel evaporation, thereby reducing or eliminating the liquid impact against the walls. Second, the induced turbulence associated with the injection velocity perturbs the fluid dynamic field, due to the collision with the incoming flow through the orifices. As highlighted in chapter 4.3, the turbulence associated with the injection is characterized by a fast dissipation rate. Thus, with high probability, the combustion improvement is mainly due to the reduction of wall wetting. Another element in support of this hypothesis is that further reducing the injection pressure to 50 MPa does not bring any further improvement. Nevertheless, advanced strategies that involve an extreme delay of the pre-chamber auxiliary injection, to achieve total stratification and maximize the effects of turbulence, are out of the scope in this analysis. Hence the Case D injection parameters are selected for all the experimental campaign.

5.3.3 Spark ignition point

The spark timing affects combustion characteristics and engine performance, especially during cold start and idle conditions [27]. Indeed, several strategies, depending on the engine speed and load, are employed in order to minimize

the emissions and probability of knocking appearance without affecting significantly the combustion efficiency [28, 29].

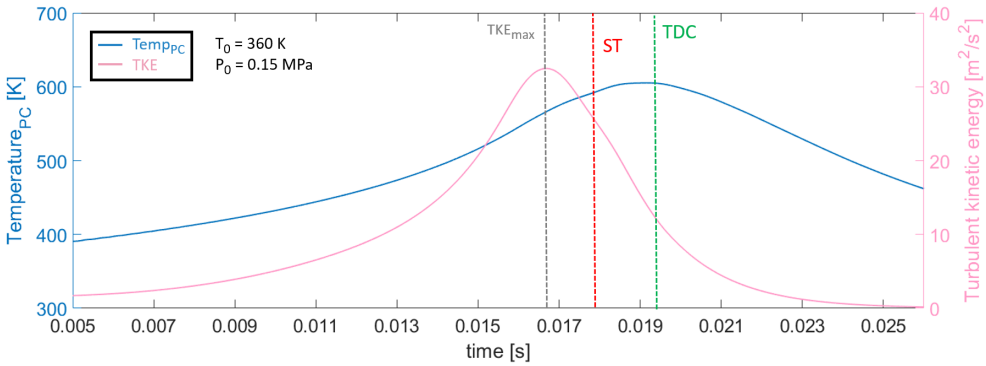

Figure 5.6: 3D CFD simulation pre-chamber temperature (blue) and turbulent kinetic energy (pink) evolution as function of time.

In this case, the calibration of the spark instant aims to maximize the flame propagation speed in the pre-chamber. Hence, the temperature and turbulent kinetic energy evolution are analysed by means of the 3D CFD simulations under motoring conditions extensively described in chapter 4.2.

Figures 5.6 underlines three possible spark activation instants along the pre-chamber temperature (blue line) and turbulent kinetic energy (pink line) trends. Theoretically, in terms of turbulence, the ignition point should coincide with the maximum TKE point (dotted gray line). In reality, an early ignition time can lead to several issues. First, the auxiliary injection should be anticipated resulting in the wall wetting problems described above. Second, the heat would be released almost entirely during the compression phase, anticipating too much the ignition in the main chamber.

Instead, in terms of temperature, the ignition point should coincide with the top dead centre, thus avoiding the problems described for the maximum TKE point. Unfortunately, although the temperature conditions are ideal for the laminar flame speed, the TKE level drops drastically close to the top dead center. Approximately, the turbulent kinetic energy peak coincides with the peak of piston velocity, which controls the pressure difference between the two chambers. In other words, when the piston speed is reduced, the velocity through the orifices and turbulence also decreases.

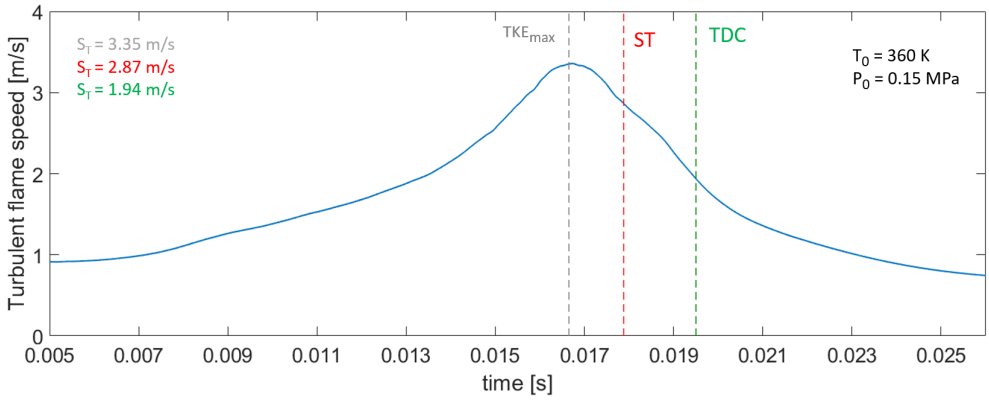

Figure 5.7: Turbulent flame speed evolution as function of time.

The figure 5.7 shows the initial theoretical values of the turbulent flame speed obtained through the Kolla equation (eq. 5.16). In addition, the left side shows the exact values at the three different points selected (respecting the order of colours). Hence, the spark activation (highlighted in the figure with a dashed red line) is triggered in a region of a good compromise between temperature and turbulence, thus ensuring a high level of turbulent flame speed also taking into consideration the injection point effects on combustion previously debated.

5.3.4 Pressure evolution description and test phases characterization

Figure 5.8 shows the pressure evolution in the main combustion chamber (continuous line) and inside the pre-chamber (dotted line) as a function of the time elapsed from the beginning of the rapid compression for the baseline test, corresponding to a fuel-to-air equivalence ratio of 0.5 in the main chamber and 1.1 in the pre-chamber (at the spark activation time).

In this graph, a vertical line shows the time at which the spark is discharged in the pre-chamber. During the compression stroke, and before the spark timing, the gases from the main chamber are pushed into the pre-chamber, filling it with the fuel-air mixture generated thanks to the fuel injection in the main chamber before the rapid compression. The difference in the pressure between both chambers is mainly a consequence of the piston velocity and the pre-chamber geometrical details, especially the discharge coefficient

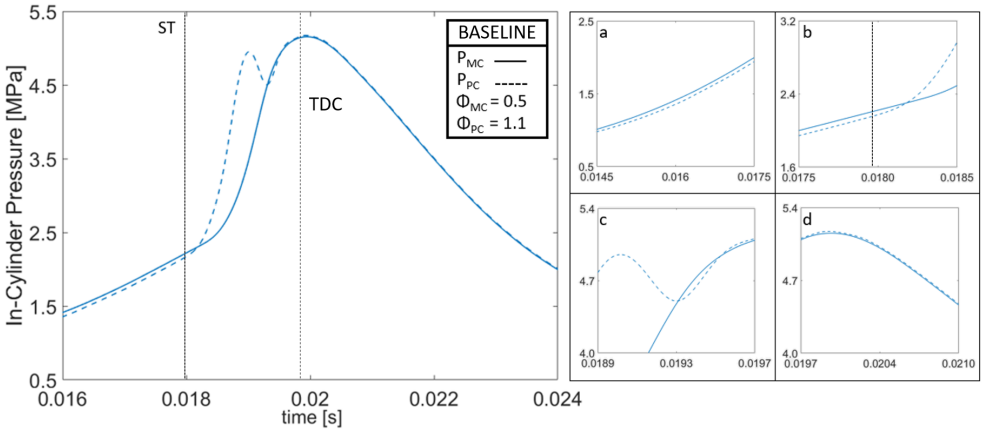

Figure 5.8: In-Cylinder pressure evolution:(a) Filling process. (b) Pre-chamber start of combustion (1st ejection). (c) Pre-chamber pressure peak and re-filling process. (d) 2nd ejection and pre-chamber emptying process

of the orifices (a). Approximately around 13-15ms from the test beginning, the auxiliary injection is carried out to reach the desired equivalence ratio in the pre-chamber at the spark timing (in the case of the figure, a fuel-to-air equivalence ratio of 1.1). Shortly after the spark activation, the pressure in the pre-chamber starts to increase as a consequence of the premixed combustion process (b). Once the pre-chamber pressure is higher than the one in the main chamber, hot gases are ejected through the pre-chamber orifices, acting as ignition sources for the main chamber lean mixture. Once the flame approaches the pre-chamber walls, the pressure starts to decrease, falling again below the main chamber pressure (which is rising due to the combustion already initiated) for a small portion of time, inducing a second filling process in the pre-chamber (c). Finally, during the expansion stroke, the combustion products available in the pre-chamber are sucked into the main chamber (d).

With the information of the instantaneous pressure in both chambers, and taking into account the compressible nozzle equation introduced in section 4.3, it is possible to estimate the evolution of the mass inside the pre-chamber, depicted in Figure 5.9. This information is shown together with the pressure ratio between the main chamber and the pre-chamber (green line), which is the physical parameter driving the mass exchange according to equation 4.3. As previously introduced, during the compression stroke the pressure ratio is greater than one, and the pre-chamber mass increases due to the filling process

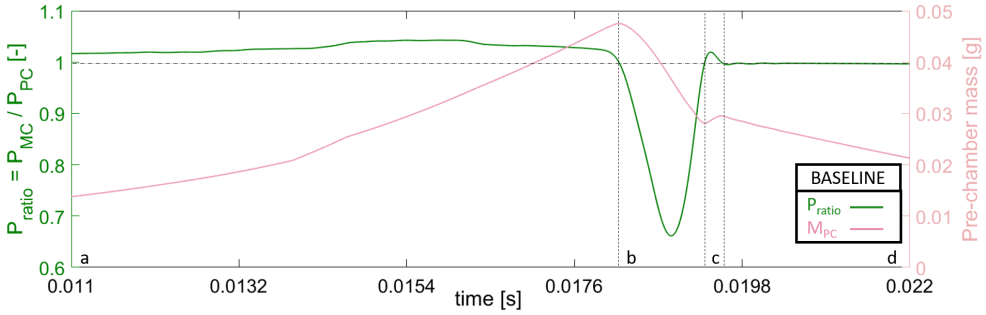

Figure 5.9: Pressure ratio and PC mass time evolutions.

from the main chamber (a). The drastic change in the mass evolution slope (around 14ms after the start of the rapid compression) is due to the auxiliary injection in the pre-chamber. Once the combustion starts and the pressure in the pre-chamber rises, both the pressure ratio and the pre-chamber mass rapidly decrease due to the first ejection (b). Subsequently, the main chamber combustion causes the pre-chamber refilling (c), and the second ejection during the expansion stroke (d).

5.3.5 Nozzle velocity, turbulence and heat release rate prediction

Figure 5.10 shows the evolution of the velocity though the orifices and the turbulent kinetic energy (TKE), computed according to the zero-dimensional model introduced and validated in section 4.3. It is well known that for the PCSI systems, the turbulence production and dissipation in the pre-chamber are strongly connected with the velocity and mass exchange through the orifices. Therefore, the maximum value of the TKE approximately coincides with the maximum velocity between the orifices at the middle of the compression stroke. However, when the auxiliary injection is performed, the temperature inside the pre-chamber decreases due to fuel evaporation, slightly affecting the velocity and TKE evolution around 14/16ms after the start of the test (aSOT).

Despite the RCEM piston and the nozzle velocity starts to slow down, the TKE level at the spark discharge instant (18ms aSOT) is still high, ensuring a strong interaction between the initial flame kernel and the flow field. As the mass flow reverses (0.2ms aST), the main turbulence source is no longer applied, and the turbulence intensity quickly dissipates until the pre-chamber

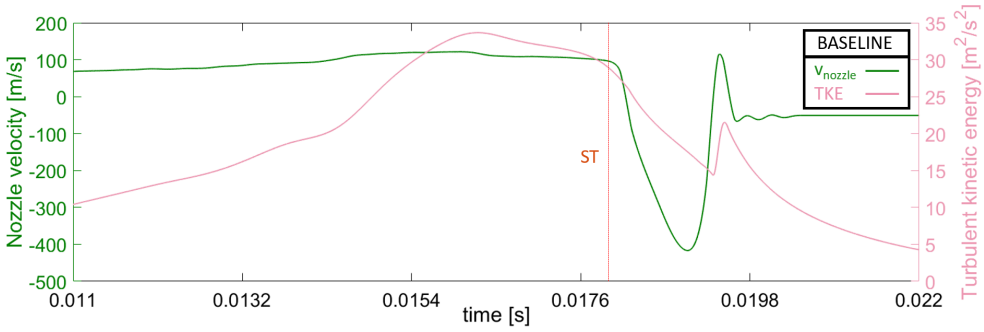

Figure 5.10: Turbulent Kinetic Energy and Nozzle velocity time evolutions.

refilling. Once again, the mass flow reverses during the expansion stroke and the turbulence extinguishes definitively under the 2nd ejection. It is important to emphasize that the first ejection of gases reaches much higher velocity levels than the second one. Indeed, the two ejections will have a different impact on combustion development in the main chamber.

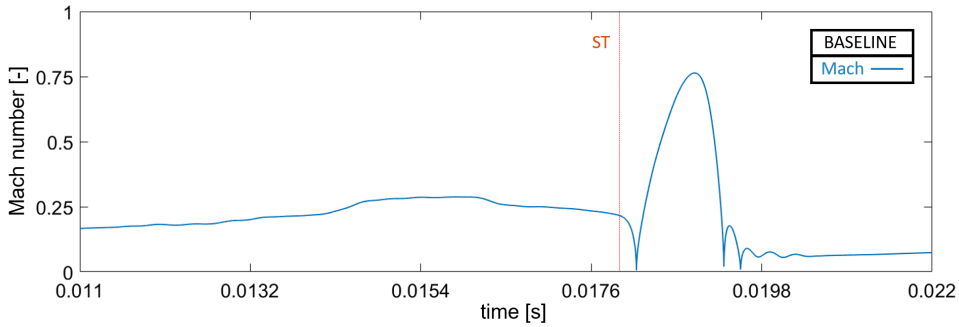

Figure 5.11: Mach number time evolution.

In order to measure the compressibility characteristics of fluid flow through the orifices, the Mach number is evaluated. The unburned mixture temperature and the specific heat ratio of the gases (γ) inside the pre-chamber are selected for the speed of sound calculation. Although the thermodynamic state of the gases flowing through the orifices are related to their composition, this conservative choice allows us to verify the Mach regime under the most critical conditions. As can be seen (figure 5.11, the highest value, reached

in the maximum nozzle speed conditions, is about 0.8. Therefore, It can be stated that the flow regime is subsonic throughout the entire working cycle.

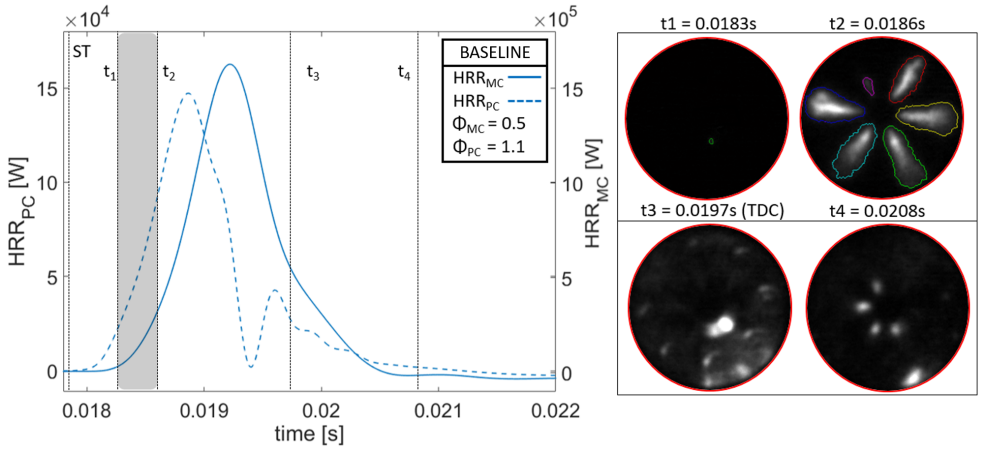

Figure 5.12: Left side: Heat Release Rate of the main chamber (continuous line) and pre-chamber (dotted line). Right side: Main chamber combustion visualization images.

Figure 5.12 shows the heat release rate in both chambers (continuous line for the main-chamber and dotted line for pre-chamber). This information is complemented by four pictures of specific stages of the main combustion event, obtained through the optical diagnostic described in 3.3. Until the spark activation, the energy balance between the heat losses through the walls and the exchanged gas enthalpy returns in a flat curve (almost equal to 0 for both chambers), confirming once again that both models are properly calibrated. Once the spark is activated, after the induction time, the premixed combustion process in the pre-chamber takes place, leading to a rapid increase in the burned mass fraction and heat released. The grey shading part highlights the start of the jets ejection in the main chamber, summarized by the 2 images on the top of fig. 5.12 (t1 = 0.0183s 1st jet / t2 = 0.0186s last jet). Due to the system geometry and the spark plug position, the ejection from the pre-chamber starts at slightly different instants for each orifice. The discharge from the pre-chamber continues until the flame approaches the pre-chamber walls and the combustion in the main chamber develops, resulting in a higher pressure in the main chamber. Once more, the re-filling takes place until TDC, which is shown in the bottom picture on the left with no ejection, leading to the second ejection during the expansion stroke (bottom picture on the right).

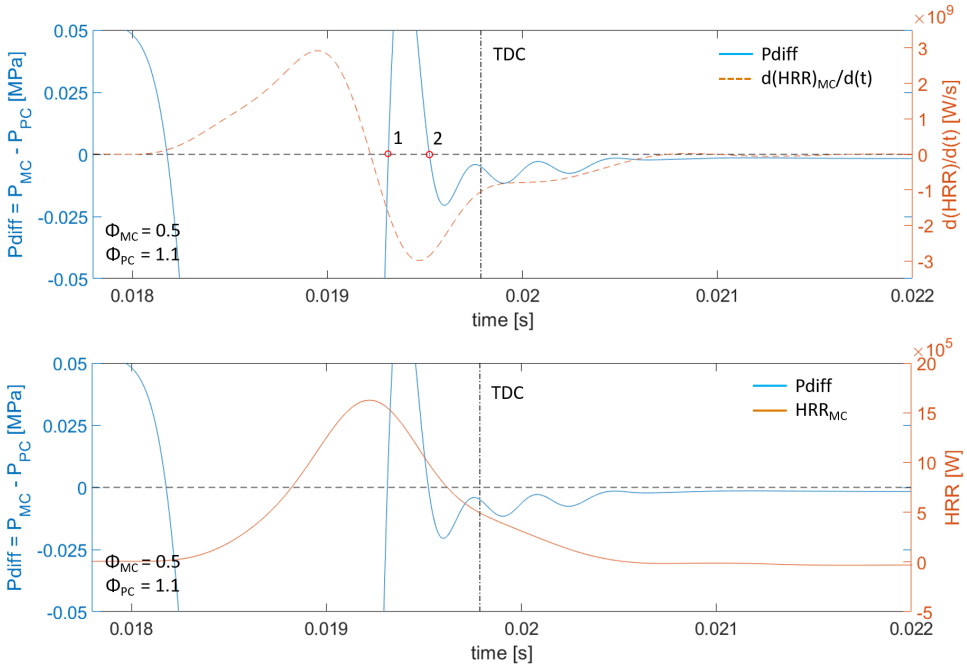

Figure 5.13: Top side: temporal derivate of the main chamber heat release rate vs the pressure difference between chambers. Bottom side: main chamber heat release rate vs the pressure difference between chambers.

In order to deeply understand the different combustion phases along the whole process, the time derivative of the heat release rate (orange dotted line) is compared with the chambers pressure difference (blue line) in the top side of figure 5.13. Additionally, the match between the heat release (orange continuous trend) and the pressure difference is depicted on the bottom.

Looking carefully at the phenomenon, the first ejection (Pdiff < 0) marks the beginning of the main combustion phase and is controlled by the hot turbulent jets coming from the pre-chamber. This phase, also called torch jet ignition stage, is characterized by a strong increase in heat release and high mixture burning rate. Once the pre-chamber mixture is burned the re-filling process takes over between the red points 1 and 2 highlighted in the picture. In this temporal range the flame propagation is considered self-sustained thanks to the main chamber turbulence enhanced. Finally after the point 2, until the end of the cycle, the second ejection is performed leading to the complete charge combustion. During the last phase, the beneficial effect of the second

ejection can be seen by the drastic reduction in the negative slope of the heat release rate.

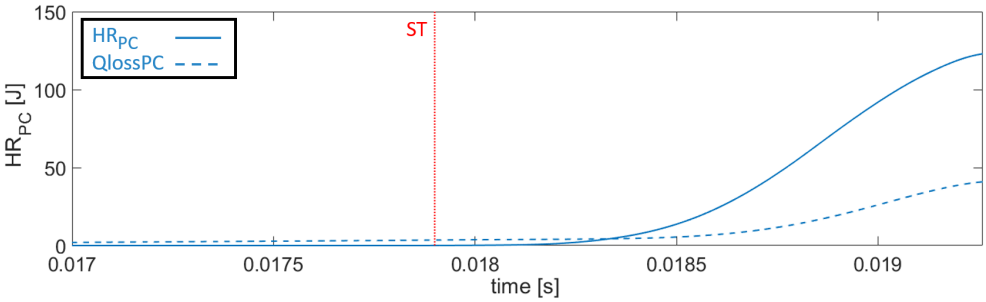

Figure 5.14: Heat release and heat losses as function of time until the end of the first ejection.

Finally the integral of the heat rate released (blue continuous line) is evaluated against the heat losses (blue dashed line) until the end of the first ejection in figure 5.14. Before the spark time no heat is released, resulting in a flat curve, while the heat losses slightly increase due to filling process that rises the mixture temperature. Once the combustion begins, both curves show an asymptotic trend until the fuel is completely burned. Then comparing the total heat losses until the final of the first ejection, it results to be equal to 33% of the total heat released. This final data is in total alignment with the analysis carried out by Chiodi and Bargende for the estimation of heat losses [14]. When using iso-octane at low engine load and speed (imep = 3.4 bar and n = 1500rpm), the percentage of the heat losses is equal to 32.7% of the total heat available.

5.3.6 Flame speed: model results and validation

Figure 5.15 shows the temporal evolution of the different terms for the predicted flame speed according to the model described in section 5.2 in terms of the time after the spark activation. This flame speed is analysed up to the time at which the flame reaches the last of the pre-chamber orifices, according to a geometrical model based on the flame speed evolution and the pre-chamber layout.

In this figure, the orange circled line represents the laminar flame speed S_L, estimated according to Distaso's correlation, which as it can be seen is around 0.4 m/s in the working conditions, and suffers a small increasing trend due to

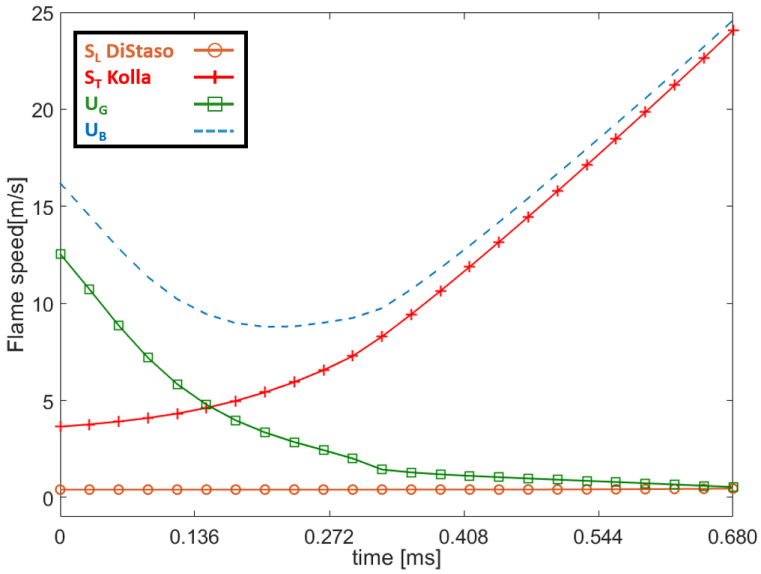

Figure 5.15: Instantaneous flame speed evaluation.

the unburned gas temperature increase induced by the compression. The red squared curve shows the evolution of the turbulent flame speed. Initially, this value is relatively low since the flame kernel after the spark discharge is still comparable to Taylor's macroscale, while an increasing trend appears later on due to the higher interaction between the flame and the turbulence field as the flame develops, leading to flame speed ratio values higher than 25. Then, the green squared line represents the mean gas speed U_G, which is maximum at the beginning of the combustion process where the volume of the burned products is small compared to the total pre-chamber volume. Finally, the blue dashed line shows the mean expansion speed U_B, calculated as the sum of the turbulent flame speed and the mean gas speed.

The estimated mean expansion speed can be validated taking into account the results from the combustion visualization. In particular, from the combustion images it is possible to detect the time at which the pre-chamber flame exits from each of the orifices. Then, a mean flame speed can be calculated taking into account the distance between the spark electrodes and the outlet section of each of these orifices (which is different due to the non-central location of the spark).

Figure 5.16 shows an example of the determination of these distances for

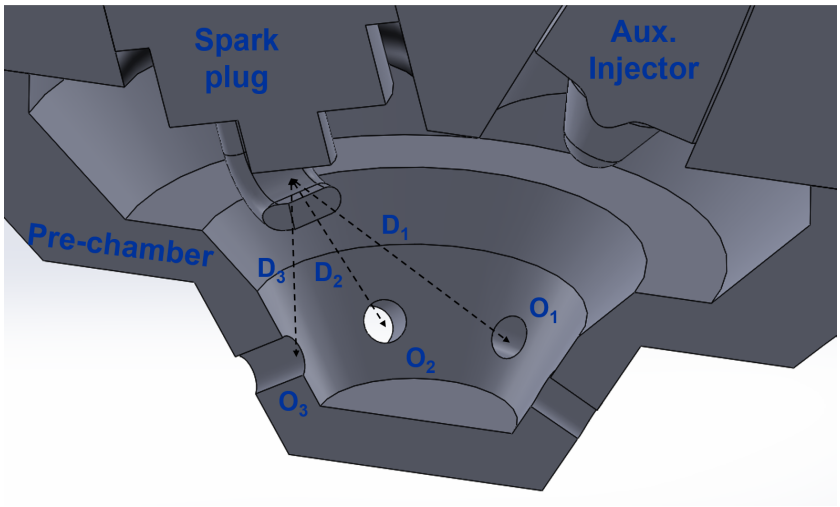

Figure 5.16: Example of determination of the distance between spark and orifices from the pre-chamber geometry.

three out of the six orifices of the pre-chamber. Considering this distance and the time calculated from the images, it is possible to calculate an equivalent mean gas speed to be compared to the one computed by the 0D model. This information is available in Table 5.3, which shows an almost perfect matching between both values.

Orifice	**D[mm]**	**Time [ms]**	**Speed [m/s]**
1	4.99	0.43	11.6
2	5.14	0.43	11.9
3	7.34	0.49	15.0
4	7.57	0.55	13.8
5	9.43	0.63	15.0
6	9.54	0.69	13.8
U_B **(experimental)**			13.52 m/s
U_B **(0D model)**			13.54 m/s

Table 5.3: Mean expansion speed estimation from the visualization images and comparison with 0D model.

5.3.7 Flame quenching distance

As extensively discussed in the chapter 2.2, when the flame approaches the walls it can extinguish for two reasons: the heat generated by the flame is lower than the heat losses through the surfaces, or due to destruction of active radicals by colliding with the wall. In the case of the pre-chamber flame approaching the orifices connecting both chambers, two situations may occur. If the heat rejection to the walls of the orifices is high enough to cool down the flame front, it will be extinguished before passing through these orifices. Therefore the discharge will be characterized mostly by fresh mixture or dissociated combustion products. Still combustion may be initiated in the main chamber by autoignition thanks to the high temperature of these combustion products. Instead, if the diameter is big enough, the flame will propagate through the orifices acting as direct ignition sources.

In order to evaluate the minimum diameter (d_{min}) needed for the flame to propagate, the following relation can be considered from applying the energy conservation equation between the flame front and the walls of the orifices:

$$\frac{\dot{Q}_{comb}}{\dot{Q}_{wall}} \approx \frac{U_B \cdot \delta_q}{\alpha} = Pe \tag{5.20}$$

where Pe is the Péclet number, $\dot{Q}_{comb}$ is the combustion heat, $\dot{Q}_{wall}$ is the heat losses through the walls, U_B is the combustion speed, δ_q is the quenching distance, and α is the thermal diffusivity function of the thermal conductivity, the specific heat at constant pressure and the gas density. Considering that the combustion speed near the wall reaches values of the laminar flame speed order, and that the flame thickness (δ_{flame}) is the ratio between the thermal diffusivity and the laminar flame speed, the Pe number can be written as:

$$Pe = \frac{\delta_q}{\delta_{flame}} \tag{5.21}$$

The flame quenching occurs when $\delta_q \approx \delta_{flame}$, thus the minimum quenching diameter can be estimated from an empirical correlation for cylindrical ducts [6]:

$$d_{min} \approx 1.54\delta_q \tag{5.22}$$

Taking into account that the average flame thickness during the pre-chamber combustion process is $50\mu m$, thus the minimum quenching diameters is around $77\mu m$. Remembering that the diameter of the orifices is 1.5mm, the flame propagation is ensured.

5.4 PC01 - Equivalence ratio influence

As previously stated, the results shared so far correspond to a single condition characterized by an fuel/air equivalence ratio of 0.5 in the main chamber and 1.1 in the pre-chamber at the time of the spark activation. In the current section, the same methodology has been extended to different values of the two aforementioned conditions, in the ranges of 0.3-0.5 for the main chamber and 0.9-1.1 for the pre-chamber.

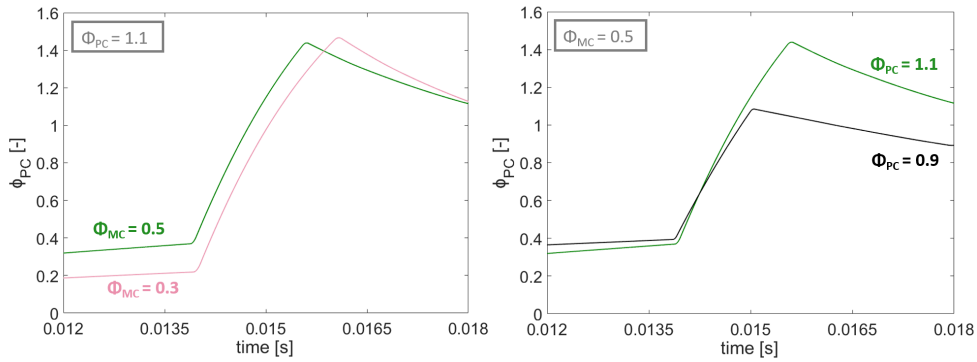

Figure 5.17: Time evolution of the pre-chamber equivalence ratio based on the 0D model

Figure 5.17 shows the evolution of the pre-chamber equivalence ratio for three of these cases. In the left side, two cases of pre-chamber equivalence ratio at 1.1 but different main chamber one are compared. As it can be seen, the case at $\phi_{MC} = 0.5$ starts at a higher level due to the filling process during the compression stroke. At approximately 14 ms since the beginning of the rapid compression (i.e. 87 mm piston position) the fuel injection in the pre-chamber starts, rapidly increasing the equivalence ratio from lean to rich conditions. Once the injection is finished, the pre-chamber filling continues until the desired equivalence ratio of 1.1 is reached at the spark activation time. In the right side of the figure, a similar evolution is seen, but in this case comparing the same main chamber equivalence ratio and two different targets

in the pre-chamber: 0.9 and 1.1. Therefore, the most significant difference is induced by the duration of the fuel injection inside the pre-chamber.

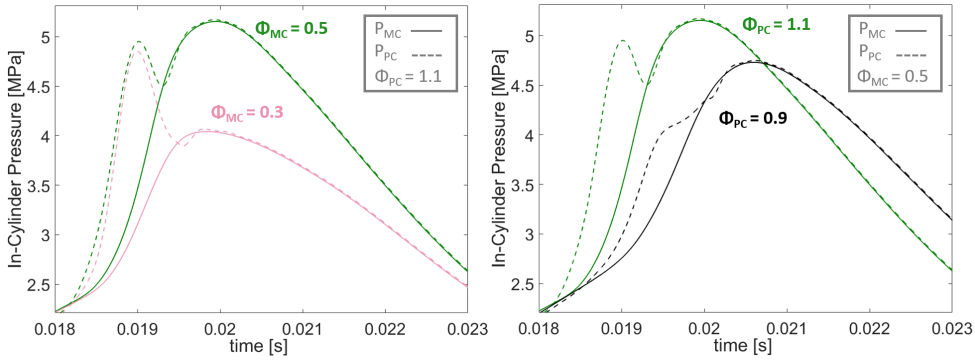

Figure 5.18: Instantaneous pressure evolution as a function of ϕ_{MC} (left) and ϕ_{PC} (right)

Figure 5.18 shows the results in terms of the main chamber and pre-chamber pressure for the same cases previously analysed. Again, in the left side the results for a same equivalence ratio in the pre-chamber (1.1) but a different one in the main chamber (0.3 vs 0.5) are compared. Since the equivalence ratio in the pre-chamber is the same, the pressure increase in the pre-chamber during the premixed combustion process is very similar, within the expected cycle-to-cycle dispersion of such kind of combustion. This can be seen as a partial confirmation of the little effect of the fuel injection in the pre-chamber on the turbulence intensity and, therefore, on the combustion characteristics: the lower value of ϕ_{MC} is compensated by a higher injected fuel mass and longer injection duration, but no significant effects seems visible from combustion perspective. Instead, the pressure evolution in the main chamber once the combustion starts as a consequence of the hot gases ejection is very different for the two cases compared. Since the tests have been performed at same initial pressure and temperature (0.15 MPa and 360 K), the total air mass trapped in the cylinder is the same, so a change in the main chamber equivalence ratio means a change not only in the combustion propagation, but also in the total fuel energy available. Therefore, a faster and higher pressure rise is produced due to the higher amount of energy released.

The right hand side of the figure compares same main chamber equivalence ratio (0.5) but different conditions in the pre-chamber (ϕ_{PC} 0.9 and 1.1). The smaller equivalence ratio produces a larger induction time for the flame kernel,

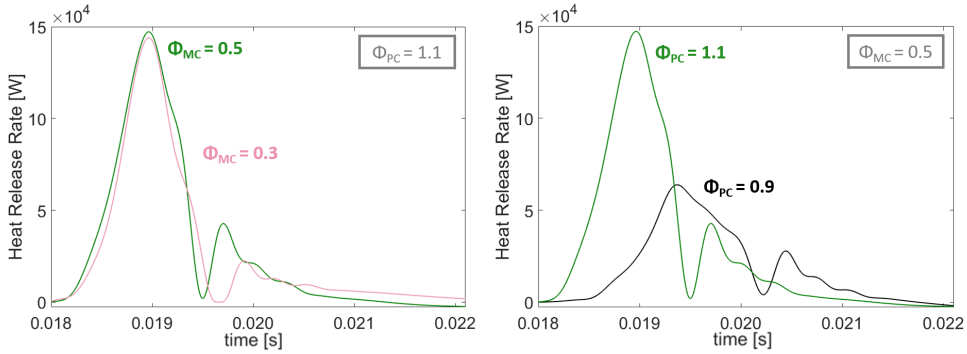

Figure 5.19: Heat release rate evolution as a function of ϕ_{MC} (left) and ϕ_{PC} (right)

leading to a longer delay between the spark discharge and the pressure rise inside the pre-chamber. Again, the lower energy available in the pre-chamber combined with the slower flame speed produced at lean mixture leads to a slower pressure rise. As a consequence, the ejection from the pre-chamber will start later and at lower velocities, impacting the combustion in the main chamber despite, in this case, the equivalence ratio (and therefore the fuel energy available) is the same.

Figure 5.19 shows the same data in terms of the heat release rate in the pre-chamber, computed according to the methodology described in section 5.2. The left chart confirms what was already discussed for figure 5.18: as long as the equivalence ratio in the pre-chamber is matched, the combustion evolution is practically equal, within the expected variability of the test. Only a slight difference is seen in the second combustion event observed after 19.5 ms. This second combustion is a consequence of a refilling processes from the main chamber, once the pressure increased due to the main combustion exceeds the one in the pre-chamber. In this case, since the pressure rise and gas composition vary as a consequence of the different ϕ_{MC}, a more intense second combustion event is seen for the case of $\phi_{MC} = 0.5$. However, when the equivalence ratio is reduced in the pre-chamber (right side) the deterioration in the flame speed coupled with the lower energy available produce a less intense heat release rate, driving the overall combustion performance.

Figures 5.20 and 5.21 help to better understand the statements asserted in the equivalence ratio analysis, showing some images from the main chamber combustion. Figure 5.20 compares the two cases under different main chamber

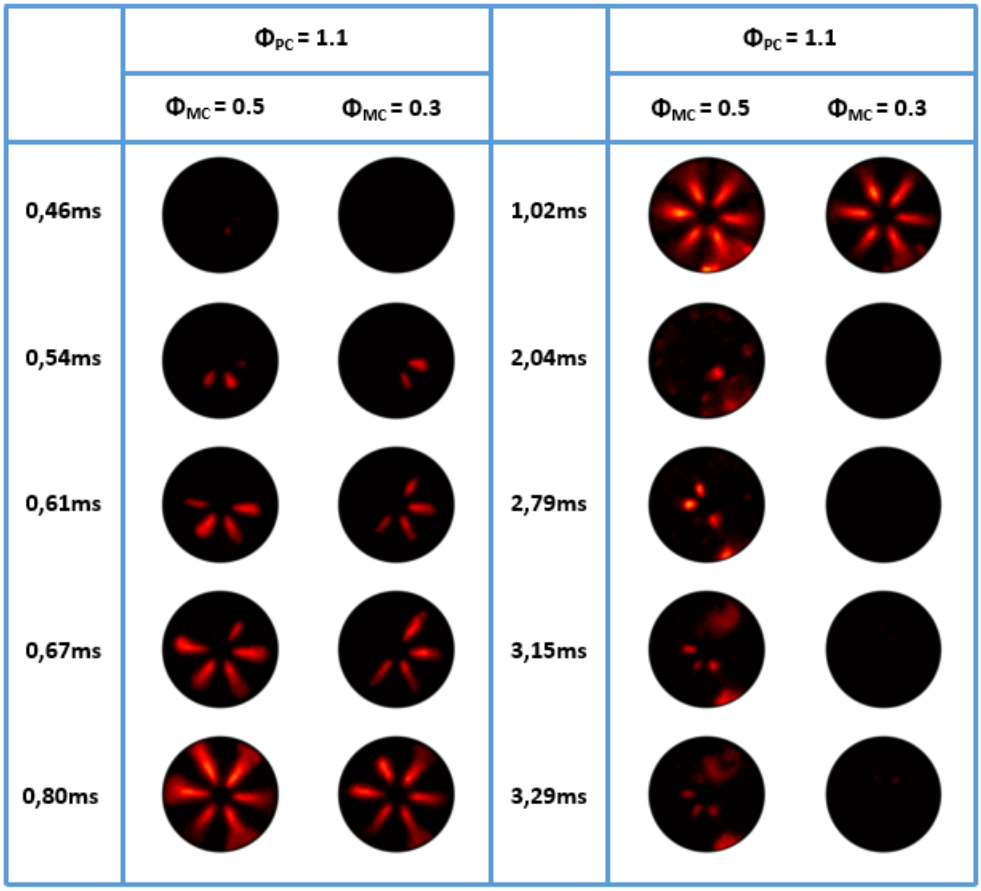

Figure 5.20: Main chamber combustion evolution as function of ϕ_{MC}.

equivalence ratio for several time steps after the spark discharge. The images confirm that as long as the pre-chamber equivalence ratio is well controlled, the first ejection induces a similar initial flame structure in the main chamber. On the contrary, as the combustion proceeds the influence of the equivalence ratio in the main chamber is more clear. The combustion is more capable to propagate in the region between the jets, leading to a larger flame area for the $\phi_{MC} = 0.5$ case (especially in the time range between 0.8 and 1 ms). This results in a higher energy released and pressure rise in the main chamber, as already discussed, inducing a stronger refilling of the pre-chamber with partially burned gases and inducing a stronger second ejection. This is seen in the images as a more intense light emission (at t = 2.79 ms), leading to a later

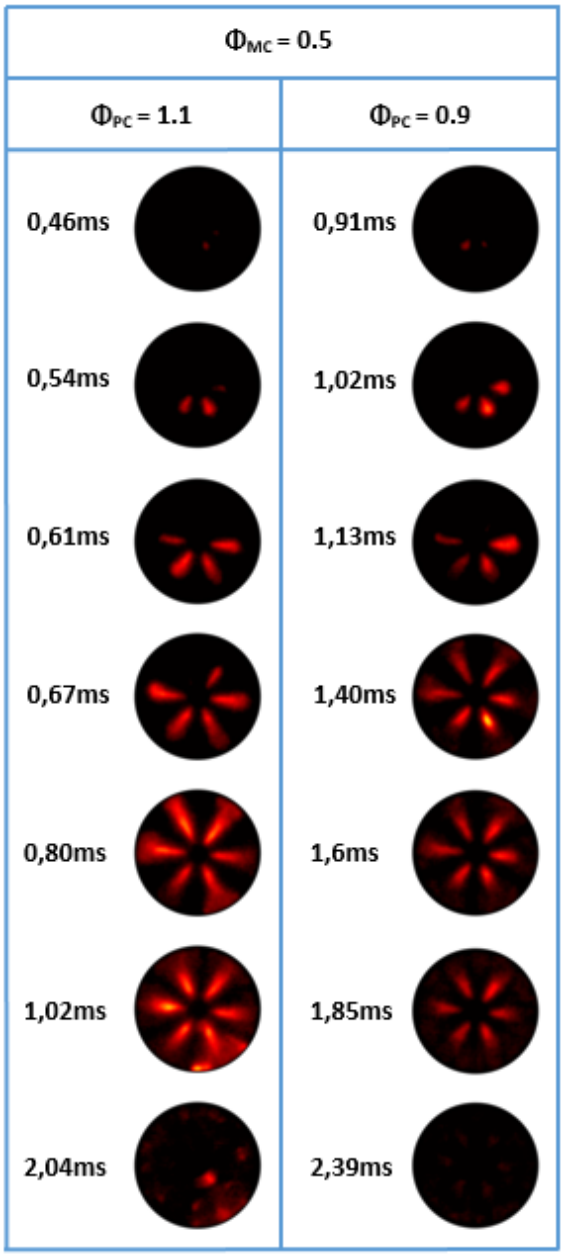

Figure 5.21: Main chamber combustion evolution as function of ϕ_{PC}.

low temperature auto-ignition of the end-gas mixture (t = 3.15 ms/3.29 ms). Figure 5.21 depicts the influence of the pre-chamber equivalence ratio under constant main chamber boundary conditions ($\phi_{MC} = 0.5$). The different induction time for the flame kernel growth is confirmed by the first picture, showing bigger elapsing time between the spark discharge and the start of the first ejection for the $\phi_{PC} = 0.9$ case. Following the temporal evolution, it can be seen that the decrease in the pre-chamber equivalence ratio leads to a performance drop, underlined by weaker light emission and longer overall combustion time.

Finally, the flame speed model can be applied to the different cases previously mentioned. These data is seen in terms of the mean expansion speed in table 5.4, again in comparison with the same value computed from the combustion visualization data.

ϕ_{MC} [-]	ϕ_{PC}[-]	$U_{B,OD}$ [m/s]	$U_{B,exp}$ [m/s]
0.5	1.1	13.54	13.52
0.5	0.9	7.85	7.6
0.3	1.1	12.82	12.89
0.3	0.9	7.22	7.17

Table 5.4: Mean expansion speed estimation as a function of ϕ_{MC} and ϕ_{PC}.

First, it can be seen how the 0D model properly catches the experimental values in the ranges covered during the experimental campaign. Then, the values obtained confirm the expectations from the pressure and heat release rate data: the mean gas speed is very similar when comparing the same equivalence ratio in the pre-chamber, but is severely deteriorated once this values falls from 1.1 to 0.9. This deterioration is coming from two sources: on the one hand, the lower equivalence ratio results in a lower pressure rise in the pre-chamber as a consequence of the lower energy available, reducing the mean gas speed; on the other hand, the smaller energy released results in a lower temperature inside the pre-chamber (for both burned and unburned zones) as combustion develops, affecting both laminar and turbulent speeds.

Finally, the flame speed results are represented in a classical Borghi diagram [30] thanks to the data extracted from the 0D turbulence model (Figure 5.22). In this diagram, the X-axis represents the ratio of Taylor's macroscale and the laminar flame thickness (estimated from the laminar flame speed and the mixture thermal diffusivity), while the Y-axis shows the ratio of the turbulence intensity and the laminar flame speed. The data is shown taking into account the temporal evolution up to the time at which the flame reaches

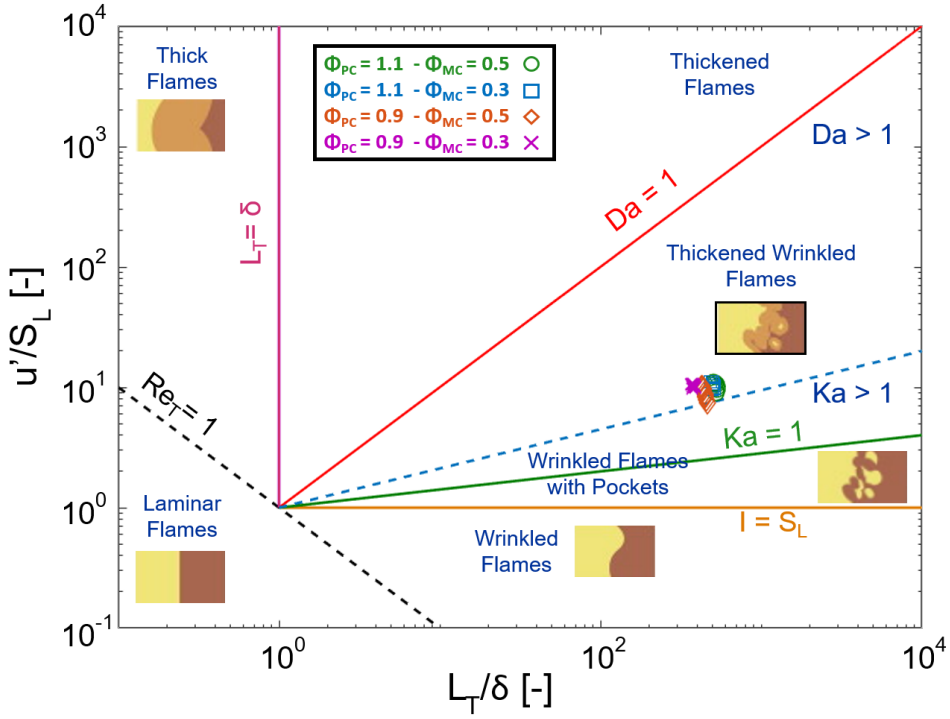

Figure 5.22: Borghi's diagram for turbulent flame regime a function of ϕ_{MC} and ϕ_{PC}

the pre-chamber orifices. It can be concluded that the combustion inside the pre-chamber is in the thickened wrinkled flames regime, which is typical for spark-ignition operation. However, the data shows that the values of Damköler number reached are in the range of 40, which combined with relatively high turbulence intensity, explain the very high flame speed ratio observed during the discussion of figure 5.15.

References

[1] Armas Vergel, Octavio. "Diagnóstico experimental del proceso de combustión en motores diesel de inyección directa". PhD thesis. Universitat Politècnica de València, 1998.

[2] Tinaut, FV. "Contribución al estudio del proceso de combustión en motores de encendido por compresión de inyección directa". PhD thesis. Tesis Doctoral, Universidad Politécnica de Valencia, Valencia, 1986.

[3] Payri, F, Molina, S, Martín, J, and Armas, O. "Influence of measurement errors and estimated parameters on combustion diagnosis". In: *Applied Thermal Engineering* 26.2-3 (2006), pp. 226–236.

[4] Yıldız, Melih and Çeper, Bilge Albayrak. "Zero-dimensional single zone engine modeling of an SI engine fuelled with methane and methane-hydrogen blend using single and double Wiebe Function: A comparative study". In: *International journal of hydrogen energy* 42.40 (2017), pp. 25756–25765.

[5] Heywood, John B. *Internal combustion engine fundamentals*. Mcgraw-hill, 1988.

[6] Turns, Stephen R et al. *Introduction to combustion*. Vol. 287. McGraw-Hill Companies, 1996.

[7] Jarquin, G, Polupan, G, and RODRÍGUEZ, J. "Cálculo de los productos de combustión empleando métodos numéricos". In: *Mecánica Computacional* 22 (2003), pp. 2442–2452.

[8] Benson, Rowland S. *Advanced engineering thermodynamics: thermodynamics and fluid mechanics series*. Elsevier, 2013.

[9] Barin, I. "Thermochemical data of pure substances VCH, Weinheim (1989)". In: (1989).

[10] Agarwal, A, Filipi, ZS, Assanis, DN, and Baker, DM. "Assessment of single-and two-zone turbulence formulations for quasi-dimensional modeling of spark-ignition engine combustion". In: *Combustion science and technology* 136.1-6 (1998), pp. 13–39.

[11] Woschni, Gerhard. "A universally applicable equation for the instantaneous heat transfer coefficient in the internal combustion engine". In: *SAE Technical Paper* (1967).

[12] López-Pintor, Darío. "Theoretical and experimental study on the autoignition phenomena of homogeneous reactive mixtures". PhD thesis. 2017.

[13] Bargende, Michael. *Ein Gleichungsansatz zur Berechnung der instationären Wandwärmeverluste im Hochdruckteil von Ottomotoren*. na, 1990.

[14] Chiodi, Marco and Bargende, Michael. "Improvement of engine heat-transfer calculation in the three-dimensional simulation using a phenomenological heat-transfer model". In: *SAE Technical Paper* (2001).

[15] Bardis, Konstantinos, Xu, Guoqing, Kyrtatos, Panagiotis, Wright, Yuri M, and Boulouchos, Konstantinos. "A zero dimensional turbulence and heat transfer phenomenological model for pre-chamber gas engines". In: *SAE Technical Paper* (2018).

[16] Huber, ML. "NIST thermophysical properties of hydrocarbon mixtures database (SUPERTRAPP)". In: *NIST Standard Reference Database* 4 (2003).

[17] Bjerkborn, Simon. "Development and validation of a turbulent flame propagation model". PhD thesis. 2011.

[18] Amirante, Riccardo, Distaso, Elia, Tamburrano, Paolo, and Reitz, Rolf D. "Laminar flame speed correlations for methane, ethane, propane and their mixtures, and natural gas and gasoline for spark-ignition engine simulations". In: *International Journal of Engine Research* 18.9 (2017), pp. 951–970.

[19] Burke, Eoin M, Güthe, Felix, and Monaghan, Rory FD. *A comparison of turbulent flame speed correlations for hydrocarbon fuels at elevated pressures*. 2016.

[20] Kolla, H, Rogerson, JW, and Swaminathan, N. "Validation of a turbulent flame speed model across combustion regimes". In: *Combustion Science and Technology* 182.3 (2010), pp. 284–308.

[21] Blint, Richard J. "The relationship of the laminar flame width to flame speed". In: *Combustion Science and Technology* 49.1-2 (1986), pp. 79–92.

[22] Kärrholm, Fabian Peng. *Numerical modelling of diesel spray injection, turbulence interaction and combustion*. Chalmers University of Technology Gothenburg, Sweden, 2008.

[23] Payri, Raul, Gimeno, Jaime, Peraza, Jesús, and Bazyn, Tim. "Spray/wall interaction analysis on an ECN single-hole injector at diesel-like conditions through Schlieren visualization." In: *Ilass Europe. 28th european conference on Liquid Atomization and Spray Systems*. Editorial Universitat Politècnica de València. 2017, pp. 200–207.

[24] Li, Jianwen, Matthews, Ronald D, Stanglmaier, Rudolf H, Roberts, Charles E, and Anderson, Richard W. "Further experiments on the effects of in-cylinder wall wetting on HC emissions from direct injection gasoline engines". In: *SAE transactions* (1999), pp. 2213–2224.

[25] Payri, Raul, Gimeno, Jaime, Bardi, Michele, and Plazas, Alejandro H. "Study liquid length penetration results obtained with a direct acting piezo electric injector". In: *Applied energy* 106 (2013), pp. 152–162.

[26] Gimeno, Jaime, Bracho, Gabriela, Martí-Aldaraví, Pedro, and Peraza, Jesús E. "Experimental study of the injection conditions influence over n-dodecane and diesel sprays with two ECN single-hole nozzles. Part I: Inert atmosphere". In: *Energy Conversion and Management* 126 (2016), pp. 1146–1156.

[27] Choi, Kwanhee, Lee, Hyungmin, Hwang, In Goo, Myung, Cha-Lee, and Park, Simsoo. "Effects of various intake valve timings and spark timings on combustion, cyclic THC and NO x emissions during cold start phase with idle operation in CVVT engine". In: *Journal of mechanical science and technology* 22.11 (2008), pp. 2254–2262.

[28] Corti, Enrico and Forte, Claudio. "Spark advance real-time optimization based on combustion analysis". In: *Journal of Engineering for Gas Turbines and Power* 133.9 (2011).

[29] Hosey, Richard J and Powell, JD. "Closed loop, knock adaptive spark timing control based on cylinder pressure". In: (1979).

[30] Borghi, R. *On the Structure and Morphology of Turbulent Premixed Flames. In: Casci C., Bruno C. (eds) Recent Advances in the Aerospace Sciences.* Springer (Boston, MA, USA), 1985.

Chapter 6

Pre-chamber spark ignition system: Geometry effects

6.1 Introduction

In this section, the results of the second experimental campaign are presented. The main objective is to shed light on how the pre-chamber number and orientation of the pre-chamber orifices affect the combustion developmenet. For the purpose, four different nozzles will be used to perform the tests in accordance to the characteristics explained in chapter 3. First of all, the impact of the tilted nozzle orifices against the standard configuration with straight holes will be depicted, comparing the baseline set-up PC01 with the PC02 geometry. Secondly, the influence of the diameter and number of orifices will be discussed, by means of PC03 (8 orifices) and PC04 (4 orifices) settings. Finally, the effects of an axial orifice are shown by comparing the PC02 (6 side orifices) with PC05 (1 axial and 6 side orifices). It is important to remember that the effect of other individual parameters on the PCSI system, such as the volume, general shape and cross-area of each pre-chamber, have been covered by other studies in the literature and are not considered for this research.

The analysis is presented according to the following structure: the general overview on the combustion process is shown by observing the main chamber and pre-chamber pressure trends. Then, the heat release rate and the combustion efficiency are evaluated. In addition, the 0D model results will be

combined with visualization tests and 3D CFD simulations (already discussed in chapter 4) with the aim of fully characterizing the related phenomena.

6.2 Straight nozzle PC01 vs tilted nozzle PC02

This paragraph is dedicated to the discussion of the results obtained with the basic PC01 and PC02 geometries under lean ($\phi_{MC} = 0.5$) and ultra-lean ($\phi_{MC} = 0.3$) cases, with the aim of evaluating the impact of the orifices position and direction on the combustion development. It is important to remember that the two geometries have the same orifice number and diameter, but a different distribution. For PC01 the symmetry axes of the orifices connect in a single central point, while for PC02 are displaced by a distance of 1.5mm (figure 3.5), thus allowing a rotary flow.

6.2.1 Main chamber lean case: $\phi_{MC} = 0.5$

In line with the methodology followed for the previous chapter, the comparison between the pressure curves in both chambers is shown in figure 6.1 for the lean case ($\phi_{MC} = 0.5$, $\phi_{PC} = 1.1$, $T_0 = 360$ K, $p_0 = 0.15$ MPa). The green lines refer to the basic PC01 geometry, the black lines indicate the PC02 set-up, and the red vertical line shows the spark activation time.

For the lean case, a slight advance is highlighted in terms of start of combustion for PC01 set-up. Furthermore, the pre-chamber pressure evolution shows the similar slope and pressure peaks. Conversely, several improvement are remarkable by observing the main chamber pressure trends, as much in the maximum achieved as in the subsequent expansion phase for PC02 case. Approximately around t = 0.02s, an evident change of the pressure slope is also recorded only for PC02 geometry. This event could be related to the auto-ignition of a residual gas spot and will be more easily explained with the help of the heat release rate and visualization analysis.

Figure 6.2 depicts the heat release rate comparison for the lean case. The continuous lines refers to the PC01 geometry, while the dashed ones are related to the PC02 setting. The green colour indicates the HRR for the main chamber, and the black one marks the HRR for the pre-chamber. Additionally, on the right side, the main chamber cumulative heat released divided by the theoretically available chemical energy is displayed (black line).

After the spark activation, the pre-chamber PC01 promotes a quicker heat release during the initial kernel growth. Subsequently, a faster development is shown for the pre-chamber PC02, which results in a steeper slope and a higher

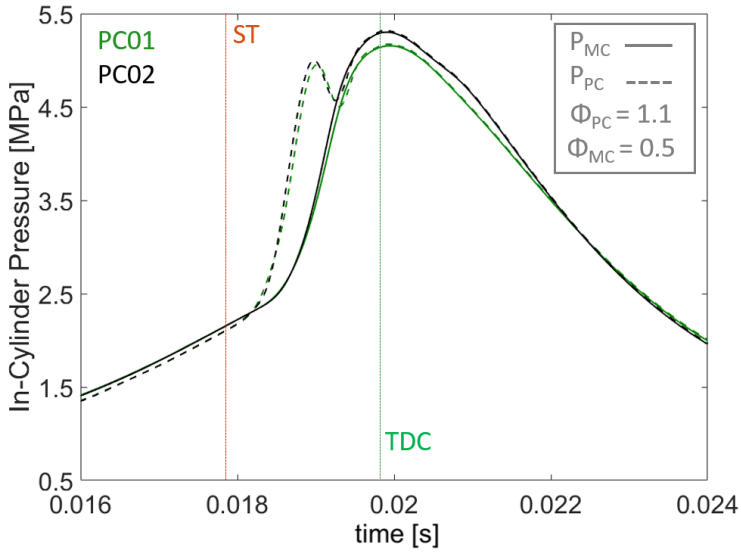

Figure 6.1: PC01 and PC02 comparison under lean ($\phi = 0.5$) conditions: Pressure evolution.

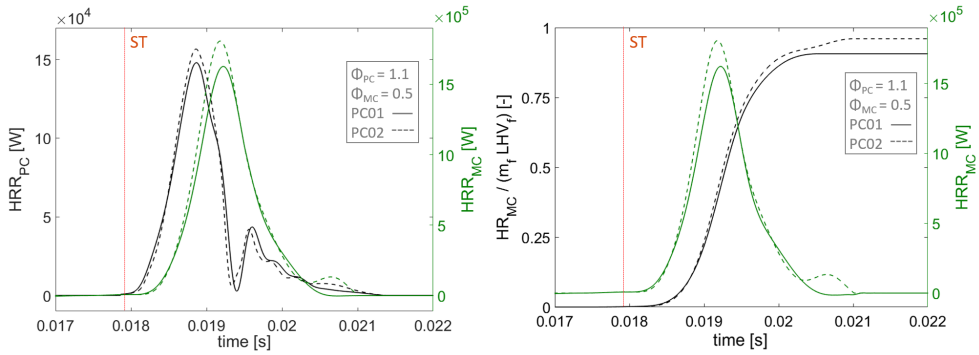

Figure 6.2: PC01 and PC02 comparison under lean ($\phi = 0.5$) conditions: Heat release rate evolution.

heat release peak. Finally, after the re-filling a similar trend is highlighted during the second ejection involving a more gradual and significantly lower heat release with comparison to the first ejection. About 0.4ms after the spark time, the interaction between the two chambers causes the start of

combustion in the main chamber due to the ejection of the first jets. As a direct consequence of the evolution of pre-chamber combustion, a higher heat release is shown for PC01 case also in the main chamber (green continuous line), during the early stage of combustion. Nevertheless, a faster heat release rate is observed in the subsequent combustion phases for PC02 geometry, while a similar slope is induced by the second jets ejection. Furthermore, during the start of the expansion stroke (t = 0.02 ms), a low-temperature auto-ignition of the mixture causes an additional heat release. Finally, the integral of the heat release rate divided by the available chemical energy associated with the mass of fuel injected shows an increase in combustion efficiency around 9%, achieved by using the swirled PC02 nozzle. It should be noted that the biggest difference on combustion efficiency is marked by the mixture auto-ignition phenomenon.

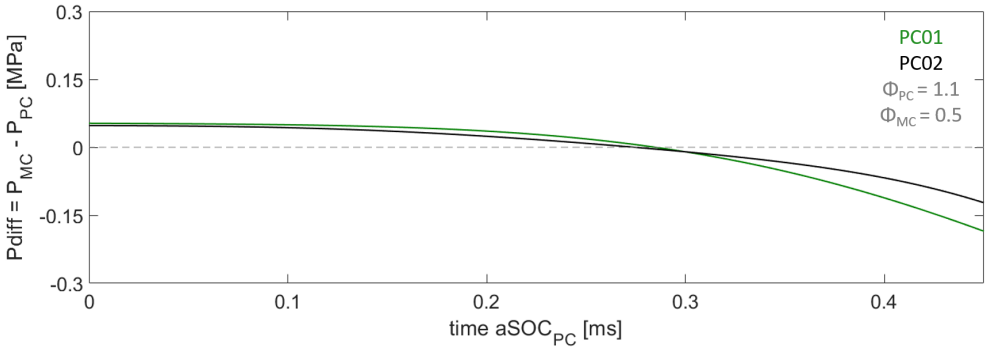

Figure 6.3: PC01 and PC02 comparison under lean (ϕ = 0.5) conditions: Pressure difference.

In order to understand the differences observed on combustion process, the local pre-chamber turbulence distribution, throughout the entire volume (previously discussed in chapter 4) is combined with the pressure difference displayed in figure 6.3. The green colour indicates the PC01 geometry, the black lines are related to the PC02 setting, and the X-axis refers to the time elapsed after the start of the pre-chamber combustion (t = 0ms). The graph refers to the early stages of combustion, in other words, until the first jets ejection into the main chamber. It is important to point out that in this time-frame the pressure difference is controlled only by the pre-chamber combustion event.

By investigating the structure of the fluid-dynamic field (figures 4.7) at the spark activation time (t = 0ms), the basic geometry generates a high local

turbulent kinetic energy close to the electrodes due to the direct collision of the jets entering the pre-chamber. Indeed, high turbulence enhance combustion in the early stages helping the flame kernel growth. Thus, the pressure difference increases faster for the PC01 layout, confirming a faster heat release rate depicted in picture 6.2.

In contrast, the geometric structure of the PC02 nozzle promotes a more homogeneous distribution of the TKE within the entire volume, at the expense of the spark plug spot. In addition, the macrovortex generated by the swirled flow also improves the homogeneity in terms of air/fuel mixture. Hence, this results in a slight slower early stage of combustion, followed by a significant advantage in terms of flame propagation in the later stages.

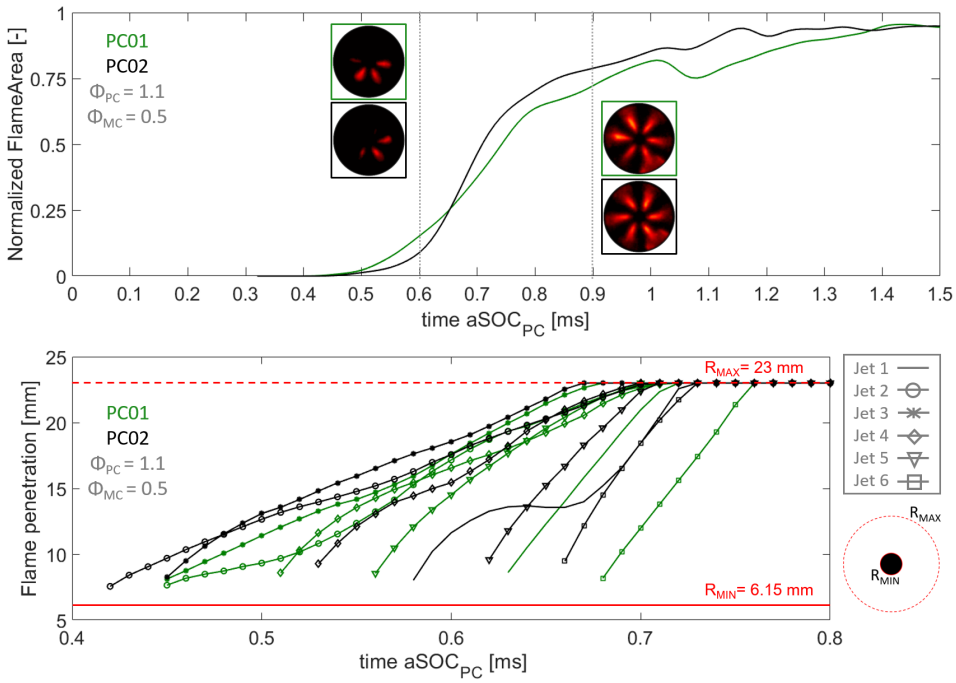

Figure 6.4: PC01 and PC02 comparison under lean ($\phi = 0.5$) conditions: Normalized Flame Area (Top). Jets penetration (Bottom).

0D model results, observed in figure 6.2, are combined with the images acquired from the direct combustion chamber visualization (as detailed in chapter chap:exptools) to shed light on the main chamber combustion evolution. Figure 6.4 (Top-side) depicts the flame propagation area, normalized

against the test window theoretically available. Furthermore, main chamber combustion pictures are displayed at time instants 0.6ms and 0.9 ms with green (PC01) and black (PC02) borders. The bottom part of the figure, is dedicated to the penetration of the jets into the combustion chamber, where R_{MIN} is the distance from the PC centre until the nozzle orifices (red continuous circle), and R_{MAX} is the quartz piston maximum radius (red dotted circle). Each line refers to a single spray, which in this case are 6 for both configurations. For all the subfigures, the green colour refers to PC01 geometry, while the black lines mark the PC02 case, and the X-axis refers to the time elapsed after the start of the pre-chamber combustion (t = 0ms).

In agreement with the heat release rate, the main chamber flame area is bigger for the baseline pre-chamber layout during the ealy stage of combustion. Then, as combustion progresses, two factors control the related phenomena: the improved flame propagation inside the pre-chamber for the PC02 configuration (discussed above) and the swirl motion induced in the main chamber linked to the tilted orientation. The first effect provides a strong ejection in the main chamber, intensifying the combustion associated with the mixture directly invested by the jets. The second one is decisive for the enhancement of combustion between adjacent sprays. The macro-vortex induced by the swirling flow outcoming the pre-chamber promotes mass and heat diffusion between the jets.

Concerning the bottom part of the figure, similar jets penetration is shown for both tests in terms of general evolution. Considering that the distance between the spark electrodes and the outlet section of each orifice is different due to the non-central location of the spark plug, around 0.2ms elapses between the ejection of the first jet (approximately t = 0.45ms) and the last one (approximately t = 0.65ms). In addition, the momentum flow of the first jets is considerably reduced compared to the last ones due to the lower pressure difference when the ejection begins. As combustion advances in the pre-chamber, the pressure difference between the two chambers increases, resulting in faster ejection speed of the last sprays. From the time derivative of the penetration, it is possible to estimate the tip average speed for each single jet. The maximum and minimum average value between the jets is summarized in the following table.

In conclusion, the two geometries show similar values inducing a significant variation between the fastest and the slowest jet.

	$JetSpeed_{max}$ [m/s]	$JetSpeed_{min}$ [m/s]
$PC01$	192	57
$PC02$	183	55

Table 6.1: Maximum and minimum average tip speed for PC01 and PC02 set-ups under lean conditions.

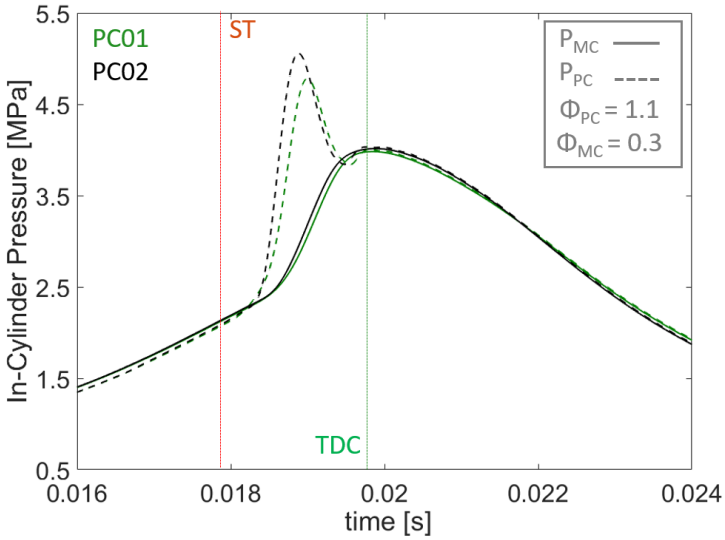

Figure 6.5: PC01 and PC02 comparison under-lean ($\phi = 0.3$) conditions: Pressure evolution.

6.2.2 Main chamber ultra-lean case $\phi_{MC} = 0.3$

The ultra-lean case ($\phi_{MC} = 0.3$, $\phi_{PC} = 1.1$, $T_0 = 360$ K, $p_0 = 0.15$ MPa) results are discussed in this paragraph using the identical format of the previous case, including colours, symbols, and lines.

Pressure trends, depicted in figure 6.5, confirms the the little difference in the start of combustion in both chambers. With respect to the pre-chamber combustion (dotted line), a steeper slope and a higher peak of pressure are shown for the PC02 case (black trend). Regarding the main chamber combustion, the advantages previously associated with PC02 layout for the $\phi_{MC} = 0.5$ case are confirmed, even if the pressure peak difference is reduced. Moreover, no evidence of the end-gas auto-ignition is observed during the expansion stroke, probably due to the lower average combustion temperature.

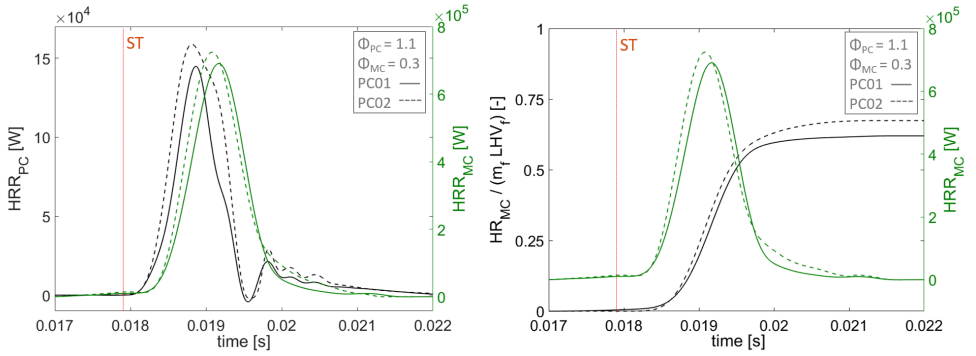

Figure 6.6: PC01 and PC02 comparison under ultra-lean ($\phi = 0.3$) conditions: Heat release rate evolution.

Figure 6.6 displays the heat release rate of the main and pre-chamber for the ultra-lean tests. The graph on the right includes the total heat released normalized respect to the total energy available (black lines). As much as the equivalence ratio is well controlled ($\phi_{PC} = 1.1$), the combustion develops as explained for the previous case. Hence, PC02 geometry exhibits a slower initial flame growth followed by a significantly acceleration of flame due to the fluid dynamic field characteristics induced by the incoming flow previously discussed.

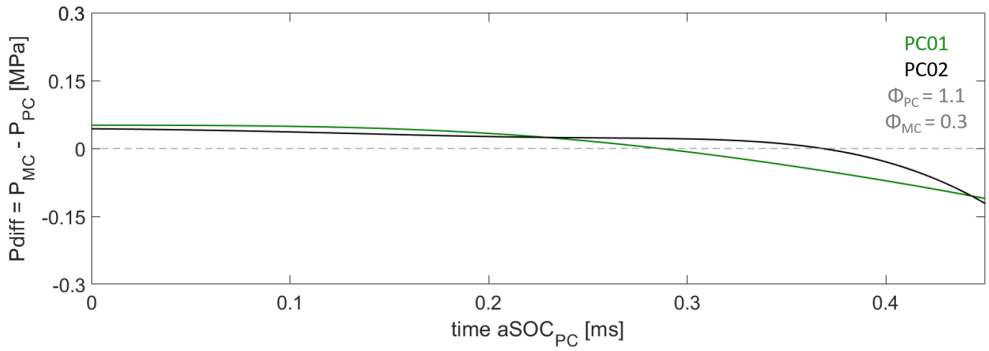

Figure 6.7: PC01 and PC02 comparison under ultra-lean ($\phi = 0.3$) conditions: Pressure difference.

The aforementioned hypothesis supports, also in this case, the behaviour of the pressure difference visible in figure 6.7. The pressure difference, over

the initial combustion phases, increases faster for PC01 setting. Despite, the benefits discussed for the main chamber combustion, are not significant under ultra-lean equivalence ratio as seen for the $\phi_{MC} = 0.5$ case. PC02 geometry exhibits a more intense and faster heat release from the beginning of combustion, which results in improvements of the efficiency of around 8%. An important difference is observed during the final stage of combustion where the second ejection has a stronger effect on the PC02 case.

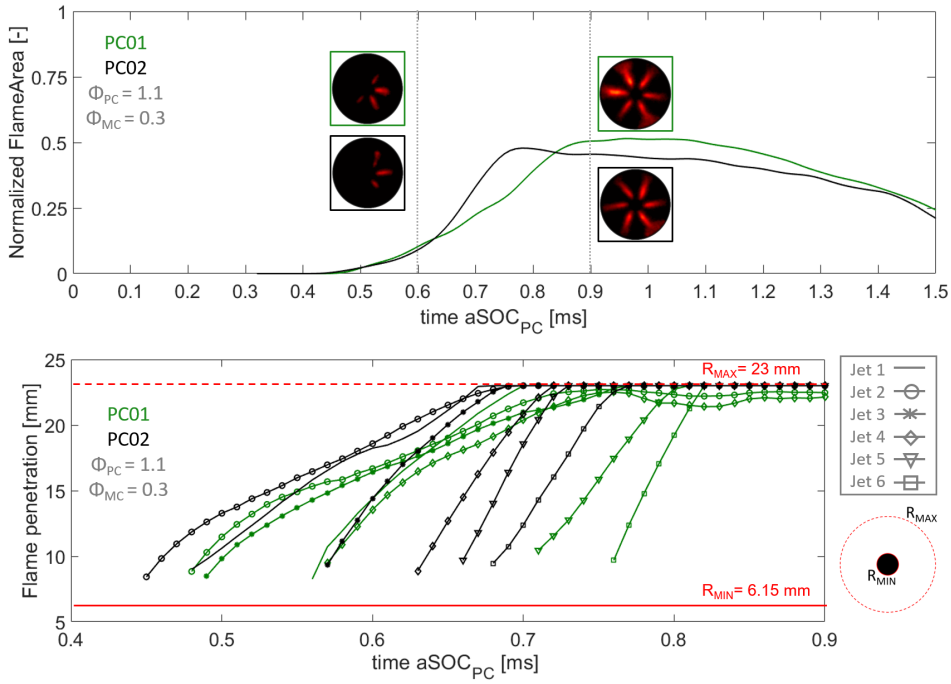

Figure 6.8: PC01 and PC02 comparison under ultra-lean ($\phi = 0.3$) conditions: Normalized Flame Area (Top). Jet penetration (Bottom).

For a deeper analysis, the figure 6.8 shows on top-side the evolution of the flame area normalized against the maximum theoretical value, and the jets penetration on the bottom part. The X- axis refers to the time elapsed after the PC ignition event. Observing the figure, an almost identical flame surface is detected in the early combustion stage until t = 0.6ms. In the following phases, a larger area is burnt by the flame in the case of PC02 geometry, until the curves finally conveyed to a similar value.

To complete the comparison between the two nozzle architectures, the penetration of the jets into the main chamber is discussed. Once again, a very similar general structure is observed between the two pre-chambers jets penetration. At local level, two results can be remarked: First,it is possible to note the faster ejection of the second group of jets(spray 4-5-6) for the swirled nozzle around t = 0.65ms. Second, the maximum and minimum tip speed ranges (depicted in table 6.2)are similar to the previous lean case.

	$JetSpeed_{max}$ [m/s]	$JetSpeed_{min}$ [m/s]
$PC01$	209	43
$PC02$	201	56

Table 6.2: Maximum and minimum average tip speed for PC01 and PC02 set-ups under ultra-lean conditions.

6.2.3 Summary

This section is dedicated to the summary of the main conclusions reached by comparing PC01 (straight orifices) with PC02 (tilted orifices) under lean and ultra-lean mixture conditions:

1. As stated in the previous chapter, the pre-chamber combustion is controlled by the internal conditions in terms of equivalence ratio and induced turbulence, independently from the thermochemical characteristics of the main chamber (lean or ultra-lean).

2. Straight orifices flow converging on the centre of the pre-chamber produces high local turbulence during the filling process, thus promoting a fast development and initial growth of the flame kernel in the early stage of combustion.

3. Swirled nozzle with tilted orifices promotes a more homogeneous distribution of turbulence and air/fuel mixture throughout the entire pre-chamber volume, resulting in a slower initial combustion phase followed by faster flame front propagation when compared with PC01 nozzle.

4. Slightly differences are detected in terms of the start of combustion for both the pre-chamber and the main chamber under lean and ultra-lean conditions.

5. Combustion in the main chamber is strongly influenced by the nozzle geometry. Thanks to the swirling flow generated by the asymmetrical ejection of the PC02 jets, the thermal and mass diffusion is improved between the adjacent sprays, thus enhancing the flame propagation. Leaner are the overall condition and bigger are the benefits of the induced rotating flow. Main chamber combustion efficiency achieve improvements around $8 - 9\%$ compared to the straight orifices configuration.

6. The main chamber equivalence ratio is a secondary influence factor in terms of jets penetration. This parameter is controlled by two factors: the chambers pressure difference and the main chamber density. The first one is the pushing force associated with the spray while the second is the resistance to jet penetration. By decreasing the equivalence ratio in the main chamber, the absolute value of the pressure difference will increase ($\Delta P_{\phi=0.5} < \Delta P_{\phi=0.3}$) resulting in a greater momentum provided to the jets. At the same time, the combustion temperature will also be lower, thus increasing the average density of the chamber ($\rho_{\phi=0.5} < \rho_{\phi=0.3}$). Analysing the average jet speed results, similar maximum and minimum values can be observed, independently from the main chamber equivalence ratio, resulting from the compensation of the two factors mentioned above.

6.3 Eight orifices tilted nozzle vs six tilted orifices nozzle: PC03 and PC02

In this sub-section the influence of the orifice numbers is assessed by analysing the PCSI system performance with PC02 and PC03 settings under lean ($\phi_{MC} = 0.5$) and ultra-lean ($\phi_{MC} = 0.3$) conditions. It is important to remember that by increasing the orifice numbers from 6 (PC02) to 8 (PC03), a reduction in the diameter is necessary to maintain an equal nozzle cross-area. Moreover, as a consequence of the previous analysis, the displacement of the orifices with respect to their symmetry axis is also included in the PC03 configuration (as detailed in chapter 3.2).

6.3.1 Main chamber lean case: $\phi_{MC} = 0.5$

Once again, combustion diagnostics starts with the analysis of the pressure evolution in both the main chamber (continuous line) and the pre-chamber (dotted line). The boundary conditions can be summarised as follows: ϕ_{PC}

= 1.1 and $\phi_{MC} = 0.5$ are the equivalence ratio at the spark time activation, while $T_0 = 360$ K, $p_0 = 0.15$ MPa are the starting temperature and pressure at the beginning of the compression stroke. The pink colour refers to the PC03 setup, while the black one indicates the pre-chamber PC02. The spark plug activation is visible due to the vertical red dashed line (figure 6.13).

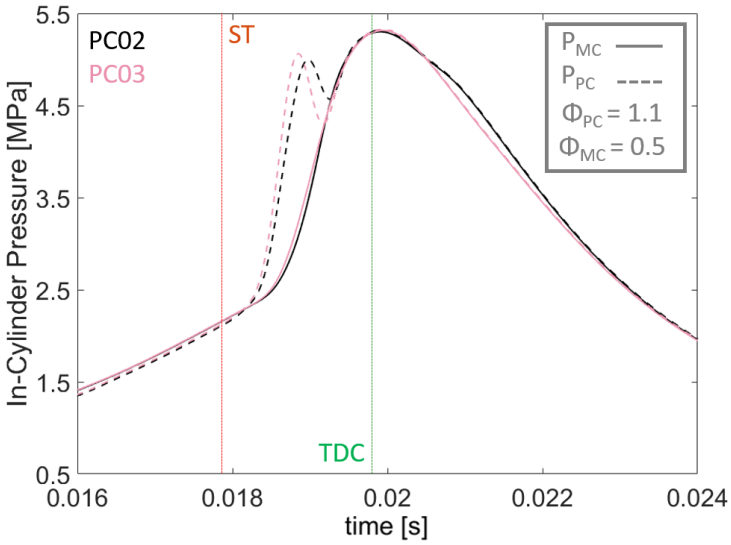

Figure 6.9: PC03 and PC02 comparison under lean ($\phi = 0.5$) conditions: Pressure evolution.

After the start of combustion, the pressure corresponding to the pre-chamber PC03 shows a steeper slope and slightly higher peak, which indicates a faster combustion development when compared to PC02. As a consequence, the flame approaches the orifice outlet section slightly earlier for the PC03 case beginning the first ejection, and thus the main chamber combustion event. In general terms, a very similar development can be observed both in the compression and in the expansion phases. The absence of low-temperature self-ignition, detected for the PC02 geometry at the instant t = 0.02s, is the main difference between the two trends.

Figure 6.10 depicts, on the left side, the main chamber and pre-chamber heat release rate for PC02 (dotted lines) and PC03 (continuous lines) settings. In addition the heat release, normalized against the chemical energy available, is presented on the right side (black colour).

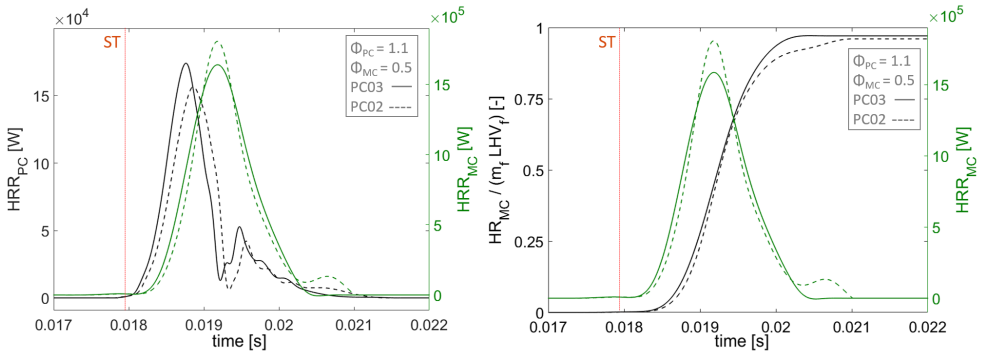

Figure 6.10: PC03 and PC02 comparison under lean ($\phi = 0.5$) conditions: Heat release rate evolution.

As observed for the pressure evolution, the heat release curve also indicates a faster and more intense combustion for the pre-chamber PC03 which allows earlier starts of ejection in the main chamber. Indeed the main chamber combustion is slightly advanced for PC03 case, even though the general trend is very similar for both setups as can be observed from the green slopes.

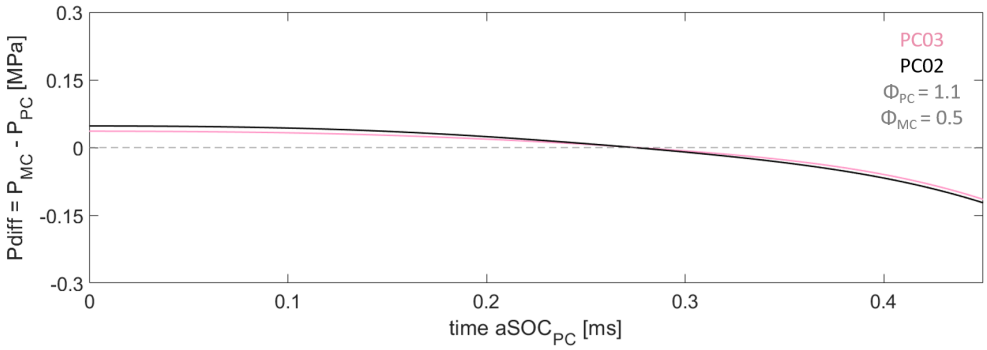

Figure 6.11: PC03 and PC02 comparison under lean ($\phi = 0.5$) conditions: Pressure difference.

The most relevant differences are observed in the peak and during the expansion phase, where there is no evidence of auto-ignition of the end-gas for the PC03. This advantage, linked to the better radial jets distribution, could be extremely important as the load in the combustion chamber increases

(linked to higher equivalence ratio or further boosting capabilities). Finally, the combustion efficiency (right side) converges to an almost identical value for both configurations, confirming a similar combustion evolution.

Looking closely at the first instants of combustion, by means of the pressure difference between main and pre-chamber showed in figure 6.11, it can be affirmed that both configurations promote a similar development during the early stages. This result is supported by the analysis of the turbulent field, which shows a similar structure in terms of direction and intensity within the two pre-chamber at the spark time (figure 4.19).

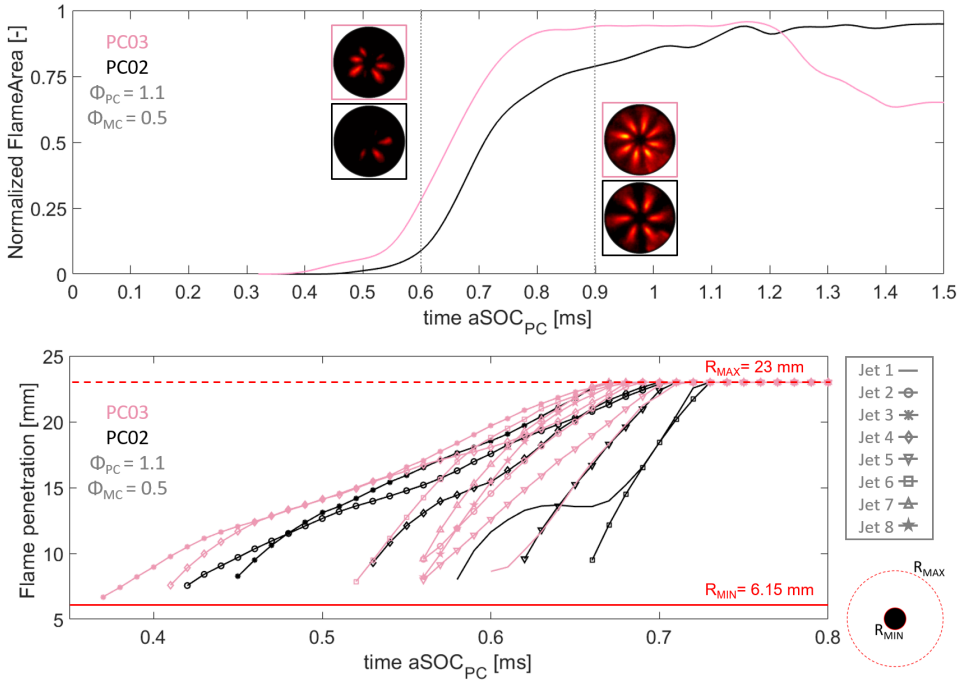

Figure 6.12: PC03 and PC02 comparison under lean ($\phi = 0.5$) conditions: Normalized Flame Area (Top). Pressure difference (Middle). Jets penetration (Bottom).

In order to deeper evaluate how the orifices number influence the main mixture combustion, the evolution of the flame surface (top side) and jets penetration (bottom side) is illustrated in figure 6.12. in addition, the pictures related to the time instants t=0.6ms and t=0.9ms, are shown in the graph.

The pink color point to the PC03 set-up, while the black colour regards the PC02 geometry. The x-axis is the elapsed time after the pre-chamber start of combustion.

In general terms, the rate of the burned area in the main chamber is a direct function of the orifices number. In detail, for PC03 case, during the initial steps of the process the burnt surface grows faster due to the increased number of sprays ejected into the combustion chamber. As can be seen from the combustion images and the flame penetration graph at instant t = 0.6ms, the ejection of seven out of eight jets has already started, which results in twice burnt surface for PC03 pre-chamber respect to the PC02 nozzle. As the pressure difference increases, the jet's speed rises, thus strongly enhancing the burnt surface as can be seen from the drastic change of the slopes. In the case of PC03 geometry, the higher orifices number allows to radially cover almost all the available volume, faster leading to the maximum burned area. On the other hand, for the PC02 case, the maximum flame area (around t = 1.2ms) is only achieved by means of the flame propagation between the adjacent sprays. Observing the last part of the black curve (from t = 0.75ms till the end), it is evident that this propagation process is slower compared to the torch jet ignition of the mixture directly invested by the ejection. Considering the final values of the combustion efficiency shown in figure 6.10, it can be concluded that both geometries ensure a correct cycle operation under lean conditions.

	$JetSpeed_{max}$ [m/s]	$JetSpeed_{min}$ [m/s]
$PC03$	150	42
$PC02$	183	55

Table 6.3: Maximum and minimum average tip speed for PC03 and PC02 set-ups under lean conditions.

Once again, the table 6.3 shows really high variation between the maximum and minimum average jets speed also for PC03. Additionally, slightly lower values are reported from the comparison with the PC02 case.

6.3.2 Main chamber lean case: $\phi_{MC} = 0.3$

The ultra-lean case ($\phi_{MC} = 0.3$, $\phi_{PC} = 1.1$, $T_0 = 360$ K, $p_0 = 0.15$ MPa) results are discussed in this section maintaining the identical format of the precedent case, including colours, symbols, and lines.

Picture 6.13 shows the comparison between PC02 (black lines) and PC03 (pink lines) nozzles in term of main and pre chambers pressure curves. The vertical dotted red line specifies the spark activation instant.

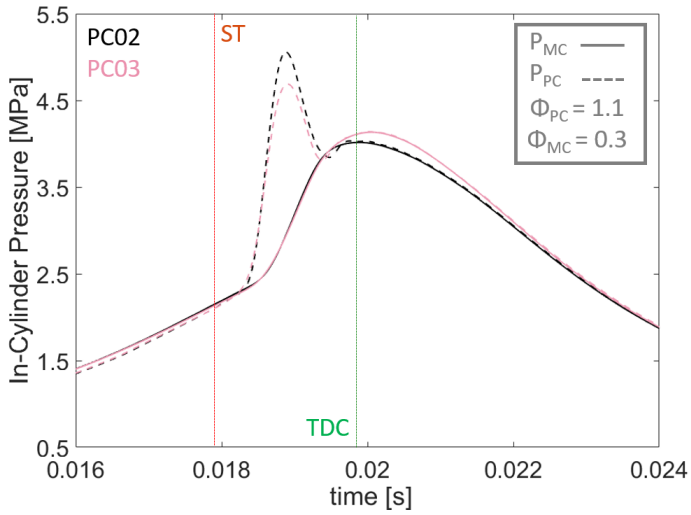

Figure 6.13: PC03 and PC02 comparison under lean ($\phi = 0.3$) conditions: Pressure evolution.

In general, pre-chamber combustion develops in a similar mode for both geometries. After the start of combustion, a similar increase occurs during the first part of combustion. Afterwards the two curves diverge, reaching higher peak value with setting PC02.

Despite the difference in the pre-chamber peak pressure, the effects of the increased orifice number are clearly beneficial in the case of main combustion. After a similar initial evolution (identical first pressure gradient), the PC03 curve shows higher pressure values over the entire expansion stroke. Figure 6.14 depicts the heat release rate for the main chamber (black lines) and pre-chamber (green line) on the left side. Moreover, the total heat released, respect to the fuel chemical energy, is shown on the right side (black trends). In line with the pressure evolution, a similar heat release rate is shown for both chambers during the first phase of combustion. Nevertheless, a slight advance of the start of combustion is remarkable for the PC03 geometry (perfectly in accordance with the lean case). Subsequently, the PC03 configuration promotes better combustion associated with higher heat release during the second part of combustion. A huge difference is observed when combustion is controlled by the second ejection, which induces an earlier change in the HRR slope for the PC03 case. As a result, a net increase in combustion efficiency of about 15% is shown in the right side of figure 6.14.

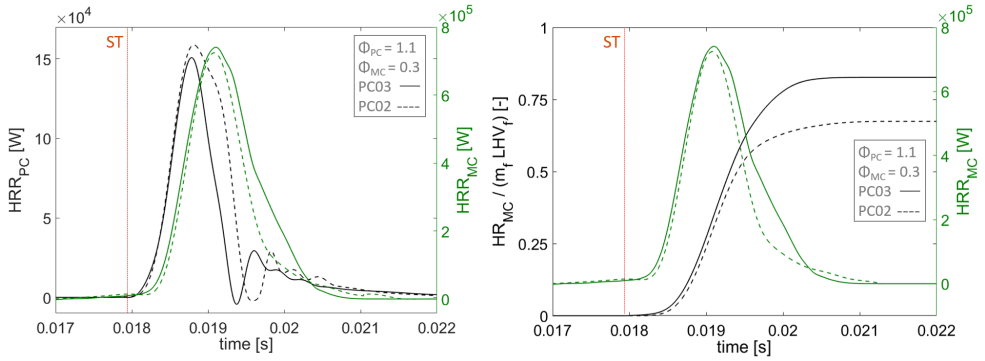

Figure 6.14: PC03 and PC02 comparison under ultra-lean ($\phi = 0.3$) conditions: Heat release rate evolution

Once again, to provide a better explanation of the results obtained by the 0D model, the pressure difference during early combustion phases (figure 6.15) with flame area and jets penetration trends (picture 6.16) are displayed below. The black colour indicates PC02 geometry, instead the pink one denotes PC03 pre-chamber. The X-axis is the elapsed time after the spark ignition.

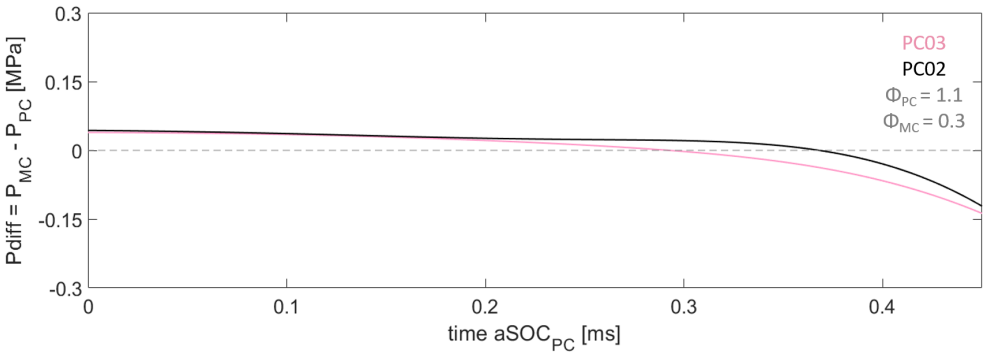

Figure 6.15: PC03 and PC02 comparison under ultra-lean ($\phi = 0.3$) conditions: Pressure difference.

The pressure difference confirms the advance in PC03 combustion (pink curve), resulting in a more rapid increase in pressure before the main chamber ejection begins. Although the slight difference, also in this case, the curves follow a very similar trend, according to 3D simulation results in terms of

turbulence field induced by the geometries. It is important to remind that, as shown in figures 4.19 and 4.20, the two geometries under examination develop a similar turbulent field at the moment of the spark release.

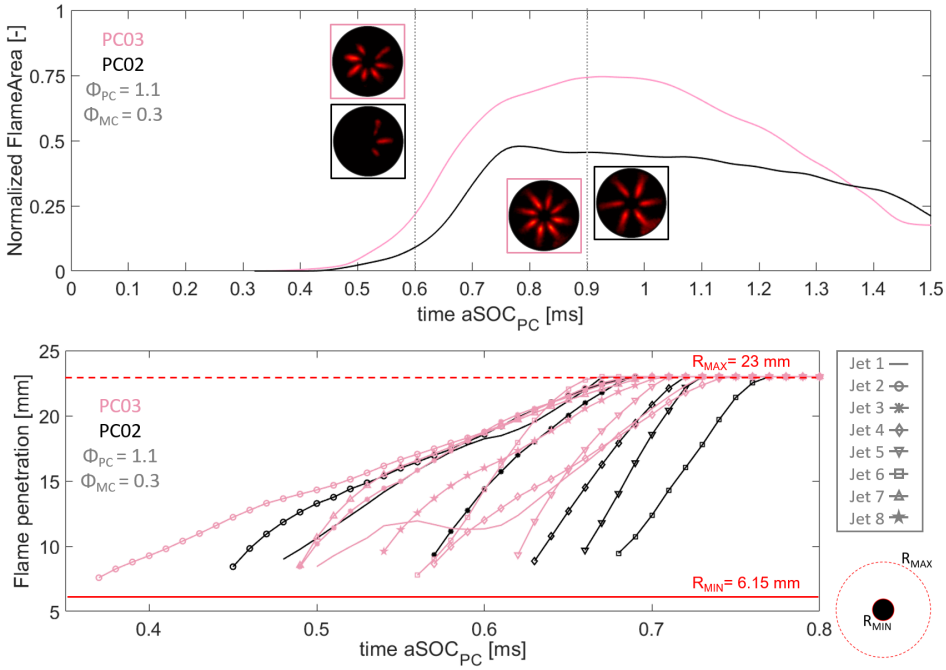

Figure 6.16: PC03 and PC02 comparison under ultra-lean ($\phi = 0.3$) conditions: Normalizel Flame Area (Top). Pressure difference (Bottom).

Regarding the flame surface evolution, three phases can be highlighted. At the beginning, as in the previous case, the ejection of a higher number of jets increases the surface covered by the flame for the PC03 case. At the instant t = 0.6ms, both the images and the jets penetration support the hypotheses stated. As combustion progresses, the pressure difference between the main and pre-chamber increases rapidly, producing a similar flame surface rate for both cases, until t = 0.75 ms. From this moment on, the phenomenon evolves in a different mode for the two configurations. The better radial distribution of the PC03 nozzle orifices enhances the mass and thermal diffusion between the adjacent jets. In contrast to the previous case ($\phi_{MC} = 0.5$), the worsened conditions in terms of the equivalence ratio, require a number of orifices capable of minimizing the adjacent space between sprays. In this way a better

flame propagation is guaranteed because of the increase in the local temperature of the unburned mixture between the ejected jets. As a result, the flame surface continues to increase for PC03 case reaching a higher value in comparison with the PC02 trend which is slowly decreasing as the momentum of the ejection dissipates.

	$JetSpeed_{max}$ [m/s]	$JetSpeed_{min}$ [m/s]
$PC03$	161	48
$PC02$	201	56

Table 6.4: Maximum and minimum average tip speed for PC03 and PC02 set-ups under ultra-lean conditions.

The values highlighted in the table 6.4, confirm what is stated for the lean case resulting in a slower maximum and minimum jet speed for the PC03.

6.3.3 Summary

In this section the most relevant conclusions, associated to the increase of the nozzle orifices number are summarized for lean and ultra-lean strategies:

1. In general terms, a very similar development of pre-chamber combustion occurs for both geometries, regardless of the mixture chemical conditions of the main chamber. A slight improvement in the initial combustion phases is highlighted for PC03 geometry, in accordance with a higher average value of the turbulent kinetic energy estimated by mean of 3D CFD simulations.

2. Regarding the main combustion, a similar results is achieved in terms of combustion efficiency for both settings under lean strategy. The thermochemical conditions in the main chamber are still able to guarantee the propagation of the flame between the adjacent sprays once all the jets are ejected. However, it is important to underline that the PC03 pre-chamber promotes the faster achievement of such efficiency as depicted by the evolution of the flame area. Finally, the absence of the end-gas auto-ignition suggest a possible combustion improvement when running the engine on higher load.

3. A significant improvement on combustion efficiency is detected for the pre-chamber PC03 in the case of ultra-lean combustion. The higher number of orifices, reduces the volume between the adjacent jets ejected

in the main chamber, thus enhancing the mass and heat diffusion under extreme ultra-lean mixture conditions during the late stages of combustion.

4. Earlier ejection of the jets are observed in PC03 case, comparing the general trends for both mixture conditions. Locally, the ejection speed of the first jets is slower than the last ones, subjected to a stronger pressure difference.

6.4 Four orifices tilted nozzle vs six tilted orifices nozzle: PC04 and PC02

In this sub-chapter, the analysis of the orifices number influence on combustion is extended by evaluating the PC04 performance under lean ($\phi_{MC} = 0.5$) and ultra-lean ($\phi_{MC} = 0.3$) conditions. As already detailed in figure 3.4, the PC04 layout is composed of 4 orifices with a diameter of 1.8 mm in order to do not change the cross-section between different set-ups.

6.4.1 Main chamber lean case: $\phi_{MC} = 0.5$

The pressure evolution in both the main chamber (continuous line) and the pre-chamber (dotted line) is evaluated in figure 6.17. The test inlet parameters are highlighted as follows: $\phi_{PC} = 1.1$, and $\phi_{MC} = 0.5$ are the equivalence ratio at the pre-chamber start of combustion, while $T_0 = 360$ K, $p_0 = 0.15$ MPa are the temperature and pressure at the beginning of the cycle. The blue colour is referred to the PC04 setup, while the black one describes the pre-chamber PC02. The ignition time is shown with a vertical red dotted line (fig. 6.17).

In general line, the pressure trends are very similar during the first part of the combustion, and clearly different in terms of peak and slope during the later stages. In detail, the PC04 configuration provides a better start of combustion both in the pre-chamber and the main chamber. Afterwards, the system demonstrates its limits showing a lower maximum peak pressure, a clear indication of a combustion deterioration. Moreover, for this geometry no evidence of the auto-ignition is detected around t = 0.02s as in the PC02 case.

In order to investigate the details of the combustion development, the heat release rate assessment is carried out. Figure 6.18 shows, on the left side, the main chamber and pre-chamber heat release rate for PC02 (dashed curve) and PC04 (continuous lines) configurations. Furthermore, the heat release,

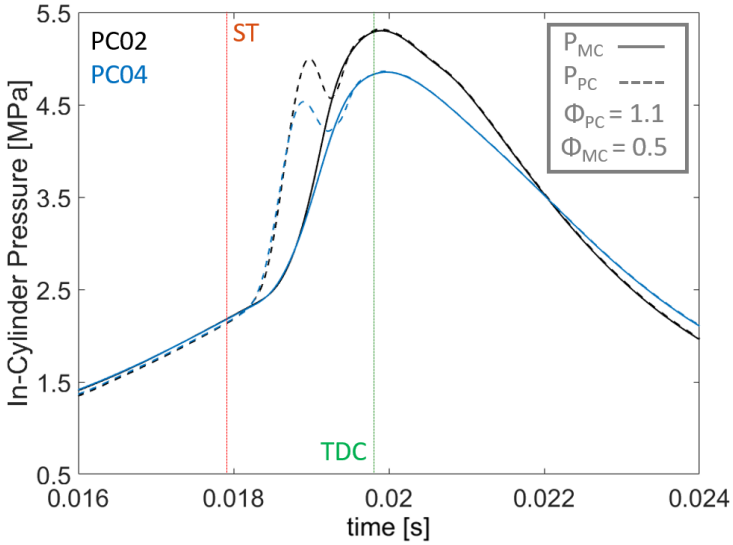

Figure 6.17: PC04 and PC02 comparison under lean ($\phi = 0.5$) conditions: Pressure evolution.

normalized against the chemical energy available, is displayed on the right side (black lines).

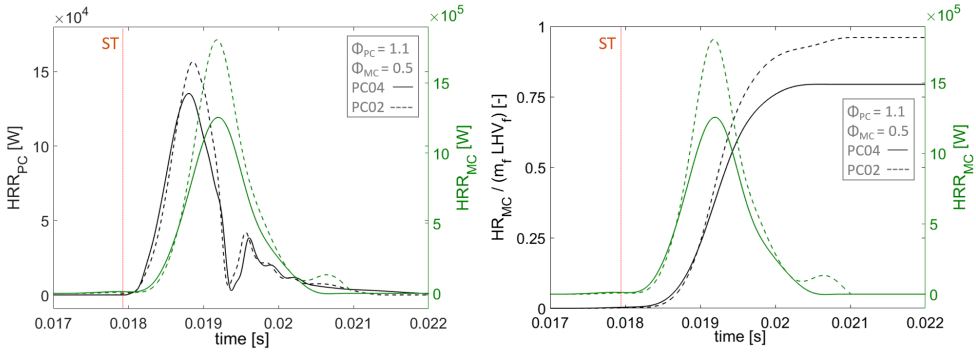

Figure 6.18: PC04 and PC02 comparison under lean ($\phi = 0.5$) conditions: Heat release rate evolution.

Observing the early stages of combustion, a faster heat release rate is depicted for PC04, resulting in better start of combustion also in the main

chamber. Nevertheless, in the subsequent combustion phases, both in the pre-chamber and in the main chamber there is a worsening of the performance which results in an evident efficiency losses shown by the graph on the right.

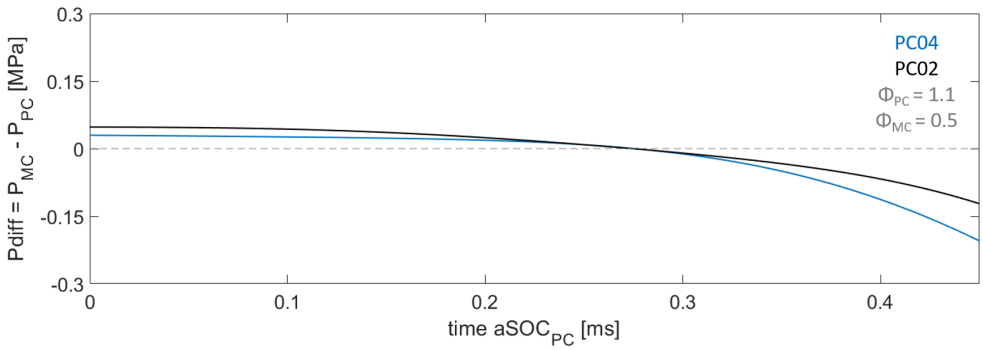

Figure 6.19: PC04 and PC02 comparison under lean ($\phi = 0.5$) conditions: Pressure difference.

Therefore, to justified the observed differences, the 3D turbulence analysis is combined with the 0D model achievements. In the next figure 6.19, the pressure difference of the early stage of combustion is illustrated. Despite a similar start of combustion, on the final part of the graph (t = 0.4ms) there is an evident difference which indicates a better development of combustion in PC04 (blue color). This result fits completely with the analysis of the turbulent field detailed in chapter 4. The PC04 configuration, through a perpendicular collision between the entering jets (figure 4.20), promotes a high turbulent kinetic intensity throughout the pre-chamber central area (figure 4.19). Hence, higher turbulence helps to spread the flame front enhancing the propagation at the beginning of combustion.

Finally, to analyze the phenomenon in terms of main chamber mixture combustion, the normalized flame surface and the jets penetration are shown in figure 6.20. Moreover, combustion pictures are illustrated in two specific time instants (t = 0.6ms and t = 0.9ms). The blue color marks the PC04 curves, while the black one represent the PC02 case. The x-axis refers to the elapsed time after the spark ignition.

As a general conclusion, the PC04 geometry is not able to guarantee the complete combustion of the mixture in the main chamber, as evidenced by the figures 6.18. Once again, three different phases in the growth of the flame surface can be highlighted. During the early combustion instants, the combined

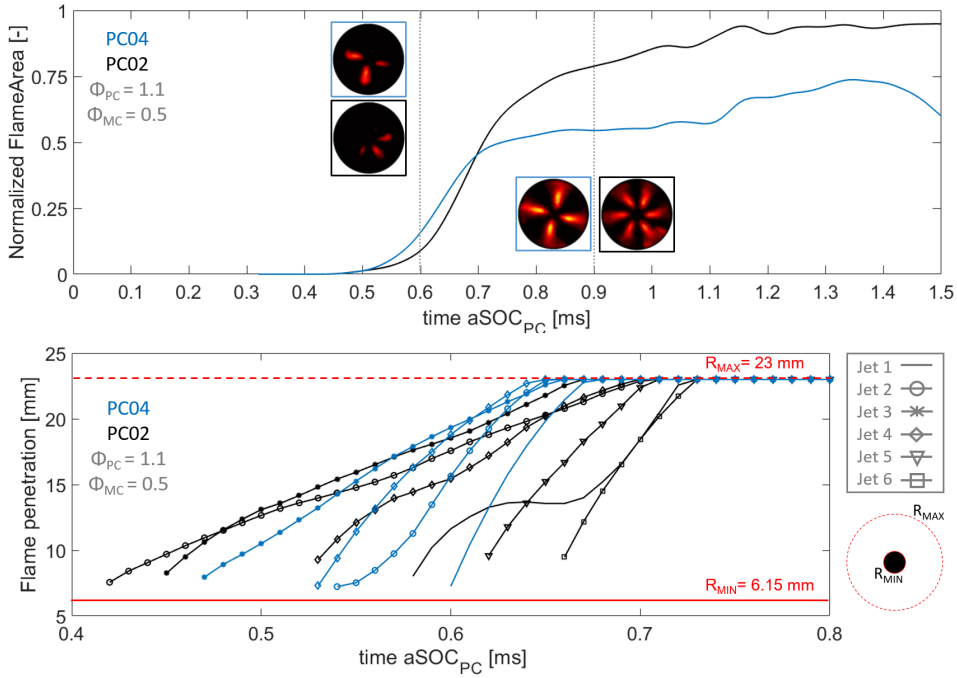

Figure 6.20: PC04 and PC02 comparison under lean ($\phi = 0.5$) conditions: Normalized Flame Area (Top). Jets penetration (Bottom).

effect between the faster pre-chamber combustion and bigger orifices diameter enhances the flame area for PC04 case. Then, once all the jets enter into the main chamber, a faster flame area increment is shown for the PC02 setting, achieving higher value as combustion develops. Finally, when the propagation between adjacent sprays plays a more important role than the torch jet ignition mode (after the flame approaches the walls), the PC04 is not able to accomplish a complete combustion process. The reduced orifices number, one each 90° distributed around the nozzle, is not sufficient to ensure the complete flame propagation between the adjacent jets. Inevitably, a decrease of combustion efficiency around 20% is observed (right side of figure 6.18).

The maximum and minimum tip average speed are also depicted for the PC04 geometry. Both geometries show similar maximum values, while the minimum is higher for the PC04 due to the bigger pressure difference (between MC and PC) associated with the first jets ejected.

	$JetSpeed_{max}$ [m/s]	$JetSpeed_{min}$ [m/s]
$PC04$	190	77
$PC02$	183	55

Table 6.5: Maximum and minimum average tip speed for PC04 and PC02 set-ups under lean conditions.

6.4.2 Main chamber ultra-lean case: $\phi_{MC} = 0.3$

The ultra-lean test results ($\phi_{MC} = 0.3$, $\phi_{PC} = 1.1$, $T_0 = 360$ K, $p_0 = 0.15$ MPa) are evaluated in this section using the identical format as the precedent case, including colours, symbols, and lines.

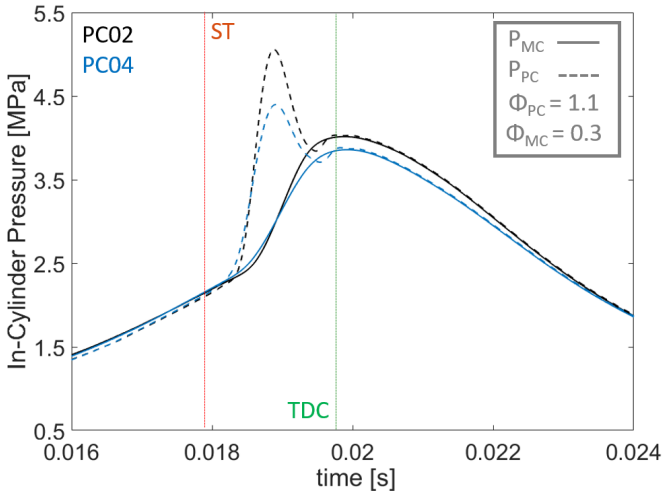

Figure 6.21: PC04 and PC02 comparison under ultra-lean ($\phi = 0.3$) conditions: Pressure evolution.

The comparison between PC04 (blue lines) and PC02 (black lines) nozzles performance in term of main and pre chambers pressure curves is shown in figure 6.21. The spark activation instant is highlighted with the red vertical line.

In this case, the deviations between both designs in terms of the pressure evolution are even more evident along all the combustion process. First of all, a clear advance in the start of combustion for both main chamber and pre-chamber is observed for the PC04 case. Moreover, the lower slope and

pressure peak indicate that even under these boundary conditions the PC04 pre-chamber suffers a deterioration of combustion.

The heat released rate, shown in figure 6.22, confirms what has already been stated by the analysis of the pressure signals. A faster initial phase with higher heat released is produced by the PC04 geometry (continuous lines) for both pre-chamber (black curves) and main chamber (green traces). Nevertheless, as time progresses, combustion burning rate slows down leading to a lower peak in both chambers. It is important to underline the almost total absence of propagation during the burning phase controlled by the second ejection for the PC04 pre-chamber. Unlike the lean case where this part is still appreciable, the ultra-lean mixture conditions lead to an almost imperceptible change in the final HRR gradient. The cumulative heat released demonstrates once again a significant efficiency loss due to the distribution of pre-chamber orifices (already discussed for the lean case).

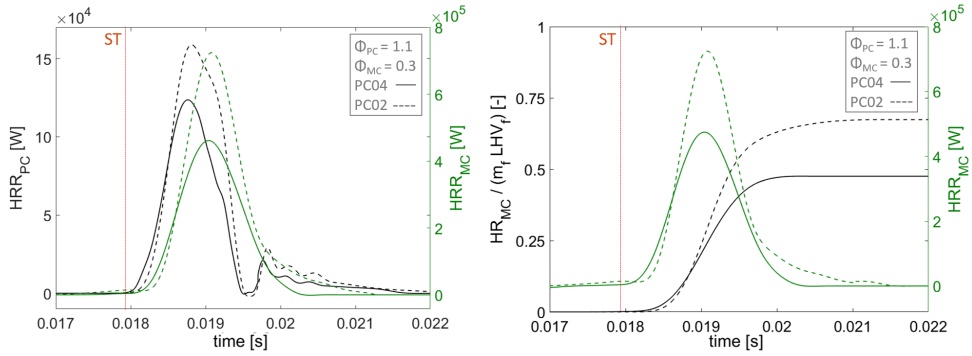

Figure 6.22: PC04 and PC02 comparison under ultra-lean ($\phi = 0.3$) conditions: Heat release rate evolution

Hence, the pressure difference during early combustion phases (figure 6.23) emphasizes the faster flame kernel growth for the PC04 (blue line). Once again, this result accords with the hypotheses formulated through the study of the pre-chamber turbulent field (detailed in chapter 4). The higher turbulent kinetic energy, observed on the central part of the pre-chamber volume (figure 4.19), promotes a faster combustion development at the beginning of combustion.

Finally, the jets penetration and the normalized flame area are illustrated in figure 6.24. In addition, combustion pictures are shown in two specific time instants (t = 0.6ms and t = 0.9ms). The blue color marks the PC04 curves,

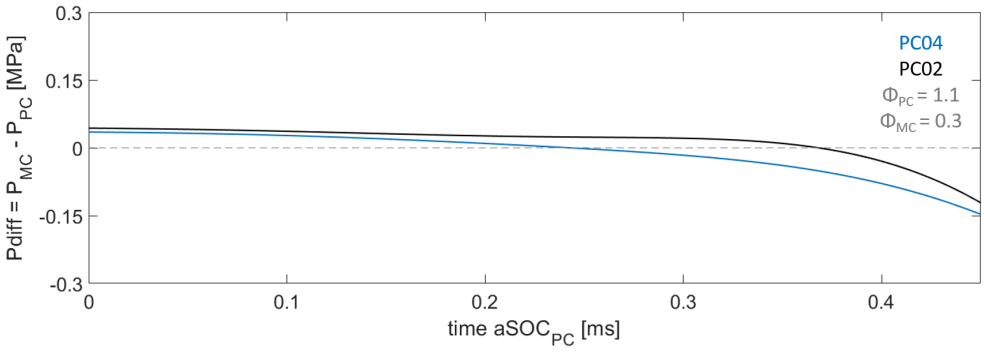

Figure 6.23: PC04 and PC02 comparison under ultra-lean ($\phi = 0.3$) conditions: Pressure difference.

while the black one refers to the PC02 case. The x-axis marks the elapsed time after the spark plug activation.

As observed for the lean case, during the initial phases of combustion the PC04 geometry promotes a faster flame surface rate leading to a bigger value at the time instant t = 0.6ms. Nevertheless, the orifice number reduction produces several negative aspects as observed for the previous geometry comparison. First of all, the torch ignition effect is reduced, as a smaller volume of the mixture is directly impacted by the highly reactive jets. Furthermore, increase the volume between adjacent sprays involves significant worsening of the flame propagation, already challenging due to the extreme conditions of the equivalence ratio. Indeed, in the later stages, once the flame propagation mode controls the surface growth, the PC04 geometry shows relevant limits to the enhancement of combustion. Finally, in the lower part of the figure 6.24 it can be observed that the four jets corresponding to the PC04 geometry penetrate in a similar mode as the first three PC02 jets.

	$JetSpeed_{max}$ [m/s]	$JetSpeed_{min}$ [m/s]
$PC04$	161	48
$PC02$	108	72

Table 6.6: Maximum and minimum average tip speed for PC04 and PC02 set-ups under ultra-lean conditions.

Concluding, the jet tip average velocity is compared for the faster and slower jet (table 6.6). In this case the maximum and minimum values diverge from the PC02, evidencing an almost similar behavior for all the ejected jets.

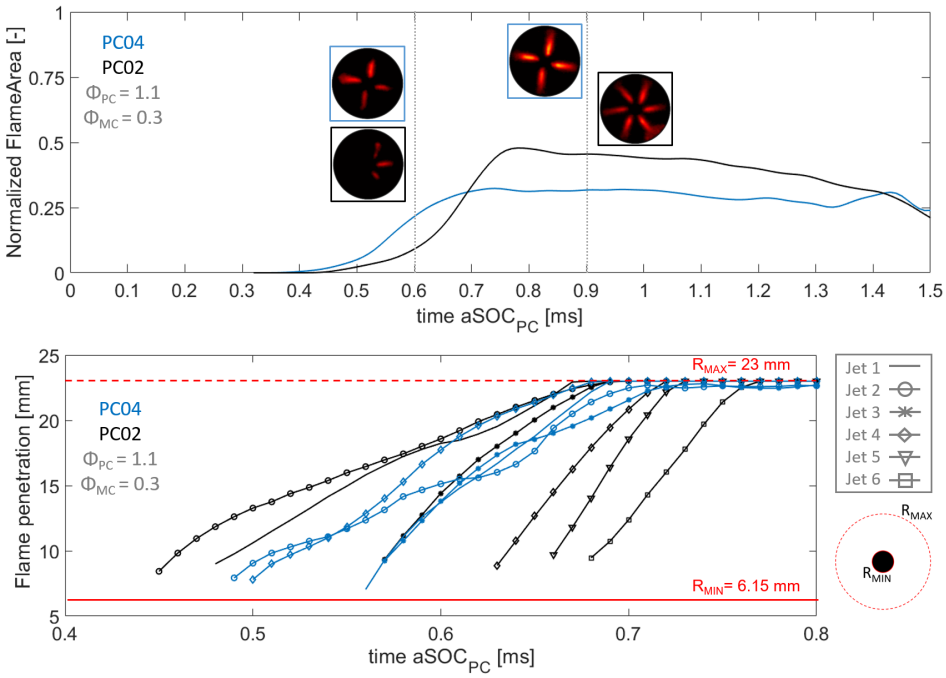

Figure 6.24: PC04 and PC02 comparison under ultra-lean ($\phi = 0.3$) conditions: Normalized Flame Area (Top). Jets penetration (Bottom).

6.4.3 Summary

In the last paragraph, the most relevant conclusions, associated to the decrease of the nozzle orifices number are summarized for lean and ultra-lean operations:

1. Concerning the pre-chamber, a slight advance in the start of combustion is induced by the PC04 set-up. In accordance with a higher average value of the turbulent kinetic energy and the local distribution (predicted by mean of 3D CFD simulations) the PC04 geometry promotes improvement during the initial combustion phases, regardless the equivalence ratio of the main chamber mixture. As combustion progresses, better results are highlighted for the PC02 setting.

2. Regarding the main combustion, the same conclusions can be pointed out in terms of combustion efficiency under both lean and ultra-lean

strategies. The PC04 setting is not able to promote a complete combustion event. As long as the combustion is controlled by torch jet ignition mode, the flame area graph illustrates a proper development of the process. Once the flame propagation between the sprays assumes the control over the phenomenon, the geometrical shape of the nozzle is not able to induce the correct combustion spreading. Indeed, high efficiency losses are observed in the main chamber combustion.

3. Later ejection of the jets are observed in PC04 case, comparing the general trends for both mixture conditions assessed.

6.5 Turbulent flame speed: all pre-chambers

Previously, in the chapter 5, the influence of the mixture equivalence ratio on the turbulent flame speed was evaluated by means of Kolla's correlation for the baseline pre-chamber. In this section, the influence of pre-chamber nozzle geometry on the turbulent flame velocity is discussed. Hence, as depicted in the chapter 4, the orifices number, diameter and distribution affect the turbulence field induced by the pre-chamber filling process.

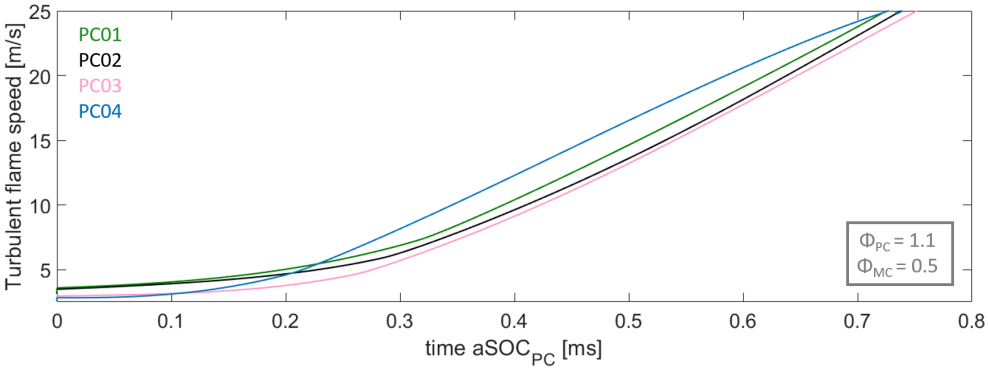

Figure 6.25: Turbulent flame speed evolution for all the pre-chamber geometries.

Figure 6.25 shows the time evolution of the turbulent flame speed from the spark ignition instant (t = 0ms) for the different pre-chamber geometries under lean conditions ($\phi_{PC} = 1.1$, $\phi_{MC} = 0.5$, $T_0 = 360$ K, $p_0 = 0.15$ MPa). The green colour refers to the PC01 case, the back line indicates the PC02 geometry, the pink colour is related to the PC03 setting, and the PC04 trend is marked in blue.

In general, the trends confirm what was observed for the pre-chamber heat release rate comparison. As a result of the stronger local turbulence conditions (close the spark plug electrodes), the pre-chamber number 1 (straight nozzle) and 4 (90° impact angle between jets) promote the higher acceleration of the flame front during the first phases of combustion. As combustion develops, the better homogeneity conditions of the pre-chamber PC02 and PC03 promote the convergence towards similar values for all the geometries considered.

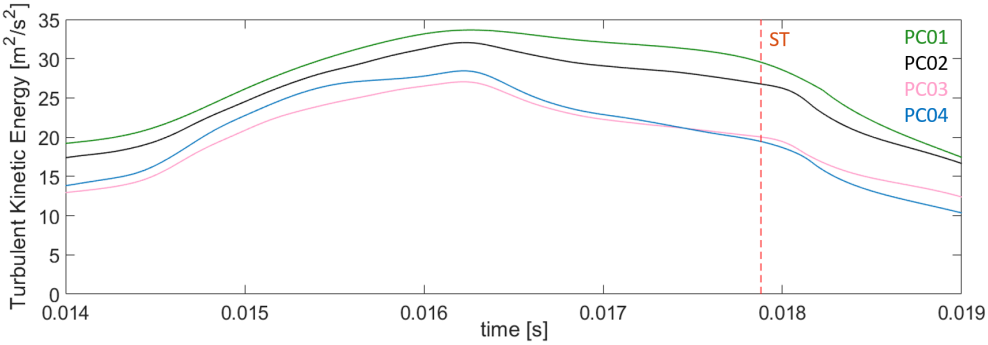

Figure 6.26: Turbulent kinetic energy evolution for all the pre-chamber geometries.

Nevertheless, it is important to underline that the initial values (t = 0ms) are not consistent with the assumptions made in chapter 4. As observed, CFD simulations have shown a clear ranking in terms of both average and local turbulent kinetic energy at the spark ignition time:

- Higher local TKE, around the spark electrodes area, and similar average values were observed by comparing straight nozzle (PC01) with tilted nozzle (PC02).
- A similar local structure and slightly higher average value was described for PC03 in comparison with PC02.
- Higher average and local TKE was found for PC04 with respect to PC02 and PC03 geometries.

Hence, observing the initial turbulent flame speed, similar values are observed for PC01 and PC02. However, as opposed to what expected from CFD simulation results, a lower initial turbulent flame speed is achieved for

PC03 and PC04 cases. Indeed, to fully understand such divergence, parameters from Kolla's correlation are analysed. Assuming that the thermochemical conditions at the spark ignition time do not change significantly as a function of the nozzle geometry, the laminar flame velocity, flame thickness, mean and unburned mixture temperature should not be severely affected by the geometry of the orifices either. On the contrary, the turbulent kinetic energy (and therefore the resulting turbulent kinetic speed) are influenced by the orifice number and distribution. However, it has to be acknowledged that some effects related to the mixing process between the pre-chamber auxiliary injection and the pre-chamber flow field induced during the filling process may exist.

Figure 6.26 shows, using the same colourmap described before, the evolution of the average turbulent kinetic energy (inside the pre-chamber) computed from the analysis of the experimental data through the zero-dimensional turbulence model for the cases considered. When the spark plug is activated, the PC01 layout shows the higher TKE value, followed by the PC02 and then by similar values for the PC03 and PC04 set-ups.

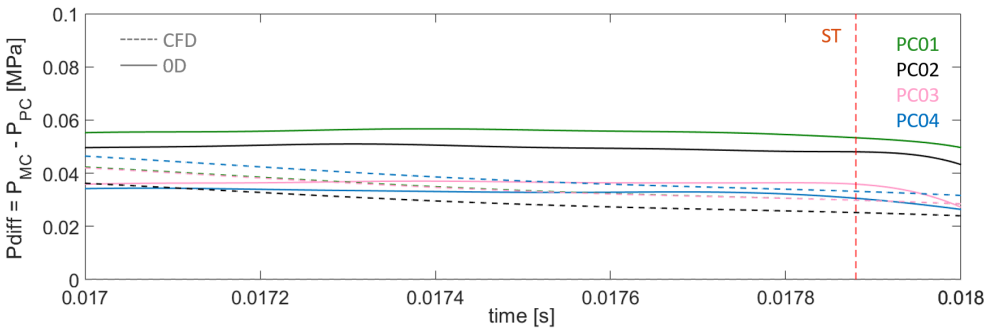

Figure 6.27: Experimental and numerical chambers pressure difference.

To shed light on these differences detected between experimental and numerical prediction, the delta pressure between the main chamber and the pre-chamber close the spark activation event is analysed. The turbulent kinetic energy mainly depends on the fluctuating component of the nozzle incoming velocity, which is controlled by the pressure difference between the two chambers. Figure 6.27 shows the pressure difference for experimental cases (continuous lines) and 3D CFD simulations (dashed lines). The PC01 and PC03 3D numerical trends are overlapping and therefore difficult to distinguish one from another.

The pressure difference between the chambers, changes depending on the pre-chamber geometry due to the variation of the orifices discharge coefficient, assuming an equal piston speed and nozzle cross-section. For 3D simulations the same piston movement law is imposed (for all the cases), and the cross-section is the theoretical one (constant parameters between geometries). Indeed the difference on the numerical trends is all controlled by the discharge coefficient.

On the other hand, the experimental piston law is function of the driving gas and combustion chamber pressure balance and no rod-crank mechanism is considered. Moreover, the experimental equipment has to face geometric tolerances, which in the case of the orifices are around $\pm 0.05mm$. Due to the absence of high precision microscope for the geometric nozzle characterization, the theoretical surface is assumed as input for the zero-dimensional post-processing model. Consequently, all the slightly differences (geometrical and operational) are accounted in the discharge coefficient, modelled for each pre-chamber. The correct calibration of the discharge coefficient is ensured by the shape of the pre-chamber heat release rate under motoring conditions, which is totally flat in case the mass transfer model works properly (figure 5.3).

In conclusion, it can be stated that the differences in the initial value of the turbulent flame velocity are in agreement with the experimental measurements of the in-cylinder pressure.

Finally the flame regime is shown in the classical Borghi diagram in figure 6.28 for all the pre-chamber configurations under lean combustion case. The X-axis represents the ratio of bigger macroscale and the laminar flame thickness (predicted from the laminar flame speed and the mixture thermal diffusivity), while the ratio between the turbulence kinetic velocity and the laminar flame speed is shown on Y-axis. The data refer to the time elapsed between the spark activation moment until the flame approaches the last orifice walls. As stated for the baseline case (PC01), the combustion inside the pre-chamber is in the thickened wrinkled flames regime, for all the geometries. Hence, the high Damköhler number combined with strong turbulence intensity explain the fast increase of the turbulent flame speed.

6.6 Ultra-lean combustion improvement: PC05 axial nozzle

In this section the comparison between the PC02 and PC05 results are described. As highlighted in the previous paragraphs, the pre-chamber PC02

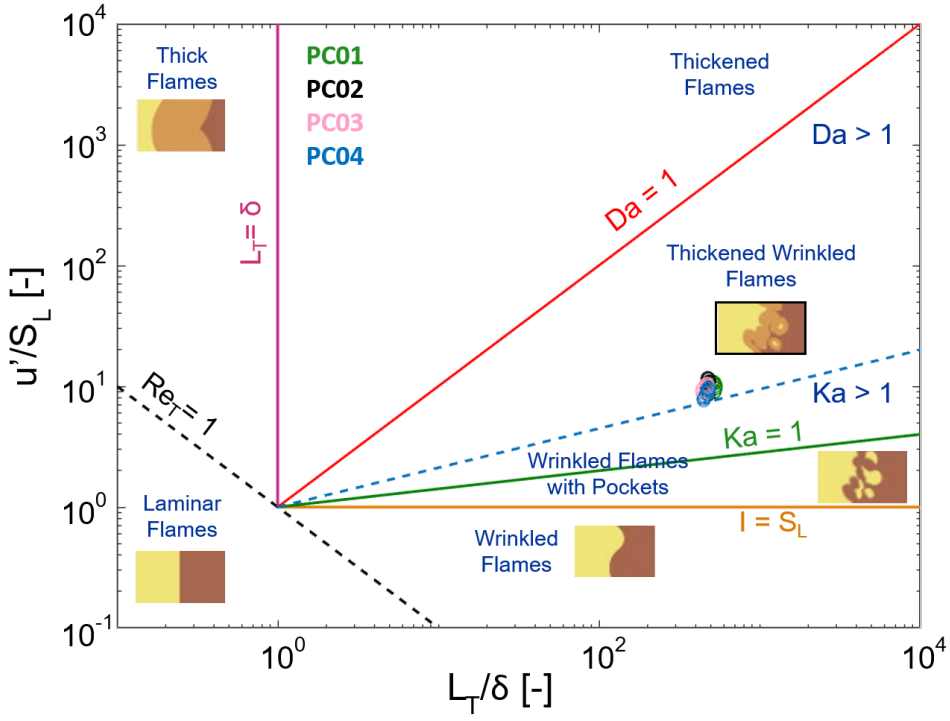

Figure 6.28: Borghi's diagram for turbulent flame regime a function of pre-chamber geometry.

shows satisfactory results under lean mixture conditions ($\phi_{MC} = 0.5$), while severe limitations in terms of combustion efficiency when running the experiments at ultra-lean conditions ($\phi_{MC} = 0.3$). By increasing the orifice numbers from six to eight the performance improves but not enough to ensure the combustion of all the cylinder charge. Hence, the PC05 geometry was designed with six side orifices and one axial orifice (a total of seven orifices with 1.4 mm of diameter) to improve combustion under extreme mixture conditions.

The ultra-lean test results ($\phi_{MC} = 0.3$, $\phi_{PC} = 1.1$, $T_0 = 360$ K, $p_0 = 0.15$ MPa) are discussed starting from the main chamber and pre-chamber pressure evolution (figure 6.29). The spark activation instant is highlighted with the red vertical line.

The violet lines refer to the PC05 geometry, and the black lines point the PC02 setting. Regarding the pre-chamber combustion, the PC02 geometry

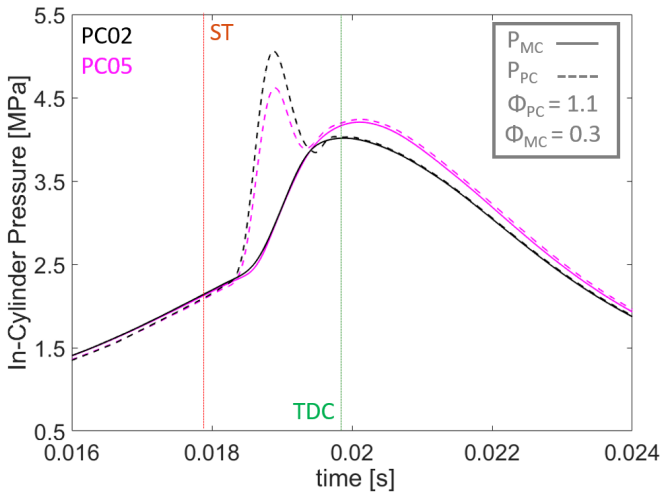

Figure 6.29: PC05 and PC02 comparison under ultra-lean ($\phi = 0.3$) conditions: Pressure evolution.

shows steeper pressure slope since the early stage of the process. Thus, the two curves diverge, reaching different peak value.

Although the difference in the pre-chamber combustion, the effects of the axial orifice are beneficial in the case of the main combustion. First of all, a slight advance in the main charge ignition moment is observed for PC02 case as a result of better pre-chamber combustion. After the early phases, a stronger pressure gradient and peak are achieved close to TDC and over the entire expansion stroke for PC05 set-up.

Figure 6.30 depicts the heat release rate for the main chamber (black lines) and pre-chamber (green line) on the left side. Furthermore, the total heat released, with respect to the available chemical energy, is displayed on the right side (black trends). The figure confirms what stated for the pressure analysis. PC02 setting promotes a combustion advance both in the pre-chamber and in the main chamber. Nevertheless, a higher heat release rate is observed after the beginning of combustion. An earlier and faster re-filling can be noted for the PC05 case, probably associated with the axial orifice position and discharge coefficient (higher than side orifices), resulting in an advanced second jets ejection.

As a results of the combustion enhancement during the late stages, the efficiency reported in the right side of the figure 6.30 demonstrate an increase

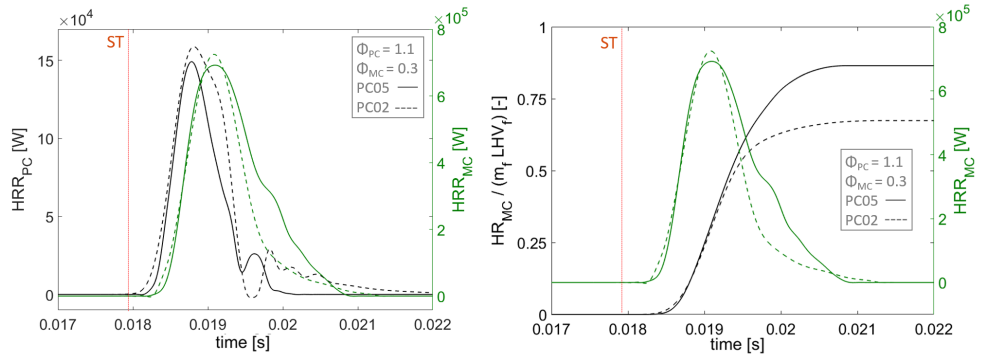

Figure 6.30: PC05 and PC02 comparison under ultra-lean ($\phi = 0.3$) conditions: Heat release rate evolution.

of about 15%. Regarding the flame surface, the temporal evolution is depicted in figure 6.31. The violet color refers to the PC05 case, and the black trend marks the PC02 set-up. Also in this case, combustion pictures are displayed at t = 0.6 ms, and t = 0.9 ms.

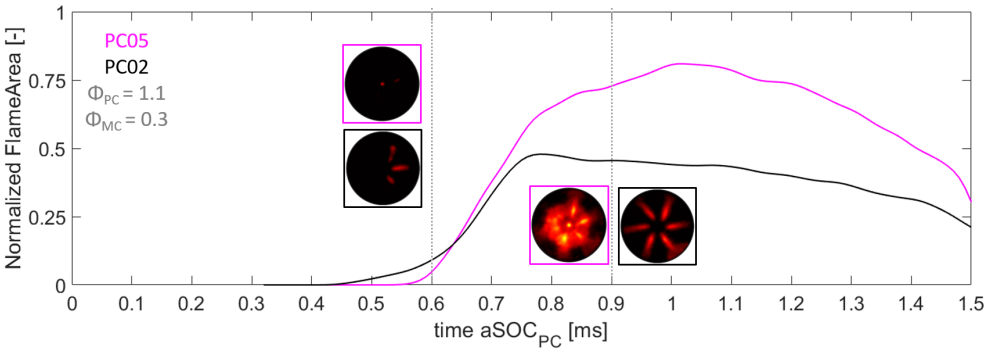

Figure 6.31: PC05 and PC02 comparison under ultra-lean ($\phi = 0.3$) conditions: Normalized Flame Area.

As a result of advanced combustion, the PC02 promotes early jets ejection leading to a bigger flame surface value in the first stages of combustion. Then, during the second phase, a fast and strong ejection with consequent rapid growth of the flame front is observed for the geometry PC05. When the process is no long controlled by the torch jet ignition mode, the acceleration

of the flame surface slows down, completing the combustion by means of flame propagation. In conclusion, the axial orifice significantly helps to improve the system performance under ultra-lean mixture conditions. In contrast to lateral ejection, the axial one, causes a direct impact of the flame on the piston surface. This impact (associated with a high jet momentum) favours the flame spreading which drastically increases the mass and thermal diffusion in the areas that are not directly exposed to the jets. However, further studies, both experimental and numerical, are needed to better understand the axial flame interaction with the piston and the others sprays.

Chapter 7

Summary and future works

This chapter intends to summarize the work carried out and described in the manuscript. Moreover, the potential future improvements and new ideas for research are listed as well.

7.1 Summary

This thesis is focused on the analysis of the combustion development of stratified pre-chamber spark ignition systems. To achieve this target a great effort has been employed in the development and design of new experimental system and techniques, including the adaptation of the facilities used for this purpose, the definition of a robust test methodology, as well as a zero-dimensional model for combustion diagnostics in both chambers. The results of the experimental campaign were analyzed using a Matlab home-made code based on the in-cylinder pressure measurement, in combination with the fast-camera images and the 3D CFD simulations. The work performed was grouped into three chapters based on their specific target, to thoroughly study different aspects of the process:

1. Development of the zero-dimensional turbulence model in the pre-chamber, using as a basis a set of 3D-CFD simulations.

2. Characterization of the stratified pre-chamber spark ignition operating for a baseline design.

3. Evaluation of the influence of the number and orientation of the orifices connecting the pre-chamber with the rest of the cylinder.

All experiments were performed by mean of the rapid compression-expansion machine. The original cylinder head layout was modified to allow the housing of the pre-chamber itself, fuel injectors, spark plug, pressure sensors, and a thermocouple, used to determine the initial temperature. The pre-chamber is screwed onto the cylinder head, thus allowing a rapid pre-chamber replacement without removing any others system elements. The test methodology involved the acquisition of the pressure evolution in both main chamber and pre-chamber, the cylinder volume, the duration of the auxiliary injection, and the spark ignition point.

These are used as input for the zero-dimensional thermodynamic model which returns the fundamental parameters aims to characterize the PCSI system working cycle. In general the thermodynamic model has allowed to gain a deeper knowledge of the following aspects:

- The mass interchanged between the two open systems was estimated by means of the equation of the compressible flow through the ducts. The trapped mass is a key factor for the system control. Knowing the time evolution of the air mass and fuel inside the pre-chamber, it is possible to calibrate the auxiliary injection according to the desired mixing conditions (rich, lean or stoichiometric).

- The velocity through the orifices, controlled by the pressure difference and the thermodynamic conditions of both chambers, allows to estimate the evolution of turbulence in the pre-chamber.

- The turbulent cascade, that transforms the kinetic energy associated with the pre-chamber incoming mass into turbulent kinetic energy that dissipates into heat, is modelled by means of the K-k-ϵ model. The turbulent kinetic energy is a crucial parameters for the prediction of combustion speed and heat losses. On the one hand, it is used to scale the laminar flame speed to obtain the turbulent flame velocity. On the other hand, it controls the the characteristic speed, according to Bargende's equation, for the pre-chamber heat losses prediction.

- The heat release rate was estimated through the first thermodynamic law, including the temporal derivative of pressure and volume, the heat losses, the energy associated with the exchanged mass, and the energy absorbed by the fuel evaporation process.

- Combustion speed was predicted by means of the Kolla's correlation, scaling the laminar flame speed modelled through the Di Staso's equation, with the turbulence parameters estimated using the K-k-ϵ model.

Subsequently, to calibrate the zero-dimensional model coefficients under motoring conditions, several 3D CFD simulations were carried out. For this purpose, the internal geometry of the combustion chamber (main chamber plus pre-chamber) used for the experiments was generated using Converge software. Once the simulation has started, the temporal evolution of the piston position acquired from the experimental test (without combustion) with a compression ratio of 11:1, an initial pressure at 0.15 MPa and an initial temperature of 360K are imposed. The main chamber is initialized with an equivalence ratio $\phi = 0.5$ mixture of air and fuel (iso-octane), representative of an early injection before the rapid compression starts. Instead, the pre-chamber is assumed to be filled initially with air. Thus, the results of the simulations in terms of interchanged mass and pre-chamber turbulent kinetic energy have been used to tune the nozzle discharge coefficient and the turbulence sub-model coefficients for the baseline case PC01. Subsequently the calibration was extended for all the pre-chamber geometries under examination in this thesis. The main geometric characteristics of the nozzles are summarized in the following table:

	$PC01$	$PC02$	$PC03$	$PC04$
$D_{orif}[mm]$	1.5	1.5	1.3	1.8
N_{orif}	6	6	8	4
$Nozzle$	Straight	Tilted	Tilted	Tilted
$\theta_{jet}[^\circ]$	60	60	45	90

Table 7.1: Main geometric characteristics of the pre-chamber nozzles.

Furthermore, the 3D CFD simulations outputs have been analysed (by means of Paraview software) to fully understand the flow field structure and the local effect induced by the different nozzles at the spark activation time. The turbulent kinetic energy in terms of intensity and direction was investigated in two horizontal sections and in one vertical plane of the pre-chamber, leading to the following conclusions:

- Straight nozzle generates high local turbulent kinetic energy close to the electrodes due to the direct collision of the jets entering the pre-chamber. However, the induced fluid dynamic field is chaotic and not able to ensure homogeneity throughout the entire volume of the pre-chamber.

- Tilted nozzle causes a local decrease in turbulent kinetic energy due to the side impact between adjacent jets. Nevertheless, side jets impact generates a macrovortex capable of distributing turbulence throughout the volume.

- The number of orifices affects the homogeneity within the pre-chamber volume, while it is a second-order influence factor on the kinetic energy conversion induced by the impact of the jets. Increase the orifice numbers helps the spreading of turbulence while reducing the number causes the opposite effect.

- The angle of impact (i.e., the angle resulting from the intersection of the symmetry axis of two adjacent sprays), influences the interaction between the adjacent jets by varying the contact area between them. Consequently, the increase of this parameter causes an improvement in local turbulence.

Preliminary to the real experimental campaign, some fundamental aspects of the system have been explored, using the baseline PC01 nozzle:

- The cycle-to-cycle dispersion has been evaluated on two levels of compression ratio, by means of the statistical assessment of fifteen test repetitions under firing conditions. The average value, standard deviation and coefficient of variation of the main chamber pressure peak have been calculated, showing very low cycle-to-cycle variation. The coefficient of variation (COV) of this peak pressure is below 2% for both compression ratios considered.

- The auxiliary injection effects have been investigated under two injection pressure levels (140MPa and 100MPa), two different start of injection timings (corresponding to 65mm and 88mm of the complete piston stroke), including two compression ratio (12 and 13). Lower injection pressure is characterized by lower injection velocity, thus helping to reduce the liquid impact against the walls. Delaying the injection point have a positive effect on combustion. As pre-chamber temperature and pressure increase during the compression, chamber conditions promote fuel evaporation, thereby reducing or eliminating the wall wetting phenomenon. A secondary effect is reported by changing the compression ratio, which slightly affects the temperature and pressure at the start of injection.

- The effect of the spark ignition point on the pre-chamber start of combustion have been analysed along the compression stroke. The spark activation is triggered in a region of a good compromise between temperature and turbulence, thus ensuring both a high level of initial turbulent flame speed and engine power delivered in the required phase.

Then, the results of the first experimental matrix point ($\phi_{MC} = 0.5$, $\phi_{MC} = 1.1$, $T_0 = 360$K, $P_0 = 0.15$MPa) were analysed to characterize all the fundamental principles of the work cycle:

- As compression starts, the pre-chamber filling process is performed. The interchanged mass is function of the piston speed and the pre-chamber nozzle cross-section.
- During the compression stroke, the auxiliary injection is performed to correct the pre-chamber equivalence ratio. Slightly rich conditions are the target to maximize the laminar flame speed once combustion is started.
- The spark plug activation marks the start of pre-chamber combustion. The flame propagates trough the volume under the thickened wrinkled regime, reaching a very high flame speed ratio due to the induced turbulence field.
- As the flame approach the orifices, the first jets ejection is performed, acting as ignition sources for the main chamber lean mixture. The combustion propagates in the main chamber under the torch jet ignition regime, characterized by a fast heat release and burning rate.
- Once the flame approach the pre-chamber walls the quenching slows down the combustion leading to the end of the first ejection. From this moment on, combustion in the main chamber is controlled by the flame propagation which is self-sustaining thanks to the thermodynamic and turbulent conditions induced by the sprays ejection. Indeed, a high thermal and mass diffusion is needed during this stage in order to achieve a complete combustion of the cylinder charge.
- In this phase, the pre-chamber pressure drops down, falling below the main chamber pressure. For several time steps, the flow is reversed realizing the second filling of the pre-chamber. Then, the second jet's ejection is performed over the whole expansion stroke, completing the last stage of combustion.

Subsequently, the experimental campaign was carried out according with the first DOE, in order to evaluate the effect of the equivalence ratio of both chambers on the combustion development. For the purpose the main chamber mixture conditions were varied from lean ($\phi_{MC} = 0.5$) to ultra-lean ($\phi_{MC} = 0.3$), while the pre-chamber equivalence ratio was explored from rich ($\phi_{PC} = 1.1$) to lean ($\phi_{PC} = 0.9$) conditions. The experimental campaign conclusions can be summarised as follows:

- The main chamber equivalence ratio has a secondary effect on the pre-chamber combustion development. The pressure evolution changes within the range of cyclic variation if the same thermo-chemical conditions are ensured at the start of combustion. Instead, the pressure evolution in the main chamber once the combustion starts (first jet ejection) is very different for the two cases due to several aspects. First, as the air amount inside the cylinder is the same at the beginning of the both tests, the total energy available decrease as less fuel is injected. Second, the equivalence ratio affects the flame propagation between the adjacent jets.

- The pre-chamber equivalence ratio highly affects the combustion development in both chambers. Leaner mixture produces a larger induction time for the flame kernel, showing a longer delay between the spark discharge and the pressure rise inside the pre-chamber. As a consequence, the first jets ejection starts later and at lower velocities. Hence the torch jet ignition phase is weaker leading to combustin efficiency loss.

Finally, the influence of the nozzle geometry, including orifices distribution number and diameter, on the PCSI system performances has been investigated, under lean ($\phi_{MC} = 0.5$, $\phi_{PC} = 1.1$) and ultra-lean conditions ($\phi_{MC} = 0.5$, $\phi_{PC} = 1.1$). Zero-dimensional model results have been coupled with 3D CFD simulations and combustion visualization to achieve the following conclusions. With respect to the pre-chamber combustion:

- Straight orifices flow converging on the center of the pre-chamber promotes high local turbulence during the filling process, thus enhancing fast development and initial growth of the flame kernel in the early stage of combustion. Swirled nozzles with tilted orifices lead to a more homogeneous distribution of turbulence and air/fuel mixture throughout the entire pre-chamber volume, resulting in a slower initial combustion phase followed by faster flame front propagation.

- 90° jets impact angle, promotes high momentum flux interchange when the adjacent jets collide, thus leading to a high turbulence generation, and to a fast combustion evolution. On the contrary, when the impact of the jets is not perpendicular less turbulence is generated by the collision.
- The orifices number affects the homogeneity within the volume. As the orifices number increases, the volume between the adjacent jets is reduced leading to better average turbulence conditions and thus to faster flame front spreading.

Regarding the main chamber mixture combustion:

- Straight nozzle shows satisfactory results, in terms of combustion efficiency under lean mixture conditions ($\phi_{MC} = 0.5$). As the mixture becomes leaner, the combustion process degrades during the flame propagation stage due to the extreme conditions in terms of flammability limits. Tilted nozzles promote a swirling flow, generated by the asymmetrical ejection of the jets, improving the thermal and mass diffusion and thus the flame propagation between the adjacent sprays. Leaner are the overall conditions and bigger are the benefits of the induced rotating flow.
- Similarly, the addition of an axial orifice shows a high potential for improving the flame propagation phase. In contrast to lateral ejection, the axial one, causes a direct impact of the flame on the piston surface. This impact (associated with a high jet momentum) favours the flame spreading which drastically increases the mass and thermal diffusion in the areas that are not directly exposed to the jets. The combination of the rotating and axial flows must be taken into account for future developments of the PCSI system.
- The number of orifices is a critical factor for the proper development of main chamber combustion. This parameter must be chosen with care during the geometric definition of the PCSI system, taking into account the mixture conditions in which it operates. A number of orifices lower than the theoretically necessary value causes a high efficiency loss due to the impossible flame propagation between adjacent jets. As the mixture becomes leaner, a higher number of orifices improves the whole combustion process. The torch ignition stage is improved by the higher number of jets incoming in the main chamber. Meanwhile, the higher number of orifices, reduces the volume between the adjacent jets ejected,

thus enhancing the mass and heat diffusion under extreme ultra-lean mixture strategy.

7.2 Future directions

During the development of the research, several aspects of the PCSI system have been deeply investigated by means of experimental and numerical tools. Pursuing efforts in these areas would allow a better understanding of the PCSI process and could potentially lead to the future implementation of this technology on commercial vehicles. Continuing on, a series of developments considered interesting by the author is listed in both the experimental and numerical fields.

7.2.1 Numerical

- The development of a complete zero-dimensional multi-zone model, including burned and unburned mixture areas for both chambers, would allow a more precise characterization of the phenomenon.
- Extension of the K-k-e turbulence model to the main chamber would allow to deepen the study of the different combustion regimes along the working cycle. It is of fundamental importance, for future developments in technology, to investigate how the torch jet ignition phase influences the subsequent flame propagation as function of the different boundary conditions.
- Using 3D CFD simulations for pre-chamber geometry optimization, starting from the knowledge generated. A big numerical matrix including the combination between orifices geometry parameters (length, distribution, number, diameter), and pre-chamber volume and shape would allow to optimize the fluid dynamic field.
- Performing 3D CFD simulations under firing conditions to validate 0D combustion model results, in terms of chamber pressure and heat release rate, would allow to generate a predictive model with low computational costs.

7.2.2 Experimental

- The use of different optical techniques would allow to study several aspects of the process. For example, the Schlieren technique would permit

to observe the ejection of the fresh mixture (preceding the flame ejection) into the main chamber caused by the pre-chamber pressure rise after start of combustion. In addition, better characterization of the jet penetration and dispersion angle could be achieved.

- An extension of the experimental matrix including different geometrical parameters (pre-chamber volume, orifice length, RCEM compression ratio, piston shape) and boundary conditions (initial temperatures, initial pressures, spark ignition times, fuels, higher equivalence ratio) is necessary. In addition, EGR strategy can be used for charge dilution also for a more effective management of the aftertreatment system.

- A complete characterization of the injectors in terms of penetration and angle of the liquid and vapour phases is necessary in order to fully understand the interaction between the fuel and the pre-chamber walls.

- The interaction of the flame with the orifices walls is a critical issue for the PCSI system. Flame may quench near to the wall, due to heat losses, thus affecting the combustion regime of the main chamber. If the flame propagates throughout the nozzles without quenching, the torch ignition mode is activated, while on the contrary the main chamber mixture is ignited by the hot radicals. This aspect should be explored by varying the diameter of the orifices and performing visualization tests with Schlieren technique.

- The potential of the PCSI system under homogeneous strategy must be taken into consideration in order to reduce the drawbacks associated with the stratified operation mode (geometry constrain, double injector, etc.).

Global Bibliography

Achuth, Munnannur and Mehta, Pramod S. "Predictions of tumble and turbulence in four-valve pentroof spark ignition engines". In: *International Journal of Engine Research* 2.3 (2001), pp. 209–227.

Adams, Tim G. *Torch ignition for combustion control of lean mixtures.* Tech. rep. SAE Technical Paper, 1979.

Agarwal, A, Filipi, ZS, Assanis, DN, and Baker, DM. "Assessment of single- and two-zone turbulence formulations for quasi-dimensional modeling of spark-ignition engine combustion". In: *Combustion science and technology* 136.1-6 (1998), pp. 13–39.

Agarwal, Avinash Kumar et al. "Effect of fuel injection pressure and injection timing of Karanja biodiesel blends on fuel spray, engine performance, emissions and combustion characteristics". In: *Energy Conversion and Management* 91 (2015), pp. 302–314.

Aleiferis, PG, Hardalupas, Y, Taylor, AMKP, Ishii, K, and Urata, Y. "Flame chemiluminescence studies of cyclic combustion variations and air-to-fuel ratio of the reacting mixture in a lean-burn stratified-charge spark-ignition engine". In: *Combustion and Flame* 136.1-2 (2004), pp. 72–90.

Alkidas, AC. "Combustion-chamber crevices: the major source of engine-out hydrocarbon emissions under fully warmed conditions". In: *Progress in energy and combustion science* 25.3 (1999), pp. 253–273.

Altaie, Mohamad A Hasan et al. "Performance and exhaust emission characteristics of direct-injection diesel engine fueled with enriched biodiesel". In: *Energy conversion and management* 106 (2015), pp. 365–372.

Amirante, Riccardo, Distaso, Elia, Tamburrano, Paolo, and Reitz, Rolf D. "Laminar flame speed correlations for methane, ethane, propane and their mixtures, and natural gas and gasoline for spark-ignition engine simulations". In: *International Journal of Engine Research* 18.9 (2017), pp. 951–970.

Armas Vergel, Octavio. "Diagnóstico experimental del proceso de combustión en motores diesel de inyección directa". PhD thesis. Universitat Politècnica de València, 1998.

Attard, William. *Turbulent jet ignition pre-chamber combustion system for spark ignition engines*. US Patent 8,857,405. 2014.

Attard, William P and Blaxill, Hugh. "A single fuel pre-chamber jet ignition powertrain achieving high load, high efficiency and near zero NOx emissions". In: *SAE International Journal of Engines* 5.3 (2012), pp. 734–746.

Attard, William P and Parsons, Patrick. "A normally aspirated spark initiated combustion system capable of high load, high efficiency and near zero NOx emissions in a modern vehicle powertrain". In: *SAE International Journal of Engines* 3.2 (2010), pp. 269–287.

Attard, William P and Parsons, Patrick. "Flame kernel development for a spark initiated pre-chamber combustion system capable of high load, high efficiency and near zero NOx emissions". In: *SAE International Journal of Engines* 3.2 (2010), pp. 408–427.

Ballesteros, R, Guillén-Flores, J, and Barba, J. "Environmental and health impact assessment from a heavy-duty diesel engine under different injection strategies fueled with a bioethanol–diesel blend". In: *Fuel* 157 (2015), pp. 191–201.

Baratta, M, Catania, AE, Spessa, E, and Vassallo, A. "Development of an improved fractal model for the simulation of turbulent flame propagation in SI engines". In: *SAE Technical Paper* (2005).

Bardis, Konstantinos, Xu, Guoqing, Kyrtatos, Panagiotis, Wright, Yuri M, and Boulouchos, Konstantinos. "A zero dimensional turbulence and heat transfer phenomenological model for pre-chamber gas engines". In: *SAE Technical Paper* (2018).

Bargende, Michael. *Ein Gleichungsansatz zur Berechnung der instationären Wandwärmeverluste im Hochdruckteil von Ottomotoren*. na, 1990.

Barin, I. "Thermochemical data of pure substances VCH, Weinheim (1989)". In: (1989).

Barnes, WB. "Improvements in or Relating to Internal Combustion Engines". In: *British Patent* 683 (1952), p. 162.

Bellenoue, M, Kageyama, T, Labuda, SA, and Sotton, J. "Direct measurement of laminar flame quenching distance in a closed vessel". In: *Experimental thermal and fluid science* 27.3 (2003), pp. 323–331.

Benajes, Jesús, García, Antonio, Monsalve-Serrano, Javier, and Martínez-Boggio, Santiago. "Emissions reduction from passenger cars with RCCI plug-in hybrid electric vehicle technology". In: *Applied Thermal Engineering* 164 (2020), p. 114430.

Benajes, Jesús, García, Antonio, Monsalve-Serrano, Javier, and Sari, Rafael Lago. "Fuel consumption and engine-out emissions estimations of a light-duty engine running in dual-mode RCCI/CDC with different fuels and driving cycles". In: *Energy* 157 (2018), pp. 19–30.

Benajes, Jesús, Pastor, José V, García, Antonio, and Monsalve-Serrano, Javier. "The potential of RCCI concept to meet EURO VI NOx limitation and ultra-low soot emissions in a heavy-duty engine over the whole engine map". In: *Fuel* 159 (2015), pp. 952–961.

Benson, Rowland S. *Advanced engineering thermodynamics: thermodynamics and fluid mechanics series*. Elsevier, 2013.

Bjerkborn, Simon. "Development and validation of a turbulent flame propagation model". PhD thesis. 2011.

Blint, Richard J. "The relationship of the laminar flame width to flame speed". In: *Combustion Science and Technology* 49.1-2 (1986), pp. 79–92.

Blomberg, Christopher Kim et al. "Extension of the phenomenological 3-Arrhenius auto-ignition model for six surrogate automotive fuels". In: *SAE International Journal of Engines* 9.3 (2016), pp. 1544–1558.

Borghi, R. *On the Structure and Morphology of Turbulent Premixed Flames. In: Casci C., Bruno C. (eds) Recent Advances in the Aerospace Sciences*. Springer (Boston, MA, USA), 1985.

Borgnakke, C, Davis, GC, and Tabaczynski, RJ. "Predictions of in-cylinder swirl velocity and turbulence intensity for an open chamber cup in piston engine". In: *SAE Transactions* (1981), pp. 964–978.

Bosch, W. "The fuel rate indicator: a new measuring instrument for display of the characteristics of individual injection. SAE paper 660749; 1966". In: *Google Scholar* ().

Bose, Bimal K and Wang, Fei. "ENERGY, ENVIRONMENT, POWER ELECTRONICS, RENEWABLE ENERGY SYSTEMS, AND SMART GRID". In: *Power Electronics in Renewable Energy Systems and Smart Grid: Technology and Applications* (2019), pp. 1–83.

Bozza, Fabio et al. "A Quasi-Dimensional Model of Pre-Chamber Spark-Ignition Engines". In: *SAE Technical Paper* (2019).

Brandstetter, Walter. "The volkswagen lean burn pc-engine concept". In: *SAE Transactions* (1980), pp. 1804–1821.

Broderson, Neil O. *Method of operating internal-combustion engines*. US Patent 2,615,437. 1952.

Bunce, Michael, Blaxill, Hugh, Kulatilaka, Waruna, and Jiang, Naibo. *The effects of turbulent jet characteristics on engine performance using a pre-chamber combustor*. Tech. rep. SAE Technical Paper, 2014.

Bureshaid, Khalifa, Feng, Dengquan, Zhao, Hua, and Bunce, Mike. "Combustion and emissions of gasoline, anhydrous ethanol, and wet ethanol in an optical engine with a turbulent jet ignition system". In: *Proceedings of the Institution of Mechanical Engineers, Part D: Journal of Automobile Engineering* 233.13 (2019), pp. 3528–3537.

Bureshaid, Khalifa, Shimura, Ray, Feng, Dengquan, Zhao, Hua, and Bunce, Mike. "Experimental Studies of the Effect of Ethanol Auxiliary Fueled Turbulent Jet Ignition in an Optical Engine." In: *SAE International Journal of Engines* 12.4 (2019), pp. 387–400.

Burke, Eoin M, Güthe, Felix, and Monaghan, Rory FD. *A comparison of turbulent flame speed correlations for hydrocarbon fuels at elevated pressures*. 2016.

Castilla Alvarez, Carlos Eduardo, Couto, Giselle Elias, Roso, Vinícius Rückert, Thiriet, Arthur Braga, and Valle, Ramon Molina. "A review of prechamber ignition systems as lean combustion technology for SI engines". In: *Applied Thermal Engineering* 128 (2018), pp. 107–120.

Caton, Jerald A. "The thermodynamic characteristics of high efficiency, internal-combustion engines". In: *Energy Conversion and Management* 58 (2012), pp. 84–93.

Chigier, Norman A. *Energy, combustion, and environment*. McGraw-Hill New York, 1981.

Chiodi, Marco and Bargende, Michael. "Improvement of engine heat-transfer calculation in the three-dimensional simulation using a phenomenological heat-transfer model". In: *SAE Technical Paper* (2001).

Cho, HM and He, B-Q. "Combustion and emission characteristics of a lean burn natural gas engine". In: *International Journal of Automotive Technology* 9.4 (2008), pp. 415–422.

Choi, Kwanhee, Lee, Hyungmin, Hwang, In Goo, Myung, Cha-Lee, and Park, Simsoo. "Effects of various intake valve timings and spark timings on combustion, cyclic THC and NO x emissions during cold start phase with idle operation in CVVT engine". In: *Journal of mechanical science and technology* 22.11 (2008), pp. 2254–2262.

Collins, Neil R and Twigg, Martyn V. "Three-way catalyst emissions control technologies for spark-ignition enginesârecent trends and future developments". In: *Topics in Catalysis* 42.1-4 (2007), pp. 323–332.

CONVERGE is a trade mark of Convergent Science. *https://convergecfd.com*.

Cordier, Matthieu, Laget, Olivier, Duffour, Florence, Gautrot, Xavier, and De Francqueville, Loic. *Increasing modern spark ignition engine efficiency: a comprehension study of high CR and Atkinson cycle*. Tech. rep. SAE Technical Paper, 2016.

Corti, Enrico and Forte, Claudio. "Spark advance real-time optimization based on combustion analysis". In: *Journal of Engineering for Gas Turbines and Power* 133.9 (2011).

Culbertson, David, Khair, Magdi, Zhang, Sanhong, Tan, Julian, and Spooler, Jacob. "The study of exhaust heating to improve SCR cold start performance". In: *SAE International Journal of Engines* 8.3 (2015), pp. 1187–1195.

Dadgostar, Nafiseh and Shaw, John M. "A predictive correlation for the constant-pressure specific heat capacity of pure and ill-defined liquid hydrocarbons". In: *Fluid Phase Equilibria* 313 (2012), pp. 211–226.

Daniel, WA. "Flame quenching at the walls of an internal combustion engine". In: *Symposium (International) on Combustion*. Vol. 6. 1. Elsevier. 1957, pp. 886–894.

Date, Tasuku, Yagi, Shizuo, Ishizuya, Akira, and Fujii, Isao. *Research and development of the Honda CVCC engine*. Tech. rep. SAE Technical Paper, 1974.

De Bellis, Vincenzo, Bozza, Fabio, and Tufano, Daniela. *A Comparison Between Two Phenomenological Combustion Models Applied to Different SI Engines*. Tech. rep. SAE Technical Paper, 2017.

De Petris, C, Diana, S, Giglio, V, and Police, G. "High efficiency stoichiometric spark ignition engines". In: *SAE transactions* (1994), pp. 1059–1067.

De Soete, GC. "Propagation behaviour of spark ignited flames in the early stages". In: *International Conference on Combustion in Engineering*. Vol. 1. 1983, p. 93.

Desantes, José M, García-Oliver, José María, Vera-Tudela, Walter, and López-Pintor, Darío. "Study of ignition delay time and generalization of auto-ignition for PRFs in a RCEM by means of natural chemiluminescence". In: *Energy Conversion and Management* 111 (2016), pp. 217–228.

Desantes, José M, López, J Javier, García-Oliver, José M, and López-Pintor, Darío. "A phenomenological explanation of the autoignition propagation under HCCI conditions". In: *Fuel* 206 (2017), pp. 43–57.

Desantes, José M, López, J Javier, Molina, Santiago, and López-Pintor, Darío. "Theoretical development of a new procedure to predict ignition delays under transient thermodynamic conditions and validation using a Rapid Compression–Expansion Machine". In: *Energy Conversion and Management* 108 (2016), pp. 132–143.

Duan, Xiongbo et al. "Performance, combustion and knock assessment of a high compression ratio and lean-burn heavy-duty spark-ignition engine fuelled with n-butane and liquefied methane gas blend". In: *Energy* 158 (2018), pp. 256–268.

Duchaussoy, Yorick, Lefebvre, Alain, and Bonetto, Robert. *Dilution interest on turbocharged SI engine combustion*. Tech. rep. SAE Technical Paper, 2003.

Durling, Harold E. *Igniter for internal combustion engines operating over a wide range of air fuel ratios*. US Patent 7,021,275. 2006.

Durling, Harold E, Johnston, Robert P, and Polikarpus, Kaius K. *Torch jet spark plug*. US Patent 5,421,300. 1995.

Durling, Harold E and Ralph, Joseph G. *Directed jet spark plug*. US Patent 6,213,085. 2001.

Einewall, Patrik, Tunestål, Per, and Johansson, Bengt. *Lean burn natural gas operation vs. stoichiometric operation with EGR and a three way catalyst*. Tech. rep. SAE Technical Paper, 2005.

Enomoto, Masaru. "Head-on quenching of a premixed flame on the single wall surface". In: *JSME International Journal Series B Fluids and Thermal Engineering* 44.4 (2001), pp. 624–633.

Evans, Robert Lancelot. *Control method for spark-ignition engines*. US Patent 6,032,640. 2000.

Feng, Dengquan, Buresheid, Khalifa, Zhao, Hua, Wei, Haiqiao, and Chen, Ceyuan. "Investigation of lubricant induced pre-ignition and knocking combustion in an optical spark ignition engine". In: *Proceedings of the Combustion Institute* 37.4 (2019), pp. 4901–4910.

Ferguson, Colin R and Keck, James C. "On laminar flame quenching and its application to spark ignition engines". In: *Combustion and Flame* 28 (1977), pp. 197–205.

Fluent, ANSYS et al. *Theory guide*. 2015.

Fogla, Navin, Bybee, Michael, Mirzaeian, Mohsen, Millo, Federico, and Wahiduzzaman, Syed. "Development of a K-k-e Phenomenological Model to Predict In-Cylinder Turbulence". In: *SAE International Journal of Engines* 10.2 (2017), pp. 562–575.

García, Antonio, Monsalve-Serrano, Javier, Martínez-Boggio, Santiago, Roso, Vinícius Rückert, and Santos, Nathália Duarte Souza Alvarenga. "Potential of bio-ethanol in different advanced combustion modes for hybrid passenger vehicles". In: *Renewable Energy* 150 (2020), pp. 58–77.

Garrett, T Ken. "Porsche stratified charge engine". In: *Environmental Science & Technology* 9.9 (1975), pp. 826–830.

Gentz, Gerald, Thelen, Bryce, Litke, Paul, Hoke, John, and Toulson, Elisa. "Combustion visualization, performance, and CFD modeling of a prechamber turbulent jet ignition system in a rapid compression machine". In: *SAE International Journal of Engines* 8.2 (2015), pp. 538–546.

Gentz, Gerald et al. "A study of the influence of orifice diameter on a turbulent jet ignition system through combustion visualization and performance characterization in a rapid compression machine". In: *Applied Thermal Engineering* 81 (2015), pp. 399–411.

Germane, Geoff J, Wood, Carl G, and Hess, Clay C. "Lean combustion in spark-ignited internal combustion engines-a review". In: *SAE Technical Paper* (1983).

Getzlaff, J, Pape, J, Gruenig, C, Kuhnert, D, and Latsch, R. "Investigations on pre-chamber spark plug with pilot injection". In: *SAE Transactions* (2007), pp. 421–433.

Gholamisheeri, Masumeh, Thelen, Bryce, Gentz, Gerald, and Toulson, Elisa. "CFD modeling of an auxiliary fueled turbulent jet ignition system in a Rapid Compression Machine". In: *SAE Technical Paper* (2016).

Gholamisheeri, Masumeh, Wichman, Indrek S., and Toulson, Elisa. "A study of the turbulent jet flow field in a methane fueled turbulent jet ignition (TJI) system". In: *Combustion and Flame* 183 (2017), pp. 194–206. DOI: 10.1016/j.combustflame.2017.05.008.

Gilbert, B. "Turbulence measurements in a flow generated by the collision of radially flowing wall jets". In: *Experiments in fluids* 7.2 (1989), pp. 103–110.

Gimeno, Jaime, Bracho, Gabriela, Martí-Aldaraví, Pedro, and Peraza, Jesús E. "Experimental study of the injection conditions influence over n-dodecane and diesel sprays with two ECN single-hole nozzles. Part I: Inert atmosphere". In: *Energy Conversion and Management* 126 (2016), pp. 1146–1156.

Grasreiner, Sebastian, Neumann, Jens, Luttermann, Christoph, Wensing, Michael, and Hasse, Christian. "A quasi-dimensional model of turbulence and global charge motion for spark ignition engines with fully variable valvetrains". In: *International Journal of Engine Research* 15.7 (2014), pp. 805–816.

Gussak, LA. "x0201C; Method of Precham ber&# x002d; Torch Ignition in Internal Combus tion Engines. &# x0201D; US Pat". In: *Off* 3.230 (1963), p. 939.

Gussak, LA, Karpov, VP, and Tikhonov, Yu V. "The application of lag-process in prechamber engines". In: *SAE Transactions* (1979), pp. 2355–2380.

Hamori, Ferenc and Watson, Harry C. "Hydrogen assisted jet ignition for the hydrogen fuelled SI engine". In: *world hydrogen energy conference*. 15. 2006.

HanZ, ReitzRD. "Turbulencemodelingofinternalcomî bustionenginesusingRNGkî models". In: *CombustSciî enceandTechnology* 106 (1995), 267r295.

Harada, Jun, Tomita, Tsutomu, Mizuno, Hiroyuki, Mashiki, Zenichiro, and Ito, Yasushi. "Development of direct injection gasoline engine". In: *SAE transactions* (1997), pp. 767–776.

Heywood, John B. *Internal combustion engine fundamentals*. Mcgraw-hill, 1988.

Hiraoka, Kenji, Nomura, Kazutoshi, Yuuki, Akihiro, Oda, Yuji, and Kameyama, Toshiyuki. "Phenomenological 0-Dimensional Combustion Model for Spark-Ignition Natural Gas Engine Equipped with Pre-Chamber". In: *SAE Technical Paper* (2016).

Hosey, Richard J and Powell, JD. "Closed loop, knock adaptive spark timing control based on cylinder pressure". In: (1979).

Huang, CC, Shy, SS, Liu, CC, and Yan, YY. "A transition on minimum ignition energy for lean turbulent methane combustion in flamelet and distributed regimes". In: *Proceedings of the Combustion Institute* 31.1 (2007), pp. 1401–1409.

Huang, Yuhan et al. "Fuel consumption and emissions performance under real driving: Comparison between hybrid and conventional vehicles". In: *Science of The Total Environment* 659 (2019), pp. 275–282.

Huber, ML. "NIST thermophysical properties of hydrocarbon mixtures database (SUPERTRAPP)". In: *NIST Standard Reference Database* 4 (2003).

Ikegami, Makoto, Shioji, M, and Koike, M. "A stochastic approach to model the combustion process in direct-injection diesel engines". In: *Symposium (International) on Combustion*. Vol. 20. 1. Elsevier. 1985, pp. 217–224.

James, Revis, Richels, Richard, Blanford, Geoff, and Gehl, Steve. "The power to reduce CO {sub 2} emissions: the full portfolio. Discussion paper". In: (2007).

Jamrozik, Arkadiusz. "Lean combustion by a pre-chamber charge stratification in a stationary spark ignited engine". In: *Journal of Mechanical Science and Technology* 29.5 (2015), pp. 2269–2278.

Jamrozik, Arkadiusz, Tutak, Wojciech, Kociszewski, Arkadiusz, and Sosnowski, Marcin. "Numerical simulation of two-stage combustion in SI engine with prechamber". In: *Applied Mathematical Modelling* 37.5 (2013), pp. 2961–2982.

Jarquin, G, Polupan, G, and RODRÍGUEZ, J. "Cálculo de los productos de combustión empleando métodos numéricos". In: *Mecánica Computacional* 22 (2003), pp. 2442–2452.

Johansson, Peter S and Andersson, Helge I. "Direct numerical simulation of two opposing wall jets". In: *Physics of Fluids* 17.5 (2005), p. 055109.

John, B. "Heywood, Internal combustion engine fundamentals". In: *Pub: McGraw Hill International Editions* (1988).

John, James EA. *Lean burn engine concepts-emissions and economy*. Tech. rep. SAE Technical Paper, 1975.

Kärrholm, Fabian Peng. *Numerical modelling of diesel spray injection, turbulence interaction and combustion*. Chalmers University of Technology Gothenburg, Sweden, 2008.

Knorr, Thomas, Ellmer, Dietmar, Baensch, Simon, and Schatz, Dr Axel. "Optimization of the 48 Volt Hybrid Technology to Minimize Local Emissions in the RDE". In: *Aachener Colloquium*. 2018, pp. 08–10.

Kojic, Aleksandar, Hathout, Jean-Pierre, Cook, David, and Ahmed, Jasim. *Control of auto-ignition timing for combustion in piston engines by prechamber compression ignition*. US Patent 6,953,020. 2005.

Kojic, Aleksandar, Hathout, Jean-Pierre, Cook, David, and Ahmed, Jasim. *Control of auto-ignition timing for homogeneous combustion jet ignition engines*. US Patent 7,107,964. 2006.

Kolla, H, Rogerson, JW, and Swaminathan, N. "Validation of a turbulent flame speed model across combustion regimes". In: *Combustion Science and Technology* 182.3 (2010), pp. 284–308.

Konig, G and Sheppard, CGW. "End gas autoignition and knock in a spark ignition engine". In: *SAE transactions* (1990), pp. 820–839.

Labeckas, Gvidonas and Slavinskas, Stasys. "Combustion phenomenon, performance and emissions of a diesel engine with aviation turbine JP-8 fuel and rapeseed biodiesel blends". In: *Energy Conversion and Management* 105 (2015), pp. 216–229.

Lapuerta, Magín, Ballesteros, Rosario, and Barba, Javier. "Strategies to introduce n-butanol in gasoline blends". In: *Sustainability* 9.4 (2017), p. 589.

Latsch, Reinhard. "The swirl-chamber spark plug: a means of faster, more uniform energy conversion in the spark-ignition engine". In: *SAE transactions* (1984), pp. 365–377.

Lee, RC and Wimmer, Donn Braden. "Exhaust emission abatement by fuel variations to produce lean combustion". In: *SAE Transactions* (1968), pp. 3025–3044.

Lezanski, T, Kesler, M, Rychter, T, Teodorczyk, A, and Wolanski, P. *Performance of pulsed jet combustion (PJC) system in a research engine*. Tech. rep. SAE Technical Paper, 1993.

Li, Jianwen, Matthews, Ronald D, Stanglmaier, Rudolf H, Roberts, Charles E, and Anderson, Richard W. "Further experiments on the effects of in-cylinder wall wetting on HC emissions from direct injection gasoline engines". In: *SAE transactions* (1999), pp. 2213–2224.

Lombardi, Lidia, Tribioli, Laura, Cozzolino, Raffaello, and Bella, Gino. "Comparative environmental assessment of conventional, electric, hybrid, and fuel cell powertrains based on LCA". In: *The International Journal of Life Cycle Assessment* 22.12 (2017), pp. 1989–2006.

López-Pintor, Darío. "Theoretical and experimental study on the autoignition phenomena of homogeneous reactive mixtures". PhD thesis. 2017.

Macián, V, Luján, JM, Bermúdez, V, and Guardiola, C. "Exhaust pressure pulsation observation from turbocharger instantaneous speed measurement". In: *Measurement Science and Technology* 15.6 (2004), p. 1185.

Maly, R, Saggau, B, Wagner, E, and Ziegler, G. "Prospects of ignition enhancement". In: *SAE transactions* (1983), pp. 405–422.

Manin, Julien, Bardi, Michele, and Pickett, Lyle M. "Evaluation of the liquid length via diffused back-illumination imaging in vaporizing diesel sprays". In: *The Proceedings of the International symposium on diagnostics and modeling of combustion in internal combustion engines*. Vol. 8. Fukuoka, 2012, pp. 665–673. DOI: 10.1299/jmsesdm.2012.8.665.

Marion, Mallory. *Internal combustion engine*. US Patent 2,121,920. 1938.

Martín, Jaime. "Contribución al diagnóstico de la combustión en motores Diesel de inyección directa". PhD thesis. Universitat Politècnica de València, 2007.

Martinez, Santiago, Irimescu, Adrian, Merola, Simona Silvia, Lacava, Pedro, and Curto-Riso, Pedro. "Flame front propagation in an optical GDI engine under stoichiometric and lean burn conditions". In: *Energies* 10.9 (2017), p. 1337.

Mayer, El. "A theory of flame propagation limits due to heat loss". In: *Combustion and Flame* 1.4 (1957), pp. 438–452.

Metghalchi, Mohamad and Keck, James C. "Burning velocities of mixtures of air with methanol, isooctane, and indolene at high pressure and temperature". In: *Combustion and flame* 48 (1982), pp. 191–210.

Muralidharan, K, Vasudevan, D, and Sheeba, KN. "Performance, emission and combustion characteristics of biodiesel fuelled variable compression ratio engine". In: *Energy* 36.8 (2011), pp. 5385–5393.

Najt, Paul M and Foster, David E. "Compression-ignited homogeneous charge combustion". In: *SAE Transactions* (1983), pp. 964–979.

Nakamura, Norihiko, Kobayashi, Tatsuo, Hanaoka, Masanori, and Takagi, Noboru. *A new platinum tipped spark plug extends the lean misfire limit and useful life*. Tech. rep. SAE Technical Paper, 1983.

Noguchi, M, Sanda, S, and Nakamura, N. "Development of Toyota lean burn engine". In: *SAE Transactions* (1976), pp. 2358–2373.

Novella, R., Gomez-Soriano, J., Martinez-Hernandiz, P. J., and Libert, C. "Evaluation of the passive pre-chamber ignition concept for future high compression ratio turbocharged spark-ignition engines". In: *Applied energy* 248 (2019), pp. 576–588.

Noyori, Takahiro. *Experimental study of smoke emission on small-displacement spark-ignition direct-injection engine*. Tech. rep. SAE Technical Paper, 2006.

Onishi, Shigeru, Jo, Souk Hong, Shoda, Katsuji, Jo, Pan Do, and Kato, Satoshi. "Active thermo-atmosphere combustion (ATAC)âa new combustion process for internal combustion engines". In: *SAE Transactions* (1979), pp. 1851–1860.

Öztürk, Erkan. "Performance, emissions, combustion and injection characteristics of a diesel engine fuelled with canola oil–hazelnut soapstock biodiesel mixture". In: *Fuel Processing Technology* 129 (2015), pp. 183–191.

Park, Cheolwoong, Kim, Sungdae, Kim, Hongsuk, and Moriyoshi, Yasuo. "Stratified lean combustion characteristics of a spray-guided combustion system in a gasoline direct injection engine". In: *Energy* 41.1 (2012), pp. 401–407.

Parrish, Scott E. "Evaluation of liquid and vapor penetration of sprays from a multi-hole gasoline fuel injector operating under engine-like conditions". In: *SAE International Journal of Engines* 7.2 (2014), pp. 1017–1033.

Payri, F, Molina, S, Martín, J, and Armas, O. "Influence of measurement errors and estimated parameters on combustion diagnosis". In: *Applied Thermal Engineering* 26.2-3 (2006), pp. 226–236.

Payri, R, Salvador, FJ, Gimeno, J, and Zapata, LD. "Diesel nozzle geometry influence on spray liquid-phase fuel penetration in evaporative conditions". In: *Fuel* 87.7 (2008), pp. 1165–1176.

Payri, Raul, Gimeno, Jaime, Bardi, Michele, and Plazas, Alejandro H. "Study liquid length penetration results obtained with a direct acting piezo electric injector". In: *Applied energy* 106 (2013), pp. 152–162.

Payri, Raul, Gimeno, Jaime, Bracho, Gabriela, and Vaquerizo, Daniel. "Study of liquid and vapor phase behavior on Diesel sprays for heavy duty engine nozzles". In: *Applied Thermal Engineering* 107 (2016), pp. 365–378. DOI: 10.1016/j.applthermaleng.2016.06.159.

Payri, Raul, Gimeno, Jaime, Peraza, Jesús, and Bazyn, Tim. "Spray/wall interaction analysis on an ECN single-hole injector at diesel-like conditions through Schlieren visualization." In: *Ilass Europe. 28th european conference on Liquid Atomization and Spray Systems*. Editorial Universitat Politècnica de València. 2017, pp. 200–207.

Payri, Raul, Salvador, FJ, Gimeno, J, and Bracho, G. "A new methodology for correcting the signal cumulative phenomenon on injection rate measurements". In: *Experimental techniques* 32.1 (2008), pp. 46–49.

Pei, Yiqiang et al. "Experimental investigation on free and impingement spray fueled with methanol, ethanol, isooctane, TRF and gasoline". In: *Fuel* 208 (2017), pp. 174–183.

Peters, Norbert. *Turbulent combustion*. Cambridge Univer, 1941.

Pham, Allen and Jeftic, Marko. *Characterization of Gaseous Emissions from Blended Plug-In Hybrid Electric Vehicles during High-Power Cold-Starts*. Tech. rep. SAE Technical Paper, 2018.

Pischinger, Stefan and Heywood, John B. "A model for flame kernel development in a spark-ignition engine". In: *Symposium (international) on Combustion*. Vol. 23. 1. Elsevier. 1991, pp. 1033–1040.

Poinsot, TJ, Haworth, Daniel Connell, and Bruneaux, Gilles. "Direct simulation and modeling of flame-wall interaction for premixed turbulent combustion". In: *Combustion and Flame* 95.1-2 (1993), pp. 118–132.

Popp, P and Baum, M. "Analysis of wall heat fluxes, reaction mechanisms, and unburnt hydrocarbons during the head-on quenching of a laminar methane flame". In: *Combustion and Flame* 108.3 (1997), pp. 327–348.

Pöschl, M and Sattelmayer, T. "Influence of temperature inhomogeneities on knocking combustion". In: *Combustion and Flame* 153.4 (2008), pp. 562–573.

Poulos, Stephen G and Heywood, John B. "The effect of chamber geometry on spark-ignition engine combustion". In: *SAE transactions* (1983), pp. 1106–1129.

Quader, Ather A. "Lean combustion and the misfire limit in spark ignition engines". In: *SAE transactions* (1974), pp. 3274–3296.

Rahmstorf, Stefan, Foster, Grant, and Cahill, Niamh. "Global temperature evolution: recent trends and some pitfalls". In: *Environmental Research Letters* 12.5 (2017), p. 054001.

Rapp, V, Killingsworth, N, Therkelsen, P, and Evans, R. "Lean-burn internal combustion engines". In: *Lean Combustion*. Elsevier, 2016, pp. 111–146.

Ricardo, Harry R. *Internal combustion engine of the liquid fuel injection type*. US Patent 2,066,228. 1936.

Richards, K, Senecal, P, and Pomraning, E. "CONVERGE Manual-CONVERGE CFD 2.3". In: *Madison, WI* (2016).

Robinet, Cyril, Higelin, Pascal, Moreau, B, Pajot, O, and Andrzejewski, J. "A New Firing Concept for Internal Combustion Engines:" I'APIR"". In: *SAE transactions* (1999), pp. 973–988.

Ronney, Paul D. "Laser versus conventional ignition of flames". In: *Optical Engineering* 33.2 (1994), pp. 510–522.

Schlatter, Stephanie, Schneider, Bruno, Wright, Yuri, and Boulouchos, Konstantinos. *Experimental study of ignition and combustion characteristics of a diesel pilot spray in a lean premixed methane/air charge using a rapid compression expansion machine*. Tech. rep. SAE Technical Paper, 2012.

Scott, Donald William. *Chemical Thermodynamic Properties of Hydrocarbons and Related Substances: Properties of the Alkane Hydrocarbons, C1 through C10, in the Ideal Gas State From 0 to 1500 K*. Vol. 666. US Department of the Interior, Bureau of Mines, 1974.

Selvam, D John Panneer and Vadivel, K. "Performance and emission analysis of DI diesel engine fuelled with methyl esters of beef tallow and diesel blends". In: *Procedia Engineering* 38 (2012), pp. 342–358.

Shim, Euijoon, Park, Hyunwook, and Bae, Choongsik. "Comparisons of advanced combustion technologies (HCCI, PCCI, and dual-fuel PCCI) on engine performance and emission characteristics in a heavy-duty diesel engine". In: *Fuel* 262 (2020), p. 116436.

Smy, PR, Clements, RM, Simeoni, D, and Topham, DR. "Plasma expulsion from the plasma jet igniter". In: *Journal of Physics D: Applied Physics* 15.11 (1982), p. 2227.

Statgraphics Centurion XVII is a trademark of Statgraphics Technologies, Inc. *http://www.statgraphics.com/*.

Stone, CR, Brown, AG, and Beckwith, P. *Cycle-by-cycle variations in spark ignition engine combustion-part ii: Modelling of flame kernel displacements as a cause of cycle-by-cycle variations*. Tech. rep. SAE Technical Paper, 1996.

Swinehart, DF. "The beer-lambert law". In: *Journal of chemical education* 39.7 (1962), p. 333.

Tabaczynski, Rodney J, Trinker, Frederick H, and Shannon, Ben AS. "Further refinement and validation of a turbulent flame propagation model for spark-ignition engines". In: *Combustion and Flame* 39.2 (1980), pp. 111–121.

Tanuma, Takeshi, Sasaki, Kenichi, Kaneko, Touru, and Kawasaki, Hajime. "Ignition, combustion, and exhaust emissions of lean mixtures in automotive spark ignition engines". In: *SAE Transactions* (1971), pp. 663–673.

Taylor, Andrew B et al. *Gasoline/alcohol blends: exhaust emissions, performance and burn-rate in a multi-valve production engine*. Tech. rep. SAE Technical Paper, 1996.

Thelen, Bryce C, Chun, Daekeun, Toulson, Elisa, and Lee, Tonghun. "A study of an energetically enhanced plasma ignition system for internal combustion engines". In: *IEEE Transactions on Plasma Science* 41.12 (2013), pp. 3223–3232.

Thring, RH. "Alternative fuels for spark-ignition engines". In: *SAE transactions* (1983), pp. 715–725.

Tinaut, FV. "Contribución al estudio del proceso de combustión en motores de encendido por compresión de inyección directa". PhD thesis. Tesis Doctoral, Universidad Politécnica de Valencia, Valencia, 1986.

Toulson, Elisa. "Applying alternative fuels in place of hydrogen to the jet ignition process". PhD thesis. 2008.

Toulson, Elisa, Schock, Harold J, and Attard, William P. "A review of prechamber initiated jet ignition combustion systems". In: (2010).

Toulson, Elisa, Watson, Harry C, and Attard, William P. *The lean limit and emissions at near-idle for a gasoline HAJI system with alternative prechamber fuels*. Tech. rep. SAE Technical Paper, 2007.

Toulson, Elisa, Watson, Harry C, and Attard, William P. *Modeling alternative prechamber fuels in jet assisted ignition of gasoline and LPG*. Tech. rep. SAE Technical Paper, 2009.

Toulson, Elisa et al. "Visualization of propane and natural gas spark ignition and turbulent jet ignition combustion". In: *SAE International Journal of Engines* 5.4 (2012), pp. 1821–1835.

Tripathi, Abhinav, Zhang, Chen, and Sun, Zongxuan. "Experimental investigation and analysis of auto-ignition combustion dynamics". In: *ASME 2018 Dynamic Systems and Control Conference*. American Society of Mechanical Engineers Digital Collection. 2018.

Truth, An Inconvenient. "directed by Davis Guggenheim". In: *Performed by Al Gore* (2006).

Turns, Stephen R et al. *Introduction to combustion*. Vol. 287. McGraw-Hill Companies, 1996.

Van Leer, Bram. "Towards the ultimate conservative difference scheme. V. A second-order sequel to Godunov's method". In: *Journal of computational Physics* 32.1 (1979), pp. 101–136.

Varde, Keshav S and Lubin, MJ. *The Roll of Connecting Nozzle and the Flame Initiation Point in the Performance of a Dual Chamber Stratified Charge Engine*. Tech. rep. SAE Technical Paper, 1974.

Villela, Antonio Carlos Scardini, Egúsquiza, Julio César Cuisano, Machado, Guilherme Bastos, and Braga, Sérgio Leal. *Rapid Compression Machine Tests for Brazilian Otto Cycle Fuels*. Tech. rep. SAE Technical Paper, 2011.

Watson, Harry C. *Internal combustion engine ignition device*. US Patent 5,611,307. 1997.

Weng, Volker et al. *Investigation of the Bowl-Prechamber-Ignition (BPI) Concept in a Direct Injection Gasoline Engine at Part Load*. Tech. rep. SAE Technical Paper, 1999.

Woschni, Gerhard. "A universally applicable equation for the instantaneous heat transfer coefficient in the internal combustion engine". In: *SAE Technical Paper* (1967).

Wyczalek, Floyd A, Harned, John L, Maksymiuk, S, and Blevins, Jerry R. *EFI prechamber torch ignition of lean mixtures*. Tech. rep. SAE Technical Paper, 1975.

Xu, Guoqing, Kotzagianni, Maria, Kyrtatos, Panagiotis, Wright, Yuri M, and Boulouchos, Konstantinos. "Experimental and numerical investigations of the unscavenged prechamber combustion in a rapid compression and expansion machine under engine-like conditions". In: *Combustion and Flame* 204 (2019), pp. 68–84.

Yamaguchi, Shigeki, Ohiwa, Norio, and Hasegawa, Tatsuya. "Ignition and burning process in a divided chamber bomb". In: *Combustion and flame* 59.2 (1985), pp. 177–187.

Yıldız, Melih and Çeper, Bilge Albayrak. "Zero-dimensional single zone engine modeling of an SI engine fuelled with methane and methane-hydrogen blend using single and double Wiebe Function: A comparative study". In: *International journal of hydrogen energy* 42.40 (2017), pp. 25756–25765.

Young, Michael B. "Cyclic dispersion in the homogeneous-charge spark-ignition engineâa literature survey". In: *SAE Transactions* (1981), pp. 49–73.

Zabetakis, Michael George. *Flammability characteristics of combustible gases and vapors*. Tech. rep. Bureau of Mines Washington DC, 1965.

Zhen, Xudong et al. "The engine knock analysis–An overview". In: *Applied Energy* 92 (2012), pp. 628–636.